Clusters et molécules dans les plasmas générés par laser : cinétique et thermodynamique

Arsène Chemin

▶ **To cite this version:**

Arsène Chemin. Clusters et molécules dans les plasmas générés par laser : cinétique et thermodynamique. Plasmas. Université de Lyon, 2021. English. NNT : 2021LYSE1152 . tel-03498759

HAL Id: tel-03498759

https://theses.hal.science/tel-03498759v1

Submitted on 21 Dec 2021

HAL is a multi-disciplinary open access archive for the deposit and dissemination of scientific research documents, whether they are published or not. The documents may come from teaching and research institutions in France or abroad, or from public or private research centers.

L'archive ouverte pluridisciplinaire **HAL**, est destinée au dépôt et à la diffusion de documents scientifiques de niveau recherche, publiés ou non, émanant des établissements d'enseignement et de recherche français ou étrangers, des laboratoires publics ou privés.

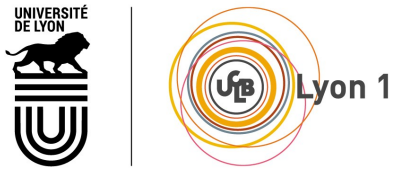

N^o d'ordre NNT : 2021LYSE1152

THESE de DOCTORAT DE L'UNIVERSITE DE LYON

opérée au sein de

l'Université Claude Bernard Lyon1

Ecole Doctorale N^o 52

PHYSIQUE ET ASTROPHYSIQUE DE LYON (PHAST)

Discipline : Physique

Soutenue publiquement le 23/07/2021, par :

Arsène Chemin

Clusters and Molecules in Laser Generated Plasmas: Kinetics & Thermodynamics

---

Devant le jury composé de :

Anne Pillonnet, Professeure à l'Université Claude Bernard Lyon 1	Présidente
Alessandro De Giacomo, Professeur à l'Université de Bari	Rapporteur
Jörg Hermann, Directeur de Recherche au CNRS	Rapporteur
Maxime Mikikian, Directeur de Recherche à l'Université d'Orléans	Examinateur
Cathy Rond, Maître de Conférences à l'Université Sorbonne Paris Nord	Examinatrice
David Amans, Maître de Conférences à l'Université Claude Bernard	Directeur de thèse

Remerciements

Les remerciements sont sans doute la partie la plus lue et appréciée d'un manuscrit de thèse. Je vais donc tâcher de les écrire à la hauteur de toutes ces personnes qui ont compté pour moi durant ces trois années de thèses. Il y a 10 ans, j'ai eu la chance de rencontrer le philosophe et généticien Albert Jacquard qui m'a fait prendre conscience que notre vie est faite de la somme de nos rencontres. J'aimerais aujourd'hui remercier celles et ceux qui m'ont permis d'en arriver là.

L'une de ces rencontres est ma professeure de Lycée Nadège Buriller qui a su m'ouvrir les portes de ce monde qu'est la recherche. Sans toi je n'aurais jamais eu le parcours qui m'a mené jusqu'ici. Déjà en terminale, tu me disais que j'intégrerais l'ENS et que je ferais une thèse. A cette époque, je ne t'avais pas cru. Aujourd'hui, je suis très heureux de t'avoir retrouvée lors de ma soutenance.

Une autre de ces rencontres fut bien évidemment David Amans, au détour d'une annonce de stage de L3. Par chance, j'ai suffisamment bien travaillé durant mon stage pour que tu me proposes une thèse. Merci pour m'avoir accordé ta confiance et ton soutien. Tu m'as toujours permis et encouragé à suivre la direction que je souhaitais. Avec toi, j'étais libre de faire la recherche que j'aime, d'explorer ma curiosité, de développer mes projets. C'est une chance d'avoir pu faire cette thèse à tes côtés et je sais que nos discussions mouvementées vont me manquer.

Merci également aux collaborateur.rice.s qui m'ont permis de mener à bien ces recherches et qui ont supporté mes questions : Abdul-Rahman Allouche, Patrice Mélinon, Amanda Ross, Patrick Crozet, Ken Miyajima et Fumitaka Mafuné. Merci aux stagiaires qui m'ont aidé dans mes recherches : Louhanne, Théo et Médhi. J'espère que vous avez pu profiter de vos stages avec moi autant que j'ai pu profiter des miens et appris autant que j'ai pu apprendre de vous. Merci pour votre travail et votre curiosité.

Merci à l'équipe et au chercheur.se.s de l'ILM. Grâce à vous, ce fut un plaisir de venir travailler et échanger chaque jour au laboratoire (ou presque...). Merci Christophe pour ton soutien indéfectible. Plus qu'un chef d'équipe, tes conseils et ta bienveillance m'ont aidé à avancer. Merci à Benoit pour nos discussions en tout genre et ton goût certain pour les trucs macérés qui se mangent et qui se boivent ! Merci à Julien pour nos débats tout aussi drôles que navrants. Merci à Vincent et Sylvain pour vos conseils précieux. Merci à l'équipe technique, Jeff, Valentin et Yann, pour leur aide et pour ces moments de détentes au détour d'une tasse de café ou d'un gâteau à l'atelier. Merci à Gilles, Amina, Jérémy, Anne, Estelle et tant d'autres pour avoir fait de ces trois ans au labo bien plus qu'un projet de recherche.

I also want to thank Alessandro De Giacomo and Jörg Hermann for rewieving my manuscript. Despite its length, you read it carefully and asked me sharp and accurate questions, challenging my conclusions and discussing very interesting

physics. Merci egalement à Cathy Rond et Maxime Mikikan d'avoir accepté de participer au jury. Ce fut un plaisir de discuter avec vous de mon travail. Enfin merci à Anne Pillonnet d'avoir accepté de présider mon jury.

Thank you so much to my English friends I met around the world, for reading my manuscript and helping me: Benedict, John, Mitchell, Austin, Andrew James, Annie and Harry, Bob, and Christopher. Merci aux thésards qui ont partagé mon bureau et mes pauses café : Amira, Gaétan, Max, Justine, Zhu, Matilde et Askhan. Merci aux gens d'en face et à leur cafetière digne de ce nom. Vous avez été pour moi une deuxième équipe d'adoption. Merci à mes amis du Domus : Tinj', Elise, Clément, Tomtom et Vicky, avec qui j'ai partagé tant de repas, tant de discussions passionnées, tant de débats. J'ai eu de la chance de vous avoir durant ces trois ans et j'espère vous garder près de moi bien plus encore.

Merci à Manu, pour nous avoir ouvert ton petit havre de paix durant ces périodes de confinement. Là-bas j'ai écrit les premières pages de ce manuscrit. Merci à Gilles pour tes conseils avisés et ton soutien dans les moments difficiles.

Et enfin merci à ma famille, ma mère Dominique, mon père Jean-Louis, mes sœurs Charlène et Maud pour avoir toujours cru en moi et m'avoir permis d'en arriver là. Merci à Constance, Camille et Catherine pour votre accueil toujours chaleureux et ressourçant. Merci à Evgenii d'avoir suivi mon chemin après que nos routes se sont croisées. Merci de m'avoir soutenu, encouragé et épaulé.

Difficile d'être exhaustif sans rajouter trop de pages à ce mémoire déjà trop long. Une chose est certaine, de cette surprenante expérience que fut cette thèse, je ne retiens que des merveilleuses personnes avec qui j'ai réfléchi, appris et ri.

Préambule

Connaissez-vous la nébuleuse du crabe ? Il s'agit d'un immense nuage interstellaire créé par l'explosion d'une étoile. Cette supernova fut si violente qu'elle fut observée par les chinois au XI^{eme} siècle. Depuis ce jour, on peut observer à sa place un surprenant nuage multicolore au milieu de l'espace. Ce nuage est en réalité constitué d'un gaz d'atomes et d'électrons libres extrêmement chauds : plusieurs dizaines de milliers de degrés ! C'est ce que l'on appelle un plasma. Bien sûr, je ne parle ici ni de plasma sanguin, ni de télévision. Mais bien d'un quatrième état de la matière, au même titre que les solides, les liquides ou les gaz. Dans ce plasma, les atomes se heurtent en permanence et parfois, parfois seulement, se lient pour former des molécules. Molécules devenant de plus en plus grosses, formant des poussières, puis des grains, des cailloux, des rochers, des planètes ! Notre planète... Et nous. Oui toi, toi aussi. Car tu es poussière... mais poussière d'étoiles. Tout ce qui nous entoure est né de ce phénomène que l'on appelle nucléation. Et c'est ce phénomène que j'étudie durant ma thèse. Au fond de mon laboratoire, je ne regarde malheureusement pas les étoiles. Caché dans l'obscurité d'une cave, j'étudie ce phénomène de nucléation en détruisant des matériaux avec un laser. C'est vrai que dit comme ça, j'ai un peu l'impression d'être *Gold Finger*, vous savez lorsqu'il essaie de découper James Bond avec un laser. Eh bien ce n'est pas si loin ! Mon laser est si puissant qu'il va provoquer une mini-explosion et un plasma de quelques millimètres. Une sorte de mini-supernova. Lorsque le plasma refroidit, les atomes créent des molécules de plus en plus grosses jusqu'à former des nanoparticules. Ce sont de tout petits cristaux de quelques nanomètres de diamètre, invisible à l'œil nu. Mes nano-planètes à moi. Or, ces nanoparticules peuvent être très utiles ! Par exemple, nous savons en fabriquer qui sont capables d'inhiber les agents chimiques présents dans les armes de guerre. Si nous comprenions comment elles se forment, nous pourrions en créer de toute sorte ! Alors, pour essayer de les voir se former, j'éclaire le plasma avec un autre laser dont je fais varier la couleur. Chaque molécule va absorber certaines couleurs et en émettre d'autres, c'est ce qu'on appelle la fluorescence. La combinaison des couleurs absorbées et émises est propre à chacune des molécules : une sorte d'empreinte digitale si l'on veut. Et tel un détective, j'essaie de reconnaitre quelles molécules se forment au court du temps. Alors bien sûr nous sommes loin de tout comprendre à ce phénomène de nucléation... Mais comme le disait Oscar Wilde, "Il faut toujours viser la lune, car même en cas d'échec, on atterrit dans les étoiles".

Written for *Ma thèse en 180 secondes*[*] in 2020

[*]French version of Three Minute Thesis

Résumé

Les plasmas générés par laser sont des systèmes complexes. L'énergie de l'impulsion laser conduit à une transition de phase brutale. Le plasma formé est composé de molécules, d'atomes, d'ions et d'électrons qui réagissent entre eux et avec l'environnement. De tels plasmas sont utilisés pour mesurer la composition d'échantillons (LIBS), pour produire des clusters et des nanoparticules, pour déposer des matériaux, etc. La compréhension de la cinétique et de la thermodynamique du plasma est essentielle afin de mieux comprendre l'évolution temporelle de la composition du plasma. Pour cela, mesurer les températures, la pression, la densité, la composition chimique au cours du temps permet de caractériser l'état du plasma, son écart à l'équilibre thermodynamique, et donc de mieux décrire l'évolution de sa composition chimique et les mécanismes de nucléation. Ce travail étudie plusieurs aspects de cette question, depuis un modèle général de nucléation capable de décrire la croissance des particules dans le plasma, jusqu'à la détermination de quantités thermodynamiques telles que la pression et la température.

Un modèle de type complexe activé est développé afin de décrire la nucléation des clusters. Il utilise l'approche micro-canonique de Weisskopf pour traiter la cinétique de la croissance lorsque la nature transitoire des processus met en défaut l'ensemble canonique. Ce modèle reproduit efficacement les distributions expérimentales de taille de clusters d'oxyde d'aluminium. L'énergie d'activation des réactions est abordée à l'aide de calculs DFT et de mesures expérimentales. Ces résultats, comparés au modèle, montrent que l'équilibre thermodynamique n'est pas atteint pendant la croissance et qu'il n'y a pas d'équipartition de l'énergie dans les clusters. L'énergie de liaison mesurée est dix fois plus faible que l'énergie donnée par les calculs DFT et que l'énergie de cohésion du cristal.

L'un des paramètres clés dans la description des plasmas générés par laser est la pression. Elle est mesurée à partir de la dynamique de l'onde de choc générée en fonction de l'énergie de l'impulsion et peut atteindre quelques dizaines de MPa dans l'air, contre quelques GPa pour un plasma à une interface liquide/solide. A l'air, Le modèle de Taylor décrit l'évolution de la pression à partir de 20 ns après l'impulsion laser si l'on tient compte de l'anisotropie de l'explosion. La température cinétique moyenne et la composition du plasma sont calculées à partir de cette pression, de la densité électronique et des équations de la LTE. Cette température apparait plus basse que la température mesurée à partir de l'émission atomique, ce qui pourrait être expliqué par des gradients de température ou une défaillance partielle de l'Equilibre Thermodynamique Local (LTE).

La température cinétique dans le plasma est étudiée plus en détail en utilisant des mesures spatio-temporelles de l'émission d'AlO fournissant la température vibrationnelle et rotationnelle de l'état excité des molécules. La température vibrationnelle apparaît beaucoup plus grande que la température rotationnelle, prou-

vant que l'équilibre thermodynamique n'est pas atteint dans la population excitée qui n'a pas assez de temps pour être thermalisée. La température rotationnelle des molécules, plus sujette aux collisions, est probablement proche de la température cinétique du gaz et permet de cartographier les gradients de température dans le plasma.

La fluorescence induite par laser (LIF) est utilisée sur les molécules d'AlO afin de mesurer la durée de vie de l'état excité et la température de l'état fondamental. En raison des collisions, la durée de vie de l'état excité est beaucoup plus courte que celle de référence et doit être caractérisée lors de la détermination de la composition chimique des plasma. Les spectres de fluorescence peuvent être décomposés en deux contributions : la fluorescence directe, qui conserve la population initiale de l'état excité, et la fluorescence induite par collision, qui peuple de nombreux autres niveaux quantiques. En ajustant les spectres de fluorescence, on peut mesurer la température de rotation des molécules dans l'état fondamental. Cette température converge vers celle de l'état excité aux temps longs et y est légèrement inférieur aux temps courts, quand la thermalisation des états rotationnels n'est pas complète.

Abstract

Laser generated plasma is a complex and interesting system. The deposition of the pulse laser energy leads to a brutal phase transition and the formation of a plasma. This plasma is composed of molecules, atoms, ions, and electrons reacting together and with the environment. Such plasmas are used for measuring the composition of a target (LIBS), for producing clusters and nanoparticles, for material deposition, etc. Understanding the kinetics and the thermodynamics of the plasma is essential in order to better understand the composition of the plasma, its temperature and the nucleation process of clusters and nanoparticles. This work investigates several aspects of this issue, from a general nucleation model able to describe the growth of particles in the plasma, to the determination of thermodynamic quantities such as the pressure and the temperature.

An activated complex-like model is developed in order to describe cluster nucleation. It uses Weisskopf's micro-canonical approach to handle the kinetics of the growth when the transient nature of the processes disregards the canonical ensemble. This model efficiently reproduces experimental size distributions of aluminium oxide clusters. The activation energy of the reactions is addressed using DFT calculations and experimental measurements. These results, compared to the model, show that the thermodynamic equilibrium is not reached during the growth and that there is no equipartition of the energy in the clusters. The bounding energy measured is ten times lower than the energy given by DFT calculations and lower than the bulk cohesive energy.

One of the key parameters in the description of laser-generated plasma is the pressure. It is measured from the dynamics of the generated shock-front as a function of the pulse energy and can reach few tens of MPa in air, and a few GPa in liquids . In air, Taylor's blast model describes the evolution of the pressure from 20 ns after the laser pulse if one takes into account the anisotropy of the blast. The average kinetic temperature and composition of the plasma is computed from the pressure and the electron density LTE equations. This temperature appears to be lower than the temperature measured from atomic emission which could be explained by temperature gradient or partial failure of LTE.

The kinetic temperature in the plasma is further investigated using spatio-temporal measurements of AlO emission providing the vibrational and rotational temperature of the excited state of the molecules. The vibrational temperature appears much larger than the rotational temperature, proving that the thermodynamic equilibrium is not reached in the excited population which has not enough time to be thermalized. The rotational temperature of the molecules, more subject to collisions, is likely to be close to the kinetic temperature of the gas and maps the temperature gradient in the plasma.

Laser-Induced Fluorescence (LIF) is achieved in AlO molecules in order to

measure le life-time of the excited state and the temperature of the ground state. Because of collision, the life-time of the excited state is much shorter than the one tabulated and should be characterized when calculating plasma chemical composition. Fluorescence spectra can be decomposed in two contributions: direct fluorescence, conserving an initial population in excited state, and collisionally-induced fluorescence, populating many other quantum levels. By fitting fluorescence spectra, one can measure the rotational temperature of the ground state molecules. The rotational temperature measured from emission of the excited state appears to be close to the ground state temperature but slightly overestimates it for short delay. The thermalization of the rotational states is not always complete.

Contents

Chapter 1

General introduction

For you are dust,
and to dust you shall return.
Genesis 3.19

When I was young my friends and I used to hike in the mountains near my hometown. One evening we decided to spend the night under the stars but as the sun disappeared, the temperature lowered down. Freezing, at the top of a cliff and in the middle of wild nature, I was unable to sleep. That night the sky offered me an incredible view. All night long I was able to watch the Milky Way slowly turning in front of me. Thousands of stars lighting my sky. That night I felt so insignificant and yet part of a wonderful universe that I craved so much to understand - or at least try to understand.

Let me begin our journey in the stars. Most of the stars you can see, including our sun, will end their lives in the so-called Asymptotic Giant Branch. At this point in their life, stars are composed of various atoms such as carbon, oxygen, or aluminum they have created by nuclear fusion. These atoms form a plasma, that is to say, an ionized gas. Just before running out of fuel for nuclear burning, the stars expand to the size of the Earth's orbit and cool down. Some atoms start to bound together forming molecules. This aggregation phenomenon, called nucleation, creates larger and larger molecules called cosmic dust. More and more

In short: *Along with the whole manuscript, "In short" boxes will provide the reader important information summing up the section in order to ease the reading. During my PhD, I worked mainly on the formation of molecules and nanoparticles in laser-generated Plasma. It is a fundamental issue with broad impact and interests such as cosmology, aerosols, cluster sources, and production of nanoparticles.*

matter is expelled in massive stellar winds rushing the stars to certain death. Yet this death is also the birth of planetary nebulae. Nothing much to do with our beloved planets if not the shape observed by the first astronomers. These nebulae are formed by all the ejected atoms and molecules enveloping the tiny, but hot remnants of the stars called white dwarfs. The ultraviolet radiation from the white dwarf excites the molecules of the nebulae which start to emit colorful light similar to the aurora borealis*. Each color is a fingerprint of the molecules composing this space cloud. This fluorescence phenomenon, just as the absorption spectrum of the molecules, enables astronomers to gauge the composition of the cosmic dust which likely plays a crucial role in the chemistry of the Milky Way. How does the dust appear? How can we describe the growth of these molecules? How can we observe them using fluorescence? Understanding the nucleation phenomenon in dusty plasma is a fundamental question with surprisingly numerous applications and not only for cosmology. The growth of organic aerosols in Titan's ionosphere gives Saturn's moon its beautiful yellow color. The nucleation of aerosols in Earth's ionosphere has great importance in climate and cloud formation. Fine particles of pollution caused by nucleation during combustion are one of the great health issues of modern times. And finally, when a laser is focused on a target, it can create a plasma in which occurs nucleation when it cools down.

For three years, I worked at the Institut Lumière Matière† in Lyon. It is a large institute condensing many research topics combining light and matter. Among them, David Amans developed the topic of laser ablation in liquids. By focussing a laser beam on an immersed target, one can obtain a colloidal suspension of nanoparticles. The atoms in the plasma aggregate just like in space and form tiny particles of a few thousands of atoms. This technique of nanoparticle generation has been used for a few decades. Yet the processes involved in the formation of the particles remain partially unknown. During my PhD, I worked with David Amans and many other collaborators in order to better understand the formation of particles in the laser-generated plasma. In this manuscript, I chose to focus on my work concerning plasma generated in a gas phase for better consistency. During my PhD, I also worked on laser ablation in liquids. In particular, I worked on the production of nanoparticles, the interaction between the liquid and the plasma, the shock-waves generated by the ablation. It led to several papers and one patent and can be found in the annexes.

*Note that most of the pictures, including the illustrations here, are using false colors in order to represent the emission of species which might not emit in the visible light.

†Light and Matter Institute

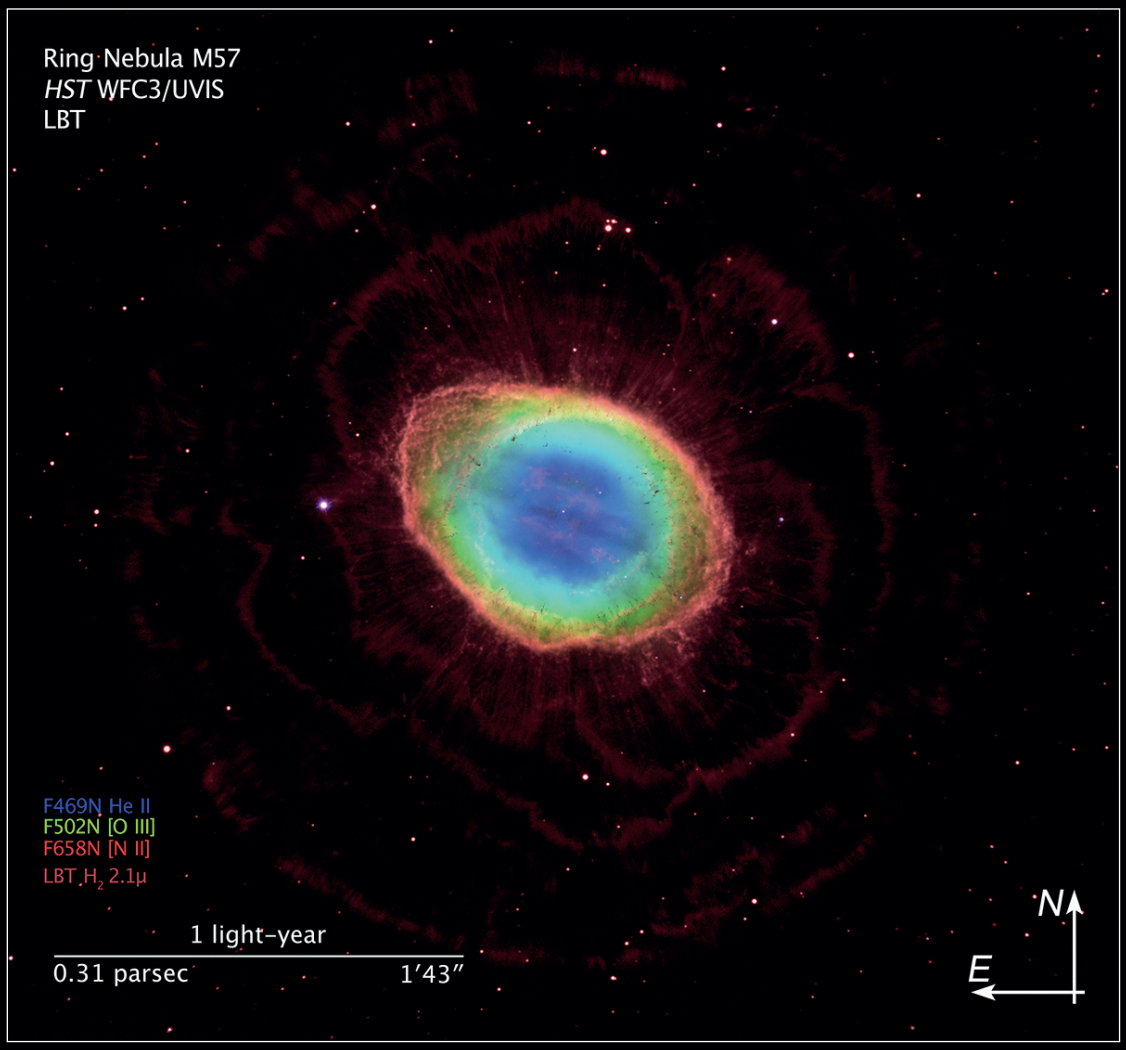

In this composite image, visible-light observations by NASA's Hubble Space Telescope are combined with infrared data from the ground-based Large Binocular Telescope in Arizona to assemble a dramatic view of the well-known Ring Nebula. The Ring Nebula is about 2,000 light-years away in the constellation Lyra. The nebula measures roughly one light-year across.

The blue gas in the nebula's center is actually a football-shaped structure that pierces the red doughnut-shaped material. Hubble also uncovers the detailed structure of the dark, irregular knots of dense gas embedded along the inner rim of the ring. The faint, scallop-shaped material surrounding the ring was expelled by the star during the early stages of the planetary nebula formation. This outer material was imaged by the Large Binocular Telescope, part of the Mount Graham International Observatory in Arizona.

The Hubble observations were taken Sept. 19, 2011, by the Wide Field Camera 3. The Large Binocular Telescope data were taken June 6, 2010. In the image, the blue color represents helium; the green, oxygen; and the red, hydrogen.

From HubbelSite
News release ID: STScI-2013-13

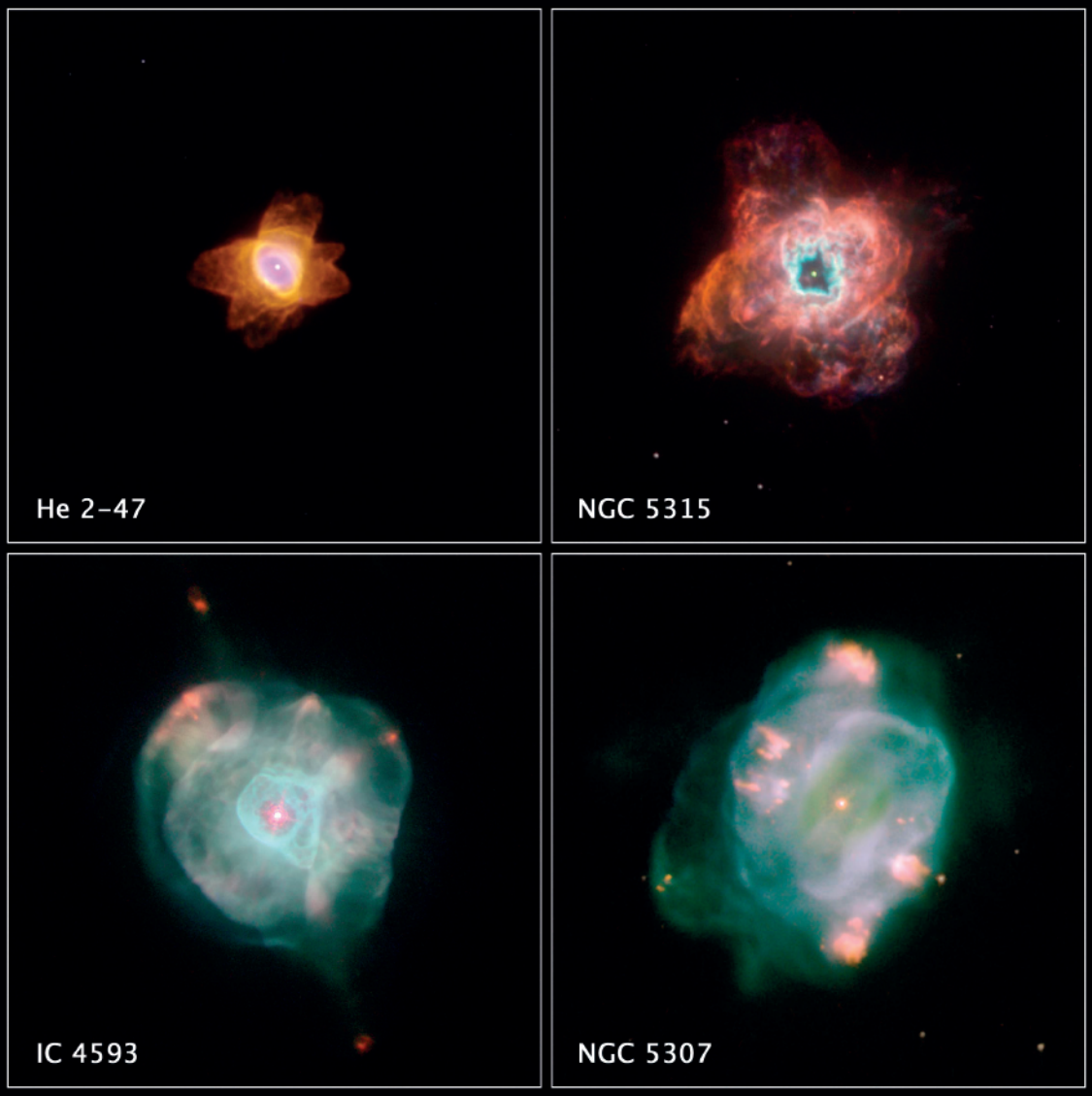

The colorful, intricate shapes in these NASA Hubble Space Telescope images reveal how the glowing gas ejected by dying Sun-like stars evolves dramatically over time. Planetary nebulae last for only 10,000 years, a fleeting episode in the 10-billion-year lifespan of Sun-like stars. The Hubble images show the evolution of planetary nebulae, revealing how they expand in size and change temperature over time. A young planetary nebula, such as He 2-47, at top, left, for example, is small and is dominated by relatively cool, glowing nitrogen gas. In the Hubble images, the red, green, and blue colors represent light emitted by nitrogen, hydrogen, and oxygen, respectively.

Over thousands of years, the clouds of gas expand away and the nebulae become larger. Energetic ultraviolet light from the star penetrates more deeply into the gas, causing the hydrogen and oxygen to glow more prominently, as seen near the center of NGC 5315. In the older nebulae, such as IC 4593, at bottom, left, and NGC 5307, at bottom, right, hydrogen and oxygen appear more extended in these regions, and red knots of nitrogen are still visible.

From HubbelSite
News release ID: STScI-2007-33

1.1 History of laser-generated plasma

1.1.1 Invention of the laser

Since 1916 and the theory of stimulated emission from Albert Einstein[1], physicists from all around the world tried to observe this phenomenon: a photon triggering the emission of another photon with the same wavelength. In the 50s, stimulated emission was observed for microwaves using resonating cavities[2]. In 1958, Townes and Schawlow, proposed the same concept for lower wavelength, that is to say, for visible light. However, progress was slow, and the laser race just started[3].

Despite having been discarded by Schawlow himself who believed it could never be used for stimulated emission, Theodore Maiman started his investigation with ruby. Townes later expressed the importance to explore the implausible because "New discoveries are unexpected, though after some time they usually seem obvious, as does laser"[4] (see figure 1.1). Rubies are no simple stones. Their red color is more intense than ever when shined by sunlight. And there is a reason for that. The crystal absorbs the ultraviolet light from the sun and emits red light around 694 nm. By enlightening a ruby rod with a flashlamp, he was able to excite the crystal which started to emit red light. On both ends of the rod, silver reflectors were used to create the resonating cavity and trap these photons in the crystal. While passing over and over in the crystal, these photons triggered more and more de-excitation. In 1960, Theodore Maiman finally achieved *Stimulated Optical Radiation in Ruby*[5]. This chain reaction produced an intense beam of red light: the first laser.

In the following years, physicists tried many systems replacing ruby with all sorts of crystals and gas. These lasers emitted light at different wavelengths but most of them were ineffective. In 1962, Alan White and Dane Rigden created the famous Helium-Neon gas laser at 632.8 nm[6]. Then in 1964, Joseph E. Geusic, H. W. Marcos and LeGrand van Uitert demonstrated an important laser emission at 1064 nm from a Nd-YAG crystal[7]. This became the most dominant solid-state laser and the one that I used throughout my PhD.

Of course, the adventure of laser continued. The invention of dye laser in the mid-60s using organic molecules gave scientists a large array of new wavelengths to work with and tunable lasers. The invention of diode laser using semi-conductors conducted to the production of cheap and powerful tiny lasers. Many other inventions followed with many applications that lead to a real technological revolution.[3]

1.1.2 Development of laser ablation

Just after Maiman's discovery, scientists started to imagine what they could do with such technology. Of course, one of the first ideas was shooting targets with this

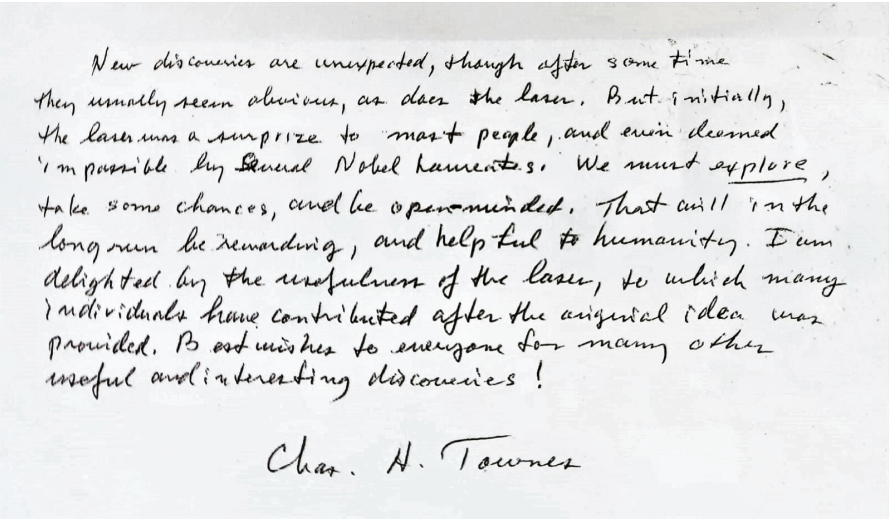
New discoveries are unexpected, though after some time they usually seem obvious, as does the laser. But initially, the laser was a surprize to most people, and even deemed impossible by several Nobel Laureates. We must explore, take some chances, and be open-minded. That will in the long run be rewarding, and helpful to humanity. I am delighted by the usefulness of the laser, to which many individuals have contributed after the original idea was provided. Best wishes to everyone for many other useful and interesting discoveries!

Chas. H. Townes

Figure 1.1: From *50 ans du laser dans la villes lumière*[4]: *"New discoveries are unexpected, though after some time they usually seem obvious, as does the laser. But initially, the laser was a surprise to most people, and even seemed impossible by several Nobel Laureates. We must explore, take some chances, and be open-minded. That will in the long run be rewarding, and helpful to humanity. I am delighted by the usefulness of the laser, to which many individuals have contributed after the original idea was provided. Best wishes to everyone for many other useful and interesting discoveries!"*

new ruby laser. In 1962 Brech and Cross published the first observation of laser-generated plasma[8]. The energy was so dense that they obtained the evaporation of the target and the creation of plasma just by focusing the beam on a target.

If one can evaporate atoms from a target using a laser, then the laser can be used as a source of matter. This was first pointed out by Smith and Turner in 1965[9]: "It suggests the use of a laser beam to evaporate materials in vacuum for the deposition of optical thin films." By investigating the feasibility of this procedure, they established the famous Pulsed Laser Deposition technique, widely used nowadays in thin-film formation. A laser is focused on a target in a vacuum chamber. In front of it stands a buffer substrate. The atoms evaporated from the target are deposited on the surface and a thin film grows on it. The use of laser gave this technique great versatility. It enables to evaporate various tricky materials as ones with high fusion temperature or, on the contrary, fragile organic molecules, and even proteins[10,11,12]. It is even possible to transfer chiral molecules from the ablated target to the substrate in order to create original wave-guides[13,14].

The use of laser ablation didn't stop there. In 1969, Lincoln and Kenneth proposed to combine a laser evaporation source with a time of flight mass spectrometer enabling them to detect the ions produced by the laser[15]. The laser is

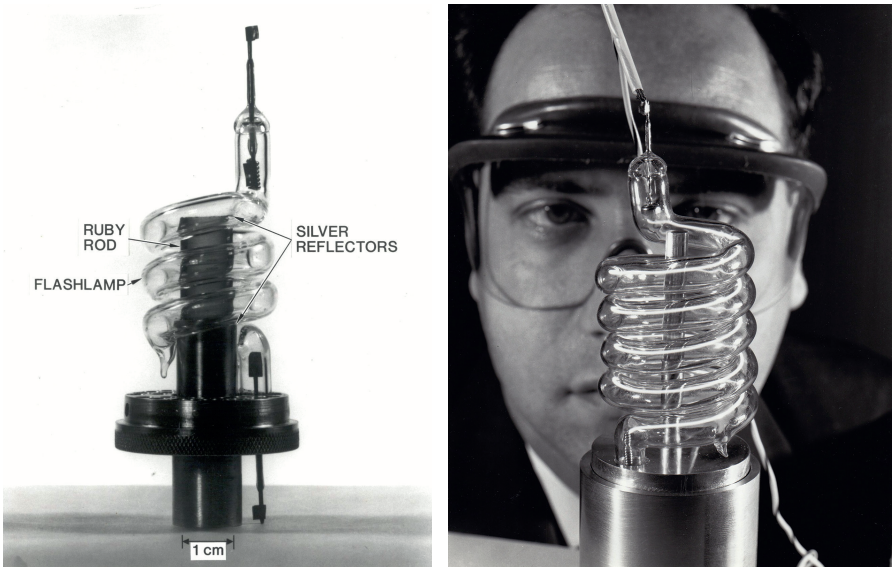

Figure 1.2: Figure from the article *Short history of Laser development*[3]. "(a) Theodore Maiman's first laser, removed from an aluminum cylinder used during the operation, and (b) photo of Maiman behind a larger ruby laser, handed out at the Hughes press conference announcing the laser. The photographer insisted on posing Maiman with the larger laser, and initially many thought this was the first laser."

focused on a target in a vacuum chamber. The ions that are produced are then accelerated by electrodes and analyzed in a mass spectrometer. This source had the great advantage of heating only the target and measurements were achieved with a high repetition rate. With the same idea, Friichtenicht used a laser in order to produce an atomic beam[16] in 1974. However, in all these applications, the ablation takes place in a vacuum, and nucleation is not really observed nor sought.

At this time, nucleation was already an important research topic. In order to study nucleation in laboratories, researchers used the so-called cluster beam sources[17]. A gas of atoms is rapidly cooled by a quick decompression. This leads to the condensation of the gas in clusters of few tens of atoms. In 1981, Professor Richard E. Smalley developed the first cluster source generated by laser vaporization. This source was very similar to the ablation set-up developed by Lincoln and Kenneth more than ten years earlier. The difference here is that Richard Smalley used a collisional gas in order to cool the ablated metal atoms and to promote condensation. From this point, laser ablation became a widely used technique to create clusters. I used such a "Smalley source" to study the alumina cluster formation in the first part of my PhD (see chapter 2).

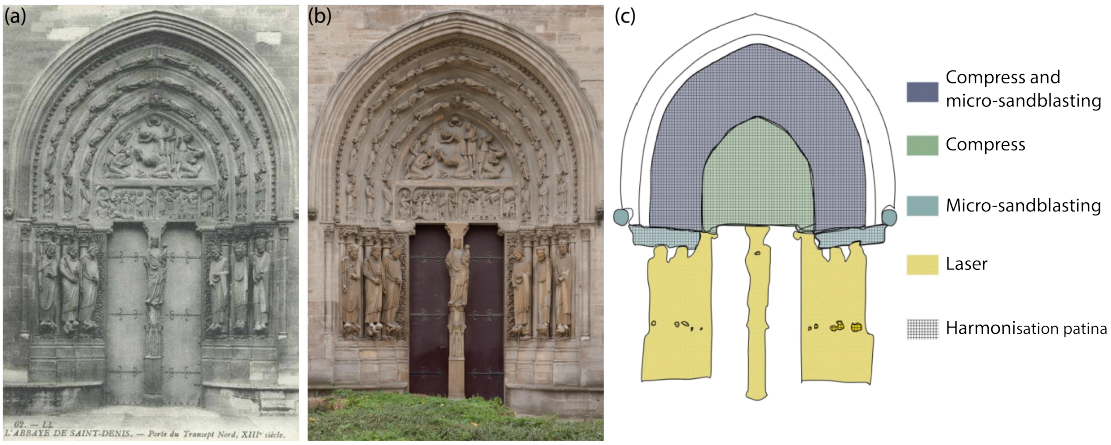

Figure 1.3: (a) Valois' portal from the Abbaye de Saint Denis before renovation. (b) Valois' portal after renovations. (c) Scheme of the different renovation techniques used between 1983 and 1998 (from Marie Godet's Thesis[37])

Finally, in 1991, Lida et al. tried to focus a laser on a brass target immersed in water. They were looking for a new technique of sampling for ICPAES (inductively coupled plasma atomic emission spectrometry). By doing so, the condensation of the plasma was so quick that much larger particles were formed. They obtained a "suspension consisting of fine particles of around 1 μm or less". They concluded that this process could be used "as a technique for solid sampling"[18]. They actually found a new way to create nanoparticles. The technique didn't gain recognition until Mafuné et al. showed in 2000 that it was possible to create size-controlled nanoparticles using ligands in the liquid. From this time, pulsed laser ablation in liquids is an active topic with an increasing number of publications. It appears to be a highly versatile technique that can be used on many materials[19,20,21] and with many liquids[22,23,24,25,26,27]. In contrast to chemical production, Pulsed Laser Ablation in Liquids (PLAL) does not need the use of surfactants or chemical precursors which is of great interest for bio-compatibility. Thus, the produced nanoparticles are used in many fields such as biomedicine[28,29], catalysis[20,30], optics[31,32], additive manufacturing[33,34] and nanoparticle-polymer composites[35,36].

Today, laser ablation is used in most of the laboratories around the world. It is used daily as cluster sources or for nanoparticles formation as we focused here. Among the other uses I can cite micro engraving, surface patterning, impressive laser cutting, but also surgical intervention. It is also commonly used for surface cleaning by removing the surface atoms not only in laboratories but also in the industries and for art conservation. For instance, after the massive fire that ravaged *Notre Dame de Paris*, part of the lead roofing literally went up in smoke.

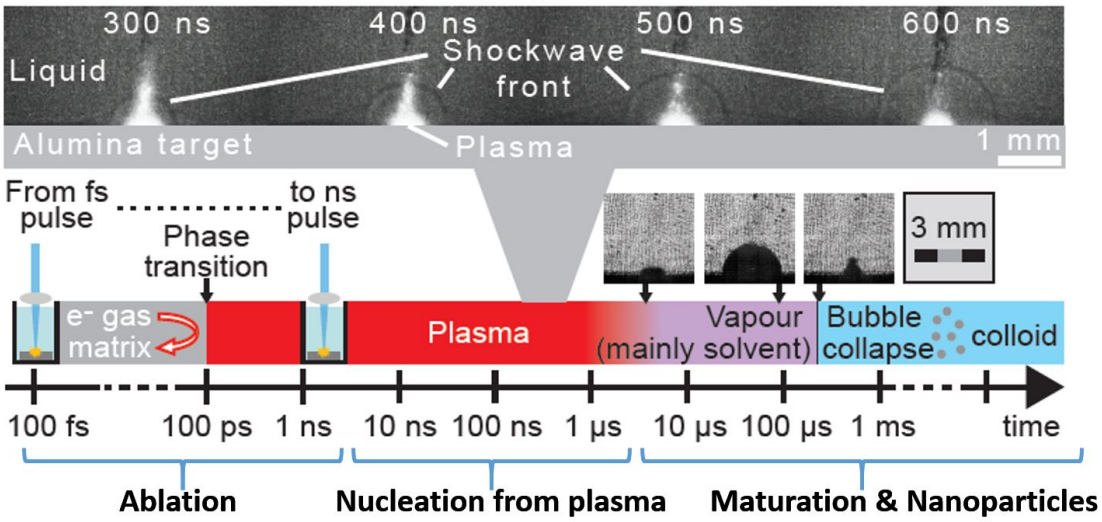

Figure 1.4: Time evolution of the different phenomena occurring during laser ablation in liquids.

The toxic atoms settled down on the stones and sculptures. In order to clean it, Bartosz Dajnowski, from the Conservation of Sculpture and Objects Studio, has used a pulsed laser to remove the deposit. This technique is used for rust, air pollution deposit, or even radioactive pollution. Nucleation appears to be important even in such applications. Indeed, art restorers noticed a yellow deposit after such interventions as one can observe on the Valois' portal sculptures from the Abbaye de Saint Denis (See on figure 1.3). Marie Godet from the Laboratoire de Recherche des Monuments Historiques found out it could be due to a crust of gypsum nanoparticles created during the ablation process[37].

1.2 Laser ablation processes and plasma formation

Following the large development of laser ablation since its first observation almost 60 years ago, lots of studies tried to determine the different processes leading to the formation of the plasma. Today, we have a good idea of the general sequence of events leading to the formation of the plasma[38,39,40,41,19,42] as sketched on figure 1.4 in the case of ablation in liquid. In the case of ablation in air, the initial sequence up to 1 μs is the same, but the plasma is less confined and last longer (a few tens of μs). Yet, the processes are very complex and difficult to investigate because of the extremely short nature of the event. Each step process is still up for debate

in the community. Furthermore, many parameters have to be taken into account. The interactions between the light and the matter are not the same depending on the laser wavelength, pulse duration or energy density. It also depends on the target nature: dielectric, conductor, semi-conductor, and all the environment parameters: vacuum, air, water, etc.[43,44,45] Here, I just want to draw an outline of the processes in order to give an idea of the origin of the plasma without being exhaustive.

When a laser pulse hits the target, electrons absorb the energy of the pulse through electromagnetic coupling. Within a few picoseconds, the energy of the electrons is transferred to the mechanical motion of the atoms (phonons), that is to say, heat. When the laser fluency is large enough (eg. $10^9 - 10^{13}$ GW/cm^2), the heating is extremely strong and violent. It can lead to fragmentation of the target, spallation, evaporation, boiling, or even phase explosion depending on the ablation conditions. The thermodynamic conditions are extreme with a large pressure and temperature expected. In the conditions of our experiments, we observe the formation of a hot gas of atoms and ions: a plasma. For laser pulses longer than a few hundred picoseconds, the free electrons of the native plasma are accelerated by absorbing photons through an inverse bremsstrahlung effect. This acceleration further warms up the native plasma that can reach several thousands of kelvin[46,47]. In air, the plasma cools down within a few tens of μs because of collisions with the environment gas and the atoms condensate to form clusters of a few tens or hundreds of atoms. In liquid, the quenching is faster and nucleation leads to larger nanoparticles.

When ablation occurs in liquids, the plasma is strongly confined and the system is going through extreme pressure up to a few GPa. I was able to measure such pressure from the propagation velocity of the shock wave it generates[48] (see annex D). The heat evaporates a large quantity of liquid (up to 100 times the amount of ablated material[49,50]) which enters the plasma[51] and can take place in the particles' nucleation. For instance, by ablating gadolinium oxide sample in a solution of europium ions, I was able to obtain gadolinium oxide doped europium nanoparticles in a single step process[50] (see annex F). The evaporation of the liquid also cools down the plasma extremely quickly: above 10 K/ns[40]. This fast quenching during nucleation could explain the observation of nanoparticles obtained in a meta-stable phase[52,53,54]. In a side work of my PhD, we observed that it is possible to produce ruby nanoparticles in the α phase despite the fact that at room conditions, the γ phase is more stable[55,56,57]. This should not be possible according to thermodynamics at equilibrium. Maiman used ruby to create the first laser defying expectations, and we can use a laser to create unpredicted nanorubies.

1.3 Toward a better understanding of nucleation

Nucleation in laser-generated plasma remains difficult to fully understand. A classical description of the nucleation fails to explain the formation of clusters and nanoparticles even in the simplest cases. Plasma is a complex state of the matter, composed of atoms, ions, electrons and molecules having their own chemical specificity. Furthermore, in the case of laser-generated plasma, the fast heating and cooling of the system raise the question of thermal equilibrium. Can we describe the processes with simple parameters such as pressure and temperature? This would imply that all the species of the system, atoms, ions, electrons, molecules and clusters, have time to exchange energy and reach the same temperature. For fast quenching, one has to question the temperature uniqueness and the equilibrium in the plasma and within the clusters.

During my PhD, my aim was to better understand nucleation in laser-generated plasma by discussing this question and bring new elements based on experimental measurements.

One of the reasons why we still know little about nucleation in plasma is the difficulty of observing it. Processes are fast (ns-μs) and the extension of the plasma is small (μm-mm). Scientists have to elaborate complicated techniques to study nucleation. In order to study the plasma and clusters, I used mostly two of them: a time of flight spectrometer coupled to a laser-generated cluster source just as Lincoln and Kenneth[15] did and the spectroscopy of the light emitted by the plasma as astronomers do. In the first case we obtain precise information on the cluster size distribution just after their formation. In the second case, we obtain pieces of information such as temperatures, densities, and composition of the hot plasma.

Most of my experimental results are achieved on clusters made of aluminum and oxygen atoms. This composition was selected first, because it is an oxide that is to say an anisotropic material that is less studied than metals. Second, because this oxide could play an important role in cosmic dust formation[58,59]. Third, the spectroscopy of AlO molecules, important in cosmology, is well known. And fourth, because aluminum oxide nanoparticles generated by laser ablation have surprising features. The nanoruby nanoparticles we obtained by laser ablation are nothing more than aluminum oxide nanoparticles doped with chromium and this oxide have been studied by Amans' team previously[46,47].

In the Chapter 2 of this manuscript, I outline the different theoretical approaches and descriptions of nucleation and their limits. Then, I present the micro-canonical model I developed in order to describe and interpret the nucleation of clusters in the gas phase. This model, in-between simple canonical formalism and complex molecular dynamics calculation is able to describe out-of-equilibrium nucleation phenomena. It is then confronted to experimental measurements I per-

formed in Japan allowing me to discuss equilibrium and equipartition of the energy in aluminum oxide clusters.

In the Chapter 3, I study the dynamics of shock-waves generated by laser ablation in order to measure the ablation pressure and I compare it to Sedov-Taylor's blast model. This model can be used with measurements of the plasma's electron density in order to determine the evolution of the composition and temperature of the plasma. Compared to temperatures measured from atoms emission, this measurement enables to discuss the difference between the excitation temperature of the atoms and the kinetic temperature of the plasma.

In the Chapter 4, I discuss in more detail the question of the temperature in the plasma and the formation of diatomic molecules. For that, I built an experimental set-up able to measure the spatio-temporal evolution of the emission of AlO and TiO molecules in the plasma. By fitting the emission of rovibrationnal transitions, one can determine the rotational and vibrational temperature of the excited molecules and discuss their evolution and equality.

Finally, in the Chapter 5, I develop the use of time-resolved light-induced fluorescence on the plasma. After describing the experimental set-up I built, I explore the spectroscopy of AlO molecules through 2D excitation/emission maps and the information I can extract from it. In particular, I fit the fluorescence emission in order to measure the temperature of the ground state AlO molecules in the plasma and compare it to the temperatures of the excited state.

In short: *When a laser with a large enough fluency is focused on a surface, it generates a plasma. The light heats up the electrons of the target that couple with the phonons within a few tens of ps leading to a phase transition. The dense and hot plasma then expands and cools down with a few tens of μs in air. Under liquids, the cooling is much quicker because of the liquid's evaporation. Shock waves can also be observed during the first few hundreds of nanoseconds followed by a bubble during the first ms. Space and time evolution of the plasma is fast and complex. In this work, I explore a new way to describe nucleation out of equilibrium based on statistical physics. I developed spectroscopic techniques to measure the time and space evolution of the plasma in order to determine its composition and temperatures.*

Chapter 2

Theoretical description of Nucleation

Quand le passé n'éclaire plus l'avenir,
l'esprit marche dans les ténèbres.
Alexis de Tocqueville, La démocratie en Amérique

Abstract: *I spent a part of my first year of my PhD developing a growth model for clusters. It is an activated complex-like model using Weisskopf's micro-canonical approach to handle the kinetics of the growth when the transient nature of the processes disregards the canonical ensemble. This model is applied to size distributions' calculation of aluminum oxide clusters and confronted to measurements I performed on a cluster source in Tokyo. It efficiently reproduces experimental size distributions of clusters formed with different buffer gas densities. The activation energy in the model is addressed using DFT calculations and experimental measurements. These results, compared to the model, show that the thermodynamic equilibrium is not reached during the growth and that there is no equipartition of the energy in the clusters. The bounding energy measured is ten times lower than the energy given by DFT calculations and lower than the bulk cohesive energy.*

2.1 State of the Art

Description of homogeneous nucleation at the micro-scale has been a research topic since the mid-30s and started with the processes of droplet formation in a gas[60,61,62]. Of course, this topic is of great interest for atmospheric research and

cloud formation. Scientists defined two different kinds of nucleation: the *homogeneous nucleation* and the *heterogeneous nucleation*. Heterogeneous nucleation is when the molecules nucleate on a pre-existing core, for instance, a microscopic solid particle. Homogeneous nucleation is when atoms and molecules self assembles without any precursors. This kind of nucleation applies to dusty plasma.

Despite numerous attempts of description, homogeneous nucleation remains a phenomenon difficult to grasp. In a recent work from 2019, Jels Boulangier writes about AGB stars: "Current models simplify dust formation, which starts as a microscopic phase transition. [...] Such simplifications for initial dust formation can have large repercussion on the type, amount, and formation time of dust."[63].

In the introduction of this chapter, I want to make an overview of the different existing models, their strengths, their limits, and how they complete each other. Then, I will detail the microcanonical model I developed in order to fill a gap in this range of description. When compared to experimental results, the model succeeds to reproduce the size distribution of aluminum oxide clusters. In particular, this model questions the formation of the cluster in the most stable state and the desorption energy of atoms from the clusters. I addressed this question by running quantum calculations and by measuring these energies directly on a cluster source in Japan.

2.1.1 Classical Nucleation Theory

On a first approach, homogeneous nucleation is nothing more than a phase transition. Gas condensates to form a liquid or a solid. Such transitions have been very well described by thermodynamics and enthalpy for more than 200 years. For instance, the energy needed for a given amount of liquid to vaporize is called enthalpy of vaporization. Conversely, when a gas condensates to form a liquid, it releases energy. Naturally, the first attempt to describe homogeneous nucleation was using classical thermodynamics concepts.

Let us consider a droplet of liquid in a gas. When gas condensates in liquid, the droplet grows. The condensation process is exothermic and the energy of the system should decrease. However, the size of the droplet increases, and consequently its surface has to stretch which requires energy. Classical Nucleation Theory (CNT)[64] simply considers this competition between the volume enthalpy G_v and surface enthalpy σ. In figure 2.1, the evolution of the volume enthalpy G_v with the radius r of the droplet is represented in red. It is negative and proportional to r^3 because the energy of the system decreases when the droplet grows. The evolution of the surface enthalpy σ in blue increases proportionally to r^2 like the surface. The total variation of energy for the system is plotted in yellow and can be expressed as:

$$\Delta G = \frac{4}{3}\pi r^3 G_v + 4\pi r^2 \sigma \tag{2.1}$$

This variation of energy first increases with the radius of the sphere until a critical radius, $r^* = -2\sigma/G_v$, above which it decreases. Until a radius r^*, a drop is not stable and the atoms would evaporate. After r^*, the drop should increase indefinitely as it becomes more and more stable. Yet, how does this explain nucleation? Why can we observe particles with a finite size? Would they grow larger if we wait long enough? This theory is a bottleneck. It fails to explain the growth of clusters[65,66] and remains controversial regarding quantitative results[67,68,69,70,71,72]. One often observes stable objects with a radius lower than r^*.

Let us consider the example of nanorubies. A ruby is a crystal of aluminum oxide in the α crystallographic phase called corundum doped by chromium atoms. aluminum oxide also exists in other phases such as the γ phase. Because the crystals are different, the atoms' arrangement is different, and the energies are different. Namely, the surface energy of the α phase is larger than the surface energy of the γ phase while the bulk energy of the γ phase is larger than the bulk energy of the α phase. For macroscopic size, one can neglect the surface contribution and the stable phase appears to be the α phase that is to say a ruby. On the contrary, for a size below 5 nm the surface effect is more important and the stable phase should be the γ phase. However, in a side project of my PhD, we managed to obtain nanorubies with sizes below 5 nm using laser ablation.

Here, thermodynamics quantities evaluated for macroscopic states are directly applied to nano-objects. Can we really consider macroscopic the surface energy or bulk energy for a cluster made of a few atoms? As we will see later, the arrangement of the atoms in tiny objects is far from the bulk organization. The Ostwald rule states that the first growing phase is not always the most stable in bulk[73,74,75]. During the crystal growth, the geometric structure may indeed reorganize with transient states potentially having a different structure and stoichiometry from the bulk[76,77,78,79]. The energies are thus different. Even the concept of the sphere is not relevant for such nano-objects. Molecules are not spherical and nano-crystals often have facets each of them with a different surface enthalpy. Nano-object should be described as a collection of interacting atoms with their own geometries and properties. These interactions can be described using quantum mechanics.

In short: *Classical Nucleation Theory explains nucleation by a phase transition described with classical thermodynamic. This first approach is too simple and fails to describe nucleation. Such a macroscopic description does not take into account the atomic and molecular nature of the early stage of nucleation. Hence, other descriptions such as quantum calculations or statistical physics are needed.*

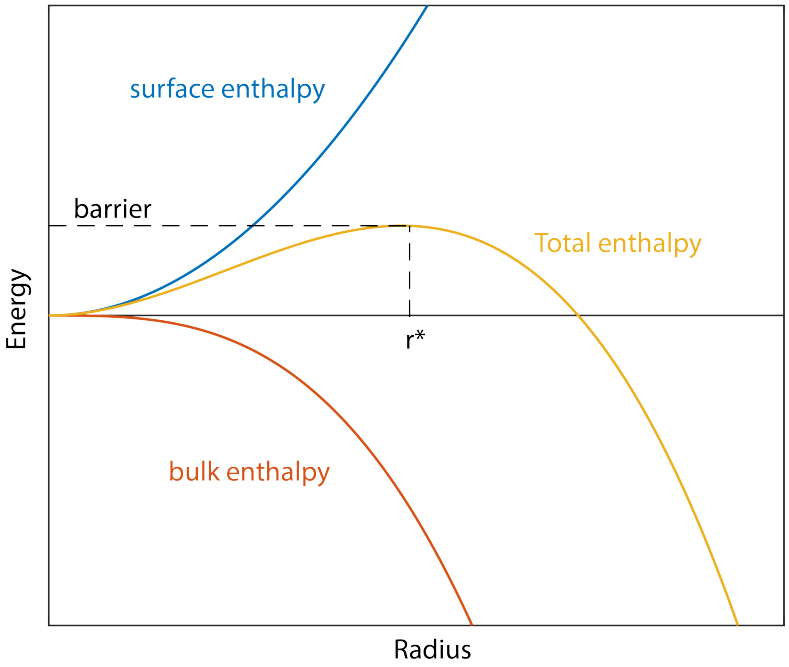

Figure 2.1: Sketch of enthalpy variation for a droplet of radius r in the case of CNT.

2.1.2 Quantum calculation

Quantum mechanics is the best formalism to describe the physics of atoms and molecules. By modelling the atoms and their electrons with such a theory, one can describe their interaction in a very precise manner. This kind of calculation appears to be much less naive than CNT calculation because it takes into account atomic interactions in the formation of the clusters. As we will see, I used such a calculation during my PhD and in particular the *Density Functional Theory* (DFT). It provided me the energy and the geometries of stable aluminum oxide clusters. From this information, it is possible to estimate the desorption energies of atoms from the clusters. The main drawbacks of the quantum description, is the high level of calculation it requires. For a system composed of more than one atom, there is no exact solution. In order to compute interactions between different atoms, one needs to make approximations and numerically solve the equations. For many atoms, the calculation time explodes. Because of it, it is almost impossible to compute the dynamics of nucleation with such a technique. Yet, it is a precious tool for nucleation investigation.

For instance, in order to understand better nucleation of cosmic dust in AGB stars, Gobrecht et al. calculated the potential energy of $(Al_2O_3)_n$ clusters[80]. As you can see on figure 2.2 (a), they found out that the energy by unit of (Al_2O_3) of

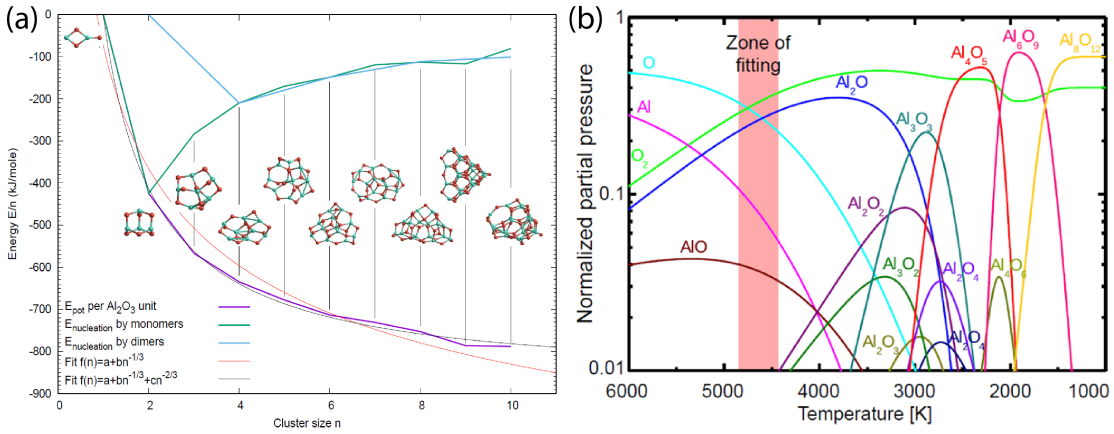

Figure 2.2: (a) Reprint from[80]. Potential energy of $(Al_2O_3)_n$ clusters calculated by DFT. (b) Reprinted from Julien Lam et al.[46]. Evolution of the gas-phase composition from 6000 K to 1000 K considering $P = 4$ bars and $n_{Al}/n_O = 0.6$. For clarity, the total pressure is normalized to one for each temperature. The partial pressure $P_{Al_xO_y}$ for a given x and a given y corresponds to the summation over all isomers.

the most stable clusters keeps decreasing. The bigger the cluster, the more stable it is. The energy of the system decreases each time an Al_2O_3 molecule is added. Contrary to CNT, no critical radius is observed in such a model.

Similarly, Julien Lam et al.[46] calculated in 2015 the formation enthalpy of various cluster stoichiometries (Al_mO_n for m and $n < 10$) and used it to calculate the ratio of each stoichiometry in the plasma for a given pressure and temperature (see figure 2.2 (b)).

The main drawback of this approach is that there is no consideration of the reactions' dynamics. In particular, one can wonder the reaction path from Al_4O_5 to Al_6O_9 when there is no more Al_2O_4 nor smaller species (see figure 2.2 (b) at 2000 K). This technique also considers a thermodynamic equilibrium in the molecules and clusters. It assumes enough time for the formed clusters to relax to their most stable state, that is to say a slow cooling process. This is reasonable in the case of a slow nucleation process like in AGB stars. In the case of laser-generated clusters, this question remains open in particular for laser ablation in water because of the extremely fast cooling process. In that case, one needs a kinetic description of the nucleation process.

2.1.3 Numerical modelling

In order to describe the kinetics of the nucleation phenomenon, one solution is to track each of the components while computing their interactions. Nowadays, it is possible to model with powerfull computers a box full of thousands of atoms, interacting together[81,82,83,84]. For instance, Prof. Zhigilei and his team are working on computing the whole laser ablation process on metals[42,85]. On figure 2.3, you can observe a time-lapse of one of their simulation. They managed to reproduce the phase transitions creating a gas of atoms in which nucleation occurs and Rayleigh instabilities creating nano-droplets of liquid target. This impressive result is of great importance in the understanding of the different phenomena taking place during laser ablation. In particular, these nano-droplets might explain the observation of large size nanoparticles for laser ablation in liquids.

Unfortunately, this kind of simulation is time-consuming and limited to a few tens of nanoseconds. It is impossible to compute the whole process of homogeneous nucleation. Furthermore, they do not use a quantum level of calculation, which is impossible with today's computers. They use classical potentials of interaction. Such potentials are determined for each material in order to describe its properties in the best way possible. It is often developed for bulk material and extrapolated for clusters. Of course, such an extrapolation raises the same question as for CNT, and one needs to check their performances at a small size. In the case of metals, that is to say homogeneous, isotope materials, classical potentials have been proved to be effective[86]. Yet in the case of ceramics and anisotropic materials, with charges localization and electrostatic effects, such as alumina, work is still going on[87].

If one wants to have a more global description of nucleation, describing the growth of particles at a longer timescale, such simulations are not affordable even with today's computers. One needs to find another approach.

In short: *Quantum calculations are very accurate to describe atomic and molecular interactions as it takes into account the quantum description of the system. However, such calculations have to be solved numerically and are very time-consuming even with strong approximations. Calculating precisely the whole nucleation process, from atoms to nanoparticles, remains impossible today. One way to overcome this is not to calculate the dynamics of the system but more simply the most stable molecules. This assumes that the whole nucleation occurs at the thermodynamic equilibrium. In this chapter, I challenge this assumption in the case of nucleation in laser-generated plasma.*

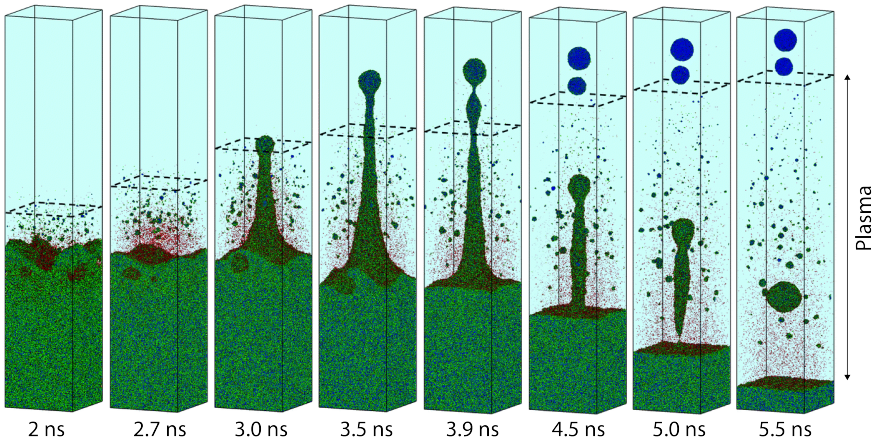

Figure 2.3: (a) Reprinted from Shih et al.[42]. Snapshots of atomic configurations and density distribution predicted in an atomistic simulation of laser ablation of a bulk silver target irradiated in water by a 10 ps laser pulse at an absorbed fluency of 600 mJ/cm^2

2.1.4 Kinetic description

Back in the 60s, when scientists developed cluster sources by a supersonic expansion of gas in a vacuum or laser ablation, studies on rare gas and metallic clusters formation flourished. However, computers were still the size of a room and far from achieving such complex calculations. Chemistry kinetics was already a mature field with strong knowledge and physicists used this knowledge and developed nucleation theories based on statistical physics from the 50's to the late 80's[60,61,62]. After all, nucleation can be seen as a succession of chemical reactions.

The growth of a cluster A is due to its fusion reaction with a tinier cluster, molecule, or atom B:

$$A + B \rightarrow C \tag{2.2}$$

The kinetics of such a reaction is driven by a chemical reaction rate $k_{A+B\rightarrow C}$ such that the concentrations of the species (noted []) evolve as:

$$\begin{aligned} \frac{d[A]}{dt} &= \frac{d[B]}{dt} = -k_{A+B\rightarrow C}[A][B] \\ \frac{d[C]}{dt} &= k_{A+B\rightarrow C}[A][B] \end{aligned} \tag{2.3}$$

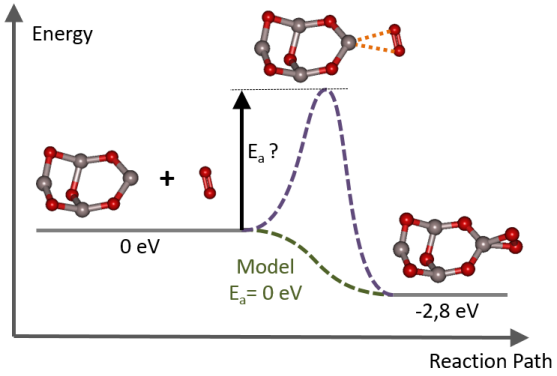

Figure 2.4: Energetic representation of the reaction $Al_4O_5 + O_2 \rightarrow Al_4O_7$. Geometries and energies are computed by *ab initio* calculation as developed later

If one knows all the possible reactions and all the reaction rates associated, it is possible to solve the system of equation and give the exact evolution for each concentration.

This reaction rate usually depends on the temperature and can be described by the empiric Arrhenius law:

$$k_{A+B\rightarrow C} = \mathcal{A}\exp\left(\frac{-\mathrm{E_a}}{\mathrm{k_B T}}\right) \tag{2.4}$$

$\mathcal{A}$ is an experimentally determined pre-factor, $\mathrm{k_B}$ is the Boltzmann constant, T is the temperature of the system and $\mathrm{E_a}$ is the activation energy. This energy is the energy needed for the reaction to occur. For instance, on figure 2.4 is represented an Al_4O_5 cluster reacting with a O_2 molecule to create a Al_4O_7 cluster. Despite the fact that the final state has an energy lower than the initial state, the chemical reaction has to go through an intermediate state which can have a larger energy. The activation energy is the energy needed by the initial state to overpass this barrier.

The main drawback of this formalism is that one needs to know the value of the reaction rate depending on the experimental condition. Even using a simple model for the temperature dependence such as the Arrhenius law, one needs to know the activation energies and the pre-factor for every considered reaction.

This technique is particularly used in dusty plasma confined by electromagnetic fields[88]. For a given plasma composition, people are considering all the different reaction rates between atoms, ions, and electrons. Then, they either solve the equations on the concentrations or adopt more complicated space-resolved simu-

lations. They track the position of the different species, their velocity, and their probability of reaction depending on the plasma geometries and the different fields. The advantage of such a model is that it is very complete and can be computed on a large scale system. Yet, in order to do that, they need to have experimental data on many constant rates. These rates are difficult to measure with all the ensuing uncertainties. This is a gigantic amount of work, and this kind of model only applies to plasma with a simple composition and usually describes only the formation of diatomic molecules.

In order to overcome the issue of not knowing these reaction rates, one can try to calculate them through quantum chemistry. Indeed, it is possible to compute the dynamics of reactions between molecules considering temperature[89]. Yet this is extremely time-consuming and applies mostly to simple systems such as carbon clusters. More simply, one can consider an Arrhenius-like relation for the expression of the reaction rate and try to compute the different factors using quantum calculations. For instance, in his last work, Tatsuo Oguchi adopts a mixed approach to describe the nucleation of alumina. He constructed a detailed chemical kinetic model of aluminum oxidation in the gas phase. He used quantum calculations in order to obtain the molecular structures of the reactions' intermediates and calculate highly accurate energy potentials. In parallel, he also calculates the coefficient rate based on VTST or RRKM* theory[90]. Similarly, Alexander Starik used in 2018 a chemical description of the combustion fuel added with aluminum considering the ignition of a single microparticle of aluminum and modeling the evolution of the plasma around it considering the diffusion of heat and particles, and reactions. They determined the reaction constants by matching the thermodynamic properties of small clusters calculated by quantum methods with characteristics of liquid droplets at a larger size[91].

Another solution is to measure these coefficients with experiments such as the one I worked with in Tokyo. There, I was able to measure the reaction constants of O_2 molecules desorption from alumina clusters. One can only access some reactions and the information is far from enough in order for me to adopt this kind

*These are kinetics theory developed further in the section 2.1.4.

In short: *In order to describe larger systems, one approach is to simulate all the atoms using not a quantum description but potentials of interaction. Yet it remains time-consuming and restricted to materials with available potential such as metals. Another option is to consider nucleation as a succession of chemical reactions with given reaction rates. However, one needs to know all the possible reactions and all the associated reaction rates, either by measuring them or calculating them.*

of description. Yet, as we will see, it is an interesting element of the discussion.

Finally, one can try to describe the reaction itself in order to determine this reaction rate from quantities such as the cluster size and velocities. One approach is to consider a general dependence of the reaction rate depending on thermodynamic values (Gibbs free energy) and the size of the clusters. It is used for instance in atmospheric cluster dynamics to describe the temporal evolution of cluster densities of a given size[92]. In complement, Monte Carlo simulation can be used to calculate the evolution of the system[93], and even to track the particles in time and space[94]. Yet, most of the time, these models remain based on classical thermochemistry considerations.

With this work, I aim to describe the kinetics of the system with a similar cluster size description but not considering classical thermochemistry but the microcanonical ensemble.

Activated complex theory

In 1934 the chemist Eyring proposed a description of what is a chemical reaction. When two reactants A and B stick together, they form an unstable intermediate I^* just like schematized on figure 2.4. If nothing happens to stabilize this intermediate, it ends up breaking apart. The reaction doesn't occur. If on the contrary, the intermediate loses some energy, the product C is formed. The reaction happens. This is the activated complex theory[95,96]:

$$A + B \underset{\text{desorption}}{\overset{\text{sticking}}{\rightleftharpoons}} I^* \xrightarrow{\text{cooling}} C$$

Cooling phenomena can be various. Among them, collisions with the environment atoms and molecules are the predominant cooling effect in most cases[97]. One can thus describe the sticking rate by a collision rate between the species depending on their concentration and velocity and the cooling rate by a collision rate between the intermediate and the environment gas. If one manages to express the desorption rate, that is to say, the rate with which an intermediate breaks apart, one can express the reaction rate without using an empirical low.

RRK(M) Model

Such a question was already answered by Rice and Ramsperger and, in parallel, Kassel in 1927. These chemists were trying to understand the decomposition of a molecule when excited by a photon or temperature which is analogous to our intermediate molecule. They had the idea to consider this molecule as a collection

of n oscillators. Each oscillator corresponds to a degree of freedom of the molecule. That is to say a vibration mode or a rotation mode. Each of these oscillators can get excited and store some energy. The molecule starts vibrating and rotating. If one of them stores too much energy, for instance, one atomic bond vibrates too much, it breaks and the molecule is destroyed. However, the energy of the molecule can also be evenly spread on the different oscillators and the molecule will not break.

Using statistical physics and micro-canonical ensemble, one can enumerate all the possible states of the molecule. The ratio between (i) the number of states where the molecule breaks and (ii) the total number of states gives the probability that the molecule has to break by unit of time. In order to have the rate of breaking, we have to multiply this probability by the frequency for this breaking to happen. They quite naturally chose the frequency of the oscillators. The idea is that every time a bond extends, it can break.

Then they considered that all the oscillators are equal and that the energy can spread the same way on each of them (equipartition of the energy). This enabled them to find a useful expression for the reaction rate depending on the temperature. That is the so-called canonical limit. This canonical model is named RRK after the initials of the three chemists[98,99,100], or RRKM[101], for a modified version by Marcus in 1952.

The RRK model has been extensively studied for chemistry and was naturally adapted for clusters in the sixties[102,103,104,105,106,107,108,109]. It describes the production of clusters made of simple isotropic materials with low cohesion energy such as noble gas[110], CO_2[110,111] or simple metals[112,113,114,115,116,117,118].

Another version of this model is inspired from nuclear physics[119]. In the 30's, nuclear physics was booming. Neutrons were discovered in 1932 by the British physicist James Chadwick. Victor Frederick Weisskopf, an Austrian theoretical physicist, was trying to understand how neutrons can be evaporated from the unstable nucleus of an atom. Just like the excited molecules of Rice, Ramsperger and Kassel, this unstable nucleus represents our reaction intermediate. Weisskopf adopted the same statistical approach that the chemists had a few years before, but he wanted to take into account the density of the state of the evaporated neutron. Instead of considering an oscillators' frequency, he used an elegant trick. He considered the inverse problem reversing time[†]. Both models are close but this time, the frequency of the oscillators doesn't have to be added arbitrarily. The desorption rate appears naturally from the calculation. Weiskopf model was later

[†]He determined the probability per unit of time for a given neutron to be captured by the nucleus. Then he calculated the probability of the reverse process by dividing it by the number of states in which the neutron can be capture and multiplying it by the number of states into which the nucleus can decay.

adapted for molecules and clusters[111,115].

However, after the 80s, these fields of research slowed down. The cluster sources became new production tools. People started to investigate the properties of the clusters more than their formation. New materials as oxides became the center of interest. Unfortunately, if one tries to use these models to explain the nucleation of anisotropic and iono-covalent clusters such as oxides, the model fails and thus the statistical modeling of nucleation was slowly forgotten.

While I was looking for a simple way to describe nucleation, I had the chance to talk with Prof. Mélinon who is a specialist in nucleation[120], and advised me to look at these theories. Thus, I decided to adapt these models in order to be more versatile and describe alumina clusters. As we will see, this becomes possible by using the micro-canonical ensemble and computer calculation. After explaining in detail the model, we will see how it manages to describe the formation of oxide clusters and why canonical models cannot. We will further discuss the results of the model with measured activation energies and DFT calculations.

In short: *One way to simply calculate a reaction constant is to decompose the reaction. When sticking together, the reactants form an unstable state: the activated complex. This complex is either stabilized (by collision for instance) or breaks apart. One can thus decompose the reaction rate in a sticking rate, cooling rate, and breaking rate. Each of them being described independently. Sticking and cooling are generally simply described through collisions and depend on simple quantities such as density and velocity of the particles. The breaking rate or desorption rate can be described by statistical physics and models such as RRK(M) and Weisskopf's model. These models use canonical ensemble enabling to write down an analytical solution depending on the temperature for instance, similarly to Arrhenius law. It was necessary at that time in order to be able to use them without computer calculations. Yet, the canonical ensemble assumes the thermal equilibrium and a notion of temperature in the cluster itself. It fails to describe anisotropic materials such as alumina in which the energy might not be spread evenly. In order to overcome this issue, these models are reconsidered in the micro-canonical ensemble which assumes neither thermal equilibrium nor temperature inside the cluster.*

2.2 A model out of Equilibrium

2.2.1 Notions of thermodynamic equilibrium and statistical physics

Since the 17$^{\text{th}}$ century, scientists explained the behaviors of a system using empirical laws relating its pressure, temperature, and volume, namely an equation of state. The concept of temperature is complex to define and measure. Variations of temperature were first observed, by Philo of Byzantium in the III$^{\text{rd}}$ century, by bubbles due to the expansion of heated air[121]. In 1597 Galileo invented the alcohol thermometer, using the dilatation of the liquid as a measure of the temperature. Both of these experiments refer to the temperature as a macroscopic variable, linking the temperature to the volume of a fluid. Later, the concept of temperature was related to the energy of a system thanks to the development of thermodynamics, as its name refers to. Temperature is defined uniquely when the system is at the thermodynamic equilibrium, that is to say when the energy of the system is equally spread on all its components and that there are no macroscopic flows of energies. However, when thermal equilibrium is not fulfilled, the energy is not spread evenly in the system. The temperature is no more unique or might simply not be defined at all.

Statistical physics

Another way to describe a system is to look at its composition at a microscopic level, considering all the possible positions, velocities, and energetic states of the components of the system. By using probability theory and statistics, one can deduce from such a description useful microscopic properties. In order to do so, one can adopt different ensembles, that is to say, different collections of microstates:

- The *microcanonical* ensemble is the statistical ensemble of the possible states for an isolated system. There is no exchange of matter nor energy. This ensemble makes no assumption of equilibrium, but the concept of temperature cannot be properly defined.
- The *canonical* ensemble is a statistical ensemble of the possible states for a system in thermal equilibrium with a heat bath at a fixed temperature and with no exchange of matter. In that case, the temperature is defined.
- The *grand-canonical* ensemble is a statistical ensemble of the possible states of a system in thermal equilibrium with a heat bath and a reservoir. The system can exchange heat and particles.

In this model, I will use statistical physics to describe nucleation. Yet, contrary to the previous model considering the canonical ensemble, I use the micro-canonical ensemble to describe the clusters. By doing so, I won't have to assume equilibrium in the clusters.

2.2.2 A micro-canonic model

In laser-generated plasma, three different populations of species can be distinguished: the quenching gas (buffer gas), in our case helium (He), the atoms of the ablated material (monomers), and the clusters (n-mers) composed of n monomers. First, I need to make an approximation for the calculation to be possible. I have to neglect all *ripening* effects. That is to say, the merging of two n-mers. Indeed, considering all the different merging possibilities between the different cluster sizes would be far too complex. Such an approximation can appear to be crude. Yet, this approximation is valid in many cases because the density of monomers is often much more important than the density of n-mers. The probability that two n-mers collide is thus very low. Furthermore, even when the density of monomers decreases because of the clusters' absorption, the density of clusters remains low. A cluster grows when a monomer sticks to it and that the excited complex is cooled quickly enough to be stabilized. Here, only the cooling due to collisions between the hot cluster and the He gas is considered. Radiative cooling is neglected because radiative lifetime for vibrational transition is typically greater than 100 μs[97], while collision time with He gas is about 10 ns in our case (see figure 2.11). One can then consider the following conceptual coalescence mechanism typical of activated complex theory[97]:

$$X_n + X_1 \underset{\text{desorption}}{\overset{\text{sticking}}{\rightleftarrows}} X_{n+1}^* \xrightarrow{\text{cooling}} X_{n+1}$$

with X_1 a monomer and X_n a cluster of n atoms. Given the three reaction constants k_{sticking}, $k_{\text{desorption}}$ and k_{cooling} and assuming a steady-state for the activated complex, one can compute a global growth constant:

$$k_{\text{growth}}^{(n)} = \frac{k_{\text{sticking}}^{(n)} \times k_{\text{cooling}}^{(n+1)}}{k_{\text{cooling}}^{(n+1)} + k_{\text{desorption}}^{(n+1)}} \tag{2.5}$$

In order for the steady-state to be true, sticking events have to be a rare event with respect to at least one of the cooling rate or desorption rate. This assumption was verified in our experimental conditions. Indeed, the desorption constant defined

below appears to be 100 times larger than the sticking constant (see figure 2.11 (b)). From there, one can write a series of coupled equations describing the evolution of the cluster densities with time:

$$\begin{aligned} \frac{d[X_1]}{dt} &= -\sum_{n\geqslant 1} k^{(n)}_{\text{growth}}[X_n][X_1] \\ \frac{d[X_{(n+1)}]}{dt} &= k^{(n)}_{\text{growth}}[X_n][X_1] - k^{(n+1)}_{\text{growth}}[X_{n+1}][X_1] \end{aligned} \tag{2.6}$$

The monomer concentration $[X_1]$ decreases because of reactions of monomers with all the different clusters, hence the sum over all the possible sizes n. The concentration of a cluster of size n increases when a monomer reacts with a cluster of size $n-1$ but also decreases when a monomer reacts with a cluster of size n and forms a cluster of size $n+1$.

Sticking and cooling constants

k_{sticking} and k_{cooling} can be expressed considering hard spheres collisions model and kinetic perfect gas theory. Indeed, one can consider that monomers stick to a cluster when they collide. Likewise, cooling occurs when an He atom collides with the cluster. In both cases, the rate can be written from a cross-section σ and the relative velocity of the objects.

In the gas of atoms, the density of He ($1.8 \pm 0.2 \times 10^{17}$ see table 2.5 and section 2.5.1) is large enough for thermalization to occur within a few nanoseconds. Thus, the canonical ensemble can be used to describe velocity in the gas and the

In short: *In the model, one considers that only monomers (single atoms) can stick to the clusters as they are usually in large excess. The sticking rate is simply the probability of collision between one monomer and a cluster of a given size taking into account their cross-sections. The cooling rate is the probability of collision between the cluster and atoms of the buffer gas times the energy transfer considering an elastic collision. The desorption rate is calculated using Weisskopf model. From there, the reaction rate for each cluster size (growth rate) is deduced from activated complex theory and one can compute the dynamics of the system by directly solving the system of equations without having to consider the canonical ensemble.*

velocity probability of the atoms is defined by the Maxwell-Boltzmann distribution:

$$\mathcal{G}(\vec{v}) = \left(\frac{m}{2\pi k_{\mathrm{B}} T}\right)^{3/2} e^{-\frac{m\vec{v}^2}{2k_{\mathrm{B}}T}} \tag{2.7}$$

with k_{B} the Boltzmann constant, m the mass of the atom, T the temperature of the gas, and $\vec{v}$ the velocity of the atom. The average relative velocity is :

$$\sqrt{\frac{8k_{\mathrm{B}}T}{\pi\mu_X(n)}} \tag{2.8}$$

with $\mu_X(n)$ the reduced mass of a couple monomer (mass m_X) and cluster (mass $n \times m_X$). Thus, the sticking constant is:

$$k^{(n)}_{\mathrm{sticking}} = \underbrace{\pi(r_X + \overbrace{n^{1/3} r_X}^{R(n)})^2}_{\sigma_X(n)} \sqrt{\frac{8k_{\mathrm{B}}T}{\pi\mu_X(n)}} \tag{2.9}$$

with $\sigma_X(n)$ the hard sphere cross-section between a monomer and a n-mer, r_X the monomer radius and $R(n)$ the radius of the clusters composed of n atoms in the drop model. Respectively, the cooling constant is:

$$k^{(n+1)}_{\mathrm{cooling}} = \rho_{\mathrm{He}}\beta(n) \underbrace{\pi(r_{\mathrm{He}} + R(n+1))^2}_{\sigma_{\mathrm{He}}(n+1)} \sqrt{\frac{8k_{\mathrm{B}}T}{\pi\mu_{\mathrm{He}}(n+1)}} \tag{2.10}$$

with $\beta(n) = m_{\mathrm{He}}/(2\,n \times m_X)$ the efficiency of the energy exchange and ρ_{He} the He gas density.

In short: *In Weisskopf's model, one considers the energy released by the sticking reaction spread on several oscillators representing the molecule or cluster. There are many ways to spread this energy. It can be all concentrated in one oscillator or evenly spread on all of them. Yet, if one oscillator has too much energy (larger than a given value D) the cluster breaks apart just as if one of the chemicals bonds vibrates too much. In order to suit anisotropic materials, the Weisskopf's model is modified. In contrary to isotropic clusters, oxides clusters cannot be considered as a collection of identical oscillators. Some vibration modes are more relevant than others. Thus, an effective number of oscillators $s(n)$ is introduced.*

Desorption constant

In the model, I described $k_{\text{desorption}}$ by a modified version of the Weisskopf model. When a monomer sticks to a cluster, the energy of the molecular bond is released in the cluster. The excited cluster is considered as an isolated system with a given energy E corresponding to its initial energy plus the bounding energy.

Just like Weisskopf model, a cluster composed of n monomers ($n > 2$) is described as a system of $s(n)$ loosely coupled harmonic oscillators of frequency ν on which the total energy E is spread. For a cluster composed of n monomers, one can count $3n-6$ oscillators[‡]. However, without assuming equipartition of the energy on all the oscillators, the effective number of oscillators $s(n)$ might be less.

A monomer can evaporate from the cluster if one oscillator has an energy larger than a desorption energy D. The desorption rate can be written as the frequency of collision multiplied by the ratio of the numbers of available micro-states after and before desorption integrated over all the kinetic emission energy ϵ of the monomer[119]:

$$\begin{aligned} &k^{(n)}_{\text{desorption}}(E) = \\ &\int_0^{E-D} f_{\text{collision}} \frac{\Omega_{n-1}(E-D-\epsilon)}{\Omega_n(E)} \Omega_{\text{atom}}(\epsilon) d\epsilon \\ &k^{(n)}_{\text{desorption}}(E) = 8\pi\mu\sigma\nu^3(s-1)\frac{(E-D)^{s-2}}{E^{s-1}} \end{aligned} \tag{2.11}$$

with $\Omega_n(E) = (E/(h\nu))^{s-1}/(s-1)!$ the number of micro-states for a cluster of n monomers with an internal energy E, $\Omega_{n-1}(E-D-\epsilon)$ the number of micro-states for a cluster of $n-1$ monomers with an internal energy $E-D-\epsilon$, and $\Omega_{\text{atom}}(\epsilon) = 8\pi\mu\epsilon V/(h^3 v_{\text{atom}})$ the density of state for an ejected atom in a volume V with an energy ϵ and a velocity v_{atom}. $\mu = \mu_X(n-1)$ is the reduced mass of the atom-cluster system and $\sigma = \sigma_X(n-1)$ is the related hard sphere cross-section.

At this point, physicists from the 60s considered the canonical ensemble and the equipartition theorem in order to state that the number of oscillators $s(n)$ is the total number of oscillators, namely $3n-6$. They introduced the temperature in order to develop analytical expressions that they can use experimentally. However, this model overestimates the number of vibrational modes[99,122,123,124]. Franklin introduces a coefficient $\alpha = 0.44$ to correct this effect[122], but it can vary from 0.1 to 0.56, depending on the system[123].

In the model, I decided not to introduce a temperature nor consider the equipartition theorem, and remain with a micro-canonical description of the clusters which

[‡]Here rotational degrees of freedom are ignored. Their associated energy is low and the relevant motion for dissociation are vibration.

are not considered at the equilibrium. Because of Franklin's coefficient success, I suggest taking $s(n)$ proportional to the cluster size. Yet, it also has to be higher than 2 in order for the Weisskopf constant to be well-defined. Thus, I take $s(n) = 3(n-3)\alpha + 2$ with $n \geqslant 3$. The more α is close to zero, the more localized is the energy. On the other hand, the closer is α to one, the more the energy is spread on all the oscillators. This parameter is a probe of the equipartition of energy, and thus, of the anisotropy of the cluster.

For a dimer which is simply one oscillator ($s(n) = 1$), Weisskopf constant is not defined. There is no potential barrier and the desorption energy is exactly the bond energy. Thus, one can expect the desorption constant to be simply proportional to the vibration frequency ν_{dimer} just as it is usually done for activated complexes[125]. $k^{(2)}_{\text{desorption}} = \nu_{\text{dimer}}$. In other words, a dimer is formed only if it was cooled by helium within a vibration of the oscillator[§].

Energy of the cluster

The energy E in this model is the internal energy of the activated complex, i.e. the hot cluster just after a monomer sticks to it. E is equal to the energy D realized by the bounding event added with the oscillators' energy before the sticking event E_0:

$$E = E_0 + D \tag{2.12}$$

Because the growth rate is low compared to the cooling rate (see figure 2.11), one can consider that just before a sticking event, the cluster is at equilibrium with the gas. In that case, one can use the temperature of the gas in order to define the energy before the sticking event E_0. In our model, the oscillators are not equivalent thus $E_0 = s(n)k_{\text{B}}T$.

The desorption energy D of a monomer from a cluster is much more complex to estimate. During my PhD, I first tried to calculate this desorption energy on aluminum oxygen clusters using DFT. As we have seen, such calculations require equilibrium and do not consider kinetics. Thus, I also tried to measure it using the experimental set-up of Prof. Mafuné in Tokyo. Aluminum oxygen clusters are produced by laser ablation and heated in order to measure some reaction rate from heat decomposition. In the following, I first present the DFT calculations and then the experimental measurements. These values are then compared with the value given by the microcanonical model fitted on several clusters size distributions depending on the buffer gas concentration.

[§]This is exactly the reaction we can expect for the formation of AlO molecules in the excited state $B^2\Sigma^+$ as explained in the section 4.3.

2.3 Calculation of desorption energy

Calculating the desorption energy in the case of a cluster or a large molecule is not simple. The reaction path and reaction intermediate have to be determined first in order to compute the difference in energy between the intermediate and the initial cluster. Doing so with *ab initio* calculation is possible but time-consuming. One can give a lower estimation of the desorption energy by calculating the difference in energy of the initial cluster with the energy of the two resulting fragments. In that case, the extra energy of the intermediate is not considered. This extra energy is expected low in the case of desorption reactions with little modification of the cluster geometry: one atom or one molecule detaching from the cluster. In that case the geometry of the intermediate is close to the one of the initial cluster and has a similar energy. In the following, the desorption energy is thus estimated by this energy difference considering reactions with little modification of the cluster geometry.

First, we used previous calculations of Julien Lam who already optimized the most stable geometry of many neutral clusters stoichiometries[46]. In that case, we can evaluate the weakest bound in the cluster, cut the cluster in two fragments and optimize their geometry before computing the difference in energy. This technique is time effective and enables to calculate many desorption energies. However, the clusters are neutral in contrary to the experiment run in Japan and the fragments do not necessarily correspond to the most stable geometry of the clusters. Details on the calculations are given below.

In order to complete these calculations, I also optimized the geometry for charged clusters and selected only the reactions between the most stable geometries (calculations developed below). For instance, in figure 2.5, is represented the energy of the geometries of some charged clusters. In the panel (a), one can see that the most stable geometry of $Al_3O_3^+$ is very similar to the most stable geometry of $Al_3O_5^+$ with an O_2 molecule removed. In that case, the intermediate should be similar to the $Al_3O_5^+$ geometry and the desorption energy close to the energy of $Al_3O_3^+ + O_2$ minus the energy of $Al_3O_5^+$ that is to say 2.55 eV. On the contrary, in the panel (b), one can see that the most stable geometry of the cluster $Al_3O_2^+$ is very different from the most stable geometry of the $Al_3O_4^+$. In that case the difference in energy is probably far from the desorption energy.

Calculation on neutral clusters

All the calculations presented here were performed using the Gaussian09 D01 revision[126]. Bounds energies were calculated from optimized geometries calculated by J. Lam et al.[46] on neutral clusters of aluminum and oxygen. Briefly, they calculated the most stable configurations for each stoichiometry using DFT opti-

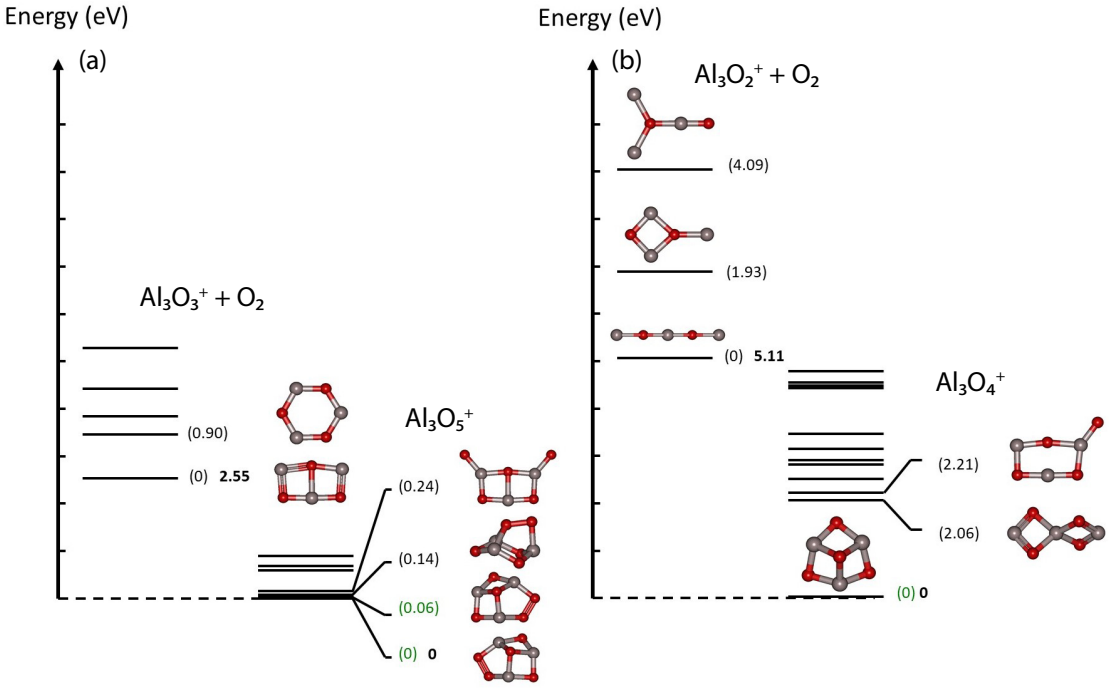

Figure 2.5: Energies of various $Al_3O_5^+$ configurations and energies of various $Al_3O_3^+$ configurations added with the energy of one O_2 molecule (a). Energies of various $Al_3O_4^+$ configurations and energies of various $Al_3O_2^+$ configurations added with the energy of one O_2 molecule (b). All the energy levels correspond to the vibrational ground state at 0 K of the most stable configurations obtained after optimization. All values are given in electron-volts. The number in brackets refers to the difference in energy between a given configuration and the most stable configuration with the same stoichiometry. If this number is green, it means that this energy is lower than the thermal energy at 1000 K.

mization. Randomly positioned sets of atoms are generated for each stoichiometry. Each of them is rapidly optimized using the Streitz potential[127]. The obtained configurations are then compared. If two configurations have a difference of energy less than 0.5 kcal.mol^{-1} and atom position differences within 0.2 Å, they are considered equal and only one is conserved. The set of random initial configurations have to be large enough to cover all the possible initial configuration. Each of these configurations is then optimized with DFT calculations using B3LYP/6-31+G* basis set. The configuration obtained are compared again, and identical configurations removed. The final geometries and frequencies were found through optimization at a higher level of DFT (B3LYP/6-311+G(3df,3pd) basis set). Finally, the energy is computed using MP2/6-311++G(3df,3pd)//B3LYP/6-311+G(3df,3pd) and only the most stable is considered¶.

On these neutral clusters, I used AIM (Atoms In Molecules) in order to find the weakest bond that is likely to break. The initial cluster and the fragments are then optimized using B3LYP/6-311+G(3df,3pd) basis set.The bond energy is calculated as the difference between the energy of the first cluster and the sum of the energies of the two fragments. All the results are presented table 2.1. The average energy was 4.5 eV with a standard deviation of 2.0 eV.

Calculation on charged clusters

In the experimental work carried out in Tokyo the clusters were charged and not neutral. A charged state can significantly change the desorption energy of atoms.

In collaboration with Professor Abdul-Raman Allouche calculations on the desorption energy of charged clusters were carried out. The method for performing these calculations was identical to that described above. Figure 2.5 (a) represents the energies of various $Al_3O_5^+$ configurations and the energies of various $Al_3O_3^+$ configurations added with the energy of one O_2 molecule. In the same way, figure 2.5 (b) represents the energies of various $Al_3O_4^+$ configurations and the energies of various $Al_3O_2^+$ configurations added with the energy of one O_2 molecule. All the energy levels correspond to the vibrational ground state at 0 K of the most stable configurations obtained after optimization. All values are given in electron-volts.

In order to consider the fragmentation of a cluster, the most stable geometry of the initial cluster has to be the same as the most stable geometry of the fragment except for the oxygen atom or O_2 molecules removed. I was able to identify 4 re-

¶Some theoretical background and the meaning of these notation are given in the annex C. The level of calculation is chosen according the nature of the cluster and the charges in order to ensure good results as demonstrated is literature.

Cluster	Fragment 1	Fragment 2	bond energy (eV)
O_2	O	O	5.38
O_3	O_2	O	0.75
O_4	O_3	O	2.74
AlO	Al	O	5.21
AlO_2	AlO	O	4.02
AlO_3	AlO	O_2	1.85
AlO_4	AlO_2	O_2	2.50
Al_2	Al	Al	2.06
Al_2O	AlO	Al	5.49
Al_2O_2	AlO_2	Al	6.10
Al_2O_3	AlO_2	AlO	4.98
Al_2O_4	AlO_3	AlO	4.81
Al_3	Al_2	Al	2.65
Al_3O	Al_2O	Al	0.88
Al_3O_2	Al_2O	AlO	3.38
Al_3O_3	Al_2O_3	Al	6.86
Al_3O_4	Al_3O_3	O	5.77
Al_4	Al_3	Al	1.56
Al_4O_2	Al_3O_2	Al	3.09
Al_4O_3	Al_3O_3	Al	5.83
Al_4O_4	Al_3O_4	Al	6.04
Al_4O_5	Al_2O_3	Al_2O_2	5.36
Al_4O_6	Al_4O_5	O	7.61
Al_6O_6	Al_5O_5	AlO	5.14
Al_6O_9	Al_6O_8	O	7.88
Al_8O_{12}	Al_8O_{11}	O	8.15

Table 2.1: DFT calculated dissociation energy from the most stable geometry of neutral clusters considering the weakest bond breaking (average of 4.4 ± 2 eV). The most stable geometries of neutral clusters are taken from Julien Lam's calculation[46].

Cluster	Fragment 1	Fragment 2	bond energy (eV)
$Al_3O_5^+$	$Al_3O_3^+$	O_2	2.55
$Al_4O_7^+$	$Al_4O_5^+$	O_2	2.81
$Al_4O_7^+$	$Al_4O_6^+$	O	3.85
$Al_4O_6^+$	$Al_4O_5^+$	O	4.38

Table 2.2: DFT calculated dissociation energy on the most stable geometry of charged clusters.

actions according to this criterion: $Al_3O_5^+ \rightarrow Al_3O_3^+ + O_2$, $Al_4O_7^+ \rightarrow Al_4O_5^+ + O_2$, $Al_4O_7^+ \rightarrow Al_4O_6^+ + O$ and $Al_4O_6^+ \rightarrow Al_4O_5^+ + O$. By computing the difference of energy, one have a lower estimation of the dissociation energy for each of these reactions: 2.55 eV, 2.8 eV, 3.85 eV and 4.3 eV respectively. The results are summarized in table 2.2 and are comparable to the bond energies for the equivalent reactions from neutral clusters.

Distribution of oscillators frequencies were also computed on 6 different charged clusters: $Al_2O_3^+$, $Al_2O_4^+$, $Al_3O_2^+$, $Al_3O_3^+$, $Al_3O_4^+$ and $Al_2O_5^+$. It will be interesting to compare them to the vibration frequency of the clusters used in the microcanonical model. The most stable geometry was calculated using the same technique as above. Vibrational frequencies were calculated from the DFT optimized geometries using single point calculation CAS-MP2(3,3)/6-311++G(3df,3pd) or CAS-MP2(2,2)/6-311++G(3df,3pd) depending on the multiplicity. The results are summarized in table 2.3. The vibrational frequencies ranged from $1.21 \times 10^{12} s^{-1}$ to $3.46 \times 10^{13} s^{-1}$. Convergence of the high level calculations on a large cluster was difficult to achieve, and only small clusters are presented here. These frequencies are interesting to discuss in regard to the model as they should be related to the frequency ν. Of course, they are not unique, but one should keep in mind the order of magnitude and the average value of $1.3 \pm 1 \times 10^{13} s^{-1}$.

In short: *Quantum calculations on many clusters (neutral and charged) provide the vibration modes of the clusters and an estimation of the desorption energy. The bound energy is calculated as the difference in energy between a cluster in the most stable geometry and the two fragments. This provides a lower estimation of the activation energy as it is the limit case with no energy barrier. For these stable clusters, the desorption energy is rather large, around 4.5 eV with a standard deviation of 2.0 eV.*

	Wavenumber (cm^{-1})	Frequency (s^{-1})
$Al_2O_3^+$	63.542	1.90×10^{12}
	160.6444	4.82×10^{12}
	426.932	1.28×10^{13}
	1070.5484	3.21×10^{13}
	64.2689	1.93×10^{12}
	264.8373	7.94×10^{12}
	857.9884	2.57×10^{13}
	153.5245	4.60×10^{12}
	269.5916	8.08×10^{12}
	1043.5521	3.13×10^{13}
$Al_2O_4^+$	69.9953	2.10×10^{12}
	197.0233	5.91×10^{12}
	571.094	1.71×10^{13}
	683.497	2.05×10^{13}
	135.7173	4.07×10^{12}
	281.3896	8.44×10^{12}
	649.4863	1.95×10^{13}
	957.9322	2.87×10^{13}
	188.5951	5.65×10^{12}
	357.9738	1.07×10^{13}
	664.3667	1.99×10^{13}
	958.0738	2.87×10^{13}
$Al_3O_2^+$	40.4703	1.21×10^{12}
	40.4703	1.21×10^{12}
	108.1641	3.24×10^{12}
	108.1641	3.24×10^{12}
	238.601	7.15×10^{12}
	238.601	7.15×10^{12}
	330.9319	9.92×10^{12}
	522.0569	1.57×10^{13}
	909.4282	2.73×10^{13}
	1152.6912	3.46×10^{13}
$Al_3O_3^+$	169.6939	5.09×10^{12}
	199.0543	5.97×10^{12}
	597.0369	1.79×10^{13}
	820.0623	2.46×10^{13}
	169.6944	5.09×10^{12}
	273.0041	8.18×10^{12}
	675.4853	2.03×10^{13}
	820.4879	2.46×10^{13}
	197.373	5.92×10^{12}
	398.6654	1.20×10^{13}
	676.5087	2.03×10^{13}
	906.6551	2.72×10^{13}

	Wavenumber (cm^{-1})	Frequency (s^{-1})
$Al_3O_4^+$	246.9103	7.40×10^{12}
	421.5448	1.26×10^{13}
	535.8503	1.61×10^{13}
	700.8694	2.10×10^{13}
	741.7171	2.22×10^{13}
	247.3633	7.42×10^{12}
	421.9822	1.27×10^{13}
	579.7824	1.74×10^{13}
	701.7165	2.10×10^{13}
	846.9449	2.54×10^{13}
	337.8109	1.01×10^{13}
	535.2298	1.60×10^{13}
	692.3588	2.08×10^{13}
	735.3846	2.20×10^{13}
	847.3825	2.54×10^{13}
$Al_3O_5^+$	86.1615	2.58×10^{12}
	146.1669	4.38×10^{12}
	285.062	8.55×10^{12}
	406.3666	1.22×10^{13}
	710.9609	2.13×10^{13}
	892.6921	2.68×10^{13}
	97.4417	2.92×10^{12}
	178.4102	5.35×10^{12}
	363.5616	1.09×10^{13}
	507.2397	1.52×10^{13}
	729.2667	2.19×10^{13}
	931.0337	2.79×10^{13}
	104.8636	3.14×10^{12}
	277.9365	8.33×10^{12}
	394.6595	1.18×10^{13}
	671.631	2.01×10^{13}
	824.6668	2.47×10^{13}
	1003.141	3.01×10^{13}

Table 2.3: DFT calculated vibration frequencies (average $1.3 \pm 1 \times 10^{13} s^{-1}$).

2.4 Measurement of desorption energies

2.4.1 Cluster source experimental set-up

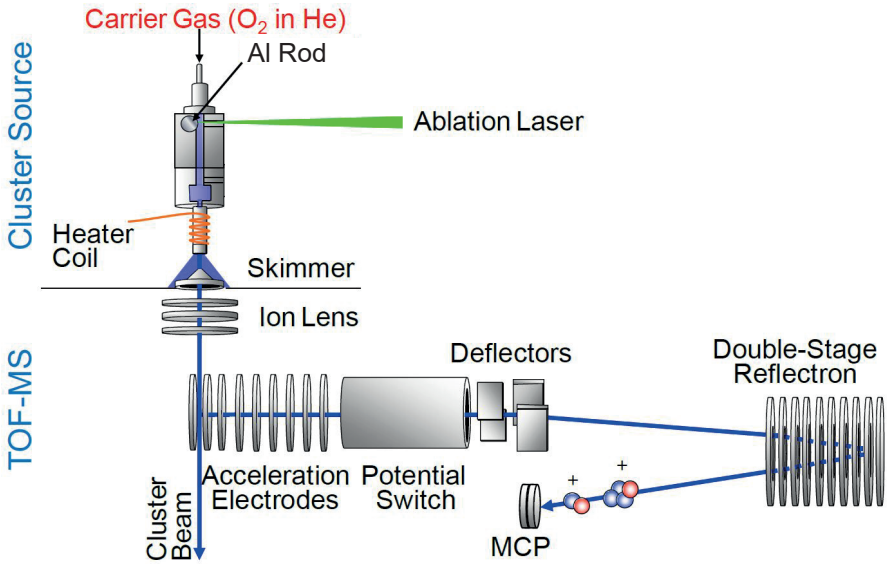

Figure 2.6: Schematic diagram of the experimental setup. *Reprinted from Nagata et al. 2015*[128]

Measuring desorption reaction rates on cluster requires a specific cutting edge experimental set-up. I was able to travel to Japan thanks to the JSPS ‖ summer program in order to perform experiments at the University of Tokyo in the team of Prof. Mafuné. They have developed with Ken Miyajima an experiment coupling a cluster source using laser ablation in a controlled environment with a heating tube and a time of flight mass spectrometer. This experiment was originally designed to study chemical reactions on clusters depending on the temperature. In my project, this experiment was used to measure the reaction constant of decomposition of aluminum oxide clusters produced by laser ablation. The team was kind enough to let me explore the possibilities of their experimental setup for 3 months. In order to test the microcanonical model, cluster distributions were measured for different growth conditions by changing the density of the quenching gas. In this experimental setup, the clusters produced are positively charged. Charges are not explicit in the model but do not change the core of the discussion. They can have an impact on the interaction potential, the geometry of the cluster and the desorption energies. In the model, charges can thus modify some parameters.

‖Japan Society for Promotion of Science

The previous calculations show that the average difference in desorption energies is low compared to the differences observed in-between clusters and should have little impact on the model.

As shown in figure 2.6, clusters were created by ablating a rotating aluminum rod (Nilaco, 5.0×30 mm, > 99 %) using the focused second harmonic (532 nm) of a Nd:YAG pulsed lasers (10 Hz repetition rate, 5-6 ns pulse duration, 7 mJ per pulse) in the presence of oxygen (1% oxygen; Japan Fine Products Co., Ltd.,>99.9% purity) diluted in helium (Japan Fine Products Co., Ltd., >99.99995%). The pressure of buffer gas can be tuned from 0.47 to 0.825 MPa, changing the cluster formation's conditions which affect the size distributions of clusters. The partial pressure of dioxygen was held constant and the partial pressure of helium was varied. The cluster beam passed through an extension tube of 4 mm inner diameter and 120 mm long. The temperature in the extension tube can be tuned from 298 to 1000 K using a resistive heater and monitored using a thermocouple (type K). Inside the tube, the density of gas was estimated to be 10^{17} molecules cm^{-3} and the flight time is about 100 μs such that the thermodynamic equilibrium is reached very quickly. This is enough time to thermalize the clusters even considering only conduction effects through collision with the He carrier gas. During this 100 μs, reactions within clusters can occur before the beam expands in the vacuum chamber (about 2×10^{-6} Torr) cooling it instantly and stopping all reactions. Positively charged clusters were selected and accelerated before entering the time of flight mass spectrometer. The ions travel in a 2.4 m field-free region. They were reflected by a dual-stage reflectron and detected using a Hamamatsu double-microchannel plate detector. Signal from the detector was amplified with a 350 MHz preamplifier (Stanford SR445A) and digitized using an oscilloscope (LeCroy LT344L).

In short: *Direct measurements of desorption energies on aluminum oxide clusters were achieved by heating clusters produced by laser ablation. The stoichiometry of the remnant clusters was measured with a TOF-mass spectrometer depending on the temperature. The hotter, the more clusters break and their size reduces. 21 O_2 desorption reactions were clearly identified during this process. Fitting the ratio of the clusters at different temperatures using Arrhenius reaction rates provides O_2 dissociation energies relative to the identified reactions. The average dissociation energy appears to be much lower than the one found through quantum calculation:* 0.4 ± 0.2 *eV against* 4.4 ± 2 *eV. This order of magnitude can be extended to the other desorption reactions happening simultaneously, even if it was impossible to directly measure them. Such a low value can be understood as the clusters are not formed in the most stable states. Thus, one needs to be careful when considering quantum calculation at the equilibrium to describe clusters in laser-generated plasma.*

Averaged time-of-flight mass spectrometry (TOFMS) distribution (typically 500 sweeps) have a resolution of $m/\Delta m = 1000$. In order to observe a large range of cluster size, each measurement was composed of 2 data acquisitions with two different sets of parameters for the TOFMS in order to observe small size clusters and large size clusters. Both acquisitions were merged in order to observe single charged clusters from 100 to 1000 atomic mass units. In the case of alumina clusters around bulk stoichiometry $(Al_2O_3)_n$, it corresponds to sizes from 6 to 49 atoms. The relative amount of species was deduced considering the integrated area of the corresponding peaks from -0.5 to $+0.5$ atomic mass units.

Figure 2.7 (a) shows an example of the mass spectra obtained. The Log-Normal shape is typical and corresponds to the expected distribution in size of the cluster derived from the nucleation theory[129]. The inset represents a zoom from 150 to 180 mass numbers. One can see that the main peaks correspond to different alumina cluster stoichiometries while the secondary peaks, much smaller, are not assigned to any stoichiometry. These are the so-called *ghost signals*. They are due to the contamination of other gas species like hydrogen or water that can attach to the cluster's surface. Some of these signals could be due to isotopes, though this is highly unlikely. The portion of aluminum and oxygen isotopes are below the detection limit ($<$0.24% for ^{14}O). Consequently, we do not consider or analyze these minor peaks in the consideration of aluminum oxide clusters**.

A color map of the cluster composition is represented in figure 2.7 (b). It is obtained by integrating the TOF spectrometer peaks for each of the possible cluster stoichiometry depending on the number of oxygen and aluminum atoms. Such a map gives a quick insight on the cluster composition and size distribution. In particular, the evolution of such a map depending on the temperature is useful in order to identify the desorption reactions on the clusters (see figure 2.8) Most of them are composed of 10 to 20 atoms and have a stoichiometry close to $(Al_2O_3)_n^+$ ((2:3) stoichiometry). This is expected because it corresponds to the stoichiometry of the bulk material. Signals above and under the red lines corresponds to unexpected stoichiometries like $Al_1O_9^+$. It is very unlikely that these signal actually corresponds to such unstable composition but are probably some *ghost signal*. In the following, only the signals corresponding to $Al_mO_n^+$ for $(2/3)n+4 \geq m \geq (2/3)n-6$ are considered (data in-between the two red lines on figure 2.7 (b)). This cut is chosen in order to remove most of the ghost signals without cutting any plausible stoichiometry no matter the experimental conditions.

Figure 2.8 shows color maps of the clusters' composition depending on the temperature. One can observe that while heating, cluster size decreases follow-

**It happens that some of the *ghost signal* have the same mass as some alumina cluster stoichiometries. In that case, it either corresponds to unexpected stoichiometries and are ignored (see figure 2.7 (b)) or can lead to background signals as for $Al_3O_7^+$ in figure 2.9 (b) (dashed line).

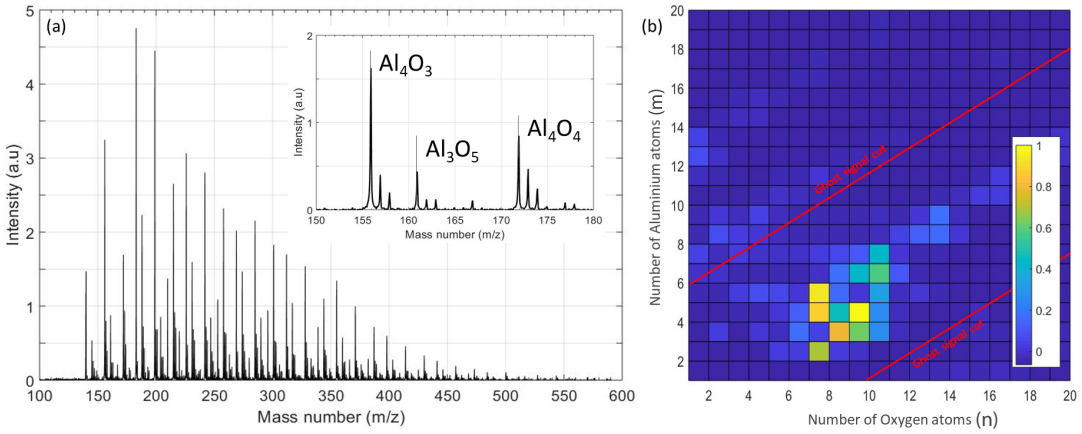

Figure 2.7: (a) Typical spectrum obtained by the TOF-MS after calibration. The inset is a zoom on some part of the spectrum with the assigned peaks. On the right side of the peaks, one can see the so-called *ghost signals*. (b) Typical color mapping of the relative integrated raw signal for the different cluster stoichiometry. The red solid lines represent the cut used in the data processing in order to remove the ghost signals.

ing the (2:3) stoichiometry (white dashed line). Clusters are desorbing aluminum and oxygen atoms. Defining precise reaction paths is impossible except for the stoichiometries inside the red square. There, the relative evolution of the cluster stoichiometries clearly match O_2 desorption reactions. Large clusters can experience several O_2 molecule desorptions. The ensemble of these reactions from a given stoichiometry is called *channel*. In the following, I focus on these evolutions in order to study these reactions. The reaction energies can be deduced from the fit of the cluster composition. Because these reactions occurred simultaneously with a general decrease of the alumina clusters, one can expect the activation energy of the cluster evaporation reaction to have a similar magnitude.

Figure 2.9 shows the relative signal intensities for each of the identified desorption channels. For each of the reaction channels, it was possible to determine the different reactions involved and the theoretical relative intensity associated. By fitting the experimental data with these reaction models (solid lines), I was able to determine the reaction rate and the activation energy of each of the reactions. The results are averaged on 10 different measurements.

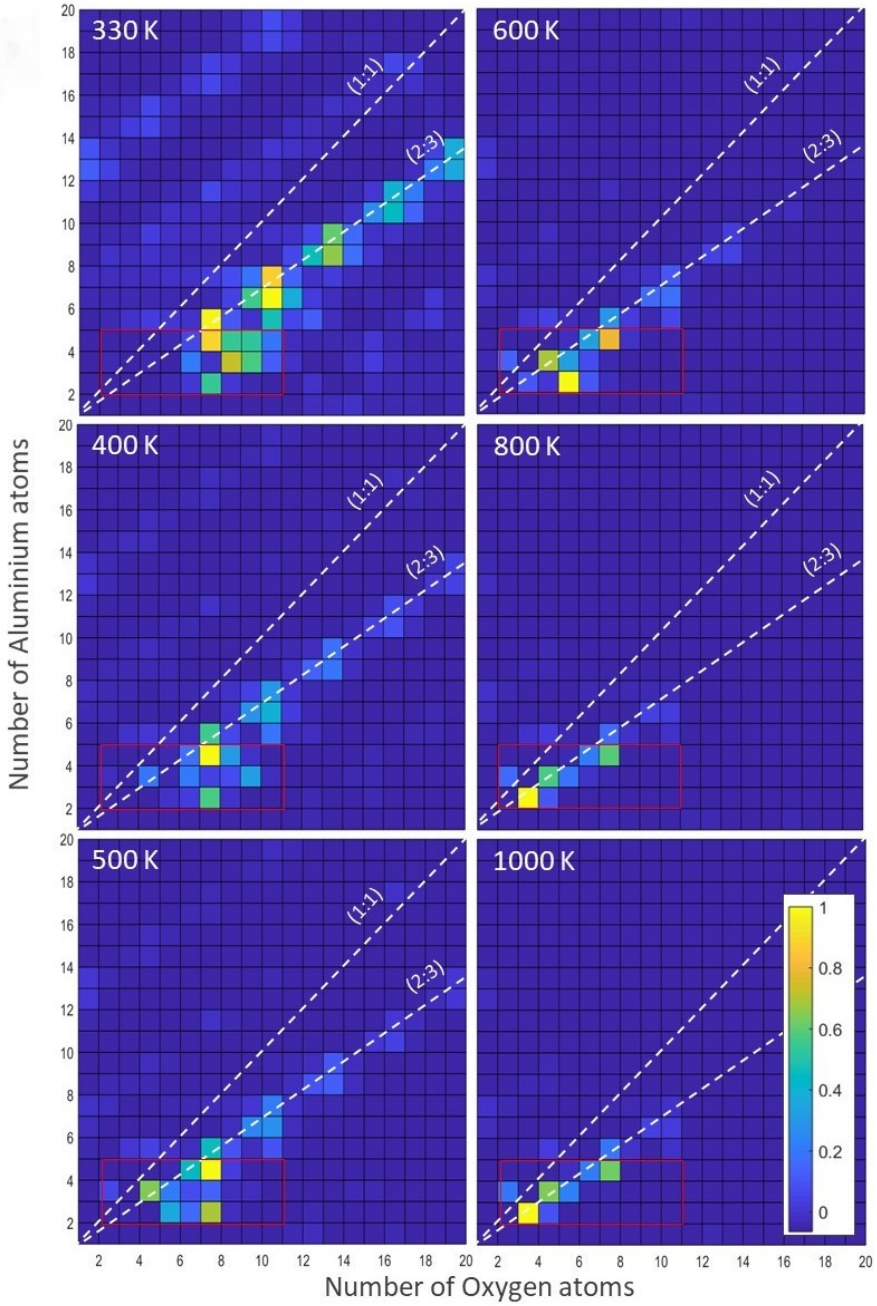

Figure 2.8: Color mapping of the relative integrated signals for the different cluster stoichiometries in terms of their composition for several temperatures. The dashed white lines represent the composition $(AlO)_k^+$ and $(Al_2O_3)_k^+$ respectively denoted (1:1) and (2:3). One can notice the presence of *ghost signals*.

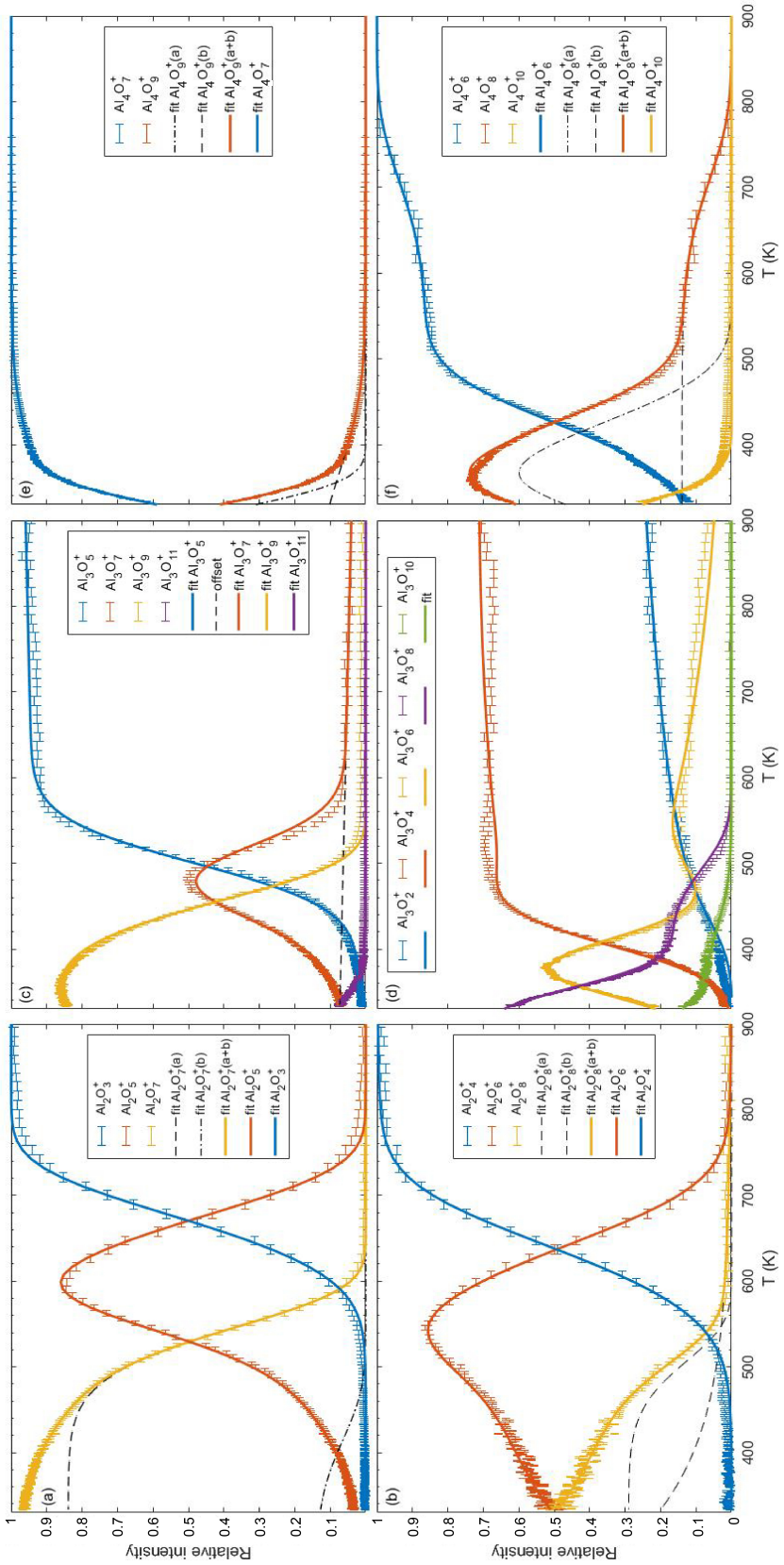

Figure 2.9: Cluster composition as a function of the temperature. For all these measurements, the ablation pressure is set at $P = 0.37$ MPa with a 0.09% O_2 concentration (100 mL/min He flow, 10 mL/min 1% O_2 flow, 0.8 MPa input pressure). In the panel (d), only the sum of the isomers are represented for clarity.

2.4.2 Construction of the model and fitting technique

Here is presented the kinetic models used to fit the evolution of the species depending on the temperature for the different channels. After detailing the reasoning by analyzing one channel, results on the other channels are given more concisely.

Detailed example of $Al_2O_n^+$ with n odd

Let us have a closer look at the graph figure 2.9 (a) corresponding to the desorption channel $Al_2O_n^+$ for n odd. One can observe the decrease of $Al_2O_7^+$ around 520 K correlated with an increase of $Al_2O_5^+$ and the decrease of $Al_2O_5^+$ around 680 K correlated with an increase of $Al_2O_3^+$. This corresponds to the two reactions $Al_2O_7^+ \rightarrow Al_2O_5^+ + O_2$ and $Al_2O_5^+ \rightarrow Al_2O_3^+ + O_2$. However, with a closer look at the evolution of $Al_2O_7^+$, one can notice a break in the exponential behavior. This is typical of the presence of two different isomers of $Al_2O_7^+$ reacting with different characteristic times.

From this observation one can deduce the different reactions and the associated rates:

$$\begin{aligned}
Al_2O_7^+(a) \rightarrow Al_2O_5^+ + O_2 \quad \text{with} \quad k_1^{(a)} = A_1^{(a)} e^{-\frac{E_{a1}^{(a)}}{k_B T}} \\
Al_2O_7^+(b) \rightarrow Al_2O_5^+ + O_2 \quad \text{with} \quad k_1^{(b)} = A_1^{(b)} e^{-\frac{E_{a1}^{(b)}}{k_B T}} \\
Al_2O_5^+ \rightarrow Al_2O_3^+ + O_2 \quad \text{with} \quad k_2 = A_2 e^{-\frac{E_{a2}}{k_B T}}
\end{aligned} \tag{2.13}$$

One can write down the temporal evolution of the relative concentration of each species considering that all the reactions are first-order reactions:

$$\begin{aligned}
\frac{d[Al_2O_7^+(a)]}{dt} &= -k_1^{(a)}[Al_2O_7^+(a)](t) \\
\frac{d[Al_2O_7^+(b)]}{dt} &= -k_1^{(b)}[Al_2O_7^+(b)](t) \\
\frac{d[Al_2O_5^+]}{dt} &= -k_2[Al_2O_5^+](t) + k_1^{(a)}[Al_2O_7^+(a)](t) \\
&\qquad + k_1^{(b)}[Al_2O_7^+(b)](t) \\
\frac{d[Al_2O_3^+]}{dt} &= +k_2[Al_2O_5^+](t)
\end{aligned} \tag{2.14}$$

with [ ] corresponding to the normalized partial pressure of the different species.

One can solve analytically this system of first-order equations. The first ones are simple exponential and do not depend on the evolution of the other species because the backward reaction is never considered[††]. On the opposite, the next ones depend on the concentration evolution of the previous species. However, one can use the previous exponential solution for the concentration of these species as input and use the variation of parameters method to solve it. Finally, some initial conditions corresponding to the initial ratio in the different species are needed to fully define the solutions. In that case we considered that there is no $Al_2O_3^+$ and that the initial proportions of $Al_2O_7^+(a)$, $Al_2O_7^+(b)$ and $Al_2O_5^+$ are respectively $\alpha^{(a)}$,$\alpha^{(b)}$ and $\beta = 1-(\alpha^{(a)}+\alpha^{(b)})$. Initial guess for these values are $\beta \simeq 0$, $\alpha^{(a)} \simeq 0.8$ and $\alpha^{(b)} \simeq 0.2$ considering the curve at low temperature (see figure 2.9 (a)).

This leads to the following evolution of the species:

$$\begin{aligned}
[Al_2O_7^+(a)] &= \alpha^{(a)} e^{-k_1^{(a)} t} \\
[Al_2O_7^+(b)] &= \alpha^{(b)} e^{-k_1^{(b)} t} \\
[Al_2O_5^+] &= \phi e^{-k_2 t} \\
[Al_2O_3^+] &= 1 - ([Al_2O_7^+(a)] + [Al_2O_7^+(b)] + [Al_2O_5^+])
\end{aligned} \tag{2.15}$$

with

$$\begin{aligned}
\phi = \frac{k_1^{(a)}\alpha^{(a)}}{k_2 - k_1^{(a)}} \left[e^{(k_2 - k_1^{(a)})t} - 1\right] + \frac{k_1^{(b)}\alpha^{(b)}}{k_2 - k_1^{(b)}} \left[e^{(k_2 - k_1^{(b)})t} - 1\right] \\
+(1 - \alpha^{(a)} - \alpha^{(b)})
\end{aligned} \tag{2.16}$$

This model might seem complicated to fit with 9 parameters: $A_1^{(a)}$, $A_1^{(b)}$, A_2, $E_{a1}^{(a)}$, $E_{a1}^{(b)}$, E_{a2}, t, $\alpha^{(a)}$ and $\alpha^{(b)}$. The time of flight in the heating tube t is estimated to be 100 μs. All the other parameters are first estimated by hand. The initial amount of each species can be deduced from the experimental data at low temperature as explained previously and coupled variables A_i and E_{ai} set the slope at the inflection point (e.g. at 500K in figure 2.9 (a)). Given the temperature and the slope of the inflection point, one can guess these values.

From this setting, an algorithm of least squares minimization is used in order to optimize the parameters by fitting the experimental data presented in figure 2.9 (a). Initially, only the bigger clusters are considered as their concentration evolution does not depend on the other species. Then, the other species are fitted step by

[††]Oxygen molecules corresponds to less than 1% of the carrier gas and most of it is consumed by the formation of the cluster. The density of clusters and O_2 molecules is low enough in the heating tube to neglect any collision between the reactants.

step in order to be sure to have a good convergence. Finally, all the evolution is fitted at once in order to adjust all the parameters together. This fitting procedure leads to fast and stable convergence. In instances where the initial guess was varied dramatically, the algorithm converges to very similar values.

The uncertainties due to the differences in convergence have been checked to be always below 1% and were found to be negligible compared to the error between the different measurements. All the different desorption channels were treated similarly.

$\mathbf{Al_2O_n^+}$ with n even

From the evolution of the species displayed in figure 2.9b, the following reactions are considered:

$$\begin{aligned} \mathrm{Al_2O_8^+}(a) &\rightarrow \mathrm{Al_2O_6^+} + \mathrm{O_2} \quad \text{with} \quad k_1^{(a)} = A_1^{(a)} e^{-\frac{E_{a1}^{(a)}}{k_B T}} \\ \mathrm{Al_2O_8^+}(b) &\rightarrow \mathrm{Al_2O_6^+} + \mathrm{O_2} \quad \text{with} \quad k_1^{(b)} = A_1^{(b)} e^{-\frac{E_{a1}^{(b)}}{k_B T}} \\ \mathrm{Al_2O_6^+} &\rightarrow \mathrm{Al_2O_4^+} + \mathrm{O_2} \quad \text{with} \quad k_2 = A_2 e^{-\frac{E_{a2}}{k_B T}} \end{aligned} \tag{2.17}$$

Initially no $\mathrm{Al_2O_4^+}$ is present, as shown by the blue traces in figure 2.9 (b). The model is thus identical to the previous one transposed to even species.

$Al_3O_n^+$ with n odd

From the evolution of the species figure 2.9 (c), the following reactions are considered:

$$\begin{aligned} Al_3O_{11}^+ &\rightarrow Al_3O_9^+ + O_2 \quad \text{with} \quad k_1 = A_1 e^{-\frac{E_{a1}}{k_B T}} \\ Al_3O_9^+ &\rightarrow Al_3O_7^+ + O_2 \quad \text{with} \quad k_2 = A_2 e^{-\frac{E_{a2}}{k_B T}} \\ Al_3O_7^+ &\rightarrow Al_3O_5^+ + O_2 \quad \text{with} \quad k_3 = A_3 e^{-\frac{E_{a3}}{k_B T}} \end{aligned} \tag{2.18}$$

Initially no $Al_3O_5^+$ nor $Al_3O_7^+$ is present, as shown by the blue and orange traces in figure 2.9 (c) however $Al_3O_7^+$ appears with an off-set (dashed line). The off-set could be some non-reactive isomer of some *host signal*[‡‡]. If it is a non-reactive isomer, one could expect the signal to be constant. Yet cluster production can drift in time and detector sensitivity may change with temperature. If it is a ghost signal or low reacting cluster, one could expect few reactions to happen when the temperature increases leading to a slow decrease. Considering the linear evolution of $Al_3O_7^+$ signal after 650 K, the off-set value was described as linear: $[\text{offset}] = aT + \gamma$. a and γ are fitted on the value above $650K$. The initial proportions of $Al_3O_{11}^+$ and $Al_3O_9^+$ are respectively α and $\beta = 1 - (\alpha + \gamma)$. γ is the off-set value for $T = 0$. Thus, the evolution of concentrations are:

$$\begin{aligned} [Al_3O_{11}^+] &= \alpha e^{-k_1 t} \\ [Al_3O_9^+] &= \phi e^{-k_2 t} \\ [Al_3O_7^+] &= \psi e^{-k_3 t} \\ [Al_3O_5^+] &= 1 - ([Al_3O_{11}^+] + [Al_3O_9^+] + [Al_3O_7^+]) \end{aligned} \tag{2.19}$$

with

$$\begin{aligned} \phi &= \frac{k_1 \alpha}{k_2 - k_1} \left[e^{(k_2 - k_1)t} - 1 \right] + \beta \\ \psi &= \frac{k_1 k_2 \alpha}{(k_2 - k_1)(k_3 - k_1)} \left[e^{(k_3 - k_1)t} - 1 \right] \\ &\qquad \left(\beta - \frac{k_1 \alpha}{k_2 - k_1} \right) \frac{k_2}{(k_3 - k_2)} \left[e^{(k_3 - k_2)t} - 1 \right] \end{aligned} \tag{2.20}$$

[‡‡]Clusters having the same mass over charge ration and thus are identified as $Al_3O_7^+$ but are not.

$Al_3O_n^+$ with n even

From the evolution of the species figure 2.9 (d), the following reactions are considered:

$$\begin{aligned}
Al_3O_{10}^+(a) &\rightarrow Al_3O_8^+(a) + O_2 \quad \text{with} \quad k_1^{(a)} = A_1^{(a)} e^{-\frac{E_{a1}^{(a)}}{k_B T}} \\
Al_3O_{10}^+(b) &\rightarrow Al_3O_8^+(b) + O_2 \quad \text{with} \quad k_1^{(b)} = A_1^{(b)} e^{-\frac{E_{a1}^{(b)}}{k_B T}} \\
Al_3O_8^+(a) &\rightarrow Al_3O_6^+(a) + O_2 \quad \text{with} \quad k_2^{(a)} = A_2^{(a)} e^{-\frac{E_{a2}^{(a)}}{k_B T}} \\
Al_3O_8^+(b) &\rightarrow Al_3O_6^+(b) + O_2 \quad \text{with} \quad k_2^{(b)} = A_2^{(b)} e^{-\frac{E_{a2}^{(b)}}{k_B T}} \\
Al_3O_6^+(a) &\rightarrow Al_3O_4^+ + O_2 \quad \text{with} \quad k_3^{(a)} = A_3^{(a)} e^{-\frac{E_{a3}^{(a)}}{k_B T}} \\
Al_3O_6^+(b) &\rightarrow Al_3O_4^+ + O_2 \quad \text{with} \quad k_3^{(b)} = A_3^{(b)} e^{-\frac{E_{a3}^{(b)}}{k_B T}} \\
Al_3O_4^+ &\rightarrow Al_3O_2^+ + O_2 \quad \text{with} \quad k_4 = A_4 e^{-\frac{E_{a4}}{k_B T}}
\end{aligned} \tag{2.21}$$

There are two different channels of desorption here: (a) and (b). That is to say that the isomer (a) of one stoichiometry always leads to the unique isomer (a) of the second stoichiometry. One can deduce that because the intensity of the channel (a) and (b) are not exchanged (about $75\% - 25\%$) and the reactions occur at different temperatures making the path quite clear. This can be easily understood because of the cluster geometries. Let us consider two different geometries of the same stoichiometry. When both of them lose one O_2 molecule, it is very likely that the remaining clusters still have different geometries leading to two different isomers.

Initially no $Al_3O_4^+$ and $Al_3O_6^+$ are present in the reaction tube. The initial proportions of $Al_3O_{10}^+$ (a) and (b) and $Al_3O_8^+$ (a) and (b) are respectively $\alpha^{(a)}$, $\alpha^{(b)}$, $\beta^{(a)}$ and $\beta^{(b)} = 1 - (\alpha^{(a)} + \alpha^{(b)} + \beta^{(a)})$. Thus, the evolutions of concentrations for $i = [a, b]$ are:

$$\begin{aligned}
[Al_2O_{10}^+(i)] &= \alpha^{(i)} e^{-k_1^{(i)} t} \\
[Al_2O_8^+(i)] &= \phi^{(i)} e^{-k_2^{(i)} t} \\
[Al_2O_6^+(i)] &= \psi^{(i)} e^{-k_3^{(i)} t} \\
[Al_2O_4^+] &= \chi e^{-k_4 t} \\
[Al_2O_2^+] &= 1 - \sum_{i=a,b} \left([Al_2O_{10}^+(i)] + [Al_2O_8^+(i)] + [Al_2O_6^+(i)] \right) - [Al_2O_4^+]
\end{aligned} \tag{2.22}$$

with

$$
\begin{aligned}
\phi^{(i)} &= \frac{k_1^{(i)}\alpha^{(i)}}{k_2^{(i)}-k_1^{(i)}}\left[e^{(k_2^{(i)}-k_1^{(i)})t}-1\right]+\beta^{(i)} \\
\psi^{(i)} &= K_1^{(i)}\left[e^{(k_3^{(i)}-k_1^{(i)})t}-1\right]+K_2^{(i)}\left[e^{(k_3^{(i)}-k_2^{(i)})t}-1\right] \\
\chi^{(i)} &= \frac{k_3^{(i)}K_1^{(i)}}{k_4-k_1^{(i)}}\left[e^{(k_4-k_1^{(i)})t}-1\right]+\frac{k_3^{(i)}K_2^{(i)}}{k_4-k_2^{(i)}}\left[e^{(k_4-k_2^{(i)})t}-1\right] \\
&\qquad -\frac{k_3^{(i)}(K_1^{(i)}+K_2^{(i)})}{k_4-k_3^{(i)}}\left[e^{(k_4-k_3^{(i)})t}-1\right] \qquad (2.23) \\
\chi &= \sum_{i=a,b}\chi^{(i)} \\
K_1^{(i)} &= \frac{k_2^{(i)}k_1^{(i)}\alpha^{(i)}}{(k_2^{(i)}-k_1^{(i)})(k_3^{(i)}-k_1^{(i)})} \\
K_2^{(i)} &= \frac{k_2^{(i)}}{(k_3^{(i)}-k_2^{(i)})}\left(\beta^{(i)}-\frac{k_1^{(i)}\alpha^{(i)}}{(k_2^{(i)}-k_1^{(i)})}\right)
\end{aligned}
$$

$Al_4O_n^+$ with n odd

From the evolution of the species figure 2.9 (e), the following reactions are considered:

$$\begin{aligned} Al_4O_9^+(a) &\rightarrow Al_4O_7^+ + O_2 \quad \text{with} \quad k_1^{(a)} = A_1^{(a)} e^{-\frac{E_{a1}^{(a)}}{k_B T}} \\ Al_4O_9^+(b) &\rightarrow Al_4O_7^+ + O_2 \quad \text{with} \quad k_1^{(b)} = A_1^{(b)} e^{-\frac{E_{a1}^{(b)}}{k_B T}} \end{aligned} \tag{2.24}$$

The initial proportions of $Al_4O_9^+$ (a) and (b) are respectively α and $1-\alpha$ such that the corresponding evolution of the different species are:

$$\begin{aligned} [Al_4O_9^+(a)] &= \alpha e^{-k_1^{(a)} t} \\ [Al_4O_9^+(b)] &= (1-\alpha) e^{-k_1^{(b)} t} \\ [Al_4O_7^+] &= 1 - ([Al_4O_9^+(a)] + [Al_4O_9^+(b)]) \end{aligned} \tag{2.25}$$

$Al_4O_n^+$ with n even

From the evolution of the species figure 2.9 (f), the following reactions are considered:

$$\begin{aligned} Al_4O_{10}^+ &\rightarrow Al_4O_8^+(a) + O_2 \quad \text{with} \quad k_1 = A_1 e^{-\frac{E_{a1}}{k_B T}} \\ Al_4O_8^+(a) &\rightarrow Al_4O_6^+ + O_2 \quad \text{with} \quad k_2^{(a)} = A_2^{(a)} e^{-\frac{E_{a2}^{(a)}}{k_B T}} \\ Al_4O_8^+(b) &\rightarrow Al_4O_6^+ + O_2 \quad \text{with} \quad k_2^{(b)} = A_2^{(b)} e^{-\frac{E_{a2}^{(b)}}{k_B T}} \end{aligned} \tag{2.26}$$

Here, $Al_4O_8^+$ (b) is not formed by the decomposition of $Al_4O_{10}^+$ but is already there. The initial proportions of $Al_4O_{10}^+$ and $Al_4O_8^+$ (a) and (b) are respectively α, $\beta^{(a)}$ and $\beta^{(b)} = 1 - (\alpha + \beta^{(a)})$ such that the corresponding evolution of the different species are:

$$\begin{aligned} [Al_4O_{10}^+] &= \alpha e^{-k_1 t} \\ [Al_4O_8^+(a)] &= \phi e^{-k_2^{(a)} t} \\ [Al_4O_8^+(b)] &= \beta^{(b)} e^{-k_2^{(b)} t} \\ [Al_4O_6^+] &= 1 - ([Al_4O_{10}^+] + [Al_4O_8^+(a)] + [Al_4O_8^+(b)]) \end{aligned} \tag{2.27}$$

with

$$\phi = \frac{k_1 \alpha}{k_2^{(a)} - k_1} \left[e^{(k_2^{(a)} - k_1)t} - 1 \right] + \beta^{(a)} \tag{2.28}$$

2.4.3 O_2 dissociation energies

From the models described above, 10 sets of parameters are obtained, one for each set of data. Table 2.4 shows the average values of (i) the logarithm of the pre-exponential factor, (ii) the activation energy, and (iii) the corresponding time of reaction at 1000 K for the different reactions. The error corresponds to the standard error of the ten different values corrected by the Student's t-distribution coefficient for a full 90 % confidence interval in order to account for the low amount of measurements. All the values are consistent with similar work carried out by Mafuné's team on different oxides[128].

The average value of the desorption energy is 0.4 ± 0.2 eV. This value is almost ten times lower than the previously calculated value (see section 2.3 and table 2.1 and 2.2). One can argue that the desorption energy is only relative to O_2 desorption reactions. These O_2 molecules could be absorbed into the surface of the cluster with weak bonds and desorb very easily. However, up to three O_2 desorption reactions were observed on a single cluster with different activation energies. It is unlikely all these are just physically adsorbed O_2 molecules. Furthermore, only O_2 desorption reactions were identified here, but many other desorption reactions involving Al atoms occurred simultaneously. One can expect the activation energies of these reactions to have the same order of magnitude as they take place in the same heating conditions. Considering the heating temperature of the experimental set-up, reactions with the activation energy of a few eV as calculated couldn't be observed at all.

The discrepancy between the measured desorption energies and the calculated desorption energy can be explained considering that the cluster formed during laser ablation are not formed in the most stable state. Indeed, the quenching is really fast and the most stable state might not be reached. Several isomers were identified in the O_2 desorption reactions, proving that it's not only the most stable configuration that is produced. It is important to be careful while considering *ab initio* calculations at the equilibrium for the cluster generated by laser ablation. These stable configurations might never be reached during the nucleation path.

$Al_2O_n^+$			
Reactions	$Log(A)$	E_a (eV)	k^{-1} (s) at 1000 K
$Al_2O_8^+(a) \rightarrow Al_2O_6^+ + O_2$	22.8 ± 0.2	0.62 ± 0.01	$1.9 \pm 0.3 \times 10^{-7}$
$Al_2O_8^+(b) \rightarrow Al_2O_6^+ + O_2$	12.9 ± 0.6	0.09 ± 0.02	$9 \pm 3 \times 10^{-6}$
$Al_2O_6^+ \rightarrow Al_2O_4^+ + O_2$	23.0 ± 0.1	0.79 ± 0.01	$9.5 \pm 0.6 \times 10^{-7}$
$Al_2O_7^+(a) \rightarrow Al_2O_5^+ + O_2$	23.3 ± 0.1	0.688 ± 0.008	$2.3 \pm 0.1 \times 10^{-7}$
$Al_2O_7^+(b) \rightarrow Al_2O_5^+ + O_2$	17.9 ± 0.3	0.304 ± 0.004	$5.6 \pm 0.3 \times 10^{-7}$
$Al_2O_5^+ \rightarrow Al_2O_3^+ + O_2$	23.0 ± 0.2	0.836 ± 0.008	$1.7 \pm 0.2 \times 10^{-6}$
$Al_3O_n^+$			
Reactions	$Log(A)$	E_a (eV)	k^{-1} (s) at 1000 K
$Al_3O_{10}^+(a) \rightarrow Al_3O_8^+(a) + O_2$	18.3 ± 0.1	0.229 ± 0.006	$1.7 \pm 1 \times 10^{-7}$
$Al_3O_{10}^+(b) \rightarrow Al_3O_8^+(b) + O_2$	21 ± 2	0.43 ± 0.06	$4 \pm 2 \times 10^{-7}$
$Al_3O_8^+(a) \rightarrow Al_3O_6^+(a) + O_2$	20.2 ± 0.1	0.328 ± 0.002	$7.5 \pm 0.1 \times 10^{-8}$
$Al_3O_8^+(b) \rightarrow Al_3O_6^+(b) + O_2$	20.4 ∓ 0.1	0.477 ± 0.006	$3.6 \pm 0.2 \times 10^{-7}$
$Al_3O_6^+(a) \rightarrow Al_3O_4^+ + O_2$	19.6 ± 0.1	0.371 ± 0.004	$2.3 \pm 0.1 \times 10^{-7}$
$Al_3O_6^+(b) \rightarrow Al_3O_4^+ + O_2$	14 ± 1	0.4 ± 0.1	$5.7 \pm 0.5 \times 10^{-5}$
$Al_3O_4^+ \rightarrow Al_3O_2^+ + O_2$	8.6 ± 0.3	0.13 ± 0.07	$1.9 \pm 1.6 \times 10^{-3}$
$Al_3O_{11}^+ \rightarrow Al_3O_9^+ + O_2$	14.4 ± 0.3	0.12 ± 0.1	$2.6 \pm 0.5 \times 10^{-6}$
$Al_3O_9^+ \rightarrow Al_3O_7^+ + O_2$	21.3 ± 0.1	0.486 ± 0.004	$1.65 \pm 0.08 \times 10^{-7}$
$Al_3O_7^+ \rightarrow Al_3O_5^+ + O_2$	18.1 ± 0.2	0.374 ± 0.008	$1.1 \pm 0.2 \times 10^{-6}$
$Al_4O_n^+$			
Reactions	$Log(A)$	E_a (eV)	k^{-1} (s) at 1000 K
$Al_4O_{10}^+ \rightarrow Al_4O_8^+(a) + O_2$	19.7 ± 0.1	0.304 ± 0.003	$9.3 \pm 0.4 \times 10^{-8}$
$Al_4O_8^+(a) \rightarrow Al_4O_6^+ + O_2$	17.8 ± 0.5	0.31 ± 0.02	$9 \pm 5 \times 10^{-7}$
$Al_4O_8^+(b) \rightarrow Al_4O_6^+ + O_2$	20.5 ± 0.4	0.71 ± 0.03	$4.7 \pm 0.6 \times 10^{-6}$
$Al_4O_9^+(a) \rightarrow Al_4O_7^+ + O_2$	20.73 ± 0.01	0.328 ± 0.002	$4.47 \pm 0.08 \times 10^{-8}$
$Al_4O_9^+(b) \rightarrow Al_4O_7^+ + O_2$	13.69 ± 0.01	0.157 ± 0.006	$7.1 \pm 0.5 \times 10^{-6}$

Table 2.4: Reaction parameters calculated from 10 fits (90% Confidence interval)

2.5 Model confrontation with experiment

Using the experiment of Prof. Mafuné, I was also able to measure the size distribution of the cluster formed for different density of Helium gas while keeping other parameters constant. The density of the buffer gas (He) has a direct impact on the nucleation as described by the microcanonical model. The higher the buffer gas density, the better the cooling and the larger the clusters. Confronting these measurements to the prediction of the model is a good way to test its validity. However, the model depends on many parameters. Some of them related to the experiment like the buffer gas density. Others related to the clusters like the partition coefficient α or the desorption energy. Determining these parameters *a priori* is impossible. In particular, the desorption energies calculated by DFT are not consistent with the ones measured.

In order to test the model on the experimental data, we chose to fit the calculated distribution on the measured one for two different buffer gas density. The obtained parameters are then discussed and compared to the expected values. To this end, we first have to determine what are the helium density, the monomer density and the temperature at the ablation point. One can calculate these parameters from the pressure at the ablation point.

2.5.1 Determination of the experimental parameters

Unfortunately, there is no direct pressure measurement at the ablation point, and its value has to be extrapolated. The gas is injected by a pulsed valve (burst of a few 100 μs) at a given pressure between 0.47 and 0.825 MPa. Then, the pressure decreases along the cluster path before reaching the vacuum chamber. Some measurements along the decompression path are reported in figure 2.10. For an injection pressure of 0.8 MPa, the pressure 70 mm after the injection valve show a maximum of 3.3 kPa while the pressure in the vacuum chamber, after about 285 mm, is measured to 3.2×10^{-4} Pa. These three values are well aligned in the semi-log plot, suggesting that the pressure decreases exponentially along the path.

There is no analytical solution of the decompression dynamic in such a complicated geometry because of the non-linearity and time dependence of the Navier-Stokes equation. However, one can expect the solution to have indeed some exponential-like behavior[130].

An exponential model is accurate enough to deduce the pressure at the ablation point. The dashed line represents the best-fitted exponential evolution of the pressure with a decay length of 13.2 mm. The dashed lines correspond to decay lengths of 13.7 and 12.7 mm estimated as the higher and lower values considering the uncertainties on the measurements. The pressure at the ablation point (red

point) can be extrapolated at 0.37 MPa with a lower value of 0.34 MPa and a higher one of 0.41 MPa that is to say an error of about 10%.

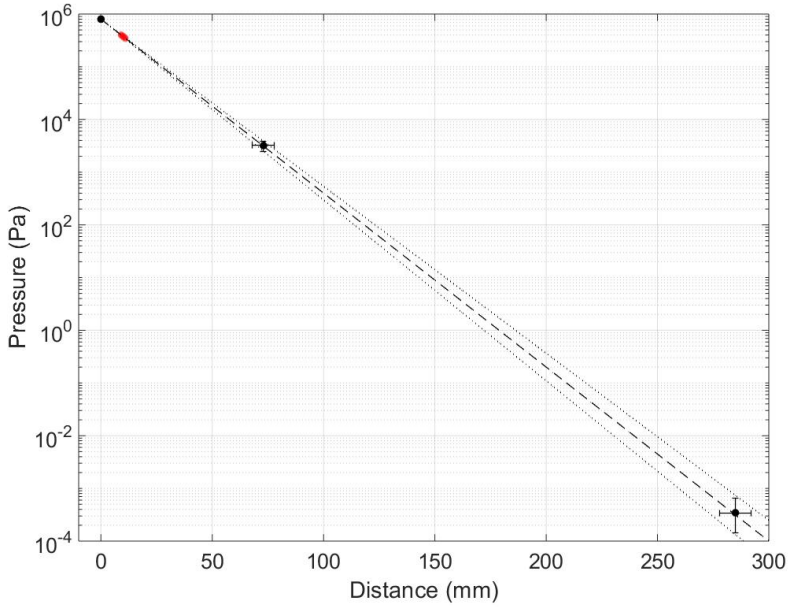

Figure 2.10: Maximal pressure measured along the decompression path at the input, in the reaction chamber, and at the output. Error bars correspond to the uncertainties on the position of the pressure gauges and uncertainties on the pressure measured. The dashed line represents the best exponential model with a decay length of 13.2 mm. The dotted lines correspond to decay lengths of 13.7 and 12.7 mm. The red dot corresponds to the ablation area. Error bars correspond to uncertainties on the position of the pressure gauge and the measure values

Considering an isentropic decompression, one can easily estimate the kinetic temperature T_2 at the ablation point from the injection temperature and pressure T_1 and p_1 and the pressure at the ablation point p_2 using:

$$T_2 = T_1 \left(\frac{p_2}{p_1} \right)^{\frac{\gamma-1}{\gamma}} \tag{2.29}$$

Because the injected gas is mostly monoatomic He, $\gamma_{\mathrm{He}} = 1.66$[131] and the injection temperature is close to room temperature, that is to say $T_1 = 293$ K. Thus, the expected temperature of the He gas at the ablation point is 216 ± 9 K.

Combined with the pressure and considering the equation of state for perfect

gas, this measurement also provides an expected density for the helium and oxygen. The density of helium is proportional to the input partial pressure and is tuned from $5.2 \pm 0.5 \times 10^{19}$ cm^{-3} to $9.2 \pm 0.9 \times 10^{19}$ cm^{-3}. In contrary, the density of oxygen atoms is kept constant to $1.8 \pm 0.2 \times 10^{17}$cm^{-3}.

The density of monomers depends both on the density of oxygen we just calculated and the density of aluminum atoms. Because the amount of oxygen was set to optimize the cluster formation in the experiment, one can expect the ratio between aluminum and oxygen to be close to 2/3. Yet, it is important to verify aluminum is not in excess nor deficient. Determining the density of aluminum is more complicated as it is driven by complex phenomena during laser ablation. It depends on many parameters such as the material, the surface aspect, the focalization of the laser, its wavelength, the pulse energy, etc. However, in the experiment, these parameters are kept constant and the average amount of ablated material per pulses is determined by weighing the rod before and after experiments. Knowing the number of pulses, one can calculate the amount of ablated aluminum atom per pulse. The measurement was systematically done after a long enough period of ablation in order to be able to measure the difference in mass (typically 30 hours). Thus, one can assume that the number of atoms ablated per pulse is $2.3 \pm 0.3 \times 10^{14}$. The error is estimated from the mass loss measured after three different experiment runs and considering the precision of the weight scale.

The amount of aluminum ablated gives a density of $1.2 \pm 0.2 \times 10^{17}$ cm^{-3} (2/3 of the oxygen density) if one considers an isotropic and homogeneous plasma with a volume of 2 mm^3. Such a volume is consistent with the observation of the plasma plume. However, the uncertainty on the plasma volume leads to uncertainties on the aluminum atom density which is probably not constant in the plasma plume.

The density of monomers is difficult to properly estimate but should have the same order of magnitude as the density of oxygen atoms. In the discussion, the density of the monomers will be discussed compared to the density of the oxygen atoms which is better estimated.

2.5.2 Comparison with experimental distribution

In order to compare the model to experimental data, cluster distributions are measured for various density of the buffer gas (He). In the model, only one kind of monomer is considered. However, aluminum oxide, composed of two kinds of atoms, was chosen in order to study an ionocovalent system. The number of aluminum and oxygen atoms in the cluster is summed for each stoichiometry and only the total number of atom (n) is considered. Experimental data in figure 2.11 (a) shows in black the typical Log-Normal distribution of the number of atoms

(n) in the clusters disregarding their composition in oxygen or aluminum. This distribution was obtained for $\rho_{\mathrm{He}} = 6 \times 10^{19}\mathrm{cm}^{-3}$.

Similarly, the average stoichiometric mass and Van der Waals radius are considered in the model: $m_X = (2m_{\mathrm{Al}} + 3m_{\mathrm{O}})/5 = 3.39 \times 10^{-26}$ kg and $r_X = (2r_{\mathrm{Al}} + 3r_{\mathrm{O}})/5 = 1.65$ Å. Van der Waals radius is chosen because it refers to the potential which is more relevant for collision cross-sections. $r_{\mathrm{He}} = 1.40$ Å and $m_{\mathrm{He}} = 6.64 \times 10^{-27}$ kg.

The other parameters of the model are optimized in the fitting procedure and then compared to the previous estimations and calculations.

Fitting is done using the least-square optimization between experimental distributions and calculated distributions for two different He densities simultaneously: $\rho_{\mathrm{He}} = 6\times10^{19}\mathrm{cm}^{-3}$ and $\rho_{\mathrm{He}} = 9.2\times10^{19}\mathrm{cm}^{-3}$. Only clusters of size between 15 and 49 are considered, given that the model is expected to overestimate the clusters of tiny size because it does not consider ripening. Furthermore, some O_2 molecules adsorptions observed on tiny clusters lead to uncertainties for cluster size below 15.

On the experimental distribution, one can observe peaks for given sizes called magic numbers ($n = 12, 17, 22, 27, 32, 37, 42$ and 47). In metal clusters, magic numbers are explained by the completion of layers within an electronic or geometrical shell model[132,133,134]. In oxides, it is mainly due to stoichiometric effect (charge effect) such that $(Al_2O_3)_n$ clusters are more produced compared to others. Here, because the clusters are charged, they always correspond to the charge balance $[(Al_2O_3)_i(AlO)]^+$ composition. Magic number features are implemented qualitatively in our model by modulating the desorption energy. The idea is simple, if a cluster is stable, its desorption energy is high. If the cluster is unstable,

In short: *In order to test the model, the size distributions of aluminum oxide clusters produced by laser ablation is measured by a TOF mass spectrometer for different densities of the buffer gas (He). The pressure at the ablation spot is estimated considering an exponential decrease along the decompression path. The temperature at the ablation point is estimated to* 216 ± 9 K *considering an isotropic decompression. From there, one can deduce that the density of the buffer gas is tuned from* $5.2 \pm 0.5 \times 10^{19}$ cm^{-3} *to* $9.2 \pm 0.9 \times 10^{19}$ cm^{-3} *and that the density of oxygen atoms is* $1.8 \pm 0.2 \times 10^{17}$ cm^{-3}. *This density is equivalent to the one of aluminum atoms calculated from the mass of ablated matter per pulse and the volume of the plasma plume. By fitting the calculated distributions on the measured ones, we obtain parameters that are then discussed and compared to these expected values and to the bounding energy that have been calculated and measured previously.*

its desorption energy is low. Thus, for a cluster of size n the energy D becomes:

$$D(n) = D + \delta . \cos\left(\frac{2\pi n}{\lambda} - \phi\right) \tag{2.30}$$

where δ is the amplitude of the modulation, λ the period of the modulation (in our case 5 atoms) and ϕ a phase.

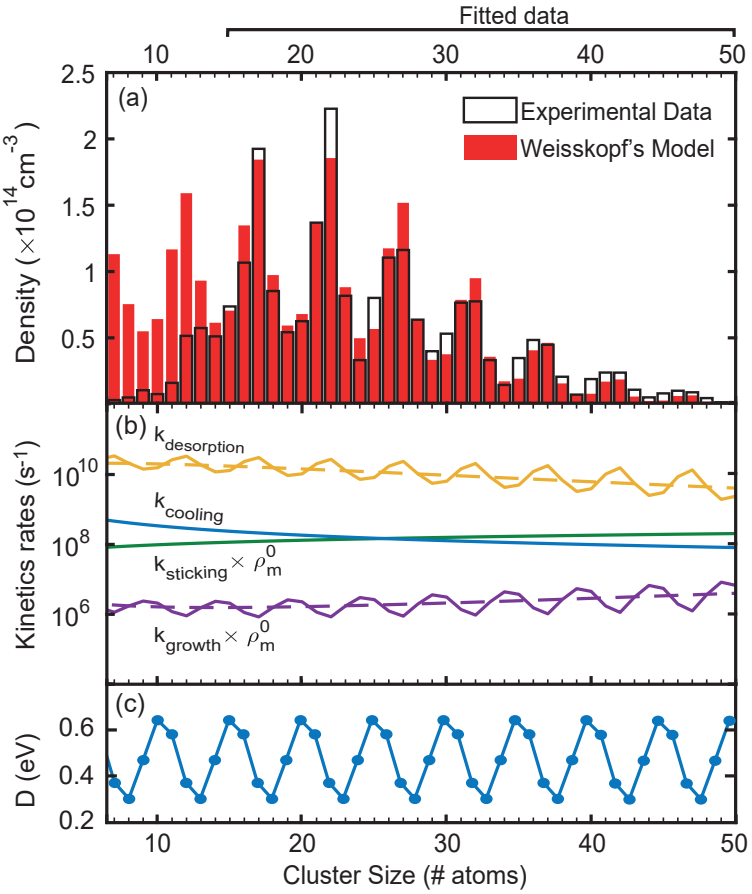

Figure 2.11: (a) Experimental distribution obtained for $\rho_{\mathrm{He}} = 6 \pm 0.6 \times 10^{19}\mathrm{cm}^{-3}$ (black) and calculated distribution (red) at the same helium density given the fitted parameters table. The cluster size corresponds to the total number of atoms in each identified cluster, whatever the cluster stoichiometry. (b) Cooling rates, desorption rates, sticking, and growth rate for the initial monomer concentration and the parameters of table 2.5. Dashed lines correspond to a constant value of D, while solid lines correspond to D modulated by a sine as shown in (c) and leading to the observed magic number features.

Parameters	Fitted values	Expected values
Monomer density ρ_X^0 (cm^{-3})	1.66×10^{17}	$1.8 \pm 0.2 \times 10^{17}$
He density ρ_{He} (cm^{-3})	6×10^{19}	$6 \pm 0.6 \times 10^{19}$
Gas temperature T (K)	215	216 ± 9
Dimer frequency ν_{dimer} (s^{-1})	7.89×10^{13}	$\sim 2 \times 10^{13}$
Cluster frequency ν (s^{-1})	1.47×10^{11}	$\sim 8 \times 10^{12}$
Equipartion coefficient α	0.014	0-1
Growth time t_{growth} (μs)	35	30-40
Dissociation Energy D	0.47 eV	0.4 ± 0.2 (3)
Modulation amplitude δ (eV)	0.18	~ 0.2 (1)
Modulation wavelength λ (atom)	5	5 (2)
Modulation phase ϕ (rad)	0.34	

Table 2.5: Parameters fitted on experimental distributions for $\rho_{He} = 6 \times 10^{19} cm^{-3}$ and $\rho_{He} = 9.2 \times 10^{19} cm^{-3}$ and expected values for these parameters according to the experimental set-up. (1) Variations observed on the measured dissociation energies. (2) Alumina stoichiometry. (3) Statistics on 21 desorption reactions observed.

In order to improve the fitting process, a first fit is done on smoothed versions of the experimental distributions without modulating the desorption energy. In this case, the last three parameters $(\epsilon, \lambda, \phi)$ are not considered. Then, these parameters are optimized on the raw data considering the previously optimized parameters. $\lambda = 5$ is easily guessed from the experimental observations and only ϵ and ϕ are numerically fitted. Finally, the last optimization of all the parameters is run on the raw data starting from the previously found values.

The resulting rates for $\rho_{He} = 6 \times 10^{19} cm^{-3}$ are shown figure 2.11 (b), with and without the desorption energy modulation plotted in figure 2.11 (c). Desorption constant is always much larger than the sticking constant and there is no critical size where this changes. The corresponding experimental and calculated distributions are compared in figure 2.11 (a). One can notice that the simulation fits very well the experimental measurement for cluster size larger than 15 and reproduces the magic numbers despite the simplicity of the model. As expected, the main difference is the overestimation of tiny clusters (between 5 and 15 atoms). Ripening might not be negligible despite the fact that monomers remain in large excess ($> 10^{17}$ cm^{-3}) compared to clusters ($< 10^{15}$ cm^{-3}) during the whole process.

Discussion of the parameters

Most of the values are in very good agreement with their experimental or theoretical estimation (See table 2.5). The density of monomer is close to the density of oxygen at the ablation point estimated to be $1.8 \pm 0.2 \times 10^{17} \mathrm{cm}^{-3}$. This density has the same order of magnitude as the density of the aluminum atoms in the plasma plume assuming a plasma volume of a few mm^3 and measuring the number of ablated atoms per pulse, $2.3 \pm 0.3 \times 10^{14}$. The temperature of the system is close to the temperature of the He gas following an adiabatic expansion (216 ± 9 K). The vibration frequency of the dimer (ν_{dimer}) is around the one of AlO ($\nu_{\mathrm{AlO}} \sim 2 \times 10^{13}$ s^{-1})[124]. The time of growth (t_{growth}) of few tens of μs is typical of the flying time inside the cluster source before entering the reaction chamber and the heating tube (see figure 2.6). Maximal desorption energies are for cluster size multiple of 5 (see figure 2.11 (c)) which is consistent with the alumina stoichiometry.

The cluster frequency ν is usually associated to the Debye frequency[116,117,118,112,113] of the considered material (about 2.2×10^{13} s^{-1} for alumina[135]). This frequency is much larger than the fitted one (1.47×10^{11} s^{-1}). Yet, the use of Debye frequency, derived from acoustics considerations in an infinite crystal, has to be questioned in the case of tiny clusters of ionocovalent materials with high anisotropy and low coupling between the oscillators. Einstein frequency considering independent oscillators[136] (about 8×10^{12} s^{-1} for α-alumina[137]) might be more relevant. Furthermore, *ab initio* calculations on alumina clusters show a large dispersion in the vibration modes frequencies. Such physical interpretations of ν parameter should be considered cautiously, especially if the clusters are not at the thermodynamic equilibrium.

The coefficient α of the effective number of clusters oscillators $s(n)$ is very low, meaning that the equipartition of energy is not reached. After a monomer sticks to a cluster, the energy is localized in a few oscillators only.

Finally, the desorption energy $D = 0.47$ eV might be surprisingly low. Indeed, it is well below the tabulated cohesive energy of bulk alumina (6.35 eV[138]) of the bond dissociation energies of the different dimers (respectively 5.20, 5.17 and 2.74 eV for AlO, O_2 and Al_2[139]) and the average value calculated by DFT on the clusters in the most stable geometries (4.4 ± 2 eV). However, the experimental measurements seem to confirm such a low value. It appears that despite large dispersion, the average activation energy is 0.4 ± 0.2 eV which is in total agreement with the value fitted in the model. It means that neither bulk material data nor DFT calculations at thermodynamic equilibrium are effective to describe such clusters. They might not reach the most stable state.

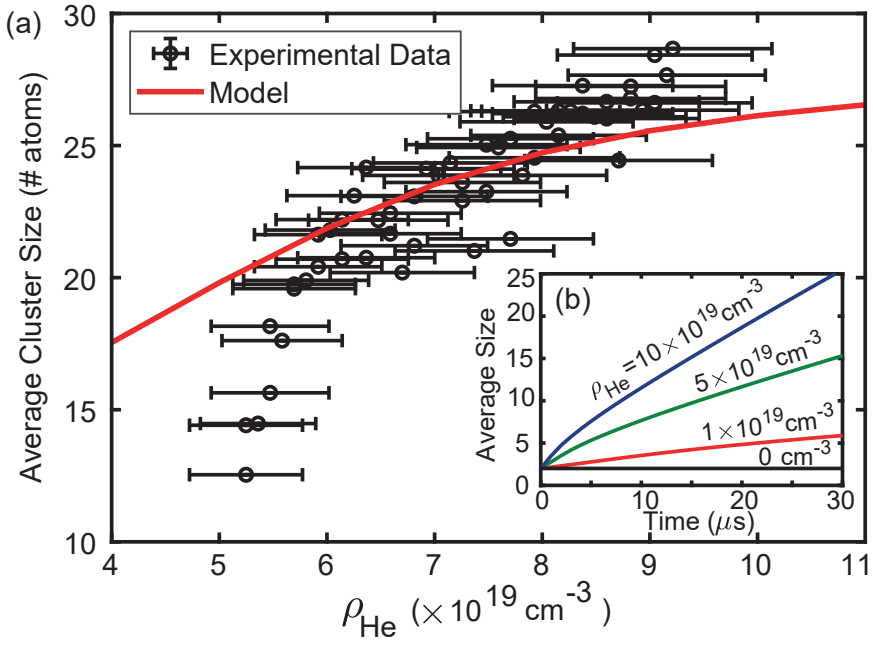

Figure 2.12: (a) Evolution of the average size of alumina clusters larger than 10 atoms for different density of helium gas (black dots) and average cluster size predicted by the model (red line) for the parameters of table 2.5 fitted on the distribution measured at $\rho_{\mathrm{He}} = 6 \times 10^{19}$ cm^{-3} and $\rho_{\mathrm{He}} = 9.2 \times 10^{19}$ cm^{-3}. (b) Average cluster size of calculated distributions versus time for different pressure in helium.

Buffer Gas Effect

Theoretical distributions for different values of helium pressure are calculated and their average size (red line) is compared to our experimental measurements (black dots) in figure 2.12 (a). Averages are calculated for clusters from 10 to 45 atoms in order to avoid the systematic bias of tiny cluster overestimation. The model follows the general decrease of the cluster size. The higher the density of helium, the larger the clusters formed. Indeed, when the helium density increases, the frequency of collisions increases as well as the cooling efficiency of the unstable intermediate. The global growth constant increases. Thus, for the same growth time, larger clusters are obtained for higher He gas density. The deviation from the experimental data at high pressure could be due to the confinement effect. When the He pressure rises, the confinement of the aluminum atoms leads to higher spatial densities of monomers. At low He pressures, the clusters formed are much tinier than the size predicted by the theory. However, at lower pressure, the signal simply disappears. For such a low pressure, the gas valve is no more fully reliable

and the gas burst density and timing are no more fully controlled, explaining the signal lost. As shown in figure 2.12 (b), the model predicts that the growth of the clusters begins as soon as the ablation takes place. The growth speed is the largest at the early stage then decreases. There is no critical radius above which growth accelerates as in CNT. The higher the pressure in the quenching gas, the faster is the growth. When there is no helium, there is no growth.

In short: *In order to compare the model with experiments, calculated size distributions are fitted on experimental distributions measured for different buffer gas density. It appears that the model is robust and reproduces well the experimental distributions. The parameters converged close to the expected values. In particular, the dissociation energy appeared to converge to 0.47 eV, which corresponds to the average measured dissociation energy. The equipartition coefficient is very low, meaning in this model that the energy is localized in a few oscillators. This is expected for anisotropic and inocovalent materials such as oxides. With these parameters, the model also achieves reproducing the behavior of the system when the density of the quenching gas changes.*

2.6 Conclusion

In this chapter, I explored the different ways to describe nucleation in plasma. Nucleation is a complex phenomenon that cannot be described by classical physics and thermodynamics. It is challenging to describe both the early stage of the nucleation dealing with atoms and molecules and the late stage of the process dealing with large nanoparticles and crystals. The description of nucleation should also consider the dynamics of the system that might evolve out of equilibrium, especially for laser-generated plasma.

With this work, I was looking for a simple and versatile theory, able to describe nucleation with general concepts and fast calculation. The aim was not to describe precisely the chemical path of the nucleation process but to be able to better understand the general physics of nucleation and the behaviors of the system depending on various parameters. Luckily, I was able to talk to Prof. Patrice Mélinon who worked a lot on nucleation theories based on statistical physics developed in the 70s. In this work, we adapted these theories to anisotropic clusters by working directly with the micro-canonical ensemble. It led to a model based on the activated complex theory and Weisskopf model in order to describe the growth of the cluster and the influence of the quenching gas. This model successfully reproduces experimental size distributions and even magic number features of alumina clusters and their dependence on the quenching gas pressure. However, it neglects the ripening effect and thus overestimates the density of tiny clusters if the amount of monomers is not large enough compared to the cluster population. We also show that there is no critical cluster size over which nucleation can occur, but rather that growth speed is the greatest at the early time. Yet it takes place only if clusters can be cooled down while growing.

This work questions the physical meaning of the prefactor ν in Weisskopf's model. It is well below the Debye frequency usually considered. It appears that a better frequency to consider in the case of iono-covalent material would be the Einstein frequency. Yet, considering clusters far from bulk geometries, such a frequency should not be over-interpreted. Furthermore, the equipartition of energy is not verified and only some oscillators are excited. The non-convergence between the microcanonical and canonical ensembles shows that the system is not at the thermodynamic equilibrium. It could explain that the desorption energy, deduced from this model and confirmed by direct measurements, is almost 10 times lower than DFT calculation and bulk cohesive energy.

Chapter 3

Pressure in the plasma and thermodynamics

Under pressure
Freddy Mercury

Abstract: *One of the key parameters in the description of laser-generated plasma is the pressure. As a thermodynamics parameter it is important for nucleation processes and for the plasma description. As a mechanical parameter it is interesting for phase transition in the target and damage to the surface. The ablation generates very large pressure and shock-waves. I measured the dynamics of the generated shock-wave as a function of the pulse energy using a shadowgraph setup which gives the jump pressure using Rankine–Hugoniot relations. Generated pressure can reach few tens of MPa for atmospheric pressure ablation.* I show that the dynamics of the shock-wave is fully determined by Taylor's blast model if one takes into account anisotropy in the energy spreading. The main interest of using Taylor's model for laser ablation, is that it is extremely simple and universal and depends on the laser pulse energy only. Using this model, one can determine the pressure from 20 ns after the laser pulse only from the pulse energy and the density of the surrounding atmosphere. Considering Saha's law, I show that one can determine the average temperature of a plasma from measurement of the electrons density and energy of the pulse only. This temperature appears to be lower than the temperature measured from atomic emission which could be explained by tempera-*

*I also measured the shock-wave dynamics in water (see in the annex D) and pressure up to few GPa.

ture gradient in the plasma or partial failure of Local Thermodynamic Equilibrium (LTE).

3.1 The pressure in laser-generated plasma

In the previous chapter, I developed a model able to grasp the physics behind nucleation processes. In particular, the initial conditions of the plasma (density of molecules and temperature) are driving the nucleation process. However, these quantities are difficult to measure, in particular for uncontrolled environments such as atmospheric ablations. The next step to understand nucleation would be to determine such quantities in laser-generated plasma.

When hearing about densities and temperature, many physicists would think about pressure. Indeed, these three quantities are related by *state equations*. The most famous equation of state being that for a perfect gas, $PV_m = RT$ with P the pressure of the gas, V_m its molar volume, R a constant and T the temperature. It was introduced by Émile Clapeyron in 1834 and combines the Boyle's law (1662) and the law of Charles and Gay-Lussac (1787). This equation of state was first written from experimental observations. Yet, one can also derive it from kinetic gas theory as achieved soon after by August Krönig in 1856 and Rudolf Clausius in 1857. The pressure can be described by the force exerted on a surface due to the collisions of the particles. This force increases with the number density of the particle and their kinetic energy.

One can rewrite this relation as $P = Nk_BT$ with N the density of particles and k_B the Boltzmann constant. The density of particles and temperature of the gas is directly related to the pressure. Of course this is a very simple model. In particular, it does not take into account interactions in-between particles nor charge effects. Yet, in laser-generated plasma, the density of particles is usually not far from the atmospheric density and the plasma is mostly neutral. Actually, this simple state relation is already used in some laser-generated plasma models (see section 3.2 and section 3.4.2).

Knowing the pressure generated by laser ablation is useful as a nucleation parameter[140] and often difficult to estimate[49]. It is also important for plasma spectroscopy and LIBS[141,142,143]. During ablation, the high pressures can induce phase transitions in the target[40]. It can also damage the target[144,145] which is a concern for laser surgery and diagnostics on biological tissue[146,147,148], but also recently in mechanics with laser micromachining and laser remelting[149,150]. On Mars, the Super Cam microphone could use the shock-wave generated by the LIBS in order to determine the amount of matter removed and the softness of the target[151].

The phase transition that occurs during laser ablation is so abrupt that it creates a shock-wave propagating in the air. Images of the plasma and shock-wave evolution are shown in figure 3.1 (a). The evolution of the plasma is observed using the shadowgraph method. The images presented correspond to a different delay between the ablation pulse and the recording such that it is possible to reconstruct the evolution of the plasma despite its extremely fast dynamics. The plasma also expands in the air. Within a few hundreds of ns. At the very early times, the velocity of the plasma front evolves up to 5 μm/ns. Yet, very rapidly, the expansion slows down. After 100 or 200 ns, the plasma expansion stabilizes around 0.3 μm/ns.

In this chapter, I study the dynamics of the laser-generated shock-fronts. I first come back to some models used to determine the pressure in laser ablation processes. In particular, Taylor's blast theory gives a link between the pulse energy and the dynamics of a shock-wave. According to this model, the pressure behind the shock-front should be rather homogeneous and one could use it to describe the pressure in the plasma. Then, I present the shadowgraph set-up I used to measure the shock-front velocity. These measurements enable me to measure the pressure behind the shock-front and discuss Taylor's model. The main interest of using Taylor's model for laser ablation, is that it is extremely simple and universal and depends on the laser pulse energy only. Thus, it is very simple to use in many fields. In particular, it does not depend on the ablation process and should work for any material. More than just determining the pressure in the plasma, I strive to prove that this model works for many combinations of laser pulse energies and materials. In particular, I studied ablation of a metal (gold), an oxide (alumina), and paraffin which is a soft organic material. Finally, I will explore a way to determine the densities of different species and the temperature in the plasma considering measured pressure and local thermodynamics equilibrium.

In short: *For this part of my PhD work, I studied plasma generated by a UV pulse of 5 ns in the air. The generated plasma has a typical size from one to a few millimeters depending on the energy of the pulse and a lifetime of a few tens of microseconds. The phase transition is so strong and fast, it leads to very high pressure and creates the shock-front. By studying this shock-wave one can measure the pressure. The determination of the ablation pressure can then be used as a thermodynamic parameter for the plasma emission, the nucleation but also as a mechanical parameter to study the impact of the ablation on the target.*

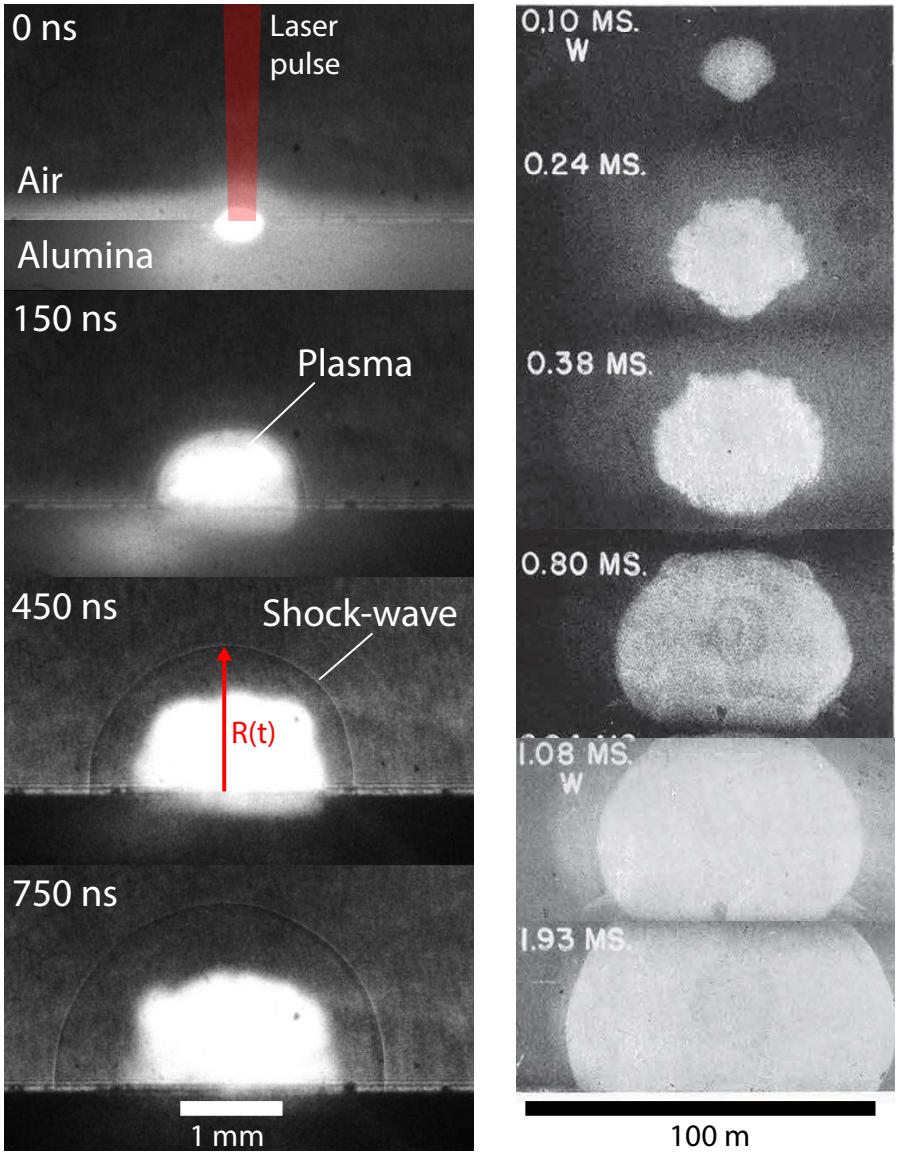

Figure 3.1: (left) Shadowgraph images of the ablation of an alumina target in air for different delay. (right) Image of the New Mexico atomic explosion from Taylor's article[152].

3.2 Models for laser ablation pressure

3.2.1 The unexpected relation between laser ablation and nuclear explosions

The 27$^{\text{th}}$ of January 1996, at 10 am, 6 nuclear bombs exploded in Fangataufa's atoll. These were the last nuclear tests of France. A relief for most as the nuclear tests were catastrophic for the environment and local populations and an open puzzle for engineers and scientists. If one cannot test atomic bombs, how to be sure they are safe? This question remains topical. Today most countries such as the USA, the United Kingdom or France, have renounced physical tests of atomic bombs but still have to secure the development of new warheads. They use numerical calculations with the same code they developed in the 90s based on experimental data recorded from explosions. Indeed, despite tremendous progress in computers, it would be dangerous to modify the code without proper experimental data to validate the changes. Quite surprisingly, the answer to this impasse is laser ablation. In order to reproduce the experimental condition of nuclear explosion (pressure, temperature, abrupt phase transition...), the USA and France built what are called Mega-Joules Lasers. These are actually composed of hundreds of extremely powerful laser focused to the same spot in order to achieve an extremely strong energy concentration recreating nuclear fusion conditions. This is called inertial confinement fusion (ICF).

The first category of model I will discuss here were mostly developed in the 80s for ICF. They are all based on a description of the light absorption of the plasma and energy flux balance[153,154,155,156,157,158,159,160]. I will not go into details of these models as I won't use them directly, and I invite the reader to check the references if interested. All these models lead to a scaling law of the pressure with the laser fluency: $P \propto I^{\alpha}$. The exponent α depends on the laser pulse absorption process. If light absorption is dominated by inverse-bremstrahlung absorption, that is to say the free electrons absorb the light, the pressure should scale with $\alpha = 3/4$. If light absorption is dominated by resonant absorption, that is to say the ablated atoms absorb the light, the pressure should scale with $\alpha = 2/3$. The proportionality coefficient is generally dependent on characteristics of the plasma and is usually determined from experimental data. It changes depending on parameters such as the target composition but remains of the same order of magnitude in the different papers. Usually, experiments were run at very large fluency (about 10^{13} W/cm^2). For instance, Fratanduono et al.[161] in 2011, used 351-nm laser radiation with 3 ns pulse on a diamond target. The pressure was measured from the displacement of

the target. The power-law determined was:

$$P[\text{GPa}] = (42 \pm 3) \times (\text{I } [\text{TW/cm}^2])^{0.71 \pm 0.01} \tag{3.1}$$

Except for the fluency, which are about 1000 times larger than classical LIBS fluency, the characteristics of the laser used for ICF are similar to the one used in my experiments. Both are YAG:Nd laser but ICF lasers are way larger. One can wonder if such models could be extrapolated at low fluency. Considering typical fluency for LIBS of 10^{10} W/cm^2=10^{-2} TW/cm^2, the extrapolation of this expression would give pressure of 1.6 GPa. However, absorption phenomena might be different and 42 is not always the answer, even ± 3. For instance, in an equivalent work, Fabbro states about his model that it "will not apply to situations where the laser intensity and/or wavelength are so small that inverse-bremsstrahlung absorbs all the laser light"[156].

In 1947, some images of the first nuclear explosion of New Mexico (1945) were declassified (see left side of figure 3.1). On these pictures, one can see the shape of the shock-wave and the time after the explosion. Nothing more was needed by Sir Geoffrey Taylor in 1949 to calculate the energy of the bomb with a fairly good accuracy[162,152]. In order to achieve this spectacular result, Taylor developed a self-similar model able to give the dynamics of the shock-wave generated by the explosion only considering the initial energy. In particular, this model also enables to determine the pressure behind the shock-front. Such a model was actually developed simultaneously by other Physicists such as John von Neumann and the Russian Leonid Sedov. Since that time, researchers attempted to use this simple model in order to determine the pressure during laser ablation. It is discussed in many papers showing great interests despite some discrepancies[163,164,165,166,167,168,169,170,171,172].

3.2.2 Taylor's model

"An ideal problem is here discussed. A finite amount of energy is suddenly released in an infinitely concentrated form." Here is Taylor's start. A punctual source of

In short: *Pressure obtained with laser ablation is of great interest in particular for the case of inertial fusion and thus, some models were developed in order to link the pulse fluency and the ablation pressure. In parallel, Blast-Theory developed by Taylor, establishes a link between the pressure and the energy of the pulse. In this chapter, the pressure at the ablation point is measured from the shock-front dynamics, and the different models are discussed.*

energy in three dimension infinite space. The surrounding environment is air with a given specific ratio γ. The total energy is considered constant. In this problem, we only consider the energy E, the air density ρ_0 and the position of the outer edge of the disturbance $R(t)$. The only possible relation for the evolution of $R(t)$ is thus:

$$R(t) = S(\gamma)t^{2/5}E^{1/5}\rho_0^{-1/5} \tag{3.2}$$

with $S(\gamma)$ a dimensionless function of γ. Here we already have an important result of Taylor's model being that the time evolution of the position of the shock-wave has to be a power-law with an exponent 2/5. Yet, S remains to be determined. In order to do that, we have to find expressions for the pressure, density and radial velocity which satisfy the equations of motion and continuity, that is to say Euler's equations, and the equation of state of a perfect gas.

Euler's equations are a set of equations governing adiabatic and inviscid flow. It consists of Cauchy equations of conservation of mass (continuity), and Navier-Stokes equation without the viscosity corresponding to the conservation of the momentum. With spherical symmetries, this gives:

$$\begin{aligned} \frac{\partial \rho}{\partial t} + \frac{\partial(\rho u)}{\partial r} &= -\frac{2\rho u}{r} \\ \frac{\partial u}{\partial t} + u\frac{\partial u}{\partial r} &= -\frac{1}{\rho}\frac{\partial p}{\partial r} \end{aligned} \tag{3.3}$$

The equation of state for a perfect gas is:

$$\left(\frac{\partial}{\partial t} + u\frac{\partial}{\partial r}\right)(p\rho^{-\gamma}) = 0 \tag{3.4}$$

Taylor determined the following similarity assumptions for :

- the pressure $p/p_0 = R^{-3}f_1$
- the density $\rho/\rho_0 = \Psi$
- the radial velocity $u = R^{-3/2}\Phi_1$

where R is the radius of the shock-wave forming the outer edge of the disturbance and f_1, Ψ and ϕ_1 are functions of r/R where $r < R$ is the radial coordinate.

Injecting these solutions in the above equations, one can find a set of 3 differential equations on f_1, Ψ and Φ_1 depending only on γ. Solving these differential equations analytically is laborious, as shown by Sedov in 1946 and von Neumann in 1947. Taylor chose the step by step calculation in order to obtain desired results which are given in his papers[162,152] for different r and γ.

In particular, for $\gamma = 1.4$, the evolution of the position of the shock-wave $R(t)$ is given by:

$$R(t) = \left(\frac{E}{0.856\rho_0}\right)^{1/5} t^{2/5} \tag{3.5}$$

with E the energy of the explosion and ρ_0 the density of the air. Of course, precision of step by step calculation from the 50s could be improved. But here, this result is precise enough considering the other uncertainties of the measurement.

The maximum pressure at the shock-front is then given by:

$$p(R) = 0.155\frac{E}{R^3} \tag{3.6}$$

One can wonder if $\gamma = 1.4$ holds during laser ablation or nuclear explosion. Indeed, for extreme temperatures, the specific heat ratio might change. In particular, this is discussed by Taylor in his paper determining the energy of the New Mexico explosion[152]. In that case, extreme heat could lead to a value of gamma close to $\gamma = 1.3$ which would slightly change the estimation of the atomic bomb energy. However, such considerations increases the complexity of the problem and Taylor's himself do not rely much on this alternative calculation.

More than 60 years before Taylor, shock-waves have been investigated by Rankine and Hugoniot for one-dimensional flow in fluids. Later generalized, the so-called Rankine–Hugoniot relations give the gas velocity u_1, pressure p_1 and density ρ_1 immediately behind the shock-front ($r = R$) for an ideal gas by considering the conservation of mass, momentum and energy. In the case of large over-pressure, Rankine–Hugoniot relations are:

$$\begin{aligned} u_1 &= \frac{2}{\gamma+1} D \\ p_1 &= \frac{2}{\gamma+1} \rho_0 D^2 \\ \rho_1 &= \frac{\gamma+1}{\gamma-1} \rho_0 \end{aligned} \tag{3.7}$$

with $D = dR/dt$ the velocity of the shock-front. One can show that these expressions are indeed consistent with Taylor's self-similar solution. Thus, one can use both the Taylor's model considering the energy of the pulse but also Rankine–Hugoniot relations considering the velocity of the shock-wave in order to determine the pressure of the shock-wave. However, for pressures close to the atmospheric one, exact Rankine–Hugoniot relations differ from Taylor's model. In the

following, I will use the exact solution for the pressure:

$$p_1(R) = p_\infty \left(1 + \frac{2\gamma}{\gamma+1}\left(M_s^2 - 1\right)\right) \tag{3.8}$$

with $M_s = u_s/c_0$ the Mach number and $c_0 = 340$ m/s the sound velocity in the air.

Of course, Taylor's model has its limits. In particular, it cannot apply at the instant of the ablation. During laser ablation, the deposition of the energy is neither point-like, nor instantaneous and the model should apply only when the shock-wave is far enough from the ablation spot. One of the goal of the study is to determine from when Taylor's model stands true. Furthermore, the model is spherical. In the case of laser ablation, the target surface changes the geometry of the system which changes the propagation of the energy.

3.3 Measurement of shock-wave dynamics

3.3.1 Shadowgraph experimental set-up

In order to observe the shock-wave, I used a shadowgraph imaging set-up presented on figure 3.2. The strong variations of pressure and density lead to variations of the refractive index such that the light going through the shock-front is deviated. The shadowgraph apparatus is composed of a 30 mW continuous-wave diode laser (445 nm) in front of an iCCD camera from Andor. An objective Zoom 6000 from Navitar is mounted on the iCCD camera with a spatial resolution of 44 μm.

The typical size of the shock-waves generated by the laser pulses are a few mm with a thickness of only a few tens of μm. The shock-wave travels fast, around 10 times the speed of sound (about 3400 m/s) and thus travels 100 μm in less 30 ns. In order to observe the shock-front, we have to record the image on a shorter time-scale.

The interest of using iCCD camera is to achieve such a high time resolution, up to 5 ns. This camera is an amplified camera. It is composed of a 1024×1024 px

In short: *Taylor's model is a similarity model for explosion considering the expansion of a spherical shock-wave generated by a punctual source of energy in an adiabatic and inviscid flow. It is extremely general and enables to predict the pressure of the shock-wave considering only the energy of the pulse. Thus, it is very convenient to use in order to determine the ablation pressure for many laser ablation applications.*

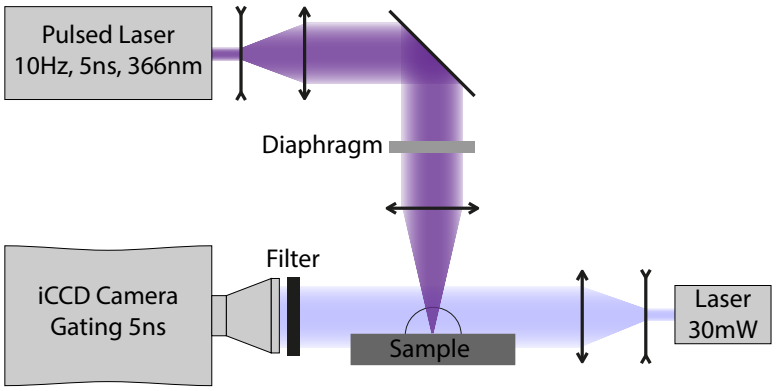

Figure 3.2: Simplified scheme of the measurement apparatus of the shock-waves in air.

CCD chip-set for which each pixel is 13.5 μm side. In front of which there is an honeycomb electronic amplifier. [†]

Fortunately, the ablation process has a good repeatability and we are able to reconstruct the dynamics of the shock-wave making one image for each pulse and changing the delay between the ablation time and the recording time on the iCCD camera. The delay between the ablation pulse and the camera is controlled by a digital delay/pulse generator DG645 from Stanford Research Systems.

This ablation is done by focussing the third harmonic of a YAG-Nd pulsed laser (355 nm, 5 ns, 9 Hz) with a 100 mm lens on various targets: pure gold (99.99% from Neyco), a sapphire crystal (alumina), and some paraffin from Roti-Plast. The sapphire crystal was grown by Czochralski (Cz) technique with radio frequency induction heating in an iridium crucible[173,174]. The ablation was performed in ambient air. The power of the laser pulse was changed using a diaphragm. The energy of the pulse was measured with a Nova II power meter mounted with a high energy pyroelectric sensor.

Figure 3.3 (a) shows some images of the shock-wave generated in the air by the ablation of a gold target for different delays with a pulse of 3.1 ± 0.1 mJ. In front

[†]The photons arrive on a W-AGT photocathodes and are converted to electrons. The electrons are accelerated and multiplied in an ensemble of micro-channels with a large electric field. Then the electrons arrives on P43 phosphors and are converted back to photons illuminating the CCD chip-set. This amplification can be tuned with the difference of potential applied to the micro-channels. The main interest of this amplification is to enable fast gating. The electronics of the camera is able to turn on and off the amplification within 5 ns. This mean that the gate of measurement can be reduced to 5 ns giving a great temporal resolution of the measurement. In return, the decay time of the phosphor is 2 ms such that is difficult to make images at a rate faster than 500 Hz.

of the camera, a band filter 450-5 nm centered on the continuous laser wavelength is used. It limits the saturation of the iCCD camera due to plasma emission and enables to measure the shock-front position down to 10 ns after the laser pulse. The position is determined by measuring the distance between the bottom of the plasma and the outer-edge of the shock-wave.

3.3.2 Results and discussion

In the following, I first show that the dynamics of the shock-front is perfectly described by Taylor's model. I also discuss the impact of anisotropy on the estimation of the pulse energy. The shock-front is not perfectly spherical, such that its dynamics measured perpendicularly to the target's surface overestimates the laser pulse energy. This discrepancy is corrected when the energy measured is averaged on all the directions. In a second part, I discuss the evolution of the pressure in time and space and the limit of Taylor's model. Finally, I suggest a user-friendly expression of the initial pressure generated from laser ablation according to Taylor's model which depends only on the pulse energy.

Impact of anisotropy on the estimation of the pulse energy

For 5 different pulse energies (0.09±0.01, 0.8±0.05, 2.6±0.2, 11±1 and 51.6±2 mJ) the positions of the shock-fronts generated from the ablation of a gold target are shown in figure 3.3 (b). The errors on the pulse energy measurements correspond to maximal fluctuation of the measured value. The positions correspond to the distance perpendicular to the target between the bottom of the plasma and the outer position of the shock-wave ($d_\perp$). Each position is averaged from 5 different measurements and error bars correspond to the standard errors corrected with student's coefficient for a 95% confidence interval. The origin of time corresponds to the laser pulse. Because of the pulse duration (5 ns), the laser jitter (a few ns) and the iCCD camera gating (5 ns), t=0 is chosen as the average time between the first frame recording the laser pulse and the next image. The solid lines correspond to Taylor's model for $E = 0.081 \pm 0.04$, 3.73 ± 0.15, 13.0 ± 0.5, 43 ± 3 and 110 ± 2 mJ respectively. The model agrees well with the experimental data except

In short: *The shock-front was imaged using shadowgraph and iCCD camera able to capture an image on 5 ns and resolve the position of the shock-wave with a velocity larger than the sound velocity in the air. In order to reconstruct the dynamics of the shock-wave, images are recorded from different laser pulses with increasing delay. Fortunately, the repeatability of the system is good enough to reconstruct consistent dynamics of the shock-wave.*

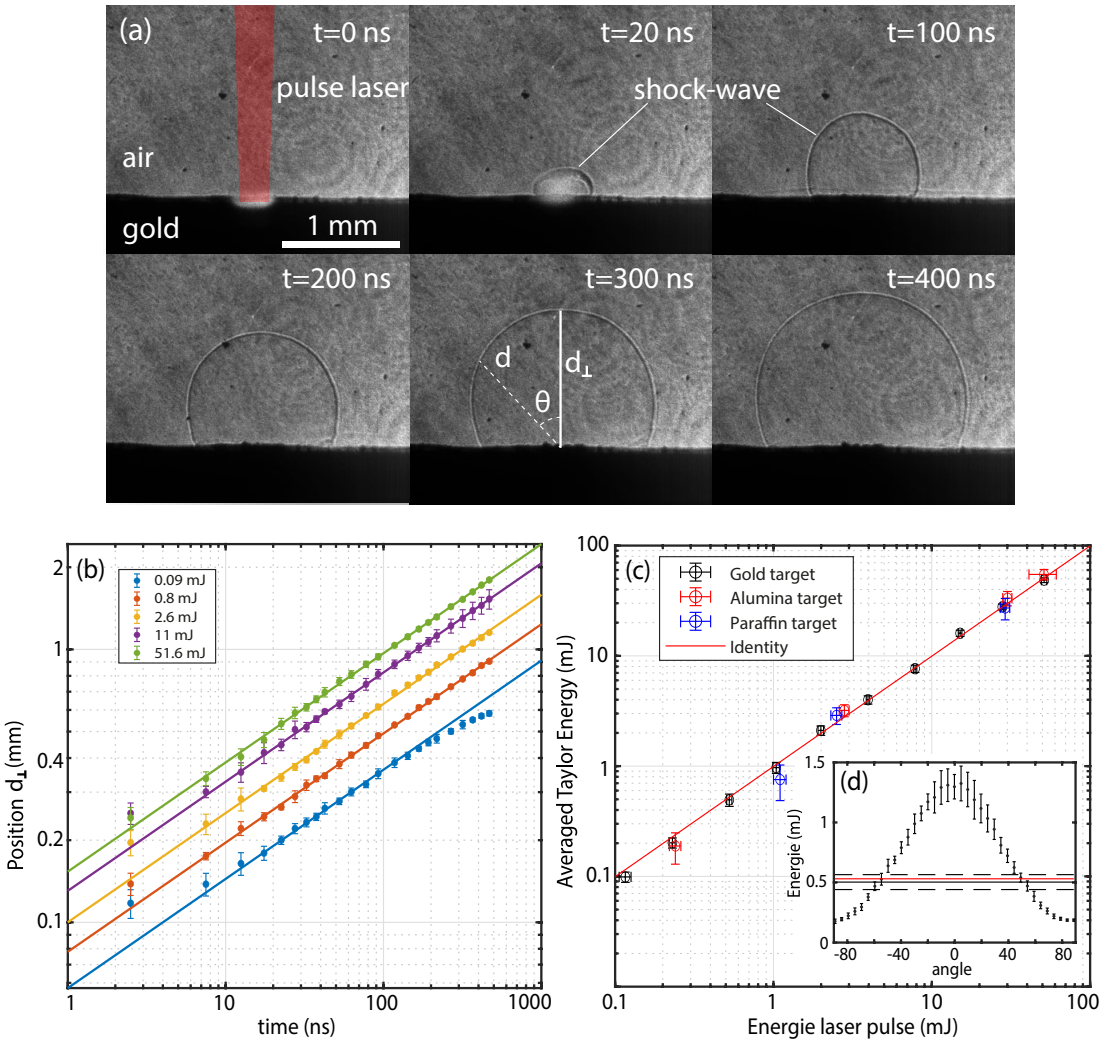

Figure 3.3: (a) Shadowgraph images of the ablation of a gold target in air for different delay times. (b) Time evolution of the shock-wave position. Solid lines correspond to Taylor's model in $t^{\frac{2}{5}}$. Errors are computed from 5 different measurements corrected by student coefficient for a 95% confidence interval. (c) Measured energy of the laser pulse compared to the angular averaged measurement from the shock-wave position at $t = 300$ ns. Black points correspond to measurements on gold, red point on alumina and blue point on paraffin. Errors are given by the angular average. (d) Energy determined from the shock-wave position at $t = 300$ ns depending on the angle for a pulse energy of 0.53 ± 0.02 mJ. Errors are given by the standard deviation of 15 different measurements. The red line corresponds to the measured pulse energy while the black line corresponds to the angular average. Dashed line corresponds to error propagation on the average.

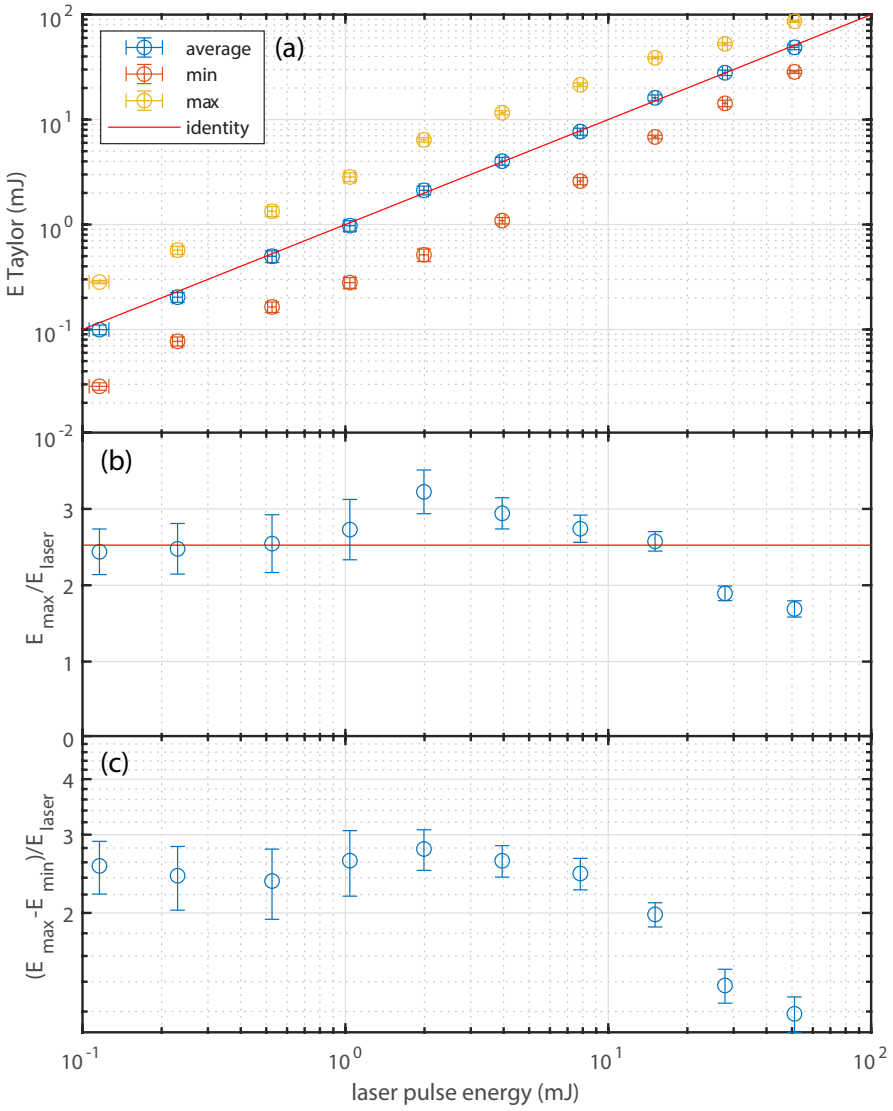

Figure 3.4: (a) Energy determined from the shock-front position at 300 ns and Taylor's model in a direction perpendicular to the target (yellow), parallel to the target (red) and its angular average (blue) in the case of gold target. (b) ratio of the energy determined using Taylor model using the position of the shock-wave in the perpendicular direction of the target and the measured energy of the laser pulse. (c) Measurement of the anisotropy of the shock-wave defined as $\frac{E_{max}-E_{min}}{<E>}$.

for the lower pulse energy where the shock-wave velocity slows down quicker after 100 ns. Furthermore, the energy is systematically over-estimated as observed in previous works[167,165].

This discrepancy is due to the anisotropy of the system. On figure 3.3 (d) is represented the energies calculated from the position of the shock-wave according to Taylor's model for a pulse of 7.8 ± 0.2 mJ at $t = 300$ ns. This delay is chosen for the size of the shock-wave to be large enough in order to obtain a good measurement of its position. For each angle, the distance of the shock-wave is measured from the center of the ablation spot. The black line corresponds to the angular average of the energy over the hemisphere. As you can see the energy measured perpendicularly to the surface (0^o angle) largely overestimates the laser pulse energy while the energy calculated along the surface ($\pm 90^o$ angle) underestimates it (see figure 3.4 (a)). The energy appears to be mostly directed in the normal direction of the target. Because of the target surface, the explosion is partially confined. The conserved quantity of this problem is the energy. One can compute the hemispherical average of the energy as:

$$< E >= \frac{\sum_{\theta_m} E(\theta_m)|sin(\theta_m)|}{\sum_{\theta_m} |sin(\theta_m)|} \tag{3.9}$$

with θ_m the measurement angle. This corresponds to the average of the energy measured for each angle weighted by the circumference of the corresponding circle.

Figure 3.3 (c) shows the excellent agreement between the energy of the laser pulse and the calculated energy from Taylor's model average over the total emission angle. Additional measurements on alumina (in red) and paraffin (in blue), show that this model is very general and does not depend on the characteristic of the target. It can apply to metals, dielectric and soft materials such as paraffin.

Such consideration of anisotropy were already suggested in previous works[171,172] discussing the fact that the shock-wave is not fully hemispherical. In most of the cases, the position of the shock-wave is measured perpendicularly to the surface. In that case, the energy is overestimated by a coefficient close to 2.5 over a large laser pulse energy range (see figure 3.4 (b)) and is consistent with previous works[163].

The anisotropy of the shock-wave can be characterized by:

$$\frac{E_{max} - E_{min}}{< E >} \tag{3.10}$$

This quantity is represented on figure 3.4 (c) in function of the laser pulse energy. It appears almost constant except for energy larger than 10 mJ where the shock-wave appears to be more isotropic.

Measurement of the pressure

The Mach numbers of the shock-front, defined as the velocity of the shock-front u_s divided by the sound velocity c_0, is presented in figure 3.5 in terms of time (a) and shock-front's position (b). Dashed lines correspond to the shock-front velocity given by Taylor's model applied to the measurement presented in figure 3.3 (b). Dots correspond to velocities determined from the difference of the shock-front position between two successive images divided by the delay between these images. Important noise comes from fluctuations in the measured position of the shock-wave. In order to improve the calculation of the shock-front velocity, lowess smoothing[‡] from MATLAB is applied on the position before differentiation and on the obtained velocity. Results are represented by solid lines. Parameters of the smoothing were chosen in order to decrease the noise in the data without adding bias.

The pressure deduced from Taylor's model are represented by dashed lines in figure 3.5 in terms of the time (c) and shock-front position (d). In comparison, solid lines and dots correspond to direct measurement of the pressure behind the shock-front using Rankine-Hugoniot relation and the Mach numbers presented above.

Taylor's model and Rankine-Hugoniot relation for the pressure are mostly in good agreement. For high pressure compared with the atmospheric pressure, Taylor's model is equivalent to the approximate asymptotic forms of Rankine-Hugoniot relations. On the contrary, when pressure is close to the atmospheric pressure, Taylor's model diverges from the Rankine-Hugoniot relations. This might explain the difference between both pressures for large delay on the low power pulse. Furthermore, at the earliest time, the pressures deduced from the velocity of the shock-wave saturate when Taylor's model diverged. Indeed, the initial speed of the shock-wave is not as great as expected by Taylor's model because the energy deposition is not point-like. Taylor's model fails to describe the pressure before 20 ns. Despite a focal point of about 100 μm, the pressure remains high even after

[‡]locally weighted scatter plot smooth

In short: *The dynamics of the laser-generated shock-wave measured perpendicularly to the surface is perfectly described by Taylor's model with the exception that the energy of the pulse is systematically overestimated by a factor 2 or 3. Such observation is consistent with previous reports. The energy is not spread equally in all the directions. Considering the average of the energy given by Taylor's model in all the directions enables to retrieve the energy of the laser pulse, confirming the ability of Taylor's model to describe laser ablation. These results have been checked from 0.1 to 50 mJ and on gold, alumina and paraffin.*

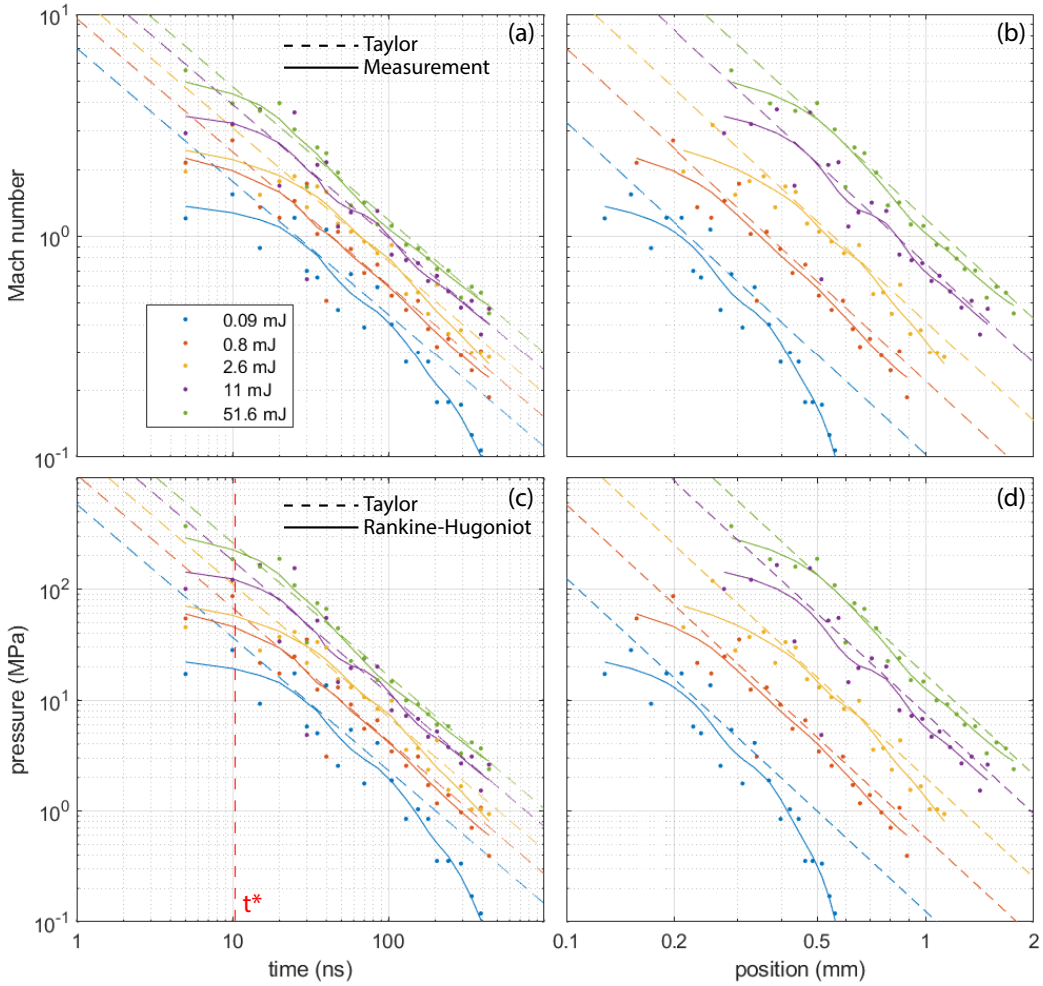

Figure 3.5: Mach number of the shock-wave in terms of time (a) and its position (b). (c-d) Pressure of the shock-wave determined from the shock-wave Mach number and Hugoniot's model. Dots correspond to discrete differential, solid lines are pressure values calculated from smoothed data as eye guideline and dashed lines correspond to Taylor's model with the energies fitted on the position.

a few mm which can explain large damage observed on soft materials like organic tissue in LIBS for instance.

Initial pressure

In these experiments, the initial pressure seems to saturate to values corresponding to the pressure predicted by the model for a delay time between 10 and 20 ns (see figure 3.5 (c)). One can estimate the initial pressure to be the one given by Taylor's model for a given t^*:

$$P(t) = 0.141 \frac{\rho_0^{3/5} E^{2/5}}{t^{*6/5}} \tag{3.11}$$

Here we see that the initial pressure should depend on the pulse energy to the exponent 2/5.

Figure 3.6 shows the initial pressure determined from the measurements presented in figure 3.5 in terms of the pulse energy. Errors on the initial pressure are estimated from the pressure measurement dispersion. Here, the energy does not correspond to the real pulse energy but to the energy given by Taylor's model on the data presented in figure 3.3 (b). Indeed, the dynamics were measured in the direction perpendicular to the target surface and the energy in this direction over-estimates the pulse energy. Errors on the energy corresponds to the fit error. In Taylor's model, for a given time, the pressure goes like the energy of the pulse to the power 2/5. In the figure, the solid line corresponds to a fit $P[\text{MPa}] = (37.4 \pm 10) \times (\text{E [mJ]})^{2/5}$ and the dashed lines correspond to the uncertainties on the fitting parameter. The measured initial pressure seems indeed to follow the expected power law. The fitted coefficient $C = 37.4 \pm 10$ MPa.mJ$^{-2/5}$ can be related to the time t^* as $t^* = (0.141\rho_0^{3/5}/C)^{5/6}$. This gives $t^* = 10.3$ $(8.4 - 13.7)$ ns which is typically the value one can expect (see figure 3.5 (c)).

Related to this work, I also studied the dynamics of shock-waves generated in water. This work can be found in the annex D. In that case, the dynamics of the shock-wave is much different and cannot be described by Taylor's model. The speed decreases very fast to reach the sound velocity within 70 ns. By estimating the initial velocity of the shock-wave, one can use Vogel's work[48] to determine the pressure of the initial point. Because of the confined environment, this pressure appears much higher than in the air and can reach up to 4 GPa for laser pulse fluency of about 70 GW/cm^2. In particular, such large pressures at the ablation point could explain the formation of metastable phases as the production of nanodiamonds from carbon target[40,175].

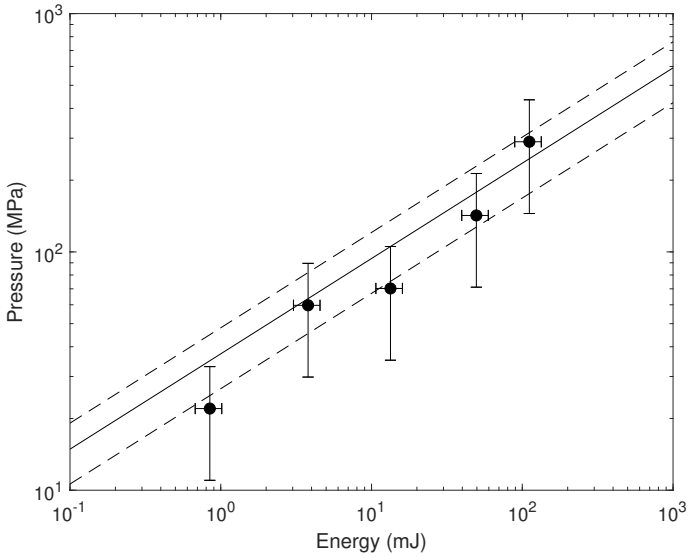

Figure 3.6: Pressure determined from the initial shock-wave velocities for the different pulse energy. Solid line corresponds to a fit $P[\text{MPa}] = (37.4 \pm 10)(\text{E}[\text{mJ}])^{2/5}$. Dashed lines correspond to uncertainties on the fitting parameter.

In liquids, shock-waves generated in the target can also generate secondary shock-waves in the water. We developed a method to deduce mechanical properties of the target from this observation. This work can be found in the annex E and has been patented.

In short: *The pressure given by Taylor's model is in good agreement with the one calculated from Rankine-Hugoniot relation's on the measured velocity of the shock-wave for times larger than 20 ns. Before that, one cannot consider the energy deposition to be instantaneous and point-like and the pressure seems to saturate. The measured initial pressures are between 10 and 300 MPa depending on the laser pulse energy which is far below the value given by ICF model extrapolated to low fluency. This initial pressure corresponds to the pressure given for Taylor's model for* $t = 10$ *ns and evolves as a power* $2/5$ *of the pulse energy.*

3.4 Calculation of densities and temperature considering LTE

Previously, I have shown that it is possible to describe laser ablation using Taylor's model. Interestingly, Taylor states that the pressure is almost homogeneous after the shock-front. We might consider this pressure in order to describe the plasma thermodynamics conditions. Here, I discuss its use for the study of the laser-generated plasma and determination of densities. As seen in the first chapter, determining the densities in a plasma has a great importance for nucleation. It is also interesting for quantitative LIBS measurements in order to determine the properties of the plasma and the relative quantities of species from emission measurements[176,177,178].

In order to link the pressure to densities and temperature, one needs to consider the Local Thermodynamic Equilibrium (LTE) in the plasma and the associated relations. In this section, I first define and discuss LTE in laser induced plasma. Then, I present some models that use LTE equations in order to link densities, pressure and temperature in the plasma. Most of the time these model are based on the measurement of the excitation temperature of atoms and ions in the plasma while the pressure is unknown. Here, I propose similar calculations but using Taylor's pressure and deducing the average kinetic temperature of the plasma.

3.4.1 Local Thermodynamic equilibrium (LTE)

Equilibrium in Plasmas

In a plasma at the thermodynamic equilibrium, there are no net macroscopic flows of matter or of energy. This means that all the chemical reactions, ionization reactions, and light emission reactions are at equilibrium and described by one unique temperature T. In that case, one can write different laws from these equilibria:

Maxwell's law gives the probability distribution $\mathcal{G}(\vec{v})$ of the particles' velocity $\vec{v}$:

$$\mathcal{G}(\vec{v}) = \left(\frac{m}{2\pi k_{\mathrm{B}} T}\right)^{3/2} \exp\left[-\frac{m\vec{v}^{\,2}}{2k_{\mathrm{B}} T}\right] \tag{3.12}$$

with k_B the Boltzmann constant, m the particles mass and T the temperature.

Plank's law gives the spectral radiance of the plasma:

$$W(\nu) = \frac{2\pi h\nu^3}{c^3}\left(e^{\frac{h\nu}{k_B T}} - 1\right)^{-1} \tag{3.13}$$

with h the Planck constant, ν the photon frequency, c the speed of light, k_B the Boltzmann constant and T the temperature.

Saha-Eggert's law links the population of ions and free electrons:

$$\frac{n_{i+1}n_e}{n_i} = \frac{2}{\Lambda^3}\frac{g_{i+1}}{g_i}\exp\left[-\frac{\epsilon_{i+1}-\epsilon_i}{k_BT}\right] \tag{3.14}$$

with n_e the electron density, n_i the density of atoms in the i^{th} degree of ionization, g_i the degeneracy of the associated state, ϵ_i the energy of the corresponding ionization, Λ the thermal de Broglie wavelength:

$$\Lambda = \sqrt{\frac{h^2}{2\pi m_e k_B T}} \tag{3.15}$$

m_e the mass of the electron. In the case of laser-generated plasma, mostly the first ionization state of the atoms is observed and one can neglect the other populations of ions.

Boltzmann's distribution gives the distribution of the species in the excited state n in terms of the temperature:

$$N_n = N\frac{g_n\exp\left[-\frac{E_n}{k_BT}\right]}{Z(T)} \tag{3.16}$$

with g_n the degeneracy of the state n, E_n its energy and $Z(T)$ the partition function of the system. This distribution can describe many systems. For instance, it can refer to the velocity distribution of the particles but also to their ionic state of excitation level.

Dalton's law states that the total pressure of the system is the sum of the partial pressures of the different species. This pressure can be related to the temperature given an equation of state valid for the conditions of the system.

Local Thermodynamic Equilibrium

If the Local Thermodynamic Equilibrium is reached in plasma, all these laws, except the Planck emission law, are verified locally in time and in space. This happens when emission and absorption of light is no longer at the equilibrium but

that the depletion of excited states due to emission is negligible compared to the other mixing processes. In other words, the characteristic time of collision between electrons, ions and neutrals is short compared to light emission time such that the equilibrium is maintained[179,180,181,182].

Determining if the local thermodynamic equilibrium is reached in Laser induced plasma is an important question in order to justify the use of these laws and the notion of temperature itself.

In order to test the existence of local thermodynamic equilibrium in the plasma, one can use the so-called Mc Whirter criterion. It is a necessary condition for the LTE to be achieved in plasma. It can be expressed as:

$$n_e[\mathrm{cm}^{-3}] > 2.55 \times 10^{11} \langle \mathrm{g} \rangle^{-1} \mathrm{T}^{1/2} \Delta \mathrm{E}_{\mathrm{mn}}[\mathrm{eV}]^3 \tag{3.17}$$

with $\langle g \rangle$ the Gaunt factor and ΔE_{mn} the energy of the main transition between two adjacent levels (usually the transition between the ground state and the first excited state)[181,183].

The density of electrons can be measured thanks to the Stark broadening effect of emission lines as developed in the section immediately following this one.

This criterion corresponds to the balance between the frequency of collision of the electrons with the atoms and the rate of emission of atomic transitions. If the density of electrons is large enough, then the collisions are fast enough to ensure the thermalization of the atoms despite radiative de-excitation. This is calculated in the case of a *thin plasma* that is to say a plasma with no self-absorbtion which is stationary and homogeneous.

This criterion is usually verified in laser-generated plasma with temperatures larger than 3000 K and an electronic density around 10^{16-19} cm^{-3}. However, one should not take the LTE for granted and it has been extensively studied. In particular, in a spatio-temporal study, Cristoforetti et al.[181] explains: "The only conclusion that can be drawn is that LTE conditions may exist. [...] LTE criteria may be successful for some elements but may fail for others [...] the right question should be not whether equilibrium conditions exist, but rather how far we are from equilibrium." Mirroring many other works[179,184,185,186,182], Cristoforetti et al. concludes local equilibrium and temperature convergence is reached only in some part of the plasma after several μs. In a review from 2013, he concludes that "results of such analysis, making use of experimental results present in the literature, converge to the picture that a LIBS plasma enters into LTE near the end of the laser pulse and maintains this status for a certain time, depending on the background pressure and on the plasma composition."[187] In 2018, Hermann et al. worked on the spectroscopy of laser-generated plasma during the first few

μs[188]. The authors show that the strongest emission line actually saturates at the black-body radiance and that the temperature of the black-body equals the excitation temperatures of the electrons and ions. The authors claim it proves "directly and unambiguously a plasma in local thermodynamic equilibrium". After all, one can conclude that LTE is true in laser-generated plasma, at least in the center, ensuring the equilibrium between the electronic state of the atoms and ions, and the gas of electrons.

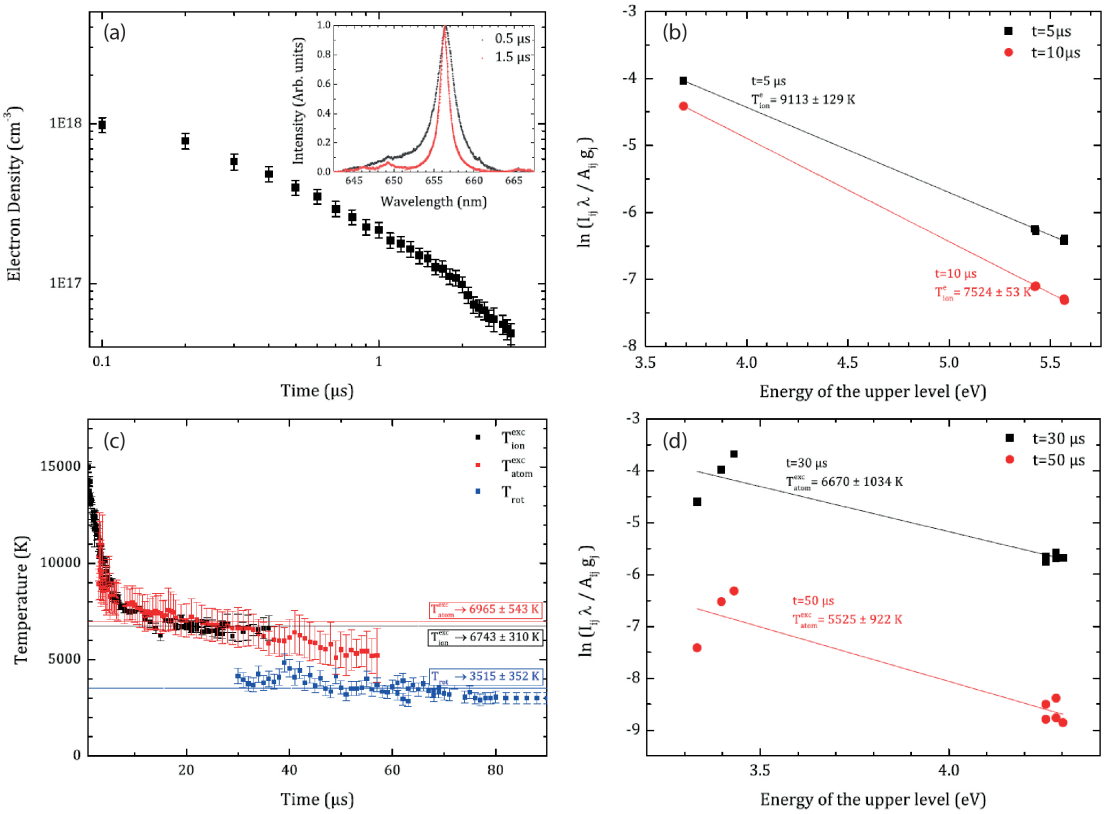

Figure 3.7: Figures extracted from a previous study of Lam and Amans on similar plasma[47]. (a) Temporal evolution of the electron density in log/log scale. The inset graph is the time evolution of the H-alpha line measured with 0.19 nm resolution. The red curve is the measured curve at 1.5 μs with a typical Voigt fit. (b) Typical Boltzmann plots using Ti II lines for delays equal to 5.0 μs and 10.0 μs. (c) Temporal evolution of the excitation temperatures of the atoms (Fe I) and the ions (Ti II) and the rotational temperature (AlO). The dotted lines stand for the mean values calculated from 10 μs. (d) Typical Boltzmann plots using Fe I lines for delays equal to 30 μs and 50 μs.

Measurement of the electronic density

The density of electrons can be measured thanks to the Stark broadening effect of emission lines. By neglecting the broadening due to the Doppler effect and Van der Waals forces, one can link the full width at half maximum (FWHM) to the density of electrons with[189]:

$$\Delta\lambda_{1/2} = 2w\frac{n_e[\mathrm{cm}^{-3}]}{10^{16}} \tag{3.18}$$

with w a parameter depending on the atom emitting. However, one needs to take care to consider emission lines with little auto-absorption. The error of such a measurement is about 20 to 30% in such laser ablation plasma. In the case of the plasma I am studying, these quantities have been measured by Julien Lam a few years ago[47] and are reported on figure 3.7 (a). These measurements are done on an alumina target with the exact same laser that I used and a pulse energy of 40 mJ. The electron density was measured through the broadening of the H-alpha line. Within 1 μs, the electron density varies from 10^{18} cm^{-3} to 10^{17} cm^{-3}.

Measurement of the temperature

In laser-generated plasma, the temperature is usually measured assuming LTE and emission of the plasma. It can be deduced from the emission ratio of different excited states of atoms and ions (excitation temperature) or from the emission ratio between atoms and ions (ionic temperature).

Excitation temperature The excitation temperature is related to the excitation level of the atoms. Atoms are excited through the collisions with the electron gas. If LTE is reached, the population $n_m(T)$ of each m state of energy E_m and degeneracy g_m is determined by the Boltzmann distribution and such defines the excitation temperature T :

$$n_m(T) = n_0\frac{g_m}{g_0}\exp\left[-\frac{E_m}{k_\mathrm{B}T}\right] \tag{3.19}$$

with n_0 the ground state density and g_0 the associated degeneracy. Here we considered the energy of the ground state $E_0 = 0$.

The emission power by unit of volume for the transition m to n at the wavelength λ_{mn} is:

$$W_{mn} = \frac{A_{mn}}{4\pi}\frac{hc}{\lambda_{mn}}n_m(T) \tag{3.20}$$

with A_{mn} the Einstein coefficient. This relation is valid for a thin plasma in a stationary state. For a given measurement setup, the intensity observed for this transition is $I_{mn} = C_1 W_{mn}$ with C_1 a proportionality coefficient depending on the partition function of the atom. Combining these equations, one can write for any transition m to n the following relation[190]:

$$ln\left(\frac{\lambda_{mn} I_{mn}}{g_m A_{mn}}\right) = ln\left(\frac{C_1 hcn_0}{4\pi g_0}\right) - \frac{E_m}{k_B T}. \tag{3.21}$$

By plotting $ln\left(\frac{\lambda_{mn} I_{mn}}{g_m A_{mn}}\right)$ in terms of the energy of the emission level E_m, one can verify the linearity of the relation as an indication of LTE and determine the coefficient and thus the excitation temperature T.

In the case of the plasma I studied, this temperature was already measured by Julien Lam[47] for atoms and ions (see figure 3.7). In order to do so, he doped an alumina target with Ti and Fe atoms and measured the relative emission of five different Ti II lines (347.718 nm, 350.489 nm, 351.084 nm, 352.025 nm, and 353.540 nm) and eight Fe I lines (370.557 nm, 370.925 nm, 371.993 nm, 372.762 nm, 373.332 nm, 375.823 nm, 376.379 nm, and 376.719 nm). Examples of $ln\left(\frac{\lambda_{mn} I_{mn}}{g_m A_{mn}}\right)$ are plotted in figure 3.7 (b) for the Ti ions and in figure 3.7 (d) for the Fe atoms with their associated linear regression. This is done as a function of time giving the evolution of the excitation temperature in the plasma which is represented in figure 3.7 (c) in black for the Ti ions and in red for the Fe atoms. As you can see, there is no significant difference between the excitation temperature of the Fe atoms and the one of the Ti ions. Such an equality in the excitation temperature of two different species in the plasma is an indication that LTE is achieved for ions and atoms in the plasma. It seems that this excitation temperature cools very quickly during the 5 first μs from 14000 K to 7500 K. After 5 μs the decrease is constant and much slower, from 7500 K to 5000 K after 60 μs.

The ionisation temperature The ionisation temperature is related to the population of ionic species in the plasma. As previously, one can write the ratio of emission line intensities between two different levels of an atom I_{atom} and its ion I_{ion} as:

$$\frac{I_{\text{ion}}}{I_{\text{atom}}} = \left(\frac{A}{\lambda}\right)_{\text{ion}} \left(\frac{\lambda}{A}\right)_{\text{atom}} \frac{n^*_{\text{ion}}}{n^*_{\text{atom}}} \tag{3.22}$$

with A the Einstein coefficients of the emissions of wavelength λ and n^* the population of the excited state regarding either the atom or the ion. If one considers LTE, the populations n^*_{ion} and n^*_{atom} of the excited states of both species are described

by Boltzmann distributions which define the temperature T:

$$n^*_{\text{ion}}(T) = n^0_{\text{ion}} \frac{g^*_{\text{ion}}}{g^0_{\text{ion}}} \exp\left[-\frac{E}{k_{\text{B}}T}\right] \tag{3.23}$$

with n_0 the population of the ground, g^* the degeneracy of the excited state, g^0 the degeneracy of the ground state. The ratio of these populations is also given by the Saha-Eggert law:

$$\frac{n^0_{\text{ion}} n_e}{n^0_{\text{atom}}} = \frac{2}{\Lambda^3} \frac{g^0_{\text{ion}}}{g^0_{\text{atom}}} \exp\left[-\frac{\epsilon_{\text{ionisation}}}{k_{\text{B}}T}\right]. \tag{3.24}$$

Combining all the equation we finally get:

$$\frac{I_{\text{ion}}}{I_{\text{atom}}} = \frac{2}{n_e} \left(\frac{2\pi m_e k_{\text{B}}}{h^2}\right)^{3/2} \left(\frac{Ag^*}{\lambda}\right)_{\text{ion}} \left(\frac{\lambda}{Ag^*}\right)_{\text{atom}} T^{3/2} \exp\left[-\frac{E_{\text{ion}} - E_{\text{atom}} + \epsilon_{\text{ionisation}}}{k_{\text{B}}T}\right]. \tag{3.25}$$

3.4.2 Equation of state and density calculation

Principle

In order to find the link between pressure, temperature and density, one needs an equation of state. The first to come to mind is the equation of state for perfect gases. This might appear quite a strong hypothesis to describe the plasma yet, it is the equation of state used in Taylor's model, ICF models and in LIBS plasma. Considering Dalton's law, the total pressure is the sum of the partial pressures and:

$$P = \sum_i n_i k_B T_i \tag{3.26}$$

In short: *The local thermodynamic equilibrium is achieved in plasma when the depletion of the excited states due to emission is negligible compared to other mixing processes. In that case, one can consider that the kinetics of the species is described by Maxwell distributions, the excitation of the atoms and ions are described by Boltzmann distributions and the ionization ratios are given by Saha's relation. All these relations depend on one parameter T being the temperature of the plasma. Yet, this temperature changes in time and space. This temperature can be measured through spectroscopy of the plasma just as the electron density. These quantities can then be used to explore the thermodynamics of laser induced plasma.*

with P the total pressure, n_i the density of the i^{th} species and T_i its kinetic temperature. In a plasma, there are different species, the atoms, the ions, the electrons and even some molecules. The temperature here should be the kinetic temperature of the i^{th} species. In particular, for a non-isothermic plasma, one can expect the temperature of the electrons to be much larger than the temperature of the neutrals and ions usually close. However, here, we consider that LTE is reached and that the temperatures are all equal. Furthermore, one could also correct this equation of state taking into account charges interactions considering the Debye pressure P_D:

$$P_D = -\frac{k_B T}{240\pi\lambda_D} \tag{3.27}$$

with λ_D the Debye length in the plasma :

$$\lambda_D = \sqrt{\frac{\epsilon k_B/q^2}{(n_e + \sum_i n_i)/T}} \tag{3.28}$$

with q the elementary charge, and ϵ the permittivity of the gas.

This state equation creates a link between the different densities in the plasma, the temperature and the pressure. In parallel, considering Saha-Eggert's law, one can describe the ionization ratios of each atomic species. In the case of a plasma with molecules, one can also add some reaction laws similarly to the model developed in chapter 2. From this set of equations, different calculation approaches are possible.

Model for densities evolution considering atmospheric pressure

One can assume the pressure and derive all the densities from temperatures. In the case of aluminum oxygen plasma, this as been studied by Hermann et al. in 2015[177].

This article is particularly interesting to us as the studied system is very similar to ours. They ablated a Ti-sapphire target, that is to say a titanium doped Al_2O_3 target. Titanium is in a negligible proportion and will not be discussed here[§]. The authors considered the plasma mostly composed of aluminum and oxygen, both atomic and in the first few ionized states, and diatomic molecules such as O_2, Al_2 and AlO. The equation of state is the one considered above with the pressure taken as the atmospheric pressure corrected by the Debye pressure. This enables the authors to consider a pressure depending only on the temperature and thus to solve the system of equation and derive the densities of the different species in

[§]Traces of Ti atoms are added in the target in order to determine the excitation temperature of these atoms.

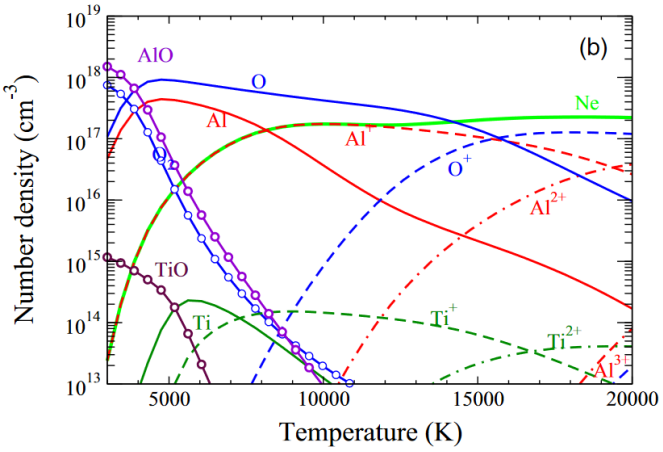

Figure 3.8: Figures extracted from Hermann et al.[177]. Number densities of species vs temperature computed for a plasma in local thermodynamic equilibrium at atmospheric pressure with the elemental composition of the Ti-sapphire crystal (b)

terms of the temperature. Their results are presented in figure 3.8. One can see that diatomic molecules appear only when the plasma is cold enough. Another interesting feature is that, up to 11000 K, the density of electrons is actually equal to the density of Al(II). Indeed, the oxygen ionization energy is much larger than the one of aluminum (E_i^O=13.62 eV compared to E_i^{Al}=5.98 eV) and higher temperatures are required for the ionization. Furthermore, the second ionization energy of aluminum is even larger (18.83 eV) such that Al(III) is also negligible.

One of the drawbacks of such a model, is the consideration of an almost constant pressure. The Debye correction is only about 0.1 % at 4000 K. Here, we have seen that the pressure during ablation can vary a lot. In particular, during the first few μs following ablation, this pressure can reach 100 to 1000 times the atmospheric pressure. Furthermore, temperature in the plasma decreases. Considering the pressure constant, it would require the density of the plasma to increase and the plasma to contract. However, the plasma is clearly expending during the first few μs (see figure 3.1).

Estimation of the pressure from LTE

Three years later, Jörg Hermann published another paper to deal with this pressure issue[178]. Another approach of this system of equations is to measure the temperature and the electron density from spectroscopy. Having both of these measurements, one can solve the system of equations depending on time and determine the evolution of the pressure. This time, the target was an iron alloy and

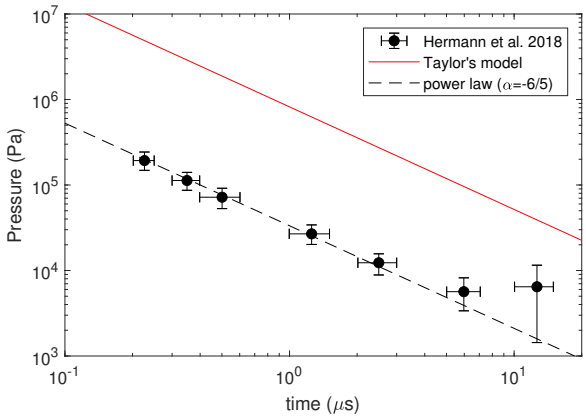

Figure 3.9: Kinetic pressure calculated by Hermann et al.[177] (black dots) compared to Taylor's model (red line). The dashed line corresponds to a power law with an exponent $\alpha = -6/5$.

the composition of the plasma cannot be directly related to our study. However, Taylor's model depends only on the laser pulse energy and not on the target material. One can thus compare the pressure determined by Hermann et al. with the expected pressure given by Taylor's model. In the article, the plasma was generated by a UV (266 nm) pulse of 4 ns with a power of 6 mJ. The pressure evolution according to Taylor's model should be:

$$P(t) = 0.141 \frac{\rho_0^{3/5} E^{2/5}}{t^{6/5}} \tag{3.29}$$

Figure 3.9 shows the pressure calculated in the paper (black dots) compared to the expected pressure from Taylor's model (solid red line). As you can see, the pressure calculated by Hermann et al. is 25 times lower that the one expected by Taylor's model. This would correspond to a tremendous difference in the pulse energy which cannot explain the discrepancy. Yet, quite interestingly, the power law (dashed line) seems to be respected up to 5 μs. At this time, the pressure predicted by Taylor's model reaches the atmospheric pressure and one can expect the pressure in the plasma to stop decreasing. And indeed, after 5 μs, the pressure calculated from Hermann et al. seems to stay constant. Furthermore, the size of the plasma measured by the authors increases with time up to 5 μs then stabilizes. This is consistent with Taylor's model and an expansion due to an over-pressure. When the pressure reaches the atmospheric pressure, the plasma stops its expansion and slowly cools down. How can we explain such a coherence in the time evolution of the pressure despite the discrepancy in the amplitude?

First, it appears unlikely that the pressure calculated by Hermann et al. corresponds to real pressure as they are mostly under the atmospheric pressure. It would be difficult to explain the expansion of the plasma.

Second, the temperature has a huge impact on the calculation of the pressure in Hermann's model. In order to simplify the reasoning, let us consider a plasma composed of only one kind of atom. The total density of the plasma n_{tot} is the density of electron n_e, plus the density of the ions, which is equal to the density of electron, and the density of the neutral n_0:

$$n_{tot} = 2n_e + n_0 \tag{3.30}$$

The density of neutrals can be computed from Saha-Eggert's law:

$$\frac{n_e^2}{n_0} = \frac{1}{\Lambda^3}\exp\left[-\frac{E_i}{k_B T}\right] = \mathcal{S}(T). \tag{3.31}$$

Such that the total density is:

$$n_{tot} = n_e\left(2 + \frac{n_e}{\mathcal{S}(T)}\right). \tag{3.32}$$

For instance, at high temperature, the ionization ratio, defined as $n_e/(n_0 + n_i)$, is almost 1 as all the atoms are ionized. The total density is close to 2 times the electron density. On the contrary, if the ionization ratio is low (usually the case for LIBS), the total density of the plasma will be directly proportional to :

$$n_{tot} \simeq n_e^2/\mathcal{S}(T) \propto \exp\left[\frac{E_i}{k_B T}\right]. \tag{3.33}$$

If $k_B T$ is close to the ionization energy of the species, a slight change in the temperature leads to a great change in the total plasma density and thus the pressure. Of course, in a complex plasma, the calculation would be more complicated. Yet, in the plasma studied in this paper, the main components are Fe and Fe^+ and the electron density is almost equal to Fe^+ density. This simplified model is thus a good approximation.

The ionization energy of Fe is 7.90 eV. For a delay time of 6 μs the temperature measured by the authors is T=7000 K while the electronic density is 2×10^{16} cm^{-3}. According to our simplified model, the total density of the plasma is 1.7×10^{17} cm^{-3}. Changing the temperature to T=5650 K, the total density is multiplied by 25 in thus is the pressure which corresponds to Taylor's model.

From the previous calculation, one can question the use of a measured temperature as a relevant parameter of the model. Indeed, the slight variation of the temperature could impact greatly the ionization of the plasma and thus the calculation of the densities.

Without a space and time resolved measurements, it is likely that the temperature of excited species, localized in hot areas, is larger than the average kinetic temperature. In 2010 Ma et al. deduced the local pressure in a plasma from LTE, perfect gas law and space resolved measurements of the temperature and electronic density[191]. Ablation conditions are quite similar[¶] but ablation takes place under Argon. Argon gas is denser and pressure from Taylor's model is expected to be 16% higher. From local measurements, Ma et al. measured strong spatial gradient for the temperature and the electrons' density. They deduced that the pressure in the plasma is indeed above the atmospheric pressure and goes from 10 atm for a delay of 0.6 μs to 1 atm after 30 μs. Here, the order of magnitude is much more consistent with the pressure expected from Taylor's model even if argon modifies models parameters. It is also interesting to note that the local pressure calculated by Ma et al. is not constant in space which questions one of the model's characteristic. The pressure in Taylor's model is considered almost constant.

Discrepancies might also appear if LTE is true for the excitation of the atoms and ions but not for their velocity. In that case, the excitation temperature of the ions and atoms is equal to the kinetic temperature of the electron gas. Yet, this temperature might be larger than the kinetic temperature of the heavy particles relevant for the pressure[‖]. In that case, the deduced pressure from excitation temperature makes no sens. In the following, I suggest using the other approach of this problem: considering Taylor's pressure as the average kinetic pressure in the plasma and measuring the electron density in order to determine the evolution of the average kinetic temperature of the plasma.

3.4.3 Model considering Taylor's pressure

I used the electronic density measured by Julien Lam a few years ago[47] (see 3.7) in order to determine the evolution of the densities and temperature in the plasma. For that, the pressure will be assumed to be given by Taylor's model:

$$P(t) = 0.141 \frac{\rho_0^{2/5} E^{2/5}}{t^{6/5}} \tag{3.34}$$

[¶]The target is mostly composed of aluminum, the pulse energy is 50 mJ and 5 ns long but the wavelength is 1064 nm.

[‖]The pressure also depends on the kinetic temperature of the electrons according to the Dalton's low but is dominated by the partial pressure of heavy particles in plasma with low ionization.

When the pressure reaches the atmospheric pressure, it will be considered constant. Here I do not consider the Debye correction as it is negligible at a short time with respect to Taylor's pressure and at a long time because of the low temperature.

In his experiment, Julien Lam created an aluminum oxygen plasma by ablating an alumina target with the same laser I used and a pulse energy of 40 mJ. Only the first ionization of aluminum is considered to describe the plasma. Up to 10 000 K, the ionization of oxygen can be neglected because of large ionization energy (13.62 eV). The second ionization energy of aluminum is even larger (18.83 eV) and is also neglected. The density of electron is thus equal to the density of aluminum ions $n_e = n_1^{Al}$ and the only Saha-Eggert's law considered here is the one for aluminum with $E_0^{Al} = 5.98$ eV:

$$\frac{n_e^2}{n_0^{Al}} = \frac{1}{\Lambda^3}\exp\left[-\frac{E_0^{Al}}{k_B T}\right] = \mathcal{S}^{Al}(T) \tag{3.35}$$

For low temperatures, the formation of diatomic molecules should not be neglected. Just like Hermann et al., we consider the formation of O_2 molecules and AlO molecules. Al_2 molecules are very unstable. Just like in chapter 2, the formation of a diatomic molecule AB occurs through the reaction of an atom A and B. Their number densities are obtained from the Guldberg-Waage law of mass action for chemical equilibrium:

$$\frac{n_A n_B}{n_{AB}} = \frac{(2\pi\mu k_B T)^{3/2}}{h^3}\frac{\mathcal{Q}_A \mathcal{Q}_B}{\mathcal{Q}_{AB}} e^{-\frac{D_0}{k_B T}} \tag{3.36}$$

In short: *Considering a given equation of state for the plasma, one can link the pressure to the temperature and the total density of the plasma. In parallel, considering LTE and Saha's relations, one can determine the densities of the different species from the temperature. If one consider perfect gas law and a constant pressure in the plasma, it is possible to determine the composition of the plasma depending on the temperature. However, for a decreasing temperature, this would imply an increasing density which is counter-intuitive at least in the first expansion phase of the plasma. Furthermore, shock-wave dynamics indicates high pressure decreasing rapidly. Another approach is to consider temperature and electron density in order to determine the pressure evolution of the plasma. Unfortunately, Saha's relations depends strongly on the temperature. If the measured temperature is not representative of the average temperature of the plasma, results on the pressure can change a lot. One should rather consider the pressure from Taylor's model as input rather than temperature.*

where $\mathcal{Q}_A$, $\mathcal{Q}_B$ and $\mathcal{Q}_{AB}$ are the partition functions of the atoms and the molecule, D_0 the dissociation energy of the molecule, and μ the reduced mass of the atoms. For AlO, $D_0 = 5.2$ eV and for O_2, which is slightly more stable, $D_0 = 5.17$ eV. The values for the partition functions are taken from Hermann et al.[177]: $\mathcal{Q}_{Al} = 5.92$, $\mathcal{Q}_O = 8.95$, $\mathcal{Q}_{AlO} = 12.7$ and $\mathcal{Q}_{O_2} = 3.34$.

The total density of the plasma is the sum of all these densities:

$$n_{tot} = n_0^{Al} + 2n_1^{Al} + n_0^O + n_0^{AlO} + n_0^{O_2} \tag{3.37}$$

and the ratio between oxygen atoms and aluminum atoms is taken equal to the target one (40% of aluminum and 60% of oxygen):

$$2(n_0^{Al} + n_1^{Al} + n_0^{AlO}) = 3(n_0^O + n_0^{O_2} + n_0^{AlO}) \tag{3.38}$$

Of course this is neglecting the atoms of the surrounding air. Yet, because of the difference of density between the air and the target, one can consider this approximation justified.

Finally, the equation of state is the perfect gas law:

$$P = n_{tot} k_B T \tag{3.39}$$

In the end one can solve this system of 6 equations (3.34, 3.35, 3.36, 3.37, 3.38, 3.39) in order to find the densities of the 5 considered elements and the temperature.

Figure 3.10 (a) represents the calculated densities using the electronic density measured by Julien Lam (red dots). The evolution of this density was fitted by a double exponential (solid red line). The solid black line represents the total density of the plasma which decreases very quickly from about 10^{20} cm^{-1} to 2.5×10^{18} cm^{-1} after three μs. The explosion's blast essentially pushes the matter outward, leading to the formation and expansion of a shock-wave. This leads to a lower gas density behind the shock-front. During that time, the pressure remains quite high. According to Taylor's model, it would reach the atmospheric pressure only after 5 μs. Oxygen atoms and Aluminum atoms are represented respectively in blue and green and make most of the total density. The aluminum ions' density is equal to the electron density and is about 50 times lower than the plasma density. The ionization ratio of the plasma defined as the density of electrons over the total density of heavy particles is represented in figure 3.10 (b). Quite surprisingly, it seems to increase first before a slow decrease with time.

The temperature is represented on figure 3.10 (c). It decreases from about 6500 K to about 5500 K after 3 μs with a constant cooling rate of about (300 K/μs).

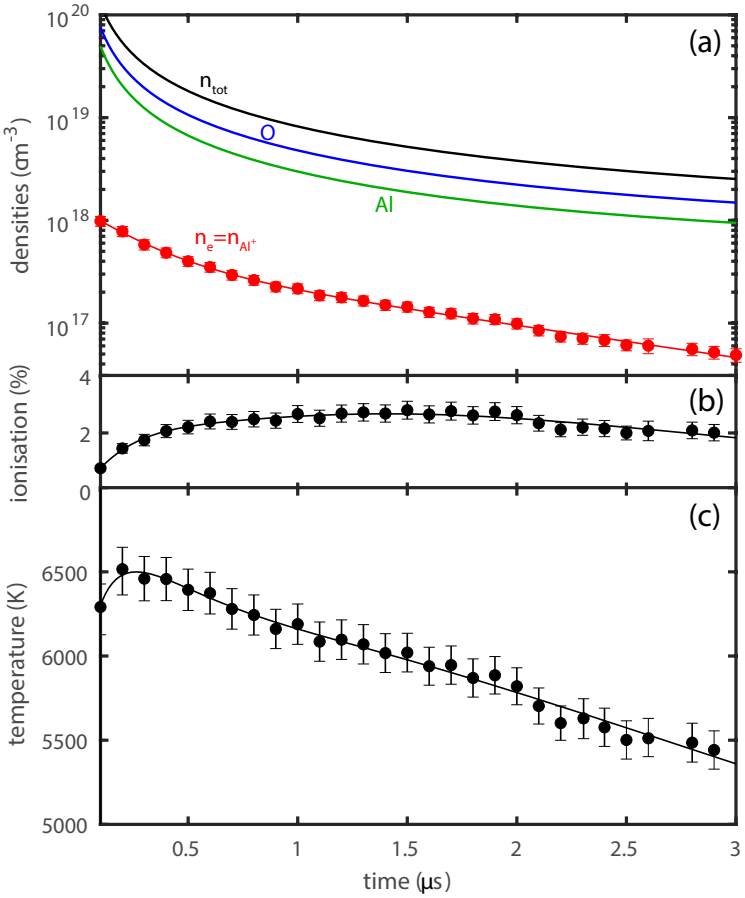

Figure 3.10: (a) Densities of the main species in the aluminum oxygen plasma generated from a 40 mJ pulse. Red dots corresponds to the measured electronic density by Julien Lam's[47] while the red line is a double exponential fit used in the calculations. (b) Ionization ratio of the plasma defined as $n_e/n_{baryons}$. (c) Temperature calculated from the measured electron density (dots) and fit (line) according to the model.

When compared to the temperatures measured by Julien Lam (see panel (c) of figure 3.7), one can notice that the excitation temperature is about twice as big. As explained previously, even if LTE is verified in the plasma, the temperature might vary a lot spatially. Emitting atoms providing the excitation temperatures are likely localized in hot areas of the plasma. This leads to an overestimation of the average kinetic temperature of the plasma. If LTE is not fully verified, one can also expect different temperatures between electrons and heavy particles. In such plasma, the temperatures of the electrons is larger than the temperature of

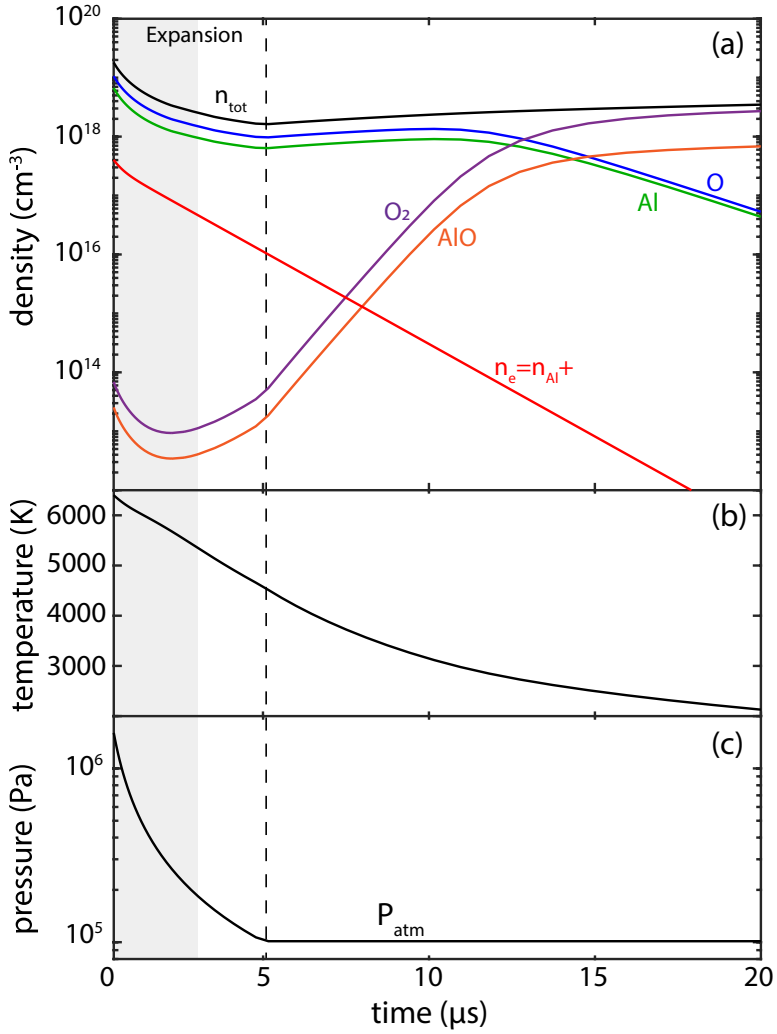

Figure 3.11: (a) Densities of the main species in the aluminum oxygen plasma generated from a 40 mJ pulse considering and extrapolation of the measured electron density's fit (solid red line). (b) Corresponding calculated temperature and pressure (c). The pressure is given by Taylor's model until it reaches the atmospheric pressure.

the heavy particles. In the model here, the kinetic temperature is dominated by heavy particles as the ionization of the plasma is low. Yet, the excitation process of ions and atoms is mostly due to collisions with electrons. This might also explain why kinetic temperature is lower than the excitation temperature but much closer to the rotational temperature measured on AlO molecules. The rotational temperature of AlO molecules might be a better probe of the kinetic temperature

of the plasma as it is directly influenced by collision with heavy particles. However, AlO is also more likely to form in colder areas of the plasma (see chapter 4). In particular, for these average pressures and temperatures, one should not be able to observe the formation of AlO and O_2 as their densities remain below 10^{14} cm^{-3}. AlO molecules do form in such a plasma before 3 μs yet only on the periphery of the plasma.

In order to discuss further the evolution of the plasma, the evolution of the electron density is extrapolated using the double exponential fit as shown in figure 3.11. After 5 μs, the pressure given by Taylor's model reaches the atmospheric pressure and is then considered constant as shown in the panel (c). The gray area corresponds to the 3 first μs where the density of electrons was measured. The evolution of the densities is given in the panel (a) and the temperature in the panel (b). During the 5 first μs, the pressure is higher than the atmospheric pressure and the plasma is in expansion. The total density of the plasma decreases. The densities of the molecules are very low, and their formation rates do not compensate the expansion of the plasma such that their densities decrease. For such temperature, the density of oxygen ions would be even lower and can indeed be neglected. After 5 μs, the plasma stops expending and the pressure is considered constant. Because the temperature keeps decreasing, the density slowly increases as the plasma contracts. The density of molecules increases rapidly and becomes predominant after about 13 μs. Such timescale is perfectly consistent with the evolution of AlO molecules emission in the plasma presented in chapter 4, section 4.3, figure 4.15 (c).

When the pressure is equal to the atmospheric pressure, the calculations of Hermann et al.[177] are fully justified. Furthermore, determining the composition of the plasma in terms of the temperature without any measurement of the electron density is very interesting because it is impossible to measure the electron density when it is too low, that is to say for low temperatures, when the pressure is constant. The time t^* such that $P(t^*) = P_{atm}$ depends on the energy of the pulse and can be calculated as:

$$t^* = \left(\frac{0.141}{P_{atm}}\right)^{5/6} E^{1/3} \rho_0^{1/2} \tag{3.40}$$

Yet, for such a long time, the temperature is quite low, and it should be necessary to consider also the formation of larger molecules. This could be done similarly to the paper of Julien Lam et al. published in 2015[46]. In this paper, the authors calculated the Gibbs free energy of reactions of various aluminum oxygen cluster using the same *ab initio* calculation I used in chapter 2 and deduced the composition of the plasma at different temperatures at a given pressure. The main

drawback of this technique would be not to consider the dynamics of formation. Another solution would be to consider reaction rates given in the model I developed in chapter 2.

3.5 Conclusion

The study of the dynamics of laser-generated shock-wave in air enables to determine the evolution of the pressure behind the shock-front. Its propagation is well described by Taylor's blast auto-similar theory on a broad range of pulse energy from 0.1 to 50 mJ and various materials. However, the blast is not perfectly hemispherical. Propagation in the direction perpendicular to the target surface is faster and overestimates the laser pulse energy using Taylor's model. Averaging the energy in all the directions of propagation leads to a surprisingly good measurement of the pulse energy on the whole range of tested energy and target material. This proves that Taylor's model is perfectly valid for laser ablation in air and can be used as a user-friendly universal model with a strong application potential.

In particular, one can use it to determine the evolution of the average pressure in the plasma depending on the laser pulse energy only. When compared to direct pressure measurements of the shock-wave from its velocity, Taylor's model gives a good estimation of the pressure after 20 ns. Before 20 ns, the pressure is not as high as the one predicted. The initial ablation pressure could be estimated using Taylor's model for $t^* \simeq 10$ ns such that $P[\text{MPa}] = (37.4 \pm 20) \times (\text{E [mJ]})^{2/5}$. This saturation is consistent with the fact that the source of energy is neither point-like nor instantaneous as considered in Taylor's model. After 20 ns, the pressure de-

In short: *Considering the pressure in the plasma to be given by Taylor's model and the electron density to be measured, one can deduce the evolution of the different species density in the plasma and the average temperature. The total density decreases as the plasma expands. The temperature appears to be lower than the excitation temperature measured by spectroscopy. This can be explained considering that the temperature is not homogeneous in the plasma. In particular, emission of excited atoms and ions might be dominated by the hot central region. Extrapolating the evolution of the electron density, one can determine the composition of the plasma for longer times. After 5 μs, the pressure reached the atmospheric pressure and is considered constant. At that time, the plasma stop expanding, but slowly contracts as the temperature keeps decreasing. The density of diatomic molecules increases quickly and are predominant after 13 μs which is consistent with the emission of AlO molecules. However, for such long time and low temperature, one should also consider the formation of larger clusters such as Al_2O.*

creases with time proportionally to $t^{-6/5}$.

Using the equation of state for perfect gas, one can determine the relation between this pressure, the average temperature of the plasma and its total density. Considering that Local Thermodynamics Equilibrium (LTE) is achieved in the plasma, one can use Saha-Eggert's law and Guldberg-Waage's law in order to determine relations between the different densities. With the state equation, this leads to an under-determined system of equations. In order to solve it, one needs to know the time evolution of two of the following quantities: the electron density, the pressure and the temperature. Using spectroscopy measurements, one can determine the electron density from Stark broadening effect and the temperature from Saha-Boltzmann plots. Yet, the system of equations is very sensitive to the temperature. An overestimation of the average temperature leads to large underestimation of the pressure. On the contrary, Taylor's model is a simple way to determine the average pressure in the plasma. Thus, it is better to consider it rather than temperature measurements. Doing so, one can determine the time evolution of the average pressure, temperature and densities in a laser-generated plasma. When applied to an aluminum oxygen plasma generated by a 40 mJ laser pulse, the pressure drops to the atmospheric pressure within 5 μs. During this time, the plasma is in expansion and the total density and temperature of the plasma decrease. The plasma is mostly composed of neutral aluminum and oxygen atoms with about 2% of Al^+ ions. After 5 μs, the pressure is assumed constant and the plasma contracts. The density increases as the plasma keeps cooling and diatomic molecules appear. AlO molecules are predominant on Al atoms after about 13 μs which is consistent with emission. When the temperature is low, one should also consider the formation of larger molecules and clusters.

The temperature given by this model appears to be almost twice lower than the temperature measured by Julien Lam from excited atoms' emission. Because of strong temperature gradients in the plasma, optical measurement of the excitation temperature can be dominated by hot areas, leading to an overestimation of the plasma temperature. Furthermore, even if LTE is true for the excited states of the atoms, the temperature deduced from their emission is the one of the electrons gas which might be higher than the kinetic temperature of heavy particles. The kinetic temperature of heavy particles is more likely to be related to the rotational temperature of diatomic molecules influenced by collisions. One can expect the measurement of rotational temperature to be a better probe of the kinetic temperature in the plasma than atomic emission. And indeed, the rotational temperature of AlO molecules measured by Julien Lam is much closer to the temperature given by the model. However, this could also be linked to some temperature gradients as AlO molecules are more likely to form in cold regions.

In order to investigate this question, I built a spectroscopy set-up which makes it possible to measure AlO emission with a resolution in time and space. As developed in the next chapter, this enables me to discuss the evolution of the rotational and vibrational temperature of excited AlO molecules and challenge the notion of equilibrium in the molecules.

Chapter 4

Temperatures & Thermalization of the Plasma

The point of life is to find equilibrium
in what is inherently unstable.
Pierre Reverdy

Abstract: *In this chapter, I present time and space resolved spectroscopy of AlO and TiO molecules in the plasma. By fitting the recorded spectra, I was able to determine the rotational and vibrational temperatures of AlO molecules and the rotational temperature of TiO molecules depending on their position in the plasma and time. The formation of the molecules occurs mainly in the outer part of the plasma where the temperature is low enough. The vibrational temperature of AlO appears much larger than its rotational temperature, proving that the thermodynamics equilibrium is not reached in the excited state of the molecules. Because of a short lifetime of the excited state, molecules formed have not enough time to be thermalized. The rotational temperature of the molecules is likely to cool down quicker due to large coupling with the gas. The rotational temperature of TiO molecules is similar to the one of AlO but slightly lower, probably due to larger collision cross-section and better thermalization. Rotational temperature of the molecules appears to be a good probe of the kinetic temperature of the gas, especially when the excited state lifetime is long and coupling with the gas is large.*

In the previous chapter, I considered the plasma at the local thermodynamic equilibrium with a given average pressure. This enabled me to compute an average kinetic temperature in the plasma. This temperature appears to be lower than the temperatures measured from atoms spectroscopy. Yet, it is close to the rotational temperature of the molecules. In the conclusion, I raised two possible explanations, (i) this could be due to temperature gradients in the plasma or (ii) this could be the consequence of LTE partial failure.

In the first case, atoms emission arising from hot areas in the plasma lead to an overestimation of the average temperature while AlO molecules are formed in colder areas. On the outer-part of the plasma, the electron density and the temperatures are lower as it is cooled down by the atmosphere. In order to take into account this spatial variation in the spectroscopic measurements, some researchers use a model considering two areas, a central one, dense and hot and an external one colder and less dense[177,192].

In the second case, the kinetic temperature of the electrons' gas is larger than the kinetic temperature of the heavy particles. The electronic states of the atoms and ions are excited by the collision with the electrons such that the excitation temperature is equal to the kinetic temperature of the electrons. On the contrary, rotations of diatomic molecules are greatly influenced by collision with heavy particles and thus could be a better probe of the average kinetic temperature of the plasma.

In order to push further this investigation, we need space resolved spectroscopy in order to take into account the spatial variations of emission and temperature in the plasma. To do so, I built a space and time resolved spectroscopy set-up able to image diatomic molecules such as AlO and determine its local temperatures.

In the introduction, I first define the different temperatures for diatomic molecules. Then, I describe how it is possible to measure these temperatures from emission spectroscopy of the plasma in the case of AlO and TiO molecules. In the second part, I describe the experimental set-up I developed in order to measure diatomic emission spectroscopy resolved in time and space. Finally, I discuss the measurement of the rotational and vibrational temperatures of AlO and the rotational temperature of TiO molecules regarding thermalization processes in the plasma.

4.1 Spectroscopy theory for TiO and AlO molecules

4.1.1 Temperatures in diatomic molecules

Molecules are composed of several atoms bound together and having other degrees of freedom than translation. They can both vibrate and rotate. Considering a molecule in the electronic state n with a vibration mode v and an angular momentum J, the energy of the molecule can be written as:

$$E = T_{\mathrm{n}} + G_{\mathrm{n}}(v) + F_v(J) \tag{4.1}$$

with T_{n} the energy of the electronic level of excitation, G_{n} the vibration energy, and F_v the rotation energy. This means that a molecule is not described by electronic transition only. Instead of having intense emission lines like single atoms, one can observe complex structures corresponding to transitions between the rotational levels of the different vibrational levels of each electronic level (see figure 4.1).

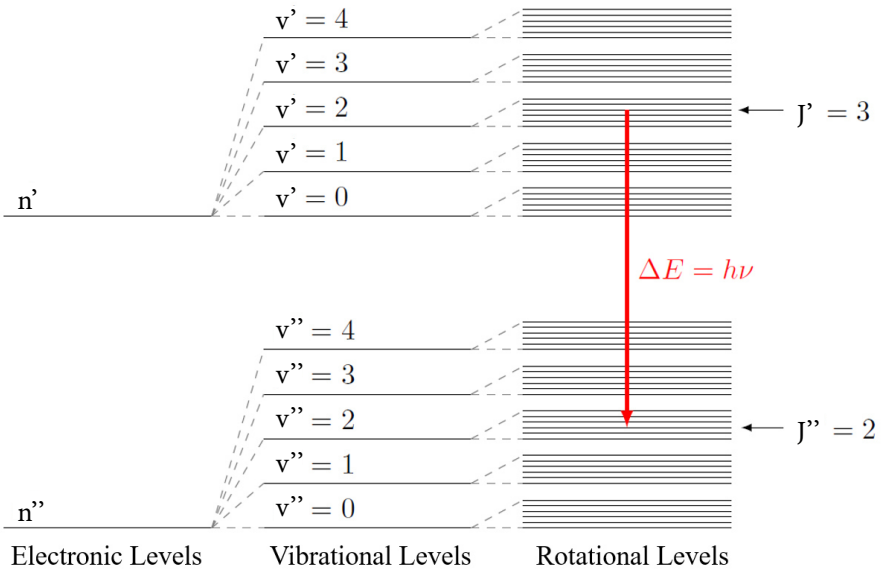

Figure 4.1: Scheme of the different energy levels of molecules. n refers to electronic levels, v to vibrational levels, and J to rotational levels.

For each of these energy modes, one can define an associated temperature by considering its population to be a Boltzmann distribution*. The excitation tem-

*Here, the use of Boltzmann distributions is an approximation of the population distributions that is true only at full equilibrium. The related temperatures are parameters that characterise the distribution. In the case of populations strongly out-of-equilibrium, one should use other descriptions of the population that are out of the scope of the work presented here.

perature of the molecule can be defined the same way as atoms. An equivalent Boltzmann diagram could be studied for molecules in order to determine its excitation temperature. Yet, in this case, it is more complicated because one needs to take care of integrating all the light coming from the different transitions from the same electronic state. This can be extremely complicated when emission bands overlap. The vibrational temperature T_{vib} is associated with the population of the vibrational states. The rotational temperature T_{rot} is associated with the population of the angular momentum states (rotational states). If the molecules reach thermodynamic equilibrium, these three temperatures should be equal. If not, Boltzmann distributions might still be a good approximation of the population of each mode, but the temperatures are not the same. If the molecules are in a state far from equilibrium one cannot use this description. For instance, in the case of stimulated fluorescence, part of the population cannot be described by a Boltzmann distribution as I show in chapter 5.

One can determine the vibrational and rotational temperatures by fitting the emission spectra and the intensities of the different transitions. In the case of molecules, the emission results from 3 different kinds of transition: (i) The purely rotational transitions between rotational levels of the same vibrational and electronic state. These transitions have very low energy and correspond to far IR radiations and radio frequencies. (ii) The rovibrational transitions between two different vibrational states of the same electronic state. These transitions correspond to IR radiations. (iii) The rovibrational transitions between two vibrational states of different electronic states. These transitions correspond to visible and UV radiations. In this manuscript, we are focusing on this kind of transitions. Note that here the temperatures measured through emission are actually probing the population of the excited state. It is not obvious that it is the same as the ground state. Yet, measurement in the IR region is much more complicated in the geometry of our experiment. Indeed, the surrounding environment (air and water) absorbs a lot in the IR region and complicates a lot the measurements. In order to probe the ground state, one can excite the ground state molecules before looking at their emission. I develop such measurements in the chapter 5.

In short: *In the case of molecules, one can determine the rotational and the vibrational temperatures. They respectively give information on the rotational and vibrational excitation of the molecules. These temperatures are interesting to study, especially in the framework of nucleation, as it gives information on the thermalization of the molecule itself. However, determining the rotational temperature from molecular spectroscopy is not simple, it requires large spectral definition. During my PhD, I built an experimental set-up enabled to achieve such ro-vibrational spectroscopy on AlO and TiO molecules with spatio-temporal resolution.*

Similar rovibrational spectroscopy on laser generated plasma has been achieved in particular in the Institut Lumière Matière by Xueshi Bai and Vincent Motto-Ros[193] or in my team with Julien Lam and David Amans[47]. For instance, we have seen on figure 3.7 (c), the evolution of the rotational temperature of AlO molecule in the plasma. Recently, Pengxu Ran et al. reported spatially resolved measurement of the rotational temperature of AlO molecules on the vertical axis of a laser generated plasma[194]. Here my goal is to go further by measuring both the vibrational and rotational temperatures and their evolution depending on time and on the position in the plasma in order to investigate the thermalization of the molecules.

4.1.2 Diatomic molecules

In order to better understand diatomic molecules' spectroscopy, one needs to adopt a quantum mechanic description of the system. Yet, one can describe diatomic molecules with easy-to-grab molecular models in order to better understand the qualitative behavior of the molecules. In this section, I will present the general formalism and description of diatomic molecules based on the book *Rotational structure in the spectra of diatomic molecules* written in 1969 by Istvan Kovacs[195]. I also base myself on the Thesis of Maxime Ribière, *Spectroscopies d'émission et d'absorption appliquées à l'analyse de plasmas produits par impulsion laser* (2008)[196] and a presentation of Professor Xavier Mercier at the Journées du réseau Plasmas Froids du CNRS (2012)[197]. For this section, I would also acknowledge the great work of the intern Louhane Jacod, with whom I had the pleasure to work in the summer of 2020. Despite difficulties due to the pandemic and lockdown, she did a great bibliographic work on AlO and TiO spectroscopy and worked on the code, initially developed by David Amans, that I used to calculate molecular spectral data.

Born-Oppenheimer approximation

Just after the description of atoms with quantum mechanics, Slater, Born and Oppenheimer, Kronig and later Van Vleck naturally started to investigate diatomic molecules during the late 20s' and beginning of the 30s'.

Of course describing a molecule, even composed of only two atoms, is much more difficult than a single one. The goal is to determine wave-functions of the system and its associated energy E. However, in contrary to simple atoms, there is

a relative motion of the nuclei. The nuclei cannot be simply considered as parameter for the Hamiltonian of the electrons through the electron-nucleus interaction potential.

The complete Hamiltonian one needs to consider is :

$$\hat{H} = \hat{T}_A + \hat{T}_B + \hat{T}_e + \hat{V}_{AB} + \hat{V}_{eAB} + \hat{V}_{ee} \tag{4.2}$$

with $\hat{T}_A$ and $\hat{T}_B$ the kinetic part of the relative motion of nuclei A and B, $\hat{T}_e$ the kinetic part of the electrons, $\hat{V}_{AB}$ the interaction potential between the nuclei, $\hat{V}_{eAB}$ the interaction potential between the nuclei and the electrons and $\hat{V}_{ee}$ the interaction potential between the electrons.

The first simplification that can be done, is the so called *Born-Oppenheimer approximation*. It states that the movements of the electrons are much faster than the movement of the nuclei which are several thousand times heavier. The relaxation of the electronic states is much faster than the nuclei dynamics such that, at each position of the nuclei, the electronic configuration of the molecule can be considered at rest in its fundamental state. Thus, the wave-function describing the system can be written as the product of a wave-function describing the nuclei $\Phi(\vec{R})$ and another wave-function describing the electrons $\phi_{\vec{R}}(\vec{r})$ depending on the position of the nuclei only in a parametric way:

$$\Psi(\vec{r}, \vec{R}) = \Phi(\vec{R})\phi_{\vec{R}}(\vec{r}) \tag{4.3}$$

The problem is simplified to the dynamic description of electrons in a rigid potential created by the atoms. This approximation neglects all the contribution of the nuclei kinetic operator on the electronic wave function. As intuited at the beginning of the reasoning, these contributions are often negligible as their magnitude is proportional to the mass ratio between the electrons and the nuclei. More on this formalism can be found in the Annex C.

In the case of a diatomic molecule, one can consider both nuclei to be punctual and separated by a distance R. One can then describe the electrons considering these nuclei immobile and solving the associated Schrodinger equation. The resulting eigen solutions for the electronic system are determined for a given distance R between the nuclei considered as a parameter.

This solution for the electronic state of the molecule is then used as a potential acting on the nuclei in the complete Hamiltonian. It enables the study of the nuclei's position depending on this potential which determines R without considering

the electrons. Yet, the study of the vibration and rotation of these two nuclei is done for a given electronic state (as the electronic state modifies the interaction between both nuclei).

Because the potential depends only on R, it is a central potential (just like for the hydrogen atom). One can decompose the solution as the product of a radial function, the vibrations, and an angular function, the rotations.

In the end, the energy of the electronic system can be decomposed in three different contributions as stated earlier:

$$E = T_{\mathrm{n}} + G_{\mathrm{n}}(v) + F_v(J) \tag{4.4}$$

Each of these contributions have very different magnitudes ($T_{\mathrm{n}} = 1 - 10\mathrm{eV}$, $G_{\mathrm{n}} = 0.1 - 1\mathrm{eV}$ and $F_v = 10^{-4} - 10^{-3}\mathrm{eV}$) with the different spectral signatures we have discussed in the introduction[†].

Vibrations

Vibrations of the diatomic molecule, that is to say the radial variation of R, corresponds very intuitively to an oscillator composed of the two nuclei linked by an electronic bound. The potential of this bound is minimal at the equilibrium distance of the nuclei R_e. Around this equilibrium position, the potential can be approximated by the one of a harmonic oscillator, hence the second order Taylor expansion of the real curve (see the green curve on figure 4.2 (a)). Yet, such an approximation is good only close to the equilibrium point. One obvious limitation of this model is that it fails to describe the dissociation of the molecule. When R increases, the potential of a harmonic oscillator diverges and no dissociation is allowed. On the contrary, when $R = 0$, the potential is not diverging as it should.

One better way to describe this potential is the Morse curve $V(r) = D_e(1 - \mathrm{e}^{-a(R-R_e)})^2 + V(R_e)$, with $a = \sqrt{k_e/2D_e}$, and D_e the well depth related to the dissociation energy of the molecule (see blue curve on figure 4.2 (a)). This potential diverges when $R = 0$ and saturates to the dissociation energy when R goes to infinity. Of course, this potential can be translated by a constant.

Solving the Hamiltonian using this potential, one can demonstrate that the

[†]By convention, in spectroscopy, the energies are divided by hc in order to obtain *wavenumbers* usually expressed in [cm^{-1}]. h is the the Plank constant and c the speed of light in vacuum. In plasma physics and in this manuscript, the energy are more likely to be given in eV.

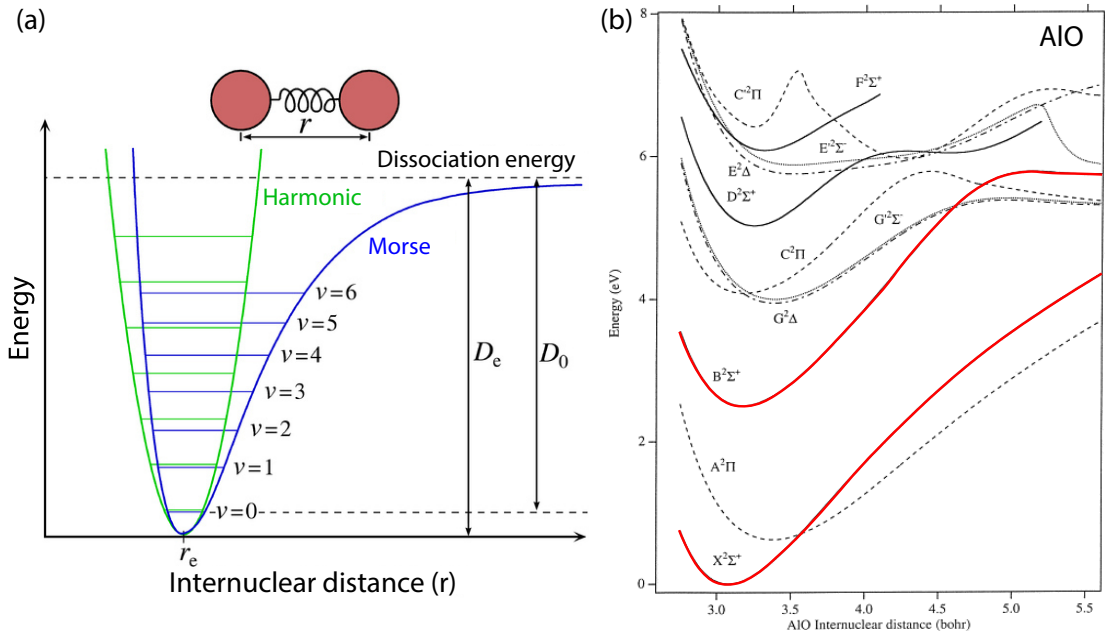

Figure 4.2: (a) Illustration from Wikipedia the shift for the energy level for a diatomic molecule considering harmonic potential of Morse potential. (b) MRCI potential energy functions of the doublet states of AlO calculated by Zenouda et al.[198]. In red are the $X^2\Sigma^+$ and $B^2\Sigma^+$ states studied in this manuscript.

eigenvalues of this potential can be written as:

$$E(v) = h\nu_0(v + 1/2) - \frac{[h\nu_0(v + 1/2)]^2}{4D_e} \tag{4.5}$$

with $\nu_0 = \frac{a}{2\pi}\sqrt{2D_e/m}$ a frequency and $v = 0, 1, 2...$ the vibration quantum number. For large values of v, one can find out that the difference in energy $E(v + 1) - E(v) < 0$, this corresponds to the dissociation limit of the molecule. For v smaller than this limit, Morse's curve provides a good approximation for the vibration levels of a diatomic molecule.

However, when it comes to describing precisely the position of vibration levels, one cannot simply rely on the Morse curve. Many other effects can modify the potential, starting by coupling between the rotations and the oscillations and the limit of the Born-Oppenheimer approximation. In figure 4.2 (b) is plotted the potential of the different electronic levels of the AlO molecules extracted from the article of Zenouda et al.[198]. Depending on the electronic state, the potential

can look much different that the Morse curve. In red are the $X^2\Sigma^+$ and $B^2\Sigma^+$ states studied in this manuscript. In practice, the energy levels for vibrations are described by a Taylor's expansion (usually to the third order) whose parameters are adjusted on experimental data:

$$G_n(v) = w_e\left(v+\frac{1}{2}\right) - w_e x_e\left(v+\frac{1}{2}\right)^2 + w_e y_e\left(v+\frac{1}{2}\right)^3 + ... \quad (cm^{-1}). \tag{4.6}$$

with w_e the wavenumber of the oscillator, $w_e x_e$ and $w_e y_e$ the anharmonicity parameters. The first two terms can be related to the previous description with the Morse's curve.

Rotations

When considering the rotations of the molecules, the first idea is to consider a rigid rotator. That is to say, the rotation of a rigid body. In that case, the inertia momentum of the molecule can be written as $I = \mu R^2$ with μ the reduced mass. One can solve the Hamiltonian and find the eigenvalues of the system as:

$$E(J) = BJ\,(J+1) \quad \text{with} \quad B \equiv \frac{\hbar^2}{2I} \tag{4.7}$$

with $J = 0, 1, 2, ..$ the rotation quantum number. Note that each of these levels are $2J+1$ times degenerated.

In reality, the molecule cannot be approximated as a rigid body. One can take the classical image of two bodies linked by a spring and rotating. Because of their inertia, both masses are ejected one from the other and the spring length increases, changing the inertia momentum of the system. In order to take into account this dependence of I with the rotation, one usually considers the non-rigid rotator:

$$F_v(J) = B_v \cdot J(J+1) - D_v \cdot \Big(J(J+1)\Big)^2 \quad (cm^{-1}). \tag{4.8}$$

with B_v and D_v fitted parameters. The non-rigid rotator contracts the transitions by reducing the energy differences. However, this model does not actually take into account the length modification due to the vibration mode but only the modification length due to the rotation.

Even if the progression of the rotational transitions are fairly described by the non-rigid rotator, precise positions of the transitions have to take into account

the interaction with the electronic orbitals, the electrons and nuclei spins. These couplings can shift the energy and lift the degeneracy of levels. Usually, it is done by introducing an energetic term $H(J, K, S, \Lambda, \Sigma...)$ in the rotational energy:

$$F_v(J) = B_v \cdot J(J+1) - D_v \cdot \Big(J(J+1)\Big)^2 + ... + H(J, K, S, \Lambda, \Sigma...) \quad (cm^{-1}). \quad (4.9)$$

J is now the total angular momentum. It takes into account the splitting due to couplings between the different contribution $(K, S, \Lambda, \Sigma...)$. The correction H depends on the rotational state J and other parameters (K, S, Λ, Σ) corresponding to the other momenta of the molecule.

Couplings and Hund rules

In order to discuss the different couplings between the momenta of the diatomic molecule, we introduce their notation and projections on inter-nuclei axis (see figure 4.3):

- $\mathbf{N}$ or $\mathbf{R}$ is the kinetic momentum of the nuclei rotation
- $\mathbf{L}$ is the total orbital kinetic momentum of the electrons
- $\mathbf{\Lambda}$ is the projection of $\mathbf{L}$ on the molecule axis
- $\mathbf{S}$ is the total spin momentum of the electrons
- $\mathbf{\Sigma}$ is the projection of $\mathbf{S}$ on the molecule axis
- $\mathbf{\Omega} = \mathbf{\Lambda} + \mathbf{\Sigma}$

In short: *In order to describe the energy levels of diatomic molecules, we first describe the vibration by an oscillator. Because the true potential is not quadratic but closer to a Morse potential, the harmonic oscillator model is added with a quadratic and cubic correction whose parameters are tabulated from experimental data. The rotation of the molecules are described by a non-rigid rotator. For a better description of rotational levels, it is possible to introduce an energetic term taking into account the different momenta interactions. In the end, one can calculate the exact position of the rovibrational transitions considering only an ensemble of tabulated constants. Yet, not all the transitions between these levels are allowed. It depends on their respective quantum state. Depending on the quantum properties of the molecules, Hund proposed several cases with precise criterion enabling the transition.*

- $\mathbf{K} = \mathbf{\Lambda} + \mathbf{N}$

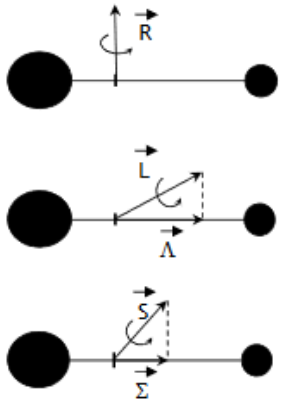

Figure 4.3: Illustration of the different momenta for a diatomic molecule and their projections on the molecular axis.

All the different momenta interact together such that it is the resulting angular momentum **J** that has to be considered in the calculations of the energy levels. Of course, the coupling depends on each molecule and electronic states involved. Yet, for calculations, Hund derived 5 limit cases[195]. Depending on the molecule and the electronic state, one has to determine which case is relevant. In this study, only the case (a) and (b) of Hund are used.

Hund's case (a) is when the total orbital kinetic momentum of the electrons **L** and the total spin momentum of the electrons **S** are highly coupled with the inter-nuclear axis as shown on the right-side of figure 4.4. In that case, **J** is the sum of their projection on the axis with the kinetic momentum of the nuclei rotation : $\mathbf{J} = \mathbf{\Omega} + \mathbf{N}$. The quantification gives $\Omega = |\Lambda + \Sigma|$ with $\Sigma \in [\![-S; S]\!]$ while Λ and S are determined by the electronic state of the molecule. For a given Ω, $J = \Omega, \Omega + 1, \Omega + 2...$ In general, this case is valid for the first rotational levels.

Hund's case (b) is when the total orbital kinetic momentum of the electrons **L** is highly coupled with the axis of the molecule but the total spin momentum of the electrons **S** is not. In that case, $\mathbf{\Sigma}$ is not defined. $\mathbf{J} = \mathbf{K}+\mathbf{S} = (\mathbf{\Lambda}+\mathbf{N})+\mathbf{S}$. Quantification gives $K = |\Lambda|, |\Lambda|+1, |\Lambda|+2...$ such that $J = K+S, K+S-1, ..., |K-S|$. This case usually corresponds to high rotational levels. It is also valid for molecules when $\Lambda = 0$, that is to say when the total orbital kinetic momentum of the electrons is perpendicular to the molecule axis. In that case the electron spin does not couple with the axis of the molecule. This remains true for light molecules where

the coupling of the electron spin remains low even if $\Lambda \neq 0$. This case describes the transitions studied for AlO. TiO molecules are more complicated. For large values of J, the molecule is mostly described by case (a). Yet, for each transition, the calculation of the energy considers a mix of both states and associated interactions.

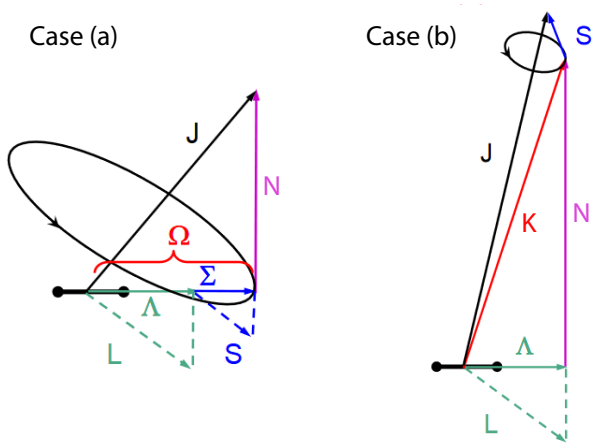

Figure 4.4: Illustration of the molecule momenta in the cases (a) and (b) of Hund.

When $\Lambda \neq 0$, the coupling splits in two the rotational component of the energy. This is called the Λ-doubling. Although, this splitting is rather small and has to be taken into account only when looking at high definition spectra.

Notation

To ease the reading, the most relevant notations and conventions used in this manuscript are summed up in the annex A. Notation in molecular spectroscopy can first appear quite obscure with vibrational transitions named $X^2\Pi_{1/2}$, $A^3\Sigma^+$ or even $B^3\Pi_g$. This notation actually corresponds to the different information needed for the calculation previously exposed. It generally follows the following form:

$$L^{2S+1}[\Lambda]_\Omega \tag{4.10}$$

The letter L corresponds to the electronic state. By convention, the ground state is called after the letter X, then comes A, B etc., as shown in the top part of table 4.1. If the multiplicity of the excited state is different from the fundamental state, then lowercase letters are used. The exponent corresponds to the value $2S + 1$. The second letter, in Greek, corresponds to the value of the projection $\mathbf{\Lambda}$ of $\mathbf{L}$ on the

interatomic axis. The convention for the correspondence of the letter and $\mathbf{\Lambda}$ are reported in the bottom part of table 4.1. Finally, the index corresponds to the value of $\Omega = |\Lambda + \Sigma|$.

The parity of the electronic wave-function with respect to a plan containing the molecular axis is referred by a + if symmetric or − if anti-symmetric in exponent of the Greek letter. Similarly, the parity of the electronic wave-function with respect to its center is refereed by the index g for the German *gerade* if symmetric and u for *ungerade* is anti-symmetric.

Selection rules

The transition happens when the molecules go from one state to another by absorbing a photon or emitting one. The energy of the photon corresponds to the difference in energy between the two states. This energy $\bar{\nu}$ can be defined as:

$$\begin{aligned} \bar{\nu} &= E(n', v', J') - E(n'', v'', J'') \\ &= [T(n') - T(n'')] + [G_{n'}(v') - G_{n''}(v'')] + [F_{v'}(J') - F_{v''}(J'')]. \end{aligned} \tag{4.11}$$

with (n', v', J') the initial state and (n'', v'', J'') the final state. T corresponds to electronic contribution of the energy, G the vibrational contribution and F the rotational contribution. Usually, T, G, F and $\bar{\nu}$ are expressed in [cm^{-1}]. By convention, in the (b) case, K is used instead of J.

In short: *Notation for diatomic molecules can appear quite elaborated and impenetrable even for someone working in the field. Especially when looking at old documents when no conventions were set. Hopefully, there is no need to read this language in order to understand the work here. If one is not interested in the detail of the calculation presented here, only a few key notations are needed. In the spectroscopy of AlO and TiO presented here, we always look at transitions from a given excited electronic state n' to the ground electronic state n'', there is no need to understand the $A^3\Phi_{\Omega'} \longrightarrow X^3\Delta_{\Omega''}$ notation. Then, within these electronic states, we consider the rovibrational transition characterized by a vibrational number v and a rotational number J or K (depending on Hund's case and convention). These levels can then be further split and precise calculations are needed for the calculation of theoretical spectra but not required for the understanding of their shape. All the relevant notations and conventions used in this manuscript are summed up in the annex A.*

Electronic state n	0	1	2	3	4
Notation L	X	A/a	B/b	C/c	D/d
$\|\Lambda\|$	0	1	2	3	4
Notation [Λ]	Σ	Π	Δ	Φ	Γ

Table 4.1: Conventional notation for molecular spectroscopy

In reality, not all the transitions are allowed. One needs only to consider transitions allowed by selection rules. These rules can vary from one molecule to another. In our cases, these rules are[195] : $\Delta\Lambda = 0, \pm 1$; $\Delta S = 0$; $\Delta J = 0, \pm 1$ but $J' = J'' = 0$ is forbidden. The transitions for different values of $\Delta J = J' - J''$ and $\Delta K = K' - K''$ are indicated by a specific letter as reported in table 4.2. These selection rules lead to transition progressions called branches defined by the value of ΔJ and ΔK. The convention for the branches name is:

$$^{\Delta K}\Delta J_{ij} \tag{4.12}$$

with ΔK and ΔJ encoded by letters according to table 4.2, and i and j indicates the spin projection (1 if $+1/2$ and 2 if -1/2). If $\Delta K = \Delta J$, only ΔJ is written and if $i = j$ only one is written.

In short: *Fortrat diagrams represent the rotational number J or K of an enabled transition in terms of its emission wavelength. Because transitions are possible for $\Delta K = K' - K'' = 0, +1, -1$, one can observe 3 branches named respectively P, R and Q for each vibrational level. In the case of the transition of AlO observed here, the probability for $\Delta K = 0$ is so low that the Q branch is not observed. If one consider the (0,0) band, that is to say the transition from the first electronic state with $v = 0$ to the ground electronic state with $v = 0$, there are 2 branches of possible transition (P and R) for various K between 484 nm and 500 nm.*

$\Delta J = J' - J''$		-1	0	1	
$\Delta K = K' - K''$	-2	-1	0	1	2
Letter	O	P	Q	R	S

Table 4.2: Notation of the transition branches

4.1.3 Spectrum calculation

Transitions intensities

The intensity $I^{n',v',J'}_{n'',v'',J''}$ of the transition $(n', v', J') \rightarrow (n'', v'', J'')$ is[199]:

$$I^{n',v',J'}_{n'',v'',J''} = hc \cdot \bar{\nu}^{n',v',J'}_{n'',v'',J''} \cdot A^{n',v',J'}_{n'',v'',J''} \cdot N_{n',v',J'} \qquad (W \cdot m^{-3}). \tag{4.13}$$

$\bar{\nu}^{n',v',J'}_{n'',v'',J''}$ is the transition wave-number (cm^{-1}), $N_{n',v',J'}$ is the density of the molecules in the initial state (m^{-3}) and $A^{n',v',J'}_{n'',v'',J''}$ is the probability of spontaneous transition (s^{-1}).

In the case of my experiment, the iCCD camera is sensitive to a number of photons. Thus, for a transition $(n', v', J') \rightarrow (n'', v'', J'')$, the signal recorded is proportional to the number of emitted photons integrated over the measurement time (gate width t_G):

$$\int_{t_G} \frac{dN^{n'',v'',J''}_{n',v',J'}}{dt} dt = \int_{t_G} A^{n'',v'',J''}_{n',v',J'} N_{n',v',J'}(t) dt \propto A^{n'',v'',J''}_{n',v',J'} N_{n',v',J'} \tag{4.14}$$

with $A^{n'',v'',J''}_{n',v',J'}$ the probability of spontaneous emission and $N_{n',v',J'}$ the population of the excited state. It is proportional to the density of the molecules in the excited state times the probability of emission. This probability coefficient can be written as:

$$A^{n',v',J'}_{n'',v'',J''} = A^{n',v'}_{n'',v''} \cdot A^{J'}_{J''} \,. \tag{4.15}$$

with $A^{n',v'}_{n'',v''}$ the Einstein coefficient referring to vibrations and $A^{J'}_{J''}$ the coefficient referring to rotations.

On one hand, $A^{J'}_{J''}$ is proportional to the **Höln-London**'s coefficient $S^{J'}_{J''}$:

$$A^{J'}_{J''} = \frac{S^{J'}_{J''}}{2J' + 1}, \tag{4.16}$$

Höln-London's coefficient, defining the probability of transition, is normalized such

that:

$$\sum_{sub-rot\ \ states} S_{J''}^{J'} = (2 - \delta_{0,\Lambda'})(2S' + 1)(2J' + 1) \tag{4.17}$$

It takes into account, the Λ-doubling when $\Lambda' \neq 0$, the spin degeneracy and the rotation degeneracy.

On the other hand, the Einstein's coefficient $A_{n'',v''}^{n',v'}$ is defined as:

$$A_{n'',v''}^{n',v'} = \frac{1}{4\pi\varepsilon_0} \frac{64\pi^4}{3h(2 - \delta_{0,\Lambda'})(2S' + 1)} \cdot (100 \cdot \bar{\nu}_{n'',v'',J''}^{n',v',J'})^3 \cdot S_{n'',v''}^{n',v'} \cdot (a_0 e)^2 \qquad (s^{-1}), \tag{4.18}$$

where ε_0 is the vacuum permittivity, a_0 is the Bohr radius, e is the elementary charge and $S_{n'',v''}^{n',v'}$ is called the *band force*. It is divided by $(2 - \delta_{0,\Lambda'})(2S' + 1)$ as these degeneracies are already considered in the Höln-London coefficient. The *band force* is tabulated and depends on the geometry of the orbits. It is proportional to the **Frank-Condon** coefficient $q_{v''}^{v'}$? :

$$S_{n'',v''}^{n',v'} = q_{v''}^{v'} \cdot |R_e(\bar{r_{v''}^{v'}})|^2 \tag{4.19}$$

with $r_{v''}^{v'}$ the average inter nuclear distance.

Franck-Condon's coefficient arises from a law of quantum chemistry describing the intensities of vibronic transitions. In the case of molecules, the absorption and emission occurs between two vibrational states of two different electronic states. When the electronic state of a diatomic molecule is changed, one can expect the nuclear configuration to experience significant changes and indeed, the potential energy of the molecule (Morse curve) is modified such that the equilibrium position is changed as presented on figure 4.5. Yet one needs to keep in mind that the atoms are never completely still and that the molecule is "vibrating" for the classical point of view. In a quantum formalism this is described by the vibrational wave-function represented in orange on figure 4.5 for different vibrational states. The classical Condon approximation stipulates that the electronic transition occurs on a short timescale compared to nuclear motion, so that one can consider a fixed position of the nuclei. This means that one shall consider only vertical transitions in the scheme presented on figure 4.5. The extension of this approximation to quantum mechanics defines the so-called Franck-Condon principle. The probability of a vibronic transition is proportional to the square of the overlap integral between the vibrational wavefunctions.

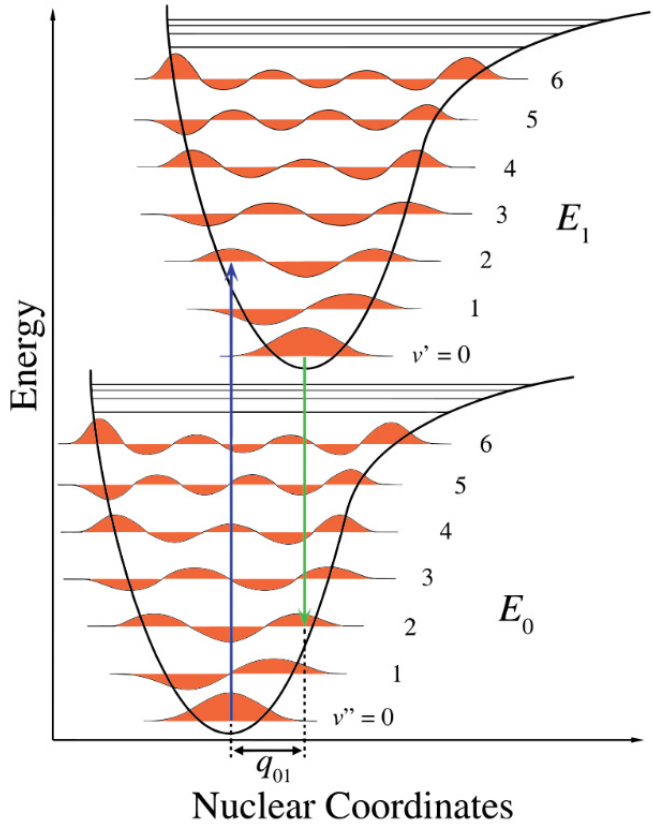

Figure 4.5: Scheme from Wikipedia of the vibrational wave-functions for two different electronic states of a diatomic molecule. The nuclear coordinates correspond to the inter-atomic distance and the black curves correspond to the typical Morse curve potential of the dimer. The blue and green arrow respectively show a fluorescence excitation and emission likely to happen between vibrational levels with high recovery of the wave-function.

Finally, the density of molecules in the initial state can be written assuming a Boltzmann distribution as previously introduced:

$$N_{n',v',J'} = N_{n'} \cdot \frac{1}{2} \cdot (2J'+1) \cdot \frac{exp\left(-\frac{hc \cdot F_{v'}(J')}{k_B \cdot T_{rot}}\right)}{Q_{rot_{n',v'}}(T_{rot})} \cdot \frac{exp\left(-\frac{hc \cdot G_{n'}(v')}{k_B \cdot T_{vib}}\right)}{Q_{vib_{n'}}(T_{vib})}. \quad (4.20)$$

$N_{n'}$ is the density of molecules in the electronic state n' and $Qrot_{n',v'}(T_{rot})$ and $Qvib_{n'}(T_{vib})$ are the partition functions for the vibration and the rotation.

In order to calculate the intensity of each transition, One needs to calculate for each molecule, the position of the levels, the partition functions, the allowed transitions, and the associated probabilities.

AlO molecule

The first molecule I got interested in is the AlO molecule. Indeed, when considering the formation of alumina clusters, it is the first molecule to appear[47,46,177]. Furthermore, despite its short lifetime on earth, this molecule is fairly well known. Indeed, it is an important molecule for astrophysics as it composes a large part of observed interstellar plasma[58,63,80]. It was extensively studied in the 60s both experimentally with high resolution spectroscopy and theoretically with theoretical transition structure.

In our case, the molecules are generated by laser ablation and a large part of them ends up in the first electronic excited state such that many de-excitation in the visible light can be observed. We focused our study on the $B^2\Sigma^+ \longrightarrow X^2\Sigma^+$ system, that is to say the transitions from the electronic excited state with $\Lambda' = 0$ to the ground electronic state with $\Lambda'' = 0$. It corresponds to singlet states with $S = 1/2$. This vibration band appears to be the brightest in our plasma, well isolated from the others, and the rotational levels are fairly separated.

Both states are Σ states and described by the Hund case (b). Because $\Lambda' = \Lambda'' = 0$, there is no Λ-doubling. K' and $K'' = 0, 1, 2...$ and J' and J'' are respectively $K' \pm \frac{1}{2}$ and $K'' \pm \frac{1}{2}$.

In short: *For each of the enabled transitions, we need to calculate the intensity of the transition, that is to say how many molecules in the plasma go from the upper state to the down state per unit of time. This intensity is proportional to the density of molecules in the upper state times the probability of transition. As discussed previously, we consider the population of the molecules in the different state to be described by a Boltzmann law such that for each energy level, it can be fully calculated using T_{rot} and T_{vib} as parameters. Then, the probability of transition depends on the Höln-London coefficient referring to the rotational state and the Frank-Condon coefficient for the vibrational state. These coefficients depend on the levels involved in the transition and some tabulated values. One can determine the expected intensity of each enabled transition depending on these tabulated coefficient and the rotational and vibrational temperature of the molecule's population.*

According to Kovacs[195], one can write the energy for the level $J' = K' + \frac{1}{2}$:

$$F_{1v}(K) = B_v \cdot K(K+1) - D_v \cdot \Big(K(K+1)\Big)^2 + \frac{1}{2}\gamma_v \cdot K, \tag{4.21}$$

while for the level $J' = K' - \frac{1}{2}$:

$$F_{2v}(K) = B_v \cdot K(K+1) - D_v \cdot \Big(K(K+1)\Big)^2 - \frac{1}{2}\gamma_v \cdot (K+1), \tag{4.22}$$

The index 1 or 2 stands for the spin projection value $+1/2$ and $-1/2$ respectively. One can notice the same expression we developed earlier except for using K instead of J and γ_v a constant corresponding to the energy correction H. The electronic configuration of these orbitals is $+$ for K even, no matter the value of J, and $-$ otherwise[199].

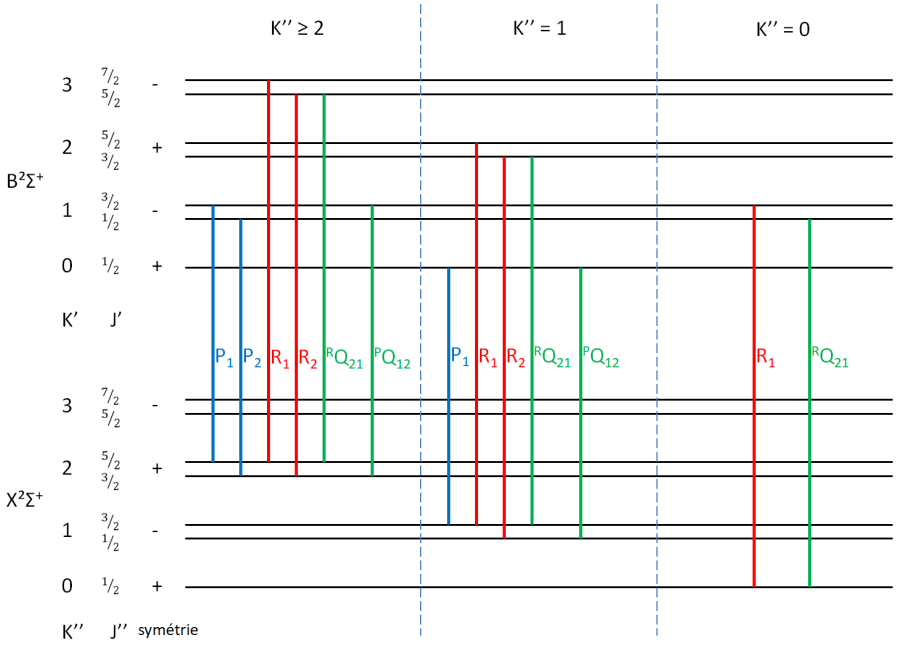

Figure 4.6: Illustration from L. Jacob's report of the AlO's $B^2\Sigma^+ \longrightarrow X^2\Sigma^+$ transitions in terms of K''. Notations of the electronic states are given by equation 4.10 and table 4.1. Notations of the branches are given by equation 4.12 and table 4.2.

Considering the selection rules previously described for the transitions $B^2\Sigma^+ \longrightarrow X^2\Sigma^+$, $\Delta\Lambda$ always equal 0, $\Delta J = 0, \pm 1$ but $J'' = J' = 0$ is forbidden, only the transitions changing the symmetry are possible meaning that $\Delta K = 0$ is forbidden.

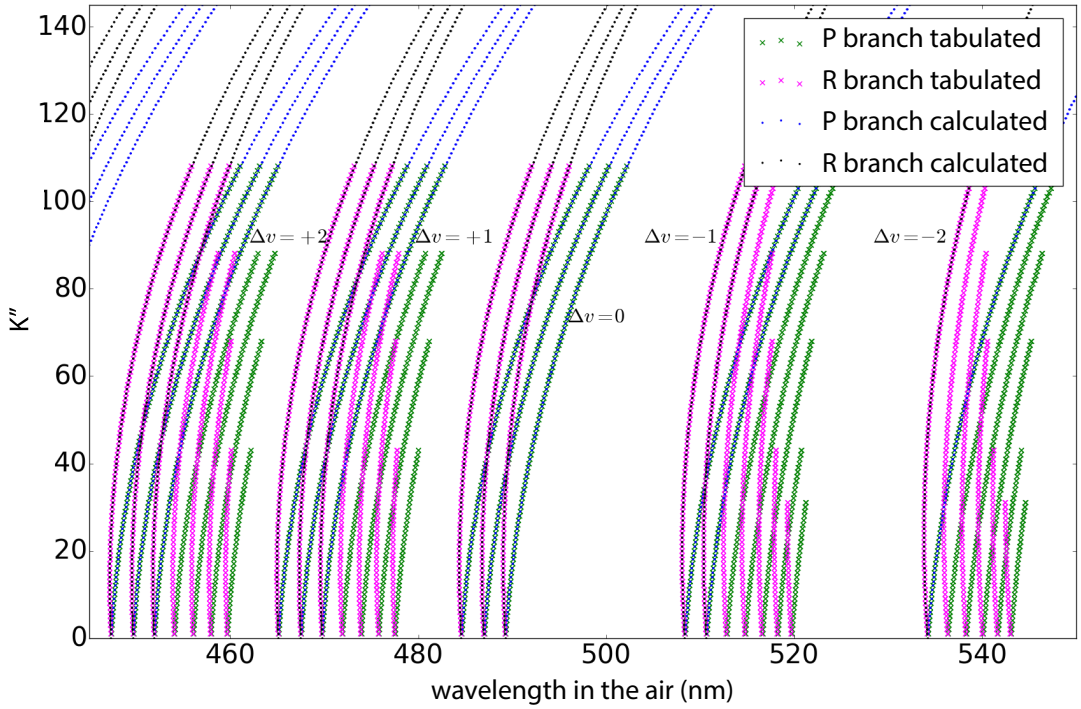

Figure 4.7: Fortrat diagram for the $B^2\Sigma^+ \longrightarrow X^2\Sigma^+$ system of AlO molecules with experimental transition measured by Launila et al.[200] (crosses) calculated transition by our program from the tabulated constant of Kovacs et al.[195] (dots). $\Delta v = v' - v''$. The branches Q are not observed because of low transition probability.

It remains 6 possible branches: $P_1, P_2, {}^PQ_{12}, R_1, R_2\, et\, {}^RQ_{21}$ as shown on figure 4.6. For each branch, Kovacs[195] provides the calculation of the Höln-London coefficients depending on K'' which are reported in the table 4.3.

One way to represent the possible transition is to plot the K or J number of the initial state versus the transition wavelength (or energy) as represented on figure 4.7. This is called a Fortrat's diagram. In such a representation, the progression of the transition for each branch is clearly visible and the denomination of *branches* takes on its full meaning. On the diagram, the branches correspond to the transition $\Delta K = \pm 1$. In the case of AlO, the branch $\Delta J = 0$ is allowed, but the probability of transition is close to 0 and the branches ${}^PQ_{12}$ and ${}^RQ_{21}$ are not observed (S_{jj} is one or two order of magnitude lower than the other branches). In the following, when speaking about R and P branches, we will refer to $\Delta K = \Delta J = \pm 1$.

P branches ($\Delta K = -1$)			R branches ($\Delta K = +1$)		
P_1	P_2	${}^{P}Q_{12}$	R_1	R_2	${}^{R}Q_{21}$
$\frac{2K''(K''+1)}{2K''+1}$	$\frac{2K''(K''-1)}{2K''-1}$	$\frac{2K''}{(2K''+1)(2K''-1)}$	$\frac{2(K''+1)(K''+2)}{2K''+3}$	$\frac{2K''(K''+1)}{2K''+1}$	$\frac{2(K''+1)}{(2K''+1)(2K''+3)}$

Table 4.3: Höln-London for the $B^2\Sigma^+ \longrightarrow X^2\Sigma^+$ system of AlO molecule[195]. Notations of the branches are given by equation 4.12 and table 4.2. The lines of the Q branches lie very close to the corresponding lines (with same K and ΔK) of the P and R branches and are therefore called *R-form Q-branches* or *P-form Q-branches*.

TiO molecule

Another molecule I got interested in is TiO. In the following, I present the structure of the molecule as described by Kovacs[195]. For the calculations, we adopted the formalism described by Hermann et al.[201] which is presented in the annex B.2. The transitions of TiO observed here correspond to the $A^3\Phi_{\Omega'} \longrightarrow X^3\Delta_{\Omega''}$ system. Both correspond to triplet states, increasing the number of transitions and the complexity of the emission. $\Lambda' = 3$; $S' = 1$ and $\Sigma' = 0, \pm 1$, and $\Lambda'' = 2$; $S'' = 1$ and $\Sigma'' = 0, \pm 1$. Because they are not Σ type and $\Lambda \neq 0$, there is Λ doubling. Yet, this splitting will be neglected as it is far below the spectral definition of the measurements. As they are triplet states, for a given J, the rotational level will be indexed 1 for $\Sigma = -1$, 2 for $\Sigma = 0$, and 3 for $\Sigma = 1$. For each of them, the rotational energy can be written as[202]:

$$F_{1v}(J) = B_v \cdot \Big[J(J+1) - [y_1 + 4J(J+1)]^{\frac{1}{2}} - \frac{2}{3}\frac{y_2 - 2J(J+1)}{y_1 + 4J(J+1)}\Big] \tag{4.23}$$

$$-D_v\big(J - \frac{1}{2}\big)^4 - \frac{\beta_v}{3} + \beta_v S^2_{\Lambda,J-1} + \gamma_v\big(J + \frac{1}{3}\big) \tag{4.24}$$

$$F_{2v}(J) = B_v \cdot \Big[J(J+1) + \frac{4}{3}\frac{y_2 - 2J(J+1)}{y_1 + 4J(J+1)}\Big] \tag{4.25}$$

$$-D_v\big(J + \frac{1}{2}\big)^4 - \frac{\beta_v}{3} + \beta_v S^2_{\Lambda,J} + \frac{\gamma_v}{3} \tag{4.26}$$

$$F_{3v}(J) = B_v \cdot \Big[J(J+1) + [y_1 + 4J(J+1)]^{\frac{1}{2}} - \frac{2}{3}\frac{y_2 - 2J(J+1)}{y_1 + 4J(J+1)}\Big] \tag{4.27}$$

$$-D_v\big(J+\frac{3}{2}\big)^4 - \frac{\beta_v}{3} + \beta_v S^2_{\Lambda,J+1} - \gamma_v\big(J+\frac{2}{3}\big) \tag{4.28}$$

with:

$$y_1 = \Lambda^2 Y(Y-4) + \frac{4}{3} \quad et \quad y_2 = \Lambda^2 Y(Y-1) - \frac{4}{9}. \tag{4.29}$$

Here, the expression of the energies are much more complicated than for AlO molecules as the coupling are more important. Y is a parameter which determines if the level is described more by the (a) case of the (b) case depending on J. Y is the ratio between the spin-orbit coupling constant A and the rigid rotator constant B_v.

The spin coupling is given for the upper state ($\Lambda = 3$) by:

$$S_{3,J'-1} = \Big[\frac{2(J'^2-9)}{C_1(J')}\Big]^{\frac{1}{2}}, \tag{4.30}$$

$$S_{3,J'} = \frac{3(Y-2)}{C_2(J')^{\frac{1}{2}}}, \tag{4.31}$$

$$S_{3,J'+1} = \Big[\frac{2(J'-2)^2(J'+4)^2}{C_3(J')}\Big]^{\frac{1}{2}}, \tag{4.32}$$

with:

$$C_1(J') = 9Y(Y-4)(J'-2)(J'+3) + 2(2J'+1)(J'-3)J'(J'+3), \tag{4.33}$$

$$C_2(J') = 9Y(Y-4) + 4J'(J'+1), \tag{4.34}$$

$$C_3(J') = 9Y(Y-4)(J'-3)(J'+4) + 2(2J'+1)(J'-2)(J'+1)(J'+4). \tag{4.35}$$

and for the lower state ($\Lambda = 2$) by:

$$S_{2,J''-1} = \frac{(J''-2)(J''+2)}{C_1(J'')^{\frac{1}{2}}}, \tag{4.36}$$

$$S_{2,J''} = \frac{(Y-2)}{C_2(J'')^{\frac{1}{2}}}, \tag{4.37}$$

$$S_{2,J''+1} = \frac{(J''-1)(J''+3)}{C_3(J'')^{\frac{1}{2}}}, \tag{4.38}$$

with:

$$C_1(J'') = 2Y(Y-4)(J''-1)(J''+2) + (2J''+1)(J''-2)J''(J''+2), \tag{4.39}$$

$$C_2(J'') = Y(Y-4) + J''(J''+1), \tag{4.40}$$

$$C_3(J'') = 2Y(Y-4)(J''-2)(J''+3) + (2J''+1)(J''-1)(J''+1)(J''+3). \tag{4.41}$$

B_v, D_v, Y, β_v and γ_v are constants.

In the case of TiO, the selection rules are: $\Delta\Sigma = 0$, $\Delta\Omega = 0, \pm 1$ which is always valid for $\Delta\Sigma = 0$, and $\Delta J = 0, \pm 1$. Selection rules on $\Delta\Lambda$ and ΔS are always valid. Because of the triplet state, the transitions are organized in three categories $\gamma_i = \gamma_1, \gamma_2, \gamma_3$ corresponding to the transitions $A^3\Phi_{\Omega'} \longrightarrow X^3\Delta_{\Omega''}$. Each of them have three different branches P, Q and R.

Table 4.5 shows a recapitulation of these selection rules which are illustrated on figure 4.8.

The expression of the Höln-London factors are given by Kovacs[195] in table 4.4.

Transition	P_1	Q_1	R_1
Factor	$\frac{(J''-2)(J''-1)}{J''}$	$\frac{(J''-1)(J''+2)(2J''+1)}{J''(J''+1)}$	$\frac{(J''+2)(J''+3)}{J''+1}$
Transition	P_2	Q_2	R_2
Factor	$\frac{(J''-3)(J''-2)}{J''}$	$\frac{(J''-2)(J''+3)(2J''+1)}{J''(J''+1)}$	$\frac{(J''+3)(J''+4)}{J''+1}$
Transition	P_3	Q_3	R_3
Factor	$\frac{(J''-4)(J''-3)}{J''}$	$\frac{(J''-3)(J''+4)(2J''+1)}{J''(J''+1)}$	$\frac{(J''+4)(J''+5)}{J''+1}$

Table 4.4: Höln-London factors for TiO $A^3\Phi_{\Omega'} \longrightarrow X^3\Delta_{\Omega''}$ system.

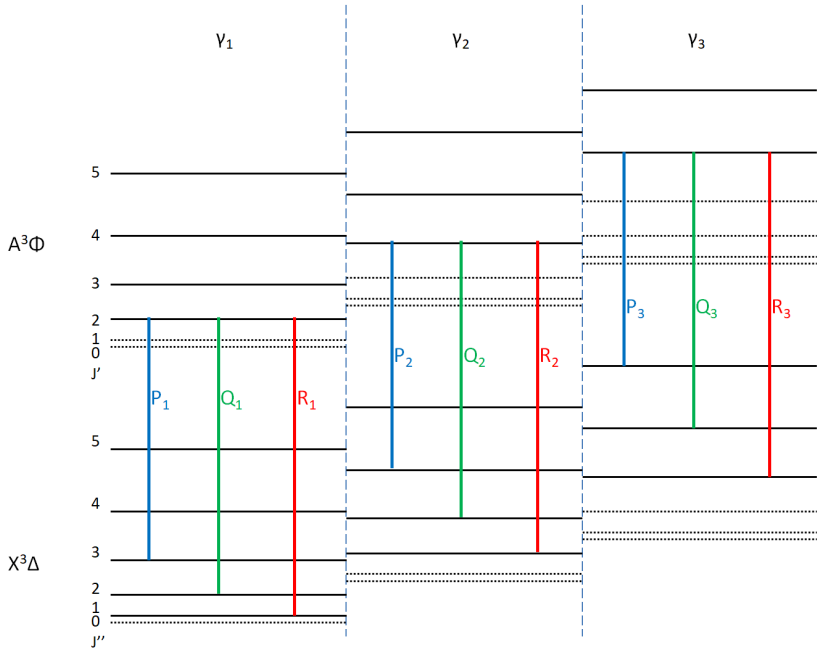

Figure 4.8: Illustration from L. Jacob's report of enabled transitions in TiO molecule for the first vibrational levels of the $A^3\Phi_{\Omega'} \longrightarrow X^3\Delta_{\Omega''}$ system. Energy scales are not respected. Dashed levels are for J' and J'' not defined

Bande	γ_1		γ_2		γ_3	
State	$A^3\Phi$	$X^3\Delta$	$A^3\Phi$	$X^3\Delta$	$A^3\Phi$	$X^3\Delta$
Σ	-1	-1	0	0	1	1
Ω	2	1	3	2	4	3
J	$2,3,4...$	$1,2,3...$	$3,4,5...$	$2,3,4...$	$4,5,6...$	$3,4,5...$

Table 4.5: Sumup of the different quantum numbers in TiO molecule transitions allowed by the selection rules.

In short: *Using this theory, one can calculate the position of the different enabled transitions observed in AlO and TiO molecules and calculate their intensities from tabulated values and two parameter T_{rot} and T_{vib}. Each of these transitions are convoluted by a Gaussian function representing the broadening mostly due to the spectroscopy instruments and summed. The shape of these spectra depend on the rotational and vibrational temperatures such that one can fit them on experimental data in order to determine these temperatures.*

Numerical calculation

In order to calculate each spectrum, David Amans developed a program in C++ able to calculate for AlO and TiO molecules, given their molecular parameters (see annex B), all the parameters for the possible transitions (states energy, partition function, allowed transitions and probability of transition).

This work was completed in 2020 by the intern Louhane Jacob who worked with us in order to clarify all the theoretical background about AlO and TiO transitions. She also stabilized the code and used it on preliminary results I measured with my experimental set-up, showing that we were able to reproduce the previous measurements and go further with this project. Despite the Covid crisis and the lockdown striking during her internship, Louhane did a wonderful job. I want to thank her for her work as it was a great help for this part of my PhD. The obtained spectra have been cross-checked in collaboration with Patrick Crozet and Amanda Ross using PGOPHER, a program for rotational, vibrational and electronic spectra, developed by Dr Colin Western from the University of Bristol.

From the value extracted from this code, I was able to develop a fitting algorithm for experimental spectra. Considering the previous expression, the intensity of a transition is:

$$A^{n'',v''}_{n',v'} \cdot \frac{S^{J'}_{J''}}{2J'+1} \cdot N_{n'} \cdot \frac{1}{2} \cdot (2J'+1) \cdot \frac{exp\left(-\frac{hc \cdot F_{v'}(J')}{k_B \cdot T_{rot}} \right)}{Q_{rot_{n',v'}}(Trot)} \cdot \frac{exp\left(-\frac{hc \cdot G_{n'}(v')}{k_B \cdot T_{vib}} \right)}{Q_{vib_{n'}}(Tvib)} \quad (4.42)$$

with $A^{n'',v''}_{n',v'}$ the Einstein coefficient, $S^{J'}_{J''}$ the Höln-London coefficient, $N_{n'}$ the total population of the electronic state and Q the partitions functions. Here $(2J'+1)$ simplifies. Furthermore, considering only transition from one electronic state $N_{n'}$ and Q_{vib} are constant. Q_{rot} changes only if one is looking at transitions from several vibrational levels which is not the case for TiO molecules between 705 and 712 nm. For AlO, various vibration transitions are observed and Q_{rot} has to be considered. A good approximation for it is[203]:

$$Q_{rot} \simeq \frac{k_B T_{rot}}{B_{v'}} \quad (4.43)$$

In the end, the intensity of each transition is proportional to the following simplified

expression:

$$A^{n'',v''}_{n',v'} \cdot S^{J'}_{J''} \cdot \frac{B_{v'}}{k_B T_{rot}} \cdot exp\left(- \frac{hc \cdot F_{v'}(J')}{k_B \cdot T_{rot}} \right) \cdot exp\left(- \frac{hc \cdot G_{n'}(v')}{k_B \cdot T_{vib}} \right) \qquad (4.44)$$

From the C++ code, I obtain the coefficients $A^{n'',v''}_{n',v'}$, $S^{J'}_{J''}$, $F_{v'}(J')$, $G_{n'}(v')$ and $B_{v'}$ for each of the transitions corresponding to the wavelength range of the measured spectra. This enables me to calculate the amplitude of each transition.

Each of these transitions are convoluted by a Gaussian function of amplitude 1 and width σ and summed. Here one could question the use of a Gaussian and not a Lorentz or Voigt function. The closest shape to reality would surely be a Voigt function. However, it really does not change much of the shape of the spectrum as it is dominated by the positions of the transitions. More on the fitting process of the spectra is given in the section 4.4.1.

4.2 Experimental Set-up

The main aim of my PhD was to develop the LIBS-LIF[‡] experimental set-up presented in the figure 4.9. The experiment was designed by Vincent Motto-Ros, Sylvain Hermelin, Christophe Dujardin, Gilles Ledoux and David Amans in the framework of the CPER optolyse managed by C. Dujardin. It had to be as versatile as possible and able to perform routine LIBS measurements with spatially-resolved atomic and molecular spectroscopy. In addition, a tunable laser can be used either to re-excite the plasma and perform LIF or to excite directly a sample for luminescence scanning microscopy. Two different light collectors are implemented. One developed for LIBS and able to maximize the collection of the light. One able to image the plasma with spatial resolution. These light collections can be coupled with three different spectrometers. The first one is for luminescence and has low temporal resolution. The second one has very high spectral resolution but cannot be used for space resolved spectroscopy. The last one can be used for time and space resolved spectroscopy. It is the one I optimized for molecular spectroscopy and used the most. In this section, only the elements used for time and space resolved spectroscopy are explained. LIF spectroscopy is described in the chapter 5.

When I arrived in the Laboratory, I discovered a room full of boxes and material ready to be assembled. I have to say I first felt a bit lost in the middle of numerous pieces to assemble. I remember Sylvain casually telling me: "here you go, you have lasers, spectrometers, the instructions for the user and all the components you need. You can start by copying the LIBS set-up I built on the other optical table and then modify it. Just be careful with the material, this for instance worth two units". Two units? "It's about 2 thousand euros" he answered with a malicious smile. "Oh and always remember to put a washer before the screw when fixing clamping forks". Alone in the room, I had no idea where to begin, and so I started sorting up all the different pieces, opening boxes and analyzing each piece. It was a sort of never ending Christmas morning, with lots of expensive Lego boxes. Fortunately, I love Lego, and some expertise in this field was very welcome. I enjoyed very much building this experimental set-up. During one year, in parallel to my work on the micro-canonical model, I tried to find the optimal mechanical and optical solution with the advice of Sylvain Hermelin and Vincent Motto-Ros. In the end, Sylvain was right: always put a washer before the screw!

[‡]Laser-Induced Breakdown Spectroscopy coupled with Laser-Induced Fluorescence

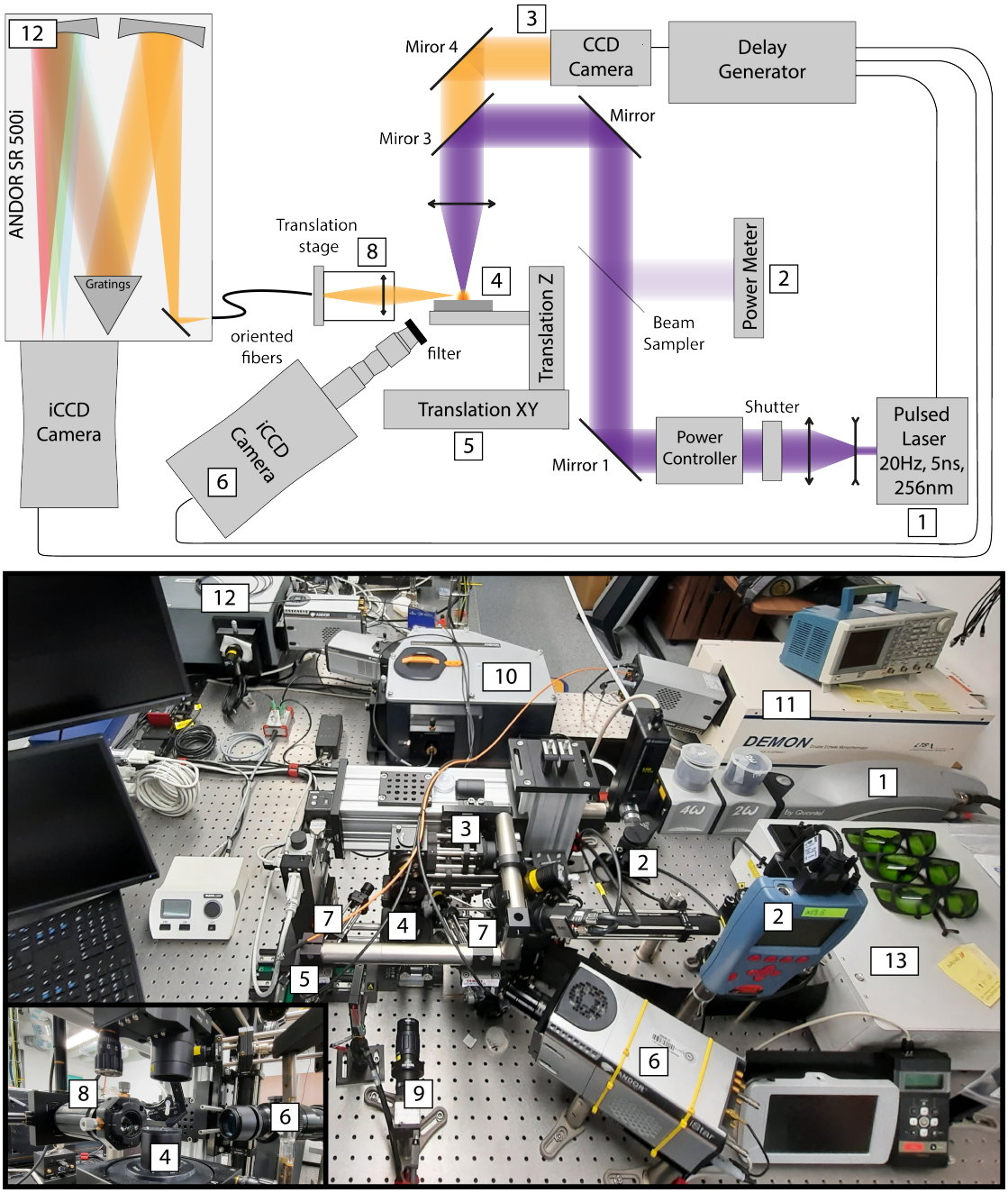

Figure 4.9: Experimental LIBS setup schematic and illustration picture. [1] Q-Smart 450, [2] powermeter, [3] CCD camera, [4] ablation spot, [5] translation stage, [6] iCCD camera for plasma imaging, [7] oblique light collection, [8] spatially resolved collection light, [9] alignment CCD, [10] Andor spectrometer for luminescence, [11] DEMON spectrometer, [12] Andor SR 500i spectrometer, [13] OPO for LIF.

4.2.1 Creation of the plasma: the ablation

The ablation pulse is generated by a Q-Smart 450 laser from Quantel ([1] in figure 4.9). It is a 20 Hz pulsed YAG:Nd laser (1064 nm). Laser pulse is about 5 ns long for a power of 400 mJ in the infrared. The infrared beam was passed through two frequency-doubling stages to generate the 4th harmonic at 266 nm with a maximum power of 50 mJ. UV pulses are less energetic because non-linear mixing processes have a low efficiency and are very sensitive to alignment of the crystals used. The Q-Smart laser has integrated software that is able to optimize the frequency mixing process by changing the temperature of the different stages. Interestingly, the thermal deformation of the crystal is enough to tune properly the angle and optimize the second harmonic generation. The main advantage of UV ablation is its versatility. Each photon has more energy and is more effective to create a plasma, especially with large gap materials such as oxides like alumina. Simply put, some materials are transparent to the IR frequency and would require large multi-photon absorption in IR range when just a few photons are enough with UV light. UV pulses are less energetic but more effective to create a plasma. Here, this choice can be questioned depending on the target. The harmonic generation stages on the laser could be removed, but it would require the adaptation of the optics on the beam line.

The laser timing (pumping and trigger time) is controlled using a digital delay/pulse generator DG645 from Stanford Research Systems. A precise control of the laser firing time is necessary to synchronize the plasma formation with the spectrum acquisition as I will describe later.

This laser line is first expanded by a telescope to avoid damages to the optics (purple beam on the scheme 4.9) and a shutter is used to block the laser when not used.

In short: *During my PhD, I developed an experimental setup in order to perform time and space resolved spectroscopy of laser-generated plasma. The plasma is generated by focusing on a target a laser pulse of 5 ns at 266 nm with a power up to 30 mJ. In order to measure the temperature in the plasma, I had to measure spectra of AlO and TiO molecules in the plasma with both temporal and spatial resolution. The spatial resolution is insured by a series of 19 optical fibers collecting the light at different height in the plasma with a spatial resolution of about 150 μm. The light is injected inside a spectrometer in order to obtain the spectrum for each of the fiber. The temporal resolution is insured by and amplified camera (iCCD). This camera records the signal for a very short time only. By tuning the delay between the ablation pulse the signal recording, I am able to probe the plasma at different time with a temporal resolution of 2 μs.*

A PowerXP Motorized attenuator from Altechna is placed on the beam line. It uses the polarization of the beam in order to reject a controlled part of the beam light and control the ablation power from few percent to full power. A set of two dichroic mirrors (not represented on the scheme) are used to adjust the beam path in the two spatial dimension and two angular dimension. They also filter the 266 nm component from the other harmonics. A beam sampler deviates about 10% of the beam onto a Nova II power meter mounted with a high energy pyroelectric sensor in order to check and measure the ablation laser power ([2] in figure 4.9). The beam is then reflected by three dichroic mirrors and focused vertically on the target by a simple UV lens ($f = 50$ mm)[§]. Because the dichroic mirrors are transparent for other wavelengths, a camera can be placed on the top in order to image the target surface in a confocal position ([3] in figure 4.9). This is particularly useful for mapping measurements.

The sample is placed at the focal point of the laser beam ([4] in figure 4.9). The height of the target can be adjusted using the motorized translation stage ([5] in figure 4.9) with a precision of about 1 μm or adjusted by changing the position of the lens along the z-axis. The consequence of adjusting the lens is to change the focal point position without modifying the position of the target with respect to the collection light. This is particularly useful for the study of focal point position on the plasma. Quite surprisingly, the best way to adjust the target at the focal point is using ablation sound. When the laser power is set to the minimum, the ablation of the target would occur only when the surface is right at the focal point. For each measurement, the position of the target is adjusted using this procedure. Sound variation is also a good indication of horizontal position issues and other modifications of the ablation.

During measurement, the target is moved in the horizontal plane by the translation stage ([5] in figure 4.9) with a precision of about 10 μm. This translation is used for surface mapping. Yet it is also needed for my measurement. If the ablation always occurs at the same spot, it forms a hole in the target and the ablation dynamics changes drastically. Thus, all my measurements were achieved with the target moving at about 1 mm/s. The horizontal position of the target can be adjusted with a tilt controlled deck. The adjustment is very important as the target is moving. If it is not perfectly horizontal, the vertical position of the surface would change during the acquisition and change the plasma formation dramatically. Note that precise translation is also used to map a surface. This is particularly useful for micro-LIBS measurement in order to map the composition of a sample.

[§]For micro-LIBS, a microscope objective can be used instead for better spatial resolution.

4.2.2 Imaging of the plasma

The shape evolution of the plasma can be imaged using the same iCCD camera and objective as presented in chapter 3 ([6] in figure 4.9). It has a spatial resolution of about 44 μm and a temporal resolution up to 5 ns. The time evolution of the plasma is too short to film. The dynamics is reconstructed from different pulses imaging just like for the shock-front (see chapter 3). The delay time, and gate width are set on the camera itself using a reference *trigger signal* from the digital delay/pulse generator DG645. In contrary to shock-front imaging, the image of the plasma is averaged on 10 to 20 laser shots. First, it increases the signal-to-noise ratio. Second, the plasma plume is not exactly the same for each pulse. It enables to have average information to compare with spectral measurements (also averaged). An example of the obtained images can be seen on figure 4.13 (a). Interferometric filters centered on emission lines are placed in front of the camera. It enables to select the emission of given species. For each measurement, the size of the image is systematically measured by imaging a ruler in the plane of the ablation.

4.2.3 Collection of the light

Two different light collection systems are implemented on the setup. The first one consists of an oblique arm composed of a 1/2 inch achromatic lens with a focal length of 25 mm imaging the plasma on bundle of optical fibers in a $2f/2f$ configuration ([7] in figure 4.9). This injection is very easy to adjust. The optical fibers bundle is composed of 16 multi-mode fibers in order to couple more light inside the fiber. The core diameter of each fiber is 100 μm. The downside of this light injection is that one cannot control precisely where the light collected comes from. This collection system is used for conventional LIBS measurement, luminescence mapping or measurement on the DEMON spectrometer ([11] in figure 4.9, figure 4.11) which is a high resolution spectrometer that requires strong signal and cannot be used for spatially resolved spectroscopy as we will discuss later.

The second light injection I developed is space resolved. It is composed of two one inch UV-Vis aspheric lens with a focal length of 50 mm and a N.A.=0.25 mounted on an adjustable length tube with a bundle of 19 aligned fibers ([8] in figure 4.9) as represented in figure 4.10 (a-b). The fibers are spaced by 125 μm and their core diameter is 100 μm. The numerical aperture of the lens is chosen to match the N.A.=0.22 of the fibers in order to have a good injection. Each fiber collects the light from a different height in the plasma. The adjustable length tube added with a horizontal translation stage enable to adjust the focal and the optical zoom of the collection. The collection is mounted on a vertical automated translation stage able to precisely translate the collection vertically and laterally

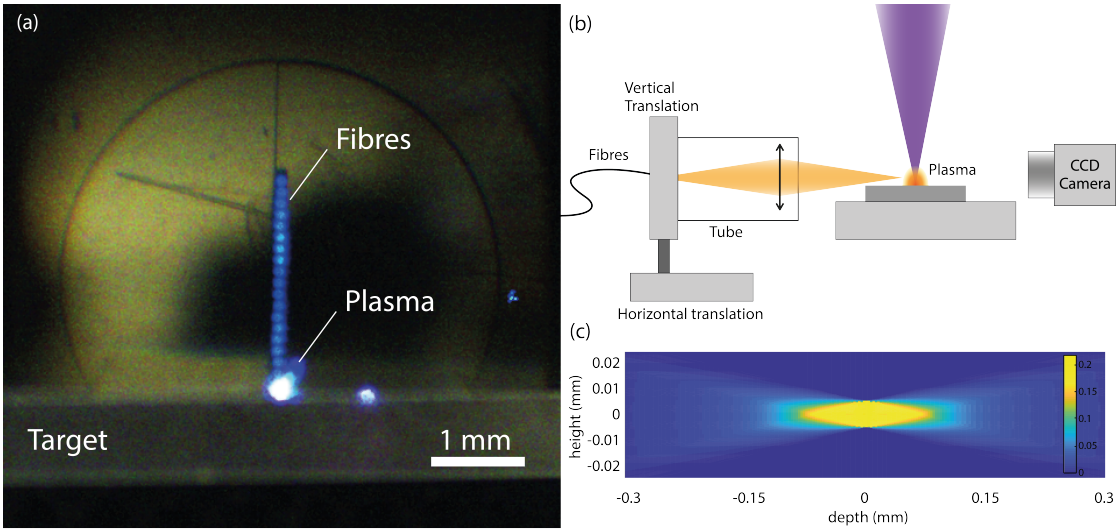

Figure 4.10: (a) Picture of the fibers image in the plane of the plasma using the alignment camera [9] on figure 4.9. Here, the plasma is 0.3 mm diameter as the laser pulse energy is set to the minimum for precise adjustment of the light collection. At full power, the plasma is several mm large. (b) Scheme of the collection of light used for tomography of the plasma [8] on figure 4.9 (c) map of the solid angle corresponding of the light entering a fiber of core radius R=100 μm with a numerical aperture AN=0.22 depending on the position in the plasma.

with a precision of about 1 μm. The vertical translation is used to adjust the first fiber at the surface of the target. The lateral translation is used to center the fibers on the ablation spot (see figure 4.10 (a) and move it precisely to map the plasma.

In order to precisely tune the focal length of the collection and its position, a CCD camera is installed on the axis of the light collection and plasma as represented in figure 4.10 (b) ([9] in figure 4.9). The objective of the camera is chosen to have a short focal length and adjusted such that only the plasma appears sharp as in the image on figure 4.10 (a). When this is done, it is easy to tune the zoom and the position of the fibers. Indeed, when they appear sharp on the camera, it means that their image is made in the plane of the plasma. Furthermore, by imaging a ruler on the camera, one can very easily obtain the spatial resolution of the system. In the case of these measurements, a good compromise between the spatial resolution of a fiber and the amount of light collected was a configuration close to a 2f/2f meaning that fibers image spots are separated by 125 μm.

On the image, fibers appear blue because some light is injected on the other end of the spectrometer. Changing the grating angle shifts the wavelength. This can be used in order to finely tune the collection and in particular the injection

lenses. These lenses are aspherical. They have little geometrical aberration but their focal lengths vary with the wavelength. For better resolution, one should take care of optimizing the system for the wavelength range of interests. Here, the blue corresponds to the AlO emission system (around 500 nm).

When considering the spatial resolution of the collection, one needs to be careful. In order to really understand spatial resolution, it is important to understand the origin of the light that enters the fiber. A beam of light enters a fiber if it intersects its core section with an angle smaller that the numerical aperture of the fiber. Figure 4.10 (c) represents for each point of space, the solid angle of light entering the fiber. The depth origin corresponds to the image plane of the fiber, that is to say the focal point of the ablation laser. As you can see, around 0 most of the light entering the fiber arrives from a cylinder of diameter 100 μm (the size one core). Outside this area, none of the light can enter the fiber. However, the more we move apart from the focal point, the larger is the area where light can enter the fiber. Fortunately, the solid angle in each point also decreases drastically. In the end, one can calculate that the contribution of the light in each plane is the same[¶]. In the end, the light entering the fiber comes from a volume of two sorts of cones intersecting the plasma. For a plasma of a few mm, the base of each cone is about 250 μm.

The spatial resolution is thus quite complicated to define. One can say that most of the light comes from a volume of about 150 μm side and 300 μm depth, added with a diffuse component coming from the whole depth of the plasma.

4.2.4 Spectrometers

This set-up was designed with three different spectrometers that can be used for different purposes.

The first one is a Kymera spectrometer from Andor ([10] in figure 4.9) which is very versatile, has three different gratings and a resolution up to about 0.2 nm. However, the acquisition of the spectrum is done by a EMCCD camera which does not have the electronic gating of the iCCD camera. It cannot be used for time resolved spectroscopy. Furthermore, the resolution is not sufficient to record rovibrational spectra from diatomic molecules. This spectrometer is used for luminescence measurements.

[¶]This result can be calculated considering a fiber of radius ω_0 and a plane normal to the fiber's axis at a distance x. For each point of this plane, the solid angle intersecting the fiber is $\Delta\Omega \simeq \pi\omega_0^2/x^2$. The intersection between the plane and the N.A. of the fiber is $S(x) = \pi(NAx)^2$. In the end, the product of both is constant: $\Delta\Omega S(x) = \pi^2\omega_0^2 NA^2$.

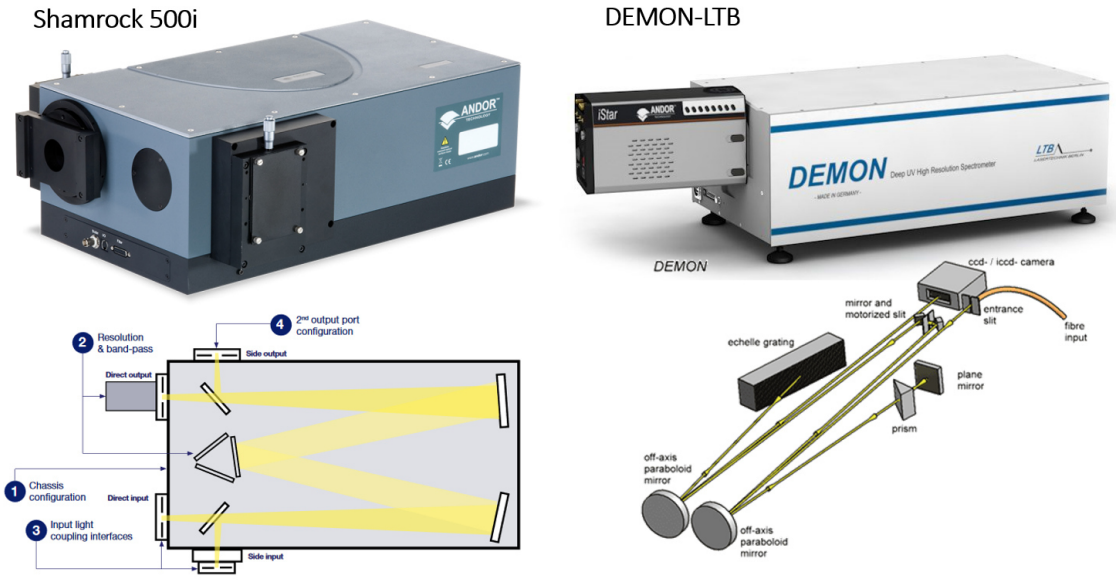

Figure 4.11: (left) Andor Shamrock 500i spectrometer. (right) DEMON-LTB spectrometer. Images are provided by the manufacturers.

The second spectrometer, is the DEMON spectrometer from LTB ([11] in figure 4.9 and right panel of figure 4.11). It is mounted with an iCMOS camera having the same gating ability as the iCCD camera and can be used for time resolved measurements. Furthermore, this spectrometer has a significantly higher resolution of 1 pm enabling rovibrational study of molecules or even isotopic measurements on atoms. On figure 4.12 is an example of the AlO spectrum in red and the corresponding Fortrat diagram in black. As you can see, many of the rotational transitions are actually resolved with such a spectrometer. In order to achieve such performance, it uses a prism to diffract the light in one direction and a grating to further diffract it in the other direction. The main drawback of such a spectrometer is that it has a 2.5 nm wavelength range. For larger spectra, we have to scan the wavelength adding some uncertainties on the peaks position and noise level. It also increases a lot the measurement's time. Furthermore, space resolved light collection cannot be used with this spectrometer because of the double stage diffraction. The entrance of the spectrometer is not a vertical slit but a pinhole. Finally, it requires a large intensity signal and can be used only on large plasma using the first light collection. Here, this spectrometer was only used to check that the calculated transitions and Fortrat diagram fit the transitions observed (see figure 4.12).

The third spectrometer is the one I used the most and optimized a lot. It is a

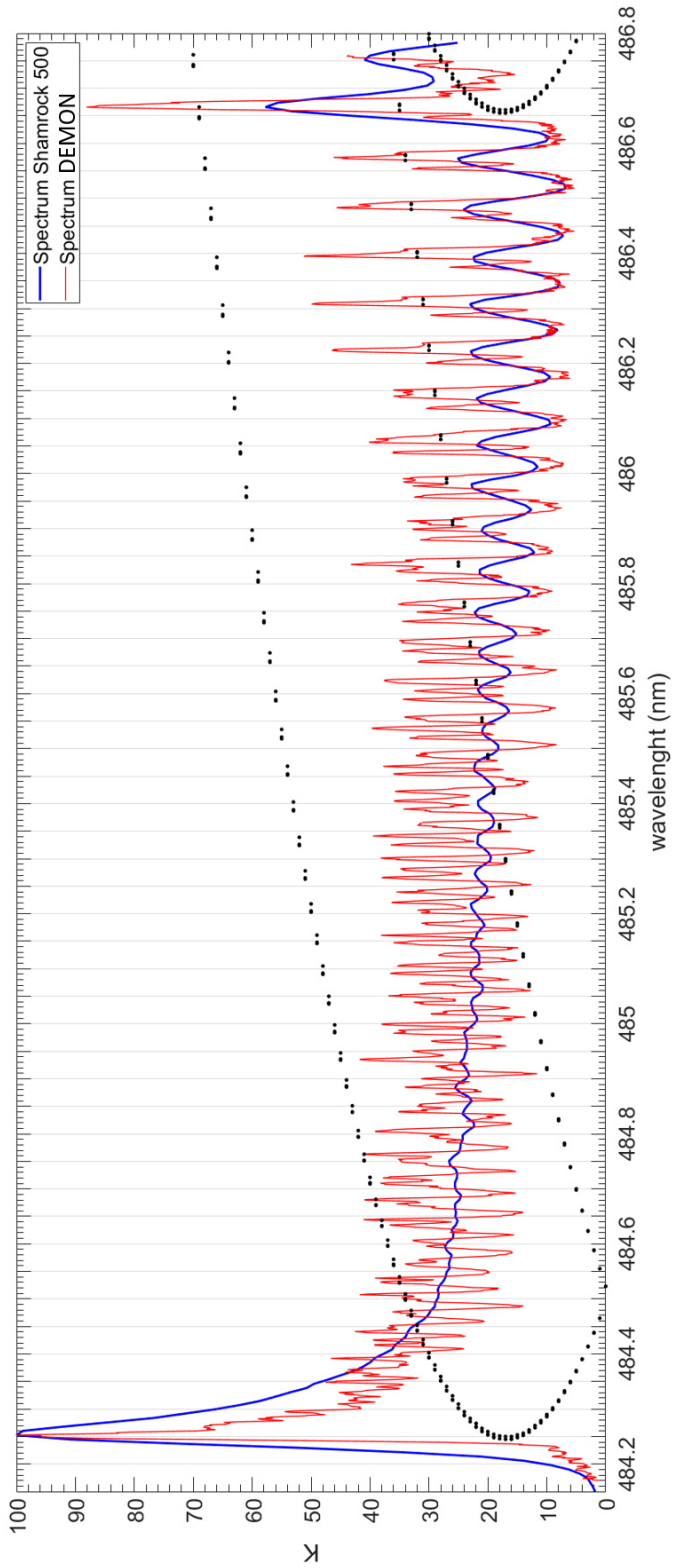

Figure 4.12: Typical AlO spectrum for the transitions (0,0) obtained with the DEMON spectrometer in red, the Shamrock 500 spectrometer in blue and the corresponding Fortrat diagram in black.

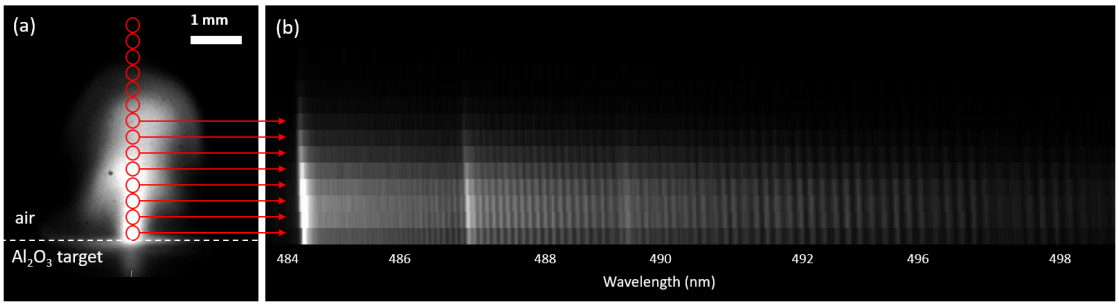

Figure 4.13: (a) image of the plasma acquired with the iCCD camera for a delay of 2 μs and a gating of 2 μs averaged on 10 pulse shots. Position of the fibers are represented in red (for this illustration, each fiber imaged 0.3 mm). (b) corresponding image of AlO emission for each fiber after dispersion in the spectrometer.

Shamrock 500i from Andor ([12] in figure 4.9 and left panel of figure 4.11). This is a conventional spectrometer based on Czerny-Turner optical design. It is composed of two entrance slits that can be used with the two different light collections. The light is collimated by a mirror on a grating and the diffracted light is focused back on a DH340T-25F-03 iCCD camera from ANDOR. The iCCD is composed of a 2048×512 px CCD sensor for which each pixel is 13.5 μm side.

Contrary to the DEMON spectrometer, the diffraction is horizontal such that the light of each fiber is diffracted on the iCCD at a different height as shown in figure 4.13 (b). The signal is vertically integrated on the pixels corresponding to each fiber leading to 19 tracks as shown in the panel (c). Using this spatially resolved light collection, the spectroscopy of the plasma is achieved for each fiber simultaneously.

The spectrometer has three different gratings whose specifications are reported in table 4.2.4. The grating 3 with 2400 l/mm (blaze 240) is used for molecular spectroscopy in order to obtain high spectral resolution. The efficiency of the grating 3 given by the manufacturer is represented in figure 4.14. It has a theoretical resolution of 0.03 nm and a measurement range of about 20 nm. In theory this should be enough for the rovibrational spectroscopy. However, the resolution actually depends a lot on light injection, the slit opening, and the camera used. In my case, the resolution was mostly limited by the injection and I had to work a lot on it to achieve a high enough resolution for the rovibrational spectroscopy.

The injection is composed of two lenses similar to the collection but with different focal lengths. The first one is an aspheric lens matching the N.A. of the fibers in order to collect most of the light coming from it and collimate it ($f = 50$ mm and N.A.=0.25). The second lens ($f = 125$ mm) is placed just after and makes the image on the entrance slit of the spectrometer with a N.A.=0.1. In theory, the

spectrometer is designed for a N.A. close to 0.22. Yet, the definition was degraded due to geometric aberration of the mirrors. This aberration mostly arises from the side of the mirrors. A classical way to deal with it is to use masks in order to block the light on the mirrors' side. In order not to lose signal, I preferred to use a smaller N.A. illuminating only the mirrors center.

Consequently, the image of the fibers in the entrance slit is 2.5 times larger. This magnification ratio is calculated for the height of the 19 fibers to match the height of the iCCD chipset. This maximizes the area of detection and decreases the numerical noise by binning the pixels over the image of each fiber. The main drawback is that when the slit is closed in order to have better resolution, more light is cut. Yet this would be the same with the mask. Here, the slit opening is an easy way to tune the signal intensity versus definition.

Finally, I had to set precisely the entrance slit and tilt the grating in order to obtain a sharp image of the fibers on the iCDD and a perfectly horizontal diffraction. Having perfectly horizontal diffraction enables to bin vertically the signal of each fiber over 12 px as shown in figure 4.13. Binning reduces the signal-to-noise ratio.

The maximal resolution used is FWHM=0.06 nm for a slit opening of 50 μm. It could be increased further by closing the slit to about the resolution of the grating for a slit of 10 μm (0.03 nm, see table 4.2.4). However, in the case of space molecular spectroscopy, the signal was not strong enough. Because of some remaining spatial aberrations, the image of the entrance slit is not perfectly vertical. This leads to some shift between the different tracks. Such shift along the vertical axis (about 0.05 nm) would decrease the spectral resolution for full vertical binning. Here, it is less of an issue as the vertical binning is done for each of the fiber, but this implies that each track is calibrated individually.

On figure 4.12 you can see in blue the typical spectrum obtained with this spectrometer compared to the one obtained with the DEMON spectrometer. The resolution is much lower, and we cannot differentiate all the transitions. In particular, the peaks of the different branches are no more differentiated. Differentiated both branches is interesting for the measurement of T_{rot} as they correspond to different values of K and thus different energy levels. Yet, we will see that it is not mandatory to determine the rotational temperature. The global shape of the spectrum is enough.

	Lines/mm	Blaze	Nominal dispersion	Resolution	Bandpass
Units	mm^{-1}	nm	nm/mm	nm	nm
Grating 1	600	300	3.18	0.13	88
Grating 2	1200	300	1.54	0.06	42
Grating 3	2400	300	0.69	0.03	19

Table 4.6: Characteristics of the different gratings given by the manufacturer. Resolution is given for a 10 μm slit and 13.5 μm pixel CCD.

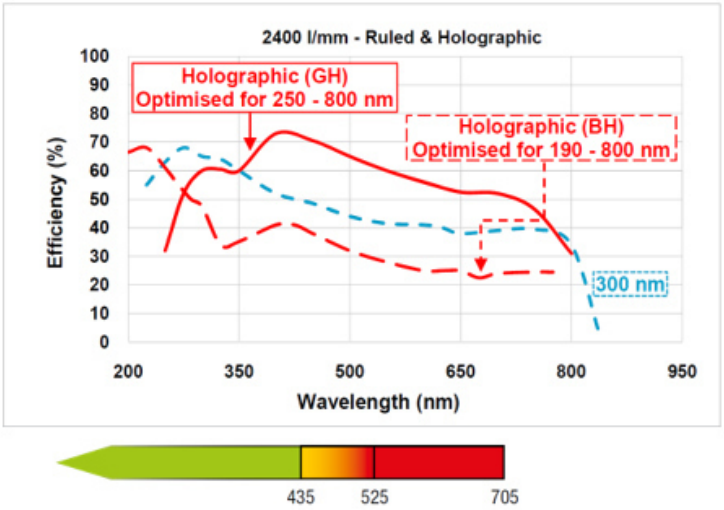

Figure 4.14: Efficiency plot of the grating 3 for a 45^o polarization given by the manufacturer. Blue curve corresponds to the grating 3 in table 4.2.4. Under the plot, the color scale represents the recommended spectral range for gratings : aberration-free region in green, possible impact on system resolution in orange and likely impact on system resolution in red.

4.3 Imaging species in aluminum oxygen plasma

Previous work on the imaging of molecules in aluminum oxygen plasma have been reported by Julien Lam and David Amans in 2014[47] on an alumina target and more recently by Ran et al. in 2017[194] on pure aluminum in air. Using filters centered on 488 nm, 780 nm and 390 nm in front of an iCCD camera, the authors were able to image respectively AlO molecules, oxygen atoms and aluminum atoms. This technique enabled them to easily and quickly determine the position of the different species using narrowband filters. Furthermore, the intensity of the emission provides good information on the density of the species even if this should not be considered a quantitative measurement as it depends on other parameters

and self-absorption.

In this section, similar measurements are used to explore the influence of the laser power and ablation's conditions on the formation of the species in the plasma. In order to investigate the origin of the oxygen in the formation of AlO, ablation from aluminum and aluminum oxide targets in air or under an argon flow are compared. Evolution of the species is recorded by an iCCD camera. Each image is averaged over 20 shots with a gate width of 2 μs. Delay between the ablation pulse and the acquisition is changed from 0 to 60 μs by steps of 2 μs. The observed species is selected using a narrow-interferometric filter. Aluminum atom Al (I) emission lines corresponding to the transition from $^2S_{1/2}$ to $^2P^0_{3/2}$ and $^2P^0_{1/2}$ (394.40 and 396.15 nm) are selected by a filter at 390 ± 5 nm. The emission of AlO molecule is selected by filters at 514±5 nm (centered on $X^2\Sigma^+$-$B^2\Sigma^+$, $\Delta v = -1$) or equivalently at 490 ± 5 nm (centered on $X^2\Sigma^+$-$B^2\Sigma^+$, $\Delta v = 0$).

Unfortunately, the emission of O_2 molecules is mostly in the IR region. Owing to this, as well as its large concentration in the air, it cannot be measured with this experimental set-up.

Oxygen atoms O (I) could be observed using a 780 ± 5 nm filter corresponding to the transition from $^5P_{1,2,3}$ to $^5S^0$. However, oxygen is difficult to excite (10.7 eV) and emission is only observed at short delay time (<5 μs) and in the center of the plasma. In these conditions, Bremsstrahlung emission cannot be neglected and one needs to correct the images using spectroscopic measurements. Such corrected measurements have been achieved by Ran et al.[194] and interested readers are invited to take a look at their study and discussion. They used spectral measurement in order to obtain the optical noise on the axis of the plasma and the cylindrical symmetry of the plasma to calculate the correction on the whole image.

In the study presented here, no spectroscopic correction is applied in order to remove Bremsstrahlung emission. For short delay, the intensity recorded with the filter is partially due to the background emission. For instance, when looking at the AlO spectrum with a delay of 2 μs, half of the intensity is due to background emission. After 5 μs, Bremsstrahlung emission becomes negligible. In that case, the intensity integrated on the image is a good indicator of the total emission of the species in the plasma[‖].

Equivalent measurement on TiO plasma is not possible. As we will see, Ti emission lines are present in the spectral range of TiO emission and differentiating both with filters is impossible.

[‖]To be fully quantitative, a correction similar to the calculation of the light entering the optic fiber should be applied to take into account the depth of the plasma.

The origin of AlO($B^2\Sigma^+$) molecules

In order to properly interpret the emission of AlO molecules, one needs to understand where it comes from. The emission recorded here corresponds to the $B^2\Sigma^+$ state of the AlO molecules. This state has an excitation energy around 1.78 eV (about 20 000 K). It can be populated because of the formation of excited $AlO(B^2\Sigma^+)$ molecules or by the excitation of molecules from the ground state $AlO(X^2\Sigma^+)$.

Ground state of $AlO(X^2\Sigma^+)$ molecules can be formed from single collision $Al+O_2 \rightarrow AlO(X^2\Sigma^+)+O$. However, this reaction is almost isoenergetic[204]. Thus, the formation of the excited state $AlO(B^2\Sigma^+)$ through single collision is impossible[194,205,206]. The excess energy required (1.78 eV) is too large**. Kasatani et al. proposed in 1990 the following three body reaction: $Al+O+O_2 \rightarrow AlO(B^2\Sigma^+)+O_2$ motivated by a quadratic dependence of the AlO emission with the O_2 pressure. This reaction path is the one introduced in the chapter 2 with the formation of a reaction intermediate that has to be cooled down by a third body within an oscillation time:

$$Al + O \underset{\text{desorption}}{\overset{\text{sticking}}{\rightleftharpoons}} AlO^* \xrightarrow{\text{cooling}} AlO(B^2\Sigma^+)$$

In the experiment of Kasatani et al., the third body has to be O_2 molecules as it is the only gas. In the case presented here, it can be any molecule of the air.

Exciting AlO molecules in the $B^2\Sigma^+$ state is more difficult than exciting atoms. In contrary to atoms, the gaps between the electronic levels of the molecule are large: 1.78 eV (about 20 000 K) between $X^2\Sigma^+$ and $B^2\Sigma^+$ and 1.32 eV (about 15 000 K) between $A^2\Pi_i$ and $B^2\Sigma^+$. Thermal excitation due to collision with the electron gas is unlikely as the temperature of the plasma, in particular in the region of AlO formation, is too low. Only few excitation paths are possible. One could consider excitation through resonant absorption from the background light (see chapter 5). However, Bremsstrahlung emission stops after a few μs. Atomic emission remains strong during a longer time (10-15 μs) but is unlikely to be resonant with AlO absorption. An excitation path to consider is collision with meta-stable excited atoms or molecules formed during ablation which can remain excited for long time. Some example relevant for ablation in air and in argon flow are given in the table 4.7. One can expect these species to be localized in the periphery of the plasma.

In similar work, the $AlO(B^2\Sigma^+)$ state is usually attributed to its formation and excitation from the ground state is usually not mentioned[206,194]. In that case,

**This excess of energy corresponds to the difference in energy between both levels. It is too large to be compensated by the kinetic energy of the reactants.

Element	State	Energy (eV)	Radiative life-time
Ar	$^3P_2$	11.54	56 s
Ar	$^3P_0$	11.72	45 s
O_2	$a^1\Delta_g$	0.978	∼55 min
O_2	$b^1\Sigma_g^+$	1.627	∼10 s
O	^1D	1.967	100 s
O	^1S	4.189	1 s
N_2	$A^3\Sigma_u^+$	6.17	10 ms
N_2	$a^1\Pi_g$	8.55	100 μs
N	$^2D^o$	2.38	10 h
N	$^2P^o$	3.57	10 s

Table 4.7: Energy and radiative life-time of metastable sates of atoms and molecules compiled from Praveen et al.[207]

emission of AlO($B^2\Sigma^+$) provides information on the formation of the molecules and their interaction with the plasma within its radiative life-time.

4.3.1 Influence of the energy of the pulse

The first set of experiments studies the influence of the pulse energy on the ablation of a pure aluminum oxide target in air. The target is single crystal grown by Czochralski (Cz) technique with radio frequency induction heating in an iridium crucible[173,174].

Figure 4.15 (a) represents the time evolution of Al atoms (in red) and AlO molecules (in green) in the plasma from 2 μs to 30 μs for 5 different power from 3.25 mJ to 31 mJ. As you can see, for the larger pulse energies, the first have a mushroom shape. But after 10 μs, one can observe an interesting torus shape as if the plasma falls back on itself. This kind of dynamics is very similar to the implosion of a cavitation bubble. An analogy would suggest that after a first expansion, the plasma implodes. This would be consistent with Taylor's model developed in chapter 3. The typical time for the pressure to fall to atmospheric pressure was 5 μs which is consistent with this observation. A similar shape was observed by Ran et al.[194] after a longer delay of 40 μs. This is again consistent considering they used larger pulse energy (50 mJ).

For lower pulse energy, the plasma follows similar dynamics, with a smaller spatial extension. But below 15 mJ, the plasma seems to have different dynamics with a reversed "T" shape.

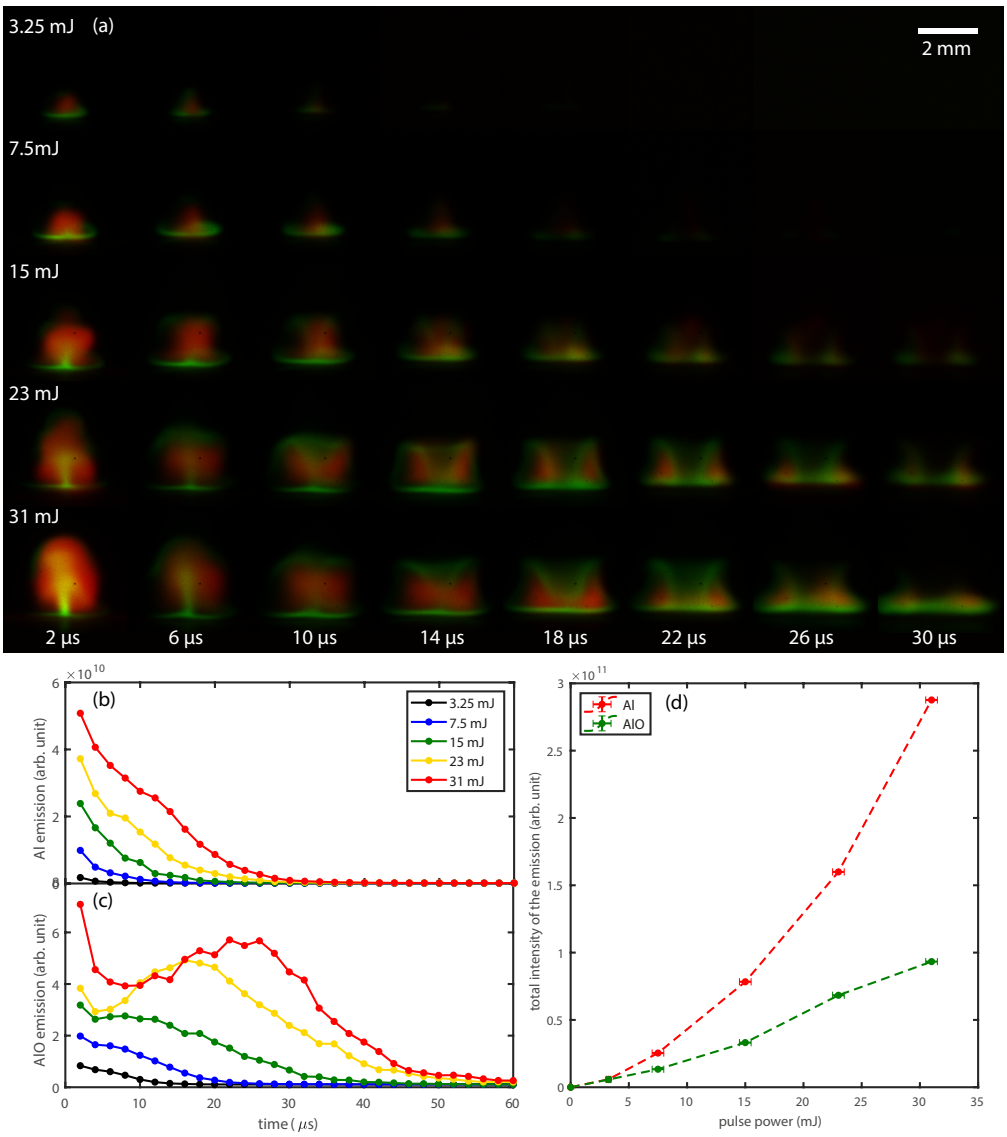

Figure 4.15: (a) dynamics of the plasma observed in false color at different delays after the ablation of an aluminum oxide target in air. Aluminum emission is in red and AlO($B^2\Sigma^+$) emission is in green. (b) Intensity of the Al(I) emission integrated on the whole image. (c) Intensity of the AlO($B^2\Sigma^+$) emission integrated on the whole image. (d) Intensities of the Al and AlO emission integrated on the whole image and time.

For large energies and early time Al atoms form a homogeneous cloud while the AlO molecules are concentrated at the surface of the target and along the

center of the plasma. Later, one can see that the AlO molecules are located on the periphery of the plasma. Again, these observations are consistent with Ran et al.[194].

It is interesting to notice that Al atoms are constantly excited by collisions with the electron gas. Al emission is thus directly correlated with the density of aluminum atoms and free electrons. On the contrary, exciting AlO molecules in the $B^2\Sigma^+$ state is much more difficult (see section 4.3). Emission is due to molecules just formed in the excited state or excited by collision with meta-stable molecules and atoms. The life-time of the excited state of AlO is very short (less than 3 ns, see chapter 5). The intensity of $AlO(B^2\Sigma^+)$ is thus directly related to (i) the formation rate of the molecules or (ii) their excitation rate. In the first case, the reaction producing $AlO(B^2\Sigma^+)$ needs cold quenching gas, explaining the localization of the emission on the periphery of the plasma. In the second case, the meta-stable molecules (N_2^* or O_2^*) excite $AlO(X^2\Sigma^+)$ molecules. $AlO(X^2\Sigma^+)$ molecules can be formed by the reaction of Al atoms with O_2 molecules of the air and are thus likely to appear in the periphery of the plasma. Furthermore, the meta-stable molecules are created by the excitation of the air during ablation and are also likely to be located on the periphery of the plasma. In both case, the location of the emission is consistent and cannot discriminate the formation path of $AlO(B^2\Sigma^+)$.

The intensity of Al emission decreases with time for all the powers (see figure 4.15 (b)). This intensity is directly correlated with the population of atoms in the $^2S_{1/2}$ excited state even if this measurement is not quantitative[††].

The decay of the Al emission seems to have two different trends particularly visible for the larger pulse energy (red curve): a first before 15 μs and a second one after. The double decay of the emission could be due to (i) a decrease of the excitation rate due to the cooling of the plasma and the decrease of the electron density and (ii) reaction of Al atoms forming AlO molecules. Indeed, the second decay is correlated with an increase of the AlO signal at 10 μs for the 23 mJ pulse and 15 μs for the 31 mJ pulse (see figure 4.15 (c)). This increase of AlO emission also corresponds to the time when the average temperature in the plasma is low enough for the AlO molecules to become predominant according to the model developed in chapter 3.

The total amount of Al and AlO emission observed in terms of the laser power is represented on the figure 4.15 (d). Note that the integration of the signal is done up to 60 μs and the remaining emission after the 60 μs does not affect the measurement. Both quantities increase with the laser power because the total amount

[††]The imaging is not corrected from self-absorption nor geometric effects of the acquisition.

of ablated atoms increases with the laser power. In the case of AlO emission being mostly related to its formation rate, the integer of the emission with time is likely to be related to the total amount of molecules produced. In contrary, Al emission is also impacted by the temperature of the plasma and the electron's density as the atoms are easily re-excited.

4.3.2 Influence of the target and gas composition

A second set of experiments addresses the influence of the target composition and the environment. Changing the environment of nucleation can provide information on the formation of the molecules. In particular, it would be interesting to determine the formation path of $AlO(B^2\Sigma^+)$ molecules. An interesting experiment to study the formation of the molecules would be to look at a plasma generated in a controlled atmosphere. By tuning the quantity of N_2/O_2 and Ar, one could investigate the excitation of $AlO(X^2\Sigma^+)$ from meta-stable atoms and molecules. It would also be interesting to have an atmosphere composed of ^{18}O. $^{27}Al^{16}O$ and $^{27}Al^{18}O$ emission are shifted such that one could discriminate the formation of AlO molecules from target's oxygen and from atmosphere's oxygen.

Unfortunately, working in a fully controlled gas environment would require important modifications of the experimental set-up. Here, the gas environment was simply changed by adding an argon flow (4.3 L/min) at the ablation point. Two kinds of targets were used, the previous one composed of Al_2O_3 and a second one composed of aluminum metal. The metal target was sanded before ablation in order to remove the oxide layer. Yet, oxidation of aluminum is almost instantaneous. The formed layer just after sanding should not exceed few nm. Even if not removing all the oxygen from the target, one can expect its amount to be reduced. The four different combinations were measured with the previous experimental set-up and a pulse energy of 23.3 $\pm$ 0.5 mJ.

Figure 4.16 (a) represents the time evolution of Al atoms (in red) and AlO molecules (in green) in the plasma from 2 μs to 30 μs in the four different configurations without any renormalization. First, one can observe that the dynamics of ablation is slightly different from the previous experiments and no mushroom shape is observed. Both sets of experiments were performed several months apart. The focusing on the target and the acquisition are not guarantied to be exactly the same. One noticeable feature is that the plasma formed in Ar is flatter than the plasma formed in the air. It is a well-known phenomenon for LIBS physicists who use it to increase the emission signal of the plasma. For micro-plasma, the intensity of the signal can be increased by several orders of magnitude. Usual explanations are (i) a better confinement because of Ar weight, (ii) less energy loss in

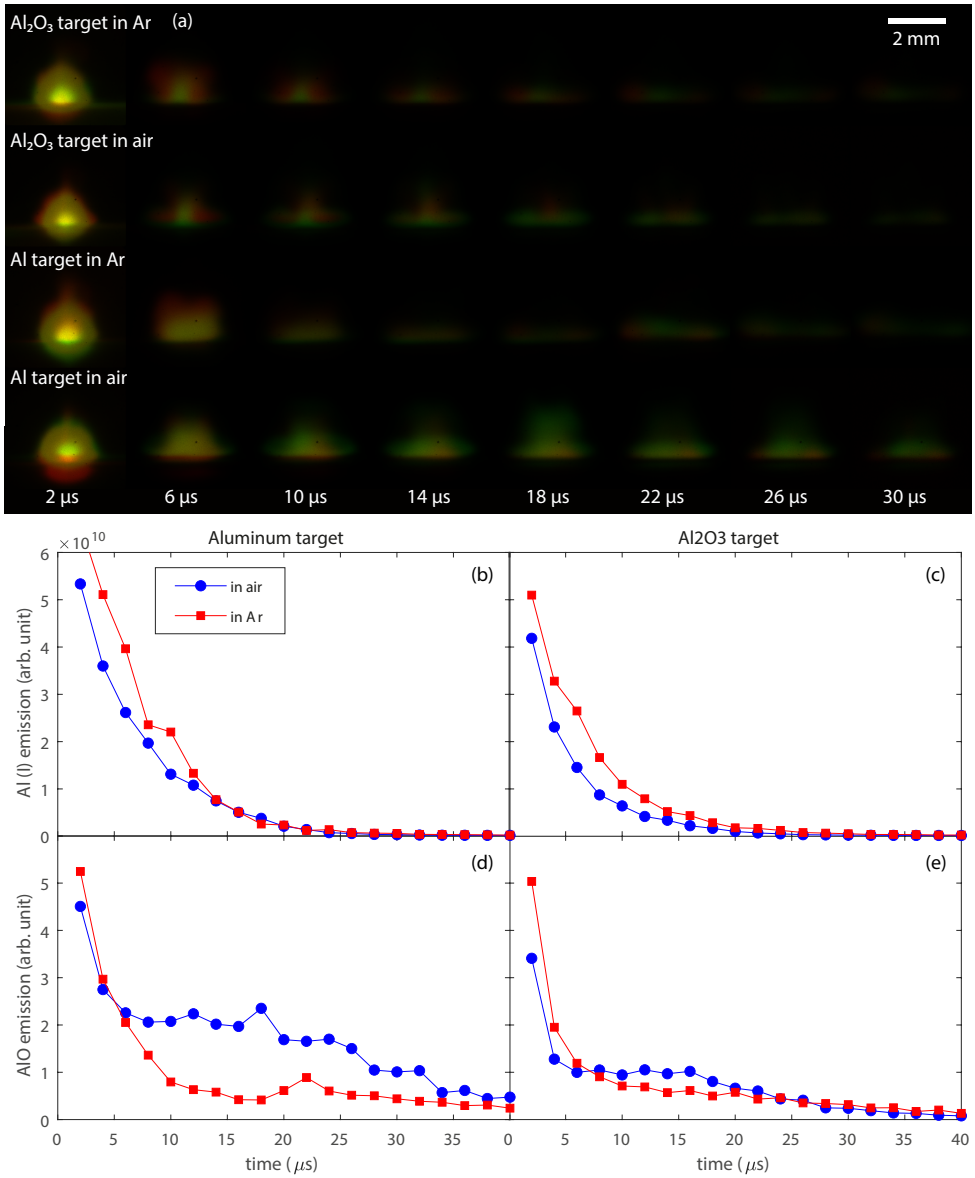

Figure 4.16: (a) dynamics of the plasma observed in false color at different delay after the ablation shot. aluminum emission is in red and AlO emission is in green. (b) and (c) represent the total emission of Al integrated on the whole image respectively from ablation of an aluminum and alumina target. (d) and (e) represent the total emission of AlO integrated on the whole image respectively from ablation of an aluminum and alumina target. Blue dots corresponds to data in air environment while red squares corresponds to data recorded in an Ar flow.

O_2 and N_2 molecules breaking and (iii) Ar atoms provide more free electrons than air.[191,208]. Note that because of the larger density of argon, Taylor's model indeed predicts an average pressure 16% larger than for ablation in the air (see chapter 3).

When looking at figure 4.16 (b) and (c) one can indeed see that the intensity of aluminum is always higher with the argon flow (red square). This observation is consistent with the fact that Al emission is directly related to the electrons density and the temperature of the plasma. The signal of aluminum is also stronger for the metallic target (b) than the oxide target (c) which is logical as the density of aluminum atoms in the target is larger. In the four cases the dynamics of Al emission are very similar.

In contrary, the total intensity of AlO molecules (d,e) changes depending on the target and environment. The initial decrease in the signal is partially due to light background and is difficult to interpret. Here, we focus on delay larger than 5 μs.

Let us first consider ablation in air (blue dots). The AlO signal appears twice as large for the aluminum target than for the oxide target. Yet, both dynamics are similar with a plateau from 5 to 20 μs. This observation suggests that the composition of the target has little influence on the formation of AlO molecules. The difference in intensity is probably due to a larger number of Al atoms from the ablation of the aluminum target. It suggests that the oxygen is in excess and that AlO can be formed with the oxygen of the air. Direct reaction of Al with O_2 molecules can form $AlO(X^2\Sigma^+)$. However, a large amount of O_2 molecules from the air is expected to be atomized during ablation and reaction of Al with O can form $AlO(B^2\Sigma^+)$.

On the contrary, the AlO signal in the argon (red squares) is this time much different. There is no plateau and the signal of the aluminum target is slightly lower despite more Al atoms expected. These observations suggest that this time aluminum is in excess.

The plateau is only observed in the air. The important production of $AlO(B^2\Sigma^+)$ molecules after 10 μs seems related to some molecules in the air. A first explanation would be an increased amount of $AlO(X^2\Sigma^+)$ molecules formed by the reaction of Al atoms and O_2 molecules. In that case, the ground state molecules have to be excited by meta-stable molecules and atoms. A second explanation would be a more effective quenching form air molecules increasing the formation rate of $AlO(B^2\Sigma^+)$ molecules formed by the reaction of Al atoms and O atoms.

Unfortunately, it is difficult to settle the question from these observations. Further more, experiments as the ones suggested in the introduction of this section are required.

4.4 Rovibrational spectroscopy

Molecular spectroscopy of laser-generated plasma is interesting from the determination of nucleation processes, measurement of the temperature and discussion on LTE. In particular, Alessandro De Giacomo and Jörg Hermann wrote in 2017[209] that the "diagnostics of these types of plasma are still challenging. Thus, the question of LTE still remains open. The need for tools for accurate analysis of molecular emission spectra that consider self-absorption and spatial variations is obvious." In this section, I present the spectroscopy measurement of AlO and TiO molecules resolved in space and time and the fitting process developed in order to obtain their rotational and vibrational temperature.

Just like plasma imaging, Pengxu Ran et al.[194] have achieved similar measurements on AlO in order to determine its rotational temperature along the vertical axis of the plasma. Having a higher resolution spectrometer, they achieved a very precise fit of the rotation system by taking into account self-absorption. In return, they were not able to properly define the vibrational temperature in itself. They used a spectrometer with higher spectral resolution and measured only a narrow spectral range around the (0,0) and (0,1) bandheads.

With this work, my goal is to discuss both vibrational and rotational temperature of AlO molecules. I imaged larger spectral ranges of both regions in order to determine both temperatures and have robust results. In contrary to Pengxu Ran et al., I used alumina target instead of aluminum as I wanted to be consistent with previous work of my team. I also investigated the influence of the pulse energy on the temperature. Using fiber for the collection of the light, I was able to translate the collection and obtain 2D mapping of the temperatures. I measured spectra along the center for four different pulse energies: $7.5, 15, 23$ and 31 ± 0.5 mJ and the energy for 2D mapping was set to 22.5 ± 2.5 mJ.

Finally, I also measured the rotational temperature on TiO molecules in the same condition in order to see the influence of the molecule. Similar fit of the temperature on TiO has been achieved by De Giacomo et al. in 2014[210].

In short: *An iCCD camera with filters centered on Al and AlO emission transitions is able to image the position of the species in the plasma. Al emission appears to be related to the temperature of the plasma and the electronic density as it is excited by collision with electrons. AlO molecules is more difficult to excite and emission is likely to track its formation rate. AlO molecules seems to form on the hedge of the Al cloud by the collision of Al atoms with cold O_2 molecules from the air. This observation is confirmed by changing the surrounding gas: in argon flow, the emission of AlO molecules decreases.*

Simple criterion to determine T_{rot}

When I started to work on the simulated spectrum of TiO and AlO, I noticed typical evolution of their shape depending on the rotational and vibrational temperature. From there, I tried to determine some criterion able to provide a good estimation of T_{rot}. For instance David Amans was able to use the cross-over of the rotational branches P and R in the CC molecules, easily identified from the spectrum intensity, to determine the temperature[40]. This could be useful as an input parameter of the fit and, more generally, for others wanting to estimate the temperature without using a complete fitting process.

On figure 4.17 (a) and (b), you can observe the shape of AlO spectra calculated for different T_{rot} and T_{vib} between 500 K and 4000 K. The change of both temperatures does not affect the shape of the spectrum the same way.

Considering the vibrational temperature, one can expect an increase of the intensity of bandheads with large v' when the temperature increases (see figure 4.17 (b)). The population of the molecules in the higher vibrational states increases with the temperature. Such a ratio could appear as a good criterion for the vibrational temperature. Yet, this intensity would actually also depend on the rotational temperature. When T_{rot} increases, the intensity of the transition in the bandhead, corresponding to low rotational numbers, decreases as one can see on figure 4.17 (a). Furthermore, high rotational number transitions overlaps with the other bandhead. And finally, the intensity of the (0,0) bandhead is subject to self-absorption.

Considering the rotational temperature, one can observe that the signal after 494 nm mostly corresponds to transitions with high rotational number. For a given rotational temperature, this part of the spectrum depends little on the vibrational temperature. Thus, a simple criterion for the rotational temperature is the integer of the intensity for $\lambda > 494$ nm divided by the total intensity: $C_{\mathrm{AlO}} = \int_{494}^{500} I / \int_{484}^{500} I$. This simple criterion is actually quite robust and almost independent of the vibrational temperature as one can see in the inset of figure 4.17 (c). In case of large self-absorption, one should not integer the first bandhead in the normalization term. Thus, one can plot the relation between C and T_{rot} (figure 4.17 (c)) and use this curve to determine the rotational temperature using this simple integration. On figure (figure 4.17 (d) one can see the comparison between the rotational temperatures in the plasma obtained using this criterion in blue and the complete fit of the spectrum as developed later in black. The results are mostly in good agreement except at the early time. Before 5 μs, self-absorption lead to the overestimation of the temperature.

In the case of TiO molecules, emission in the range 705-711.5 nm, does not de-

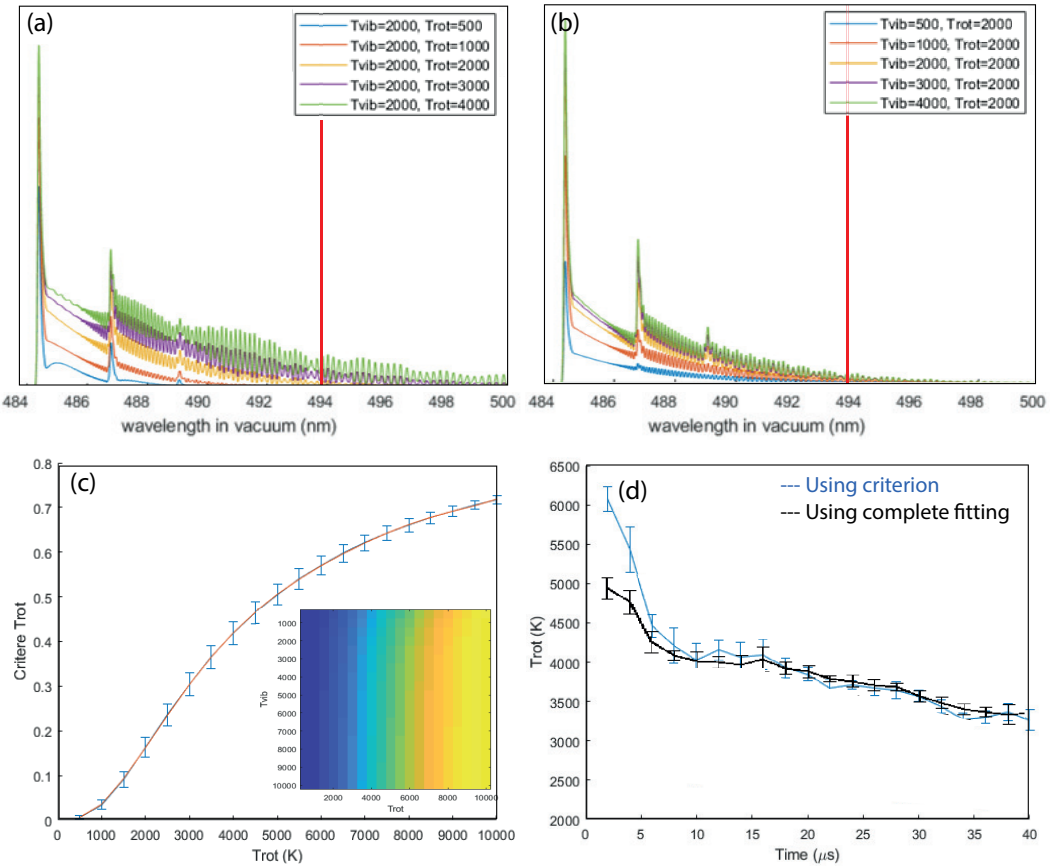

Figure 4.17: (a) Example of AlO spectrum ($\Delta v = 0$) calculated for $T_{vib} = 2000$ K and various T_{rot}. (b) Example of AlO spectrum ($\Delta v = 0$) calculated for $T_{rot} = 2000$ K and various T_{vib}, FWHM=0.06 nm. (c) Evolution of the integer of the normalized spectrum after 494 nm depending on T_{rot}, the inset represents this integer depending on both temperatures. (d) Comparison of the calculated T_{rot} from the criterion and from a complete fit on the emission recorded for a 31 mJ pulse on an aluminum target in air. Fit procedure is presented in the section 4.4.1

pend on the vibrational temperature as it corresponds to the same vibrational state. In this range, I can determine the rotational temperature of the TiO molecules by fitting the spectrum exactly like AlO but considering the molecular structure of TiO. In figure 4.18 (a) are plotted calculated spectra for different rotational temperatures. One of the difficulties is that the spectrum changes very little for temperatures above 1000 K. The intensity of the spectrum between 707 and 708.9 nm increases with the rotational temperature while the intensity of the spectrum before 707 nm decreases (see black arrows on the spectra). I can thus define criterion for the rotational temperature of TiO molecules as $C_{\mathrm{TiO}} = \int_{707}^{708.9} I / \int_{706}^{707} I$

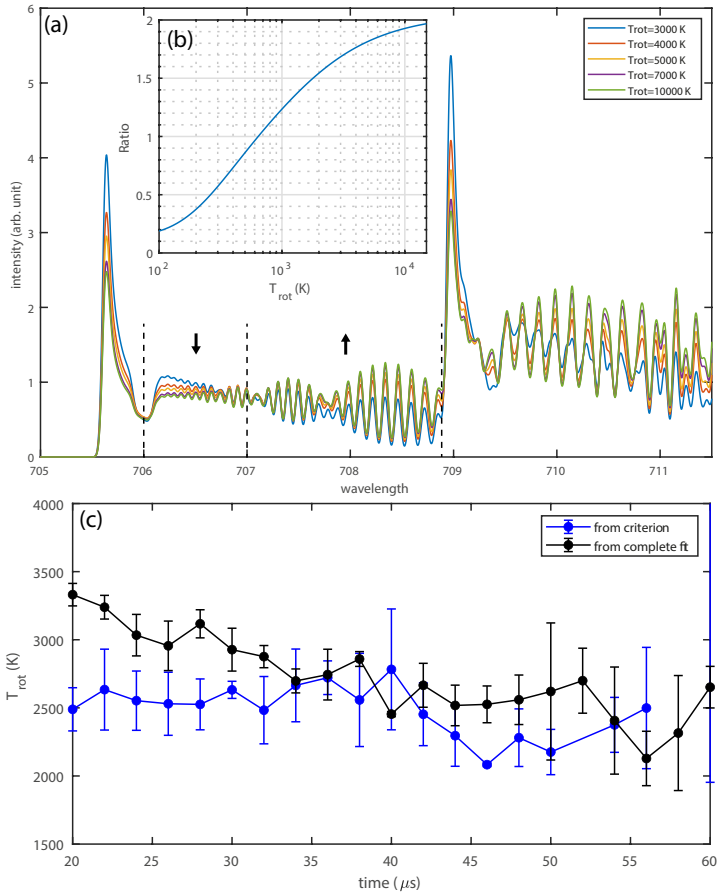

Figure 4.18: (a) Example of TiO spectrum ($\Delta v = 0$) calculated for various T_{rot} (b) ratio of the integrated spectrum $C_{\mathrm{TiO}} = \int_{707}^{708.9} I / \int_{706}^{707} I$ depending on the temperature. (c) Comparison of the calculated T_{rot} from the ratio of the integrated spectrum and from a complete fit.

depending only on the rotational temperature as plotted in figure 4.18 (b). I chose not to integer the signal of the bandhead in order to avoid any auto-absorption. This criterion is rather good for temperatures below 1000 K, but variations are low for higher temperatures. In figure 4.18 (c) is a comparison of the temperature measured on experimental spectrum using this criterion compared to complete fit. It corresponds to the temperature in the center of a plasma generated by a 31 mJ pulse. Before 20 μs, the temperature is difficult to fit because of strong atomic emission. More on the fit process will be discussed later. Here one can see that the criterion gives a good order of magnitude for the temperature, but variations are too small to obtain good precision like for AlO.

4.4.1 Experimental protocol

Measurement of the spectra

In order to study AlO molecules and TiO molecules, two different targets are used. One is a single crystal of Al_2O_3 (alumina) of diameter 25 mm and a thickness of about 3 mm. The other one is a compacted target of TiO powder of diameter 20 mm and thickness about 4 mm. Unfortunately, strong emission peaks of Ti atoms are in the spectral range of AlO molecules. It would have been difficult to measure the temperature of AlO molecules at short time with a single mixed target. Furthermore, spatial resolution implies less signal collected as developed previously. Thus, doping an alumina target with few Ti atoms wouldn't provide enough signal for TiO spectroscopy. In order to offset this difference, plasma were created in the exact same conditions.

First, the measurements have been done the same day simultaneously with the imaging of the plasma presented earlier, enabling direct comparison. The height of the target is set to optimize the ablation using low power. Then, this height is recorded using the front camera [9] (see figure 4.9) in order to set the same height for different targets. The lateral position of the fibers and the focalization of the collection is set using the front camera [9]. A picture of the fiber is taken with a ruler in order to have the scale. The grating in the spectrometer is moved to the required spectral range and the pulse power is adjusted and measured. Finally, the target is moved at 0.8 mm/s during the measurement in order not to create craters changing the ablation dynamics.

The spectra are recorded on the Shamrock 500i spectrometer with a slit of 50 μm leading a spectral resolution of about 0.06 nm. Each fiber images 0.125 mm of the plasma. For 2D spatial mapping, the position of the fibers is changed from -2.5 mm to +2.5 mm by steps of 0.25 mm from either side of the ablation point. For each position, spectra are accumulated on 83 shots with a gate width of 2 μs. The delay between the ablation pulse and the acquisition is changed from 2 to 60 μs by steps of 2 μs.

The choice of the measured spectral range is primordial in the determination of the temperature. For instance, Julien Lam and David Amans chose the (0,0) AlO bandhead in order to measure T_{rot} as it is almost only composed of transition of the same vibrational levels and thus does not depend on T_{vib}. This ensures an easier and more robust determination of T_{rot} but is not suited for the determination of T_{vib}. In this experiment, two different spectral ranges are studied. The first range is 482-497.6 nm and consist of the almost pure (0-0) band and part of the (1-1) band. The intensity of the other vibrational bands is very small. This range is very good

to determine the rotational transition but rather poor in vibrational transitions. Thus, the 506-521 nm range is also considered, in order to fit the vibrational temperature. In this range, AlO molecules have many (v',v'') transitions with $\Delta v = -1$.

For TiO to 705-711.5 nm range is composed of only one vibrational transition. The spectrum shape is independent of T_{vib} which is interesting to determine T_{rot}. In return, it is impossible to determine T_{vib} with these measurements.

For each of the measurement ranges, the spectrum of a calibrated black-body is measured in order to correct the spectra.

Spectrum preparation

First, the measured spectra have to be prepared for fitting. The electric noise of the iCCD is removed. Even if the iCDD is not shined with any photon, a constant background noise is recorded. This noise is measured on the outer part of the sensor that is never shined with light. The remaining signal is composed of the AlO spectrum and some optical noise. This spectrum is corrected from the instrument answer using the black body measurement. In order not to add noise, the obtained spectrum is fitted by a 4^{th} degree polynomial[‡‡] and divided by the tabulated spectrum of the lamp. Then this ratio is applied on all the corresponding spectra to correct the measurement from the answer of the acquisition set-up. Of course, on such short measurement range, the correction is not very important. Yet, the fit of the rotational temperature in particular is very sensitive to intensity variations and this correction is required.

Wavelength should also be calibrated, but finding a precise enough calibrations lamp with enough transitions in the observed range is not easy. A first calibration with a 3^{rd} degree polynomial is done considering the bandheads positions of the molecules' emission. The coefficients are then adjusted during the fitting process. Adding 3 parameters to the fitting increases the calculation time, but these parameters are strongly constrained and converge rapidly regardless of T_{vib} and T_{rot}.

Spectrum fitting process

In the end, there are 6 parameters to adjust: three parameters for the wavelength, one for the Gaussian width and the two temperatures[§§]. The Gaussian width depends slightly on the fiber. In average the FWHM appears larger than the

[‡‡]Polynomial fit for the blackbody is possible as the spectral range is really short.

[§§]Emission lines would rather correspond to Voigt profiles. However, it would requires more fitting parameters. It appears that Gaussian functions fit well enough emission lines and limits the amount of fitting parameters.

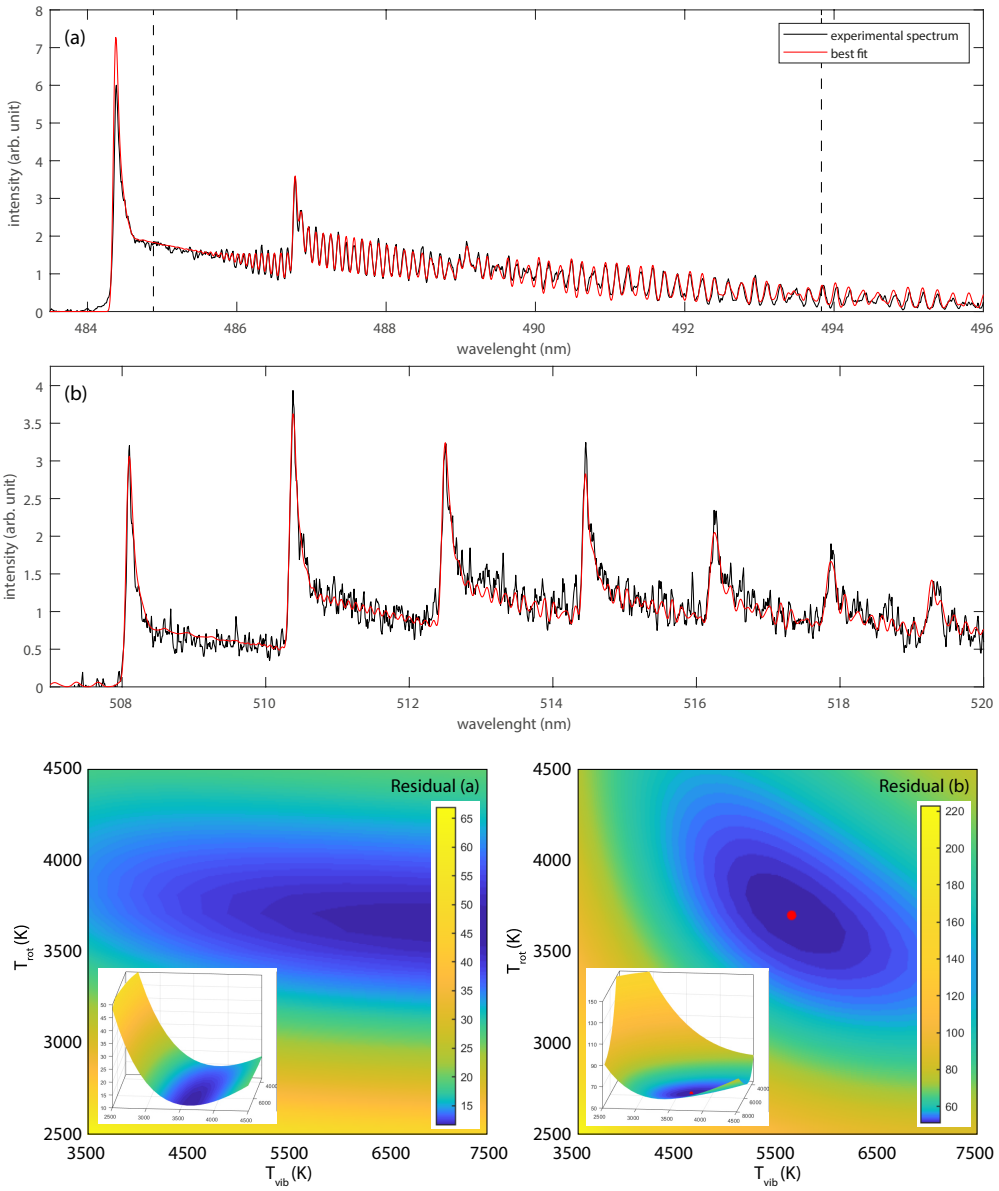

Figure 4.19: Example of AlO spectra (lateral position 0 mm, height 0 mm, delay 10 μs, pulse energy 24.5 mJ) for $\Delta v = 0$ (a) and $\Delta v = -1$ (b). Red curves correspond to the calculated spectra determined according to the fitting process described in the main text and correspond to $T_{rot} = 3693$ K and $T_{vib} = 5644$ K. Dashed lines in (a) delimit the fitting region. Below are plotted the residual maps depending on the temperatures. Other fitting parameters are kept constant. Red dots represent the fit convergence.

measured FWHM of Hg transitions from a calibration lamp (0.075 nm against 0.06 nm). This could be due to collisional broadening in the plasma. With the wavelength parameters, Gaussian width converge very easily whatever the temperature. After the first optimization, these parameters are fixed and only the temperatures are fitted.

On figure 4.19 (a) and (b), represented in black, are the typical spectra recorded for AlO $\Delta v = 0$ and $\Delta v = -1$ transition systems. In red the theoretical spectra obtained for $T_{rot} = 3693$ K and $T_{vib} = 5644$ K after fitting. On the bottom panel are the residual maps of the fitting for each of the spectrum depending on T_{rot} and T_{vib}. On the residual map of (a), one can see a clear minimum for T_{rot} which is almost the same for all T_{vib} but none for T_{vib}. This illustrates the previous affirmation that $\Delta v = 0$ range is suited to fit T_{rot} but not T_{vib}. On the contrary, one can observe a single minimum on the residual map of (b) for both T_{rot} and T_{vib}. Even if it is possible to fit both temperatures on this part of the spectrum, it is preferred to use both spectral ranges to increase the precision of the measurement.

In order to do that, an iterative process is used. First, both of the spectra are fitted independently. Then the $\Delta v = 0$ range is fitted, fixing the vibrational temperature to the value found on the $\Delta v = -1$ range. Inversely, the $\Delta v = -1$ range is fitted, fixing the rotational temperature to the value found on the $\Delta v = 0$ range. This process is iterated twice in order for the temperatures to converge. The red dot on figure 4.19 residual (b) corresponds to the fitted temperatures.

In order to have a good fit of the spectra, the signal-to-noise ratio has to be good enough. No temperature can be fitted in regions with low emission. In order to define a criterion for the selection of good fit, a threshold value on the standard deviation of the squared difference is set. This threshold is determined by hand for each experiment by checking a large enough selection of fits.

In the case of TiO, an example of emission spectrum from 705 nm to 711.5 nm (black) and fit (red) is given in figure 4.20 (b) for a delay of 30 μs and the energy pulse of 31 mJ. As explained earlier, the spectrum does not depend on T_{vib}. The convergence for T_{rot} is thus much faster yet T_{vib} cannot be determined. Furthermore, titanium oxide plasma is rich in atomic emission lines (see figure 4.20 (a)) and prevents me to determine the temperatures for short delay time when the plasma is too hot.

Errors on the fit parameters are usually dominated by the variability of the fitted spectra rather than the convergence of the fit itself. Properly estimating the error on the temperature would require to repeat the measurement and make some statistics on the fitted values of the temperatures. Considering the amount of acquisitions and data treatment it represents, we chose to estimate the error by

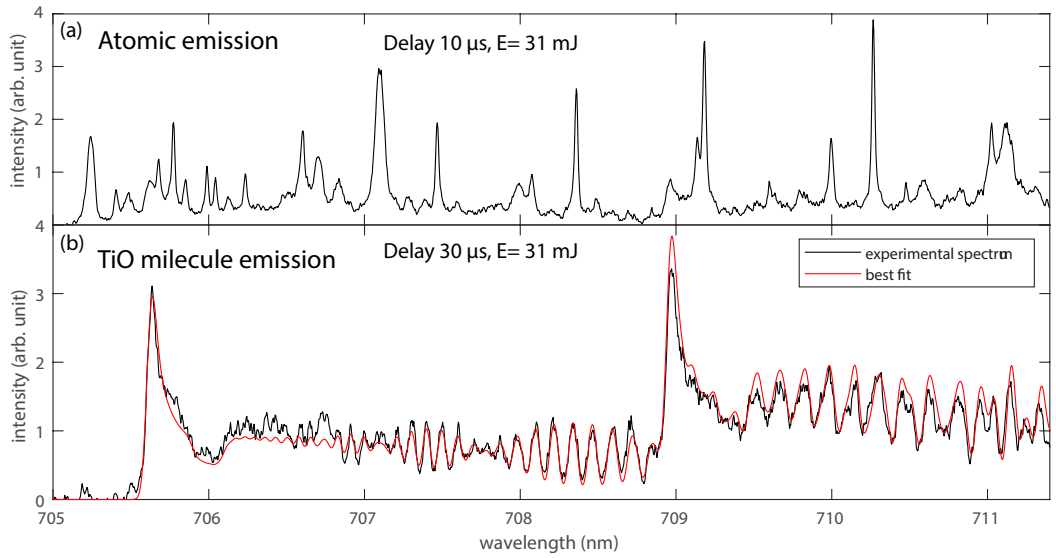

Figure 4.20: (a) TiO spectrum for a delay of 10 μs dominated by atomic emission. (b) Example of TiO spectra in black (lateral position 0 mm, height 0 mm, delay 30 μs, pulse energy 31 mJ) and corresponding best fit in red.

the difference between either two adjacent positions or two consecutive times. The variations of the measured temperatures in time and space are smooth enough to consider that this different has the order of magnitude of the error.

In short: *Thanks to the resolved spectroscopic set-up, I am able to measure the emission of AlO and TiO molecules in different points of the plasma and for various delay time. Each of these spectra are used to fit calculated spectra depending on rotational and vibrational temperature. This enables to obtain 2D mapping of both temperatures in the plasma depending on the position and time. The spatial definition is about 0.25 mm and the temporal resolution is about 2 µs.*

4.4.2 AlO rotational and vibrational temperatures

Figure 4.21 (a) shows the emission of the plasma on the central vertical axis in the AlO emission band for different laser pulse energy. During the first few μs, the bright emission is mostly due to background noise and does not correspond to high AlO emission. Figure 4.21 (b) shows the corresponding temperature mapping of the AlO molecules for different pulse energy depending on the height in the plasma and the delay time after ablation. For this measurement, the fibers were positioned in the center of the plasma as represented in the inset by red circles. Each of these fibers collect light of the plasma on its axis and lead to one spectrum. The fit of this spectrum provides one rotational temperature (T_{rot}) and one vibrational temperature (T_{vib}). The 19 fibers give simultaneously the temperature every 0.125 mm along the vertical of the plasma. In this example, it corresponds to the column indicated by the red arrow. Please note that the color scale is not the same for both temperatures. White parts correspond to areas with low signal where it was impossible to have good fit. One can notice that it was not possible to fit temperatures in the center of the plasma for small delay time. The plasma is hollow and the intensity of AlO emission is too low. Figure 4.22 (a) and (c) represents respectively the rotational temperature and vibrational temperature for the 23 mJ pulse depending on the height in the plasma. Each curve is the average of the measurement on two consecutive times (over 4 μs) and the error bar corresponds to the difference of both values in order to give an idea of the fit error. Similarly, figure 4.22 (b) and (d) represents respectively the rotational temperature and vibrational temperature for the 23 mJ pulse depending on the time in the plasma. Each curve is the average of the measurement on two consecutive heights (over 0.5 mm) and the error bar corresponds to the difference of both values in order to give an idea of the error.

Figure 4.23 (a) shows temperature mapping of the AlO molecules in 2 dimensions for an ablation pulse energy of 24.5 mJ and different delay time. Figure 4.23 (b), are the corresponding images of the AlO molecules emission in the plasma with the same scale. Again, for the shorter delay, it was not possible to determine the temperature in the center of the plasma as it is hollow. Figure 4.24 (a) and (b) represents the rotational and vibrational temperature averaged on the 3 closest fibers to the target depending on the position and for different delay times. For clarity, the error on the average is not reported. They are of the same order of magnitude of the error on figure 4.22 (a) and (c).

The general shape of the temperatures map is due to the dynamics of the plasma and can be directly compared to the localization of AlO molecules presented in figure 4.15. The larger the pulse energy, the larger the plasma and the longer the emission. Unfortunately, in the case of 31 mJ pulse, the acquisition stopped

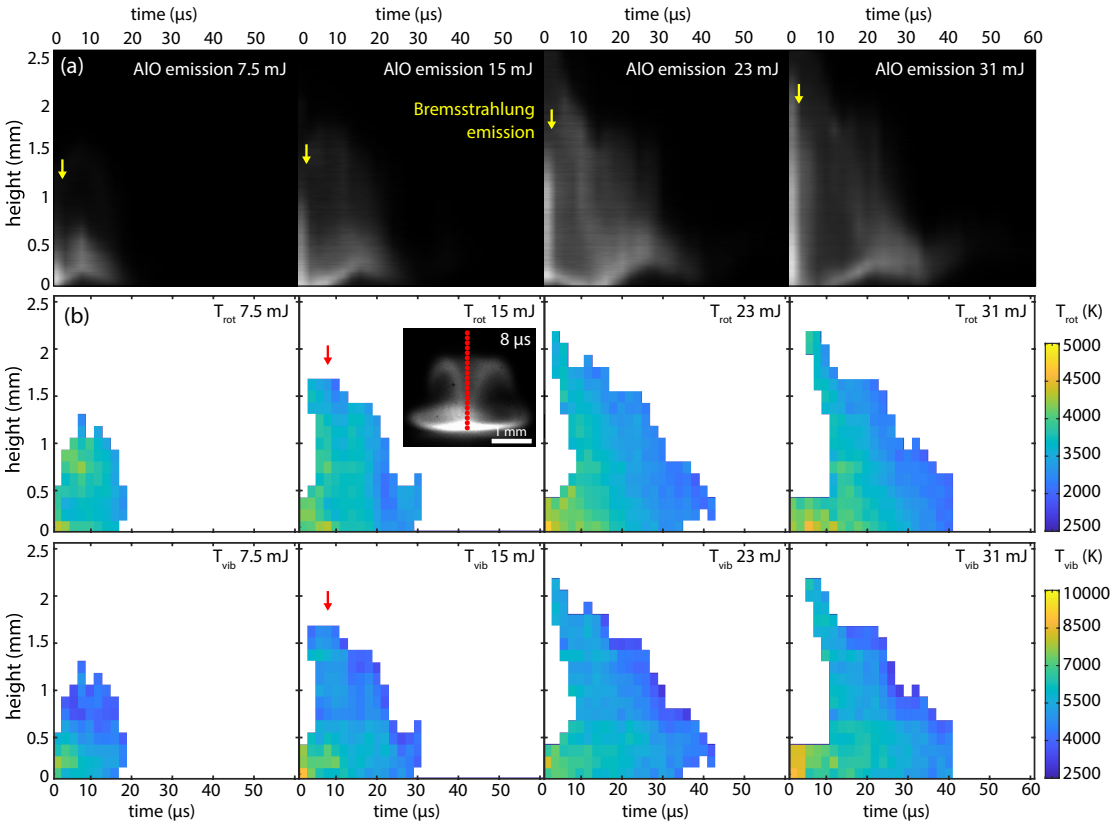

Figure 4.21: Measurements on an Al_2O_3 target in air depending on the laser pulse energy. (a) Intensity of AlO emission on the central axis of the plasma (see section 4.3). Strong initial emission (yellow arrows) is dominated by Bremsstrahlung emission. (b) Rotational and vibrational temperature determined by fitting the emission of AlO (see section 4.4.1) on the central axis. Please note, color scales are different. The inset corresponds to the image of the AlO molecules in the plasma for a delay of 8 μs and a pulse energy of 15 mJ. the position of the fibers are represented by red dot and the corresponding temperature are indicated by red arrows.

at 40 μs. First, one can observe that the temperature generally decreases with time as expected (see figure 4.22 (a) and (c) for a 23 mJ pulse). The cooling rate seems rather the same in the whole plasma (about 25 K/μs for T_{rot} and about 80 K/μs for T_{vib}). The temperature on the outside is lower than in the inside of the plasma as expected because of the cooling due to the air. Yet, close to the target, the temperature appears quite homogeneous within the measured extension. Temperature gradients seem mostly vertical. One could notice that at early time, the temperature is lower in the middle of the plasma (see maps and

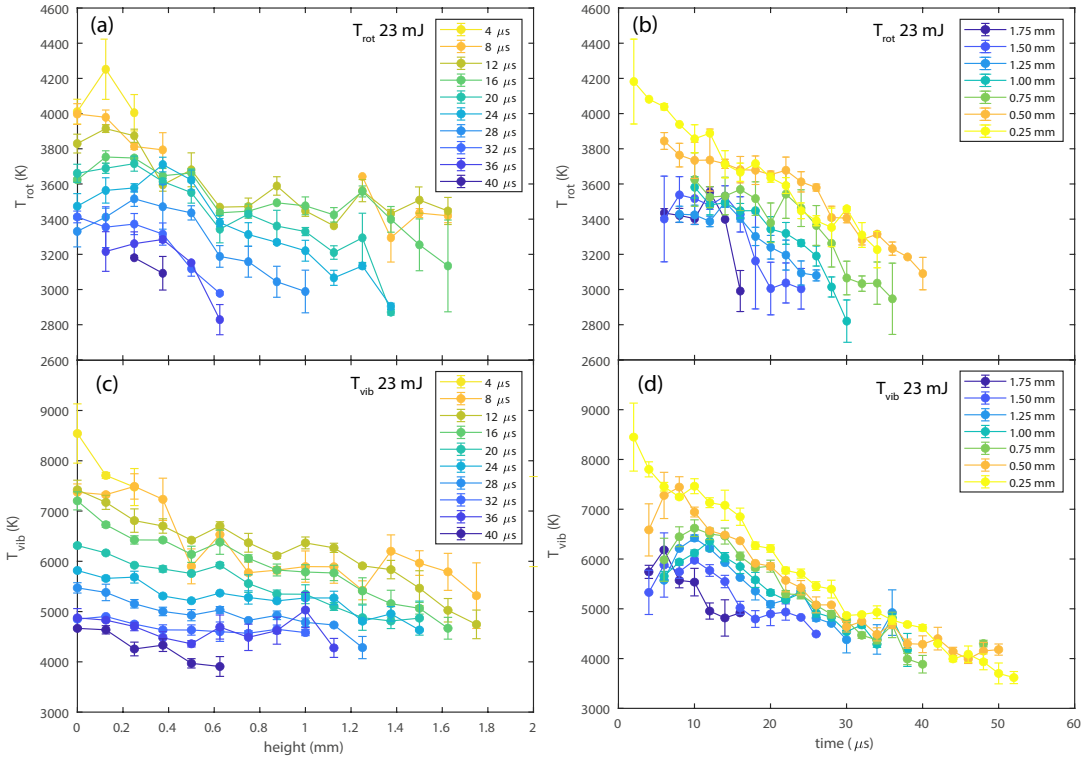

Figure 4.22: Plot of the temperatures corresponding to 23 mJ pulse measurements presented in the figure 4.21. (a) and (c) are the rotational and vibrational temperatures respectively depending on the height in the plasma averaged on two consecutive times (over 4 μs). (b) and (d) are the rotational and vibrational temperatures respectively depending on time in the plasma averaged on two consecutive heights (over 0.5 mm). Error bars are the differences between both measurements.

figure 4.21 (b) and 4.22 (b) for a 23 mJ pulse). Yet, this observation is due to the fact that there is no formation of AlO molecule in the center of the plasma and most of the light collected here comes from the front and back of the plasma which are cooler than the center.

Finally, the rotational temperature is much lower than the vibrational temperature. Figure 4.25 represents the average of the rotational and vibrational temperatures average on the two closest fibers to the target for the different energies. For each energy of the pulse, the temperatures follow a similar trend. The higher the pulse energy, the higher the temperature. Yet, for a delay of 2 μs, T_{vib} is almost two times larger than T_{rot} with 8000 K against 4300 K in average. Then the difference decreases with time as T_{vib} decreases faster than T_{rot}.

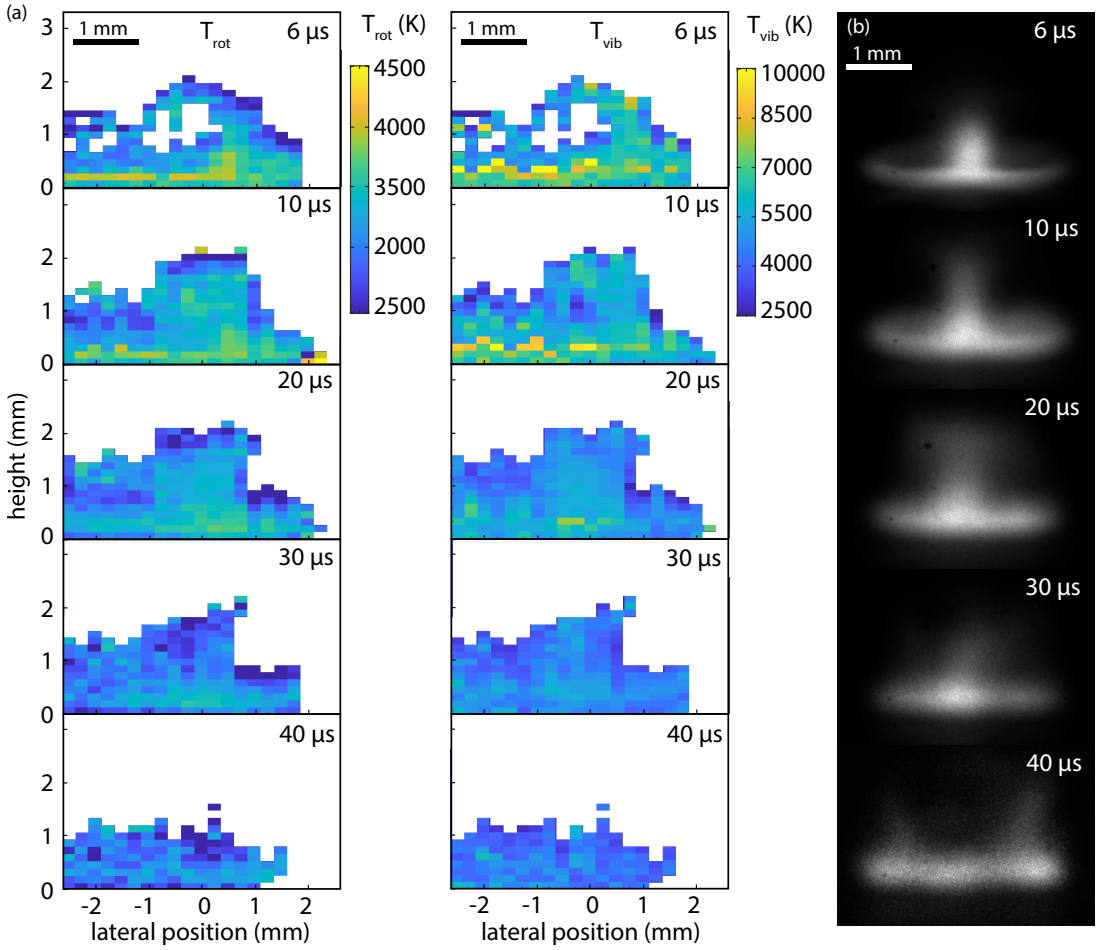

Figure 4.23: Measurements of the temperatures for the ablation of an Al_2O_3 target in air with a pulse energy is 24.5 mJ. (a) 2D map of AlO molecules T_{rot} and T_{vib} depending on time a lateral position. Lateral position corresponds to the position of the fibers with respect to the central axis. Temperatures are determined by fitting the emission of AlO (see section 4.4.1) (b) Corresponding images of AlO emission depending on time (see section 4.3).

In the next chapter, I was able to measure the emission time of $B^2\Sigma^+$ state in the plasma and found 2.7 ± 0.15 ns. This is short compared to tabulated Einstein coefficients ($\tau = 116$ ns) but consistent with similar LIBS achieved by Nagli et al.[211] who attributed this short decay time to collisional quenching and thermal quenching. Considering the density of the plasma from the chapter 3, one can estimate collision frequency with AlO molecules between $\times 10^8$ and $\times 10^{10}$ s^{-1} depending on the delay (see section 5.3.1). Apparently, this collision rate is enough to quench the life-time of molecules and partially mix the state of a large part

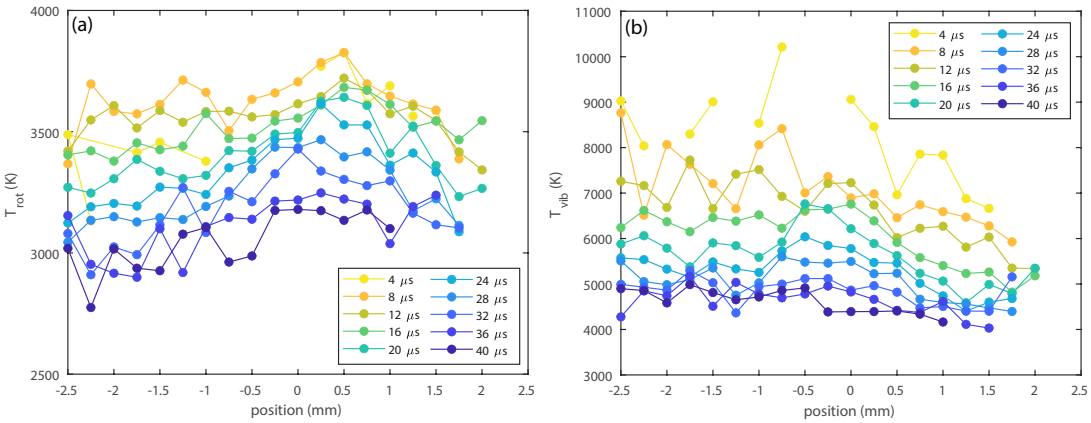

Figure 4.24: (a) and (b) represent rotational and vibrational temperature profiles depending on time for the measurement presented in figure 4.23. For each position and time, it corresponds to the average of the temperatures from the 3 closest fibers to the surface. For clarity, the error bars are not reported. They are of the same order of magnitude of the errors on figure 4.22 (a) and (c).

of the molecules. However, the fact that both the vibrational and the rotational temperature are different proves that the excited state of the molecules have no time to fully relax and reach complete thermal equilibrium. Such temperature differences are regularly observed in diatomic molecules created by plasma discharge[212,213,214,215,216]. A direct comparison with these studies is hazardous as the experimental conditions are different, in particular the pressure, but are interesting to discuss. Most of the time, the vibrational temperature is higher than the rotational temperature because the molecules are formed out of equilibrium and partially thermalized by collision with the gas. The rotational temperature is usually close to the kinetic temperature of the gas as rotation modes are more sensitive to collisions. In particular, Hofmann et al.[212] reports that the rotational temperature of OH molecules measured in their experiment follow the kinetic temperature of the gas but overestimates it. Raud et al.[215] studied the rotational temperature of OH and N_2 molecules and find out that their temperatures are different. OH molecules are more thermalized by the collision with the gas than N_2 molecules. Verreycken et al.[216] even reported rotational emission that are described by two temperatures corresponding to two excited populations, one out of equilibrium related to the formation of the molecules and one for low J that is thermalized.

Within the de-excitation time, one can expect the rotational state to be more

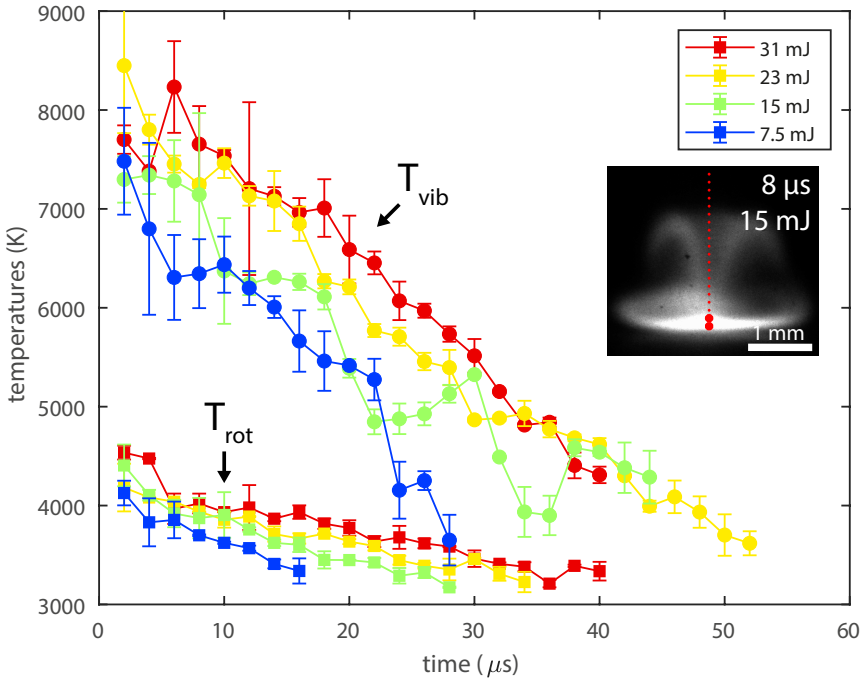

Figure 4.25: Comparison of the rotational and vibrational temperatures' evolution depending on the laser pulse energy for the ablation of an Al_2O_3 target in air. Temperatures correspond to the measurements on the central axis of the plasma presented in figure 4.21 averaged on the two closest fibers to the target (see inset). Error bars corresponds to the difference between both values.

sensitive to collisions with the plasma as shown in the next chapter[¶¶]. Thus, one can expect the rotational temperature to be closer to the kinetic temperature than the vibrational temperature but might still overestimate it. This is consistent with the kinetic temperature expected from the model developed in the chapter 3. The decrease of temperatures with time and spatial gradients show a strong link between the molecular temperatures and the kinetic temperature of the plasma. Because of low collision couplings, in particular on the vibration modes, one could expect an influence of the plasma temperature on the formation of the molecules themselves. The higher the gas temperature, the higher the excitation state of the formed molecules. This measurement is a partial fingerprint of the molecule formation and confirm the insight given by the microcanonical model in the chapter 2 that the energy is not equipartitioned during the molecule formation.

[¶¶]When AlO molecules are excited in a low vibrational and rotational state, emission of relaxed state can be described by a low vibrational temperature and a higher rotational temperature. The vibration state remains little excited because of low coupling.

4.4.3 TiO rotational temperature

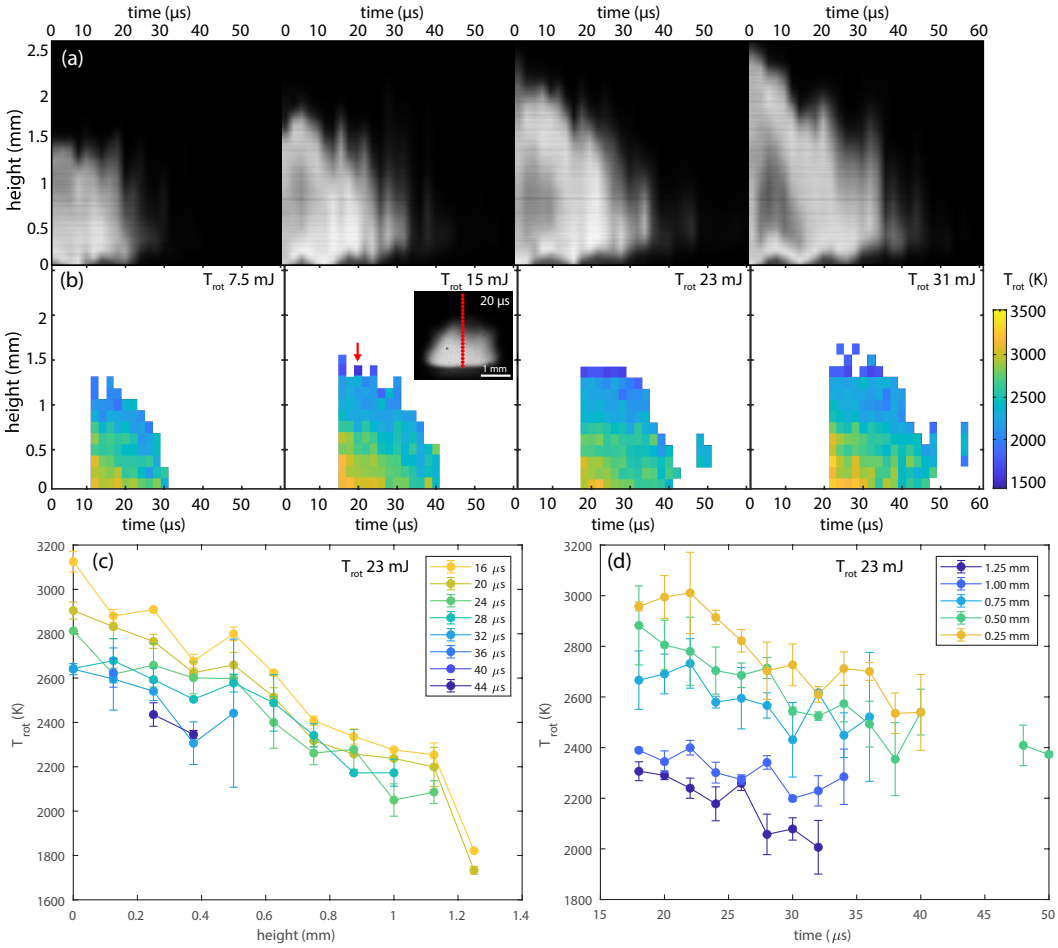

Figure 4.26: (a) Plasma emission for TiO emission range in the center vertical axis. (b) T_{rot} measured on the vertical center of the plasma. (c) and (d) rotational temperatures for the 23 mJ pulse depending on the height and delay time.

Figure 4.26 (a) shows the intensity for the TiO emission band of the center of the plasma depending on the delay time for different pulse energy. Be careful, intensity is dominated by atomic emission for early time. Figure 4.26 (b) shows rotational temperature mapping of the TiO molecules for different pulse energy depending on the height in the plasma and the delay time after ablation. For this measurement, the fibers were positioned in the center of the plasma as represented in the inset by red circles. Each of these fibers collects light of the plasma on its axis and leads to one spectrum as represented in black on figure 4.20 (b). The fit of this spectrum (red) provides the rotational temperature (T_{rot}). The 19 fibers

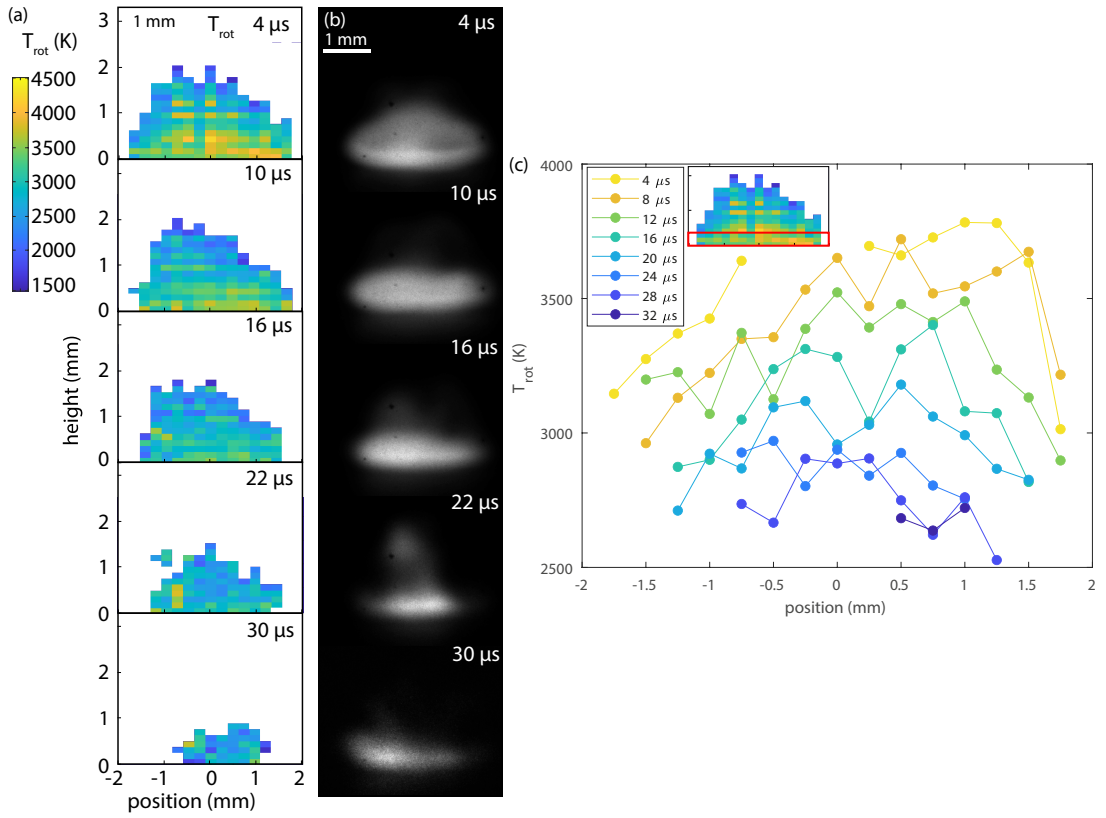

Figure 4.27: (a) 2D map of TiO molecules T_{rot} and image of TiO emission depending on time for a pulse energy is 21 mJ. (b) Corresponding emission of TiO molecules (see section 4.3). (c) average rotational temperatures on the 3 closest fibers to the surface (see red area in the inset).

give simultaneously the temperature every 0.125 mm along the vertical axis of the plasma. White parts correspond to areas with poor fitting where no temperature can be measured. It is either because of low signal or too much atomic emission as represented on figure 4.20 (a). For short delay, atomic emission dominates the spectrum.

Figure 4.26 (c) represents the rotational temperature for the 23 mJ pulse depending on the height in the plasma. Each curve is the average of the measurement on two consecutive times (over 4 μs) and the error bar corresponds to the difference of both values in order to give an idea of the error. Similarly, figure 4.26 (d) represents the rotational temperature for the 23 mJ pulse depending on the time in the plasma. Each curve is the average of the measurement on two consecutive heights (over 0.5 mm) and the error bars correspond to the difference of both values in order to give an idea of the fit error.

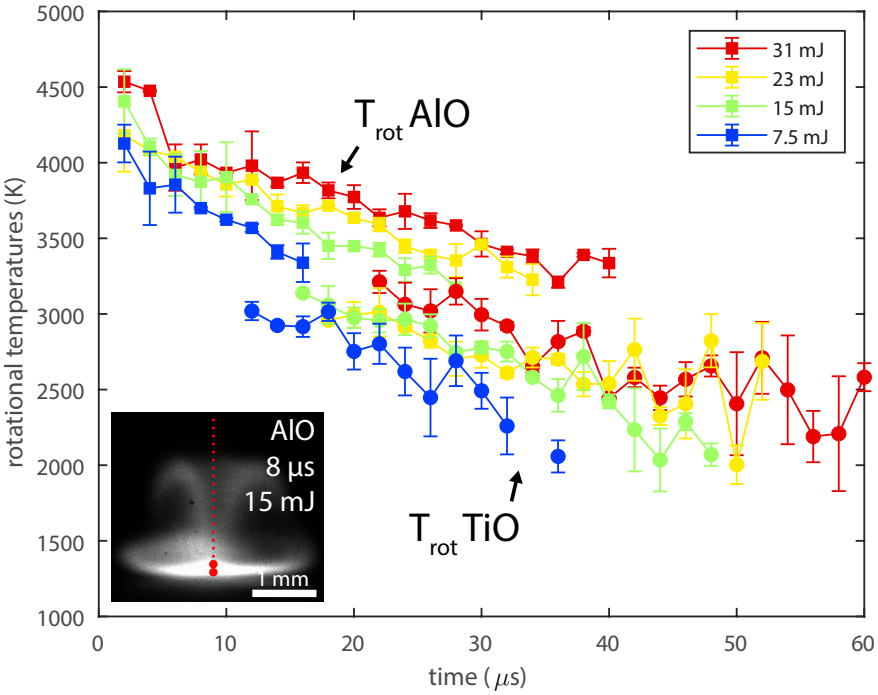

Figure 4.28: Comparison of the rotational temperatures of AlO and TiO molecules depending on delay time for different pulse energy. The temperatures are averaged on the two closest fibers to the target on the central axis of the plasma as represented in the inset.

Figure 4.27 (a) shows temperature mapping of the TiO molecules in 2 dimensions for an ablation pulse energy of 21 mJ and different delay time. On the right (b), are the corresponding images of the TiO molecules emission in the plasma with the same scale. Figure 4.27 (c) represents the rotational temperature averaged on the 3 closest fibers to the target depending on the position and for different delay times. For clarity, the error on the average is not reported. They are of the same order of magnitude as the errors on figure 4.26 (c) and (d).

TiO emission appears to be much more homogeneous and concentrated than AlO emission. This is probably due to the fact that fit of TiO emission are only possible after 10 or 20 μs, when the plasma is cold enough for atomic emission to be weak enough. At this time, the whole plasma is smaller and cold enough for TiO to form. Just like AlO, temperature decreases with time and with the height. The spatial gradient for TiO appears almost two times stronger than for AlO (800 K on 1 mm). This could be due to depth average due to the measurement. AlO formation being hollowed, center measurement could be more sensitive

to outer-part emission than in the case of TiO and appears colder than it really is.

Figure 4.28 represents the average of the AlO and TiO rotational temperatures on the two closest fibers to the target for the different energies. Just like AlO, the rotational temperature of TiO increases with the pulse energy and its decrease with time follows the same trend. TiO rotational temperature seems systematically about 500 K lower than AlO temperature. One could imagine that (i) TiO molecules are created less excited than AlO molecules or (ii) TiO molecules are more thermalized than AlO molecules.

Hypothesis (i) is unlikely. For temperatures of several thousand Kelvin, the standard formation enthalpy of TiO is about 10 % bellow the one of AlO[217]. This means that in the case of formation from single atoms, the remaining energy of TiO reaction is larger.

Hypothesis (ii) could be justified either by a greater lifetime of the excited state or a larger cross-section, increasing the number of collision. The radiative lifetime in vacuum for the $A_3\Phi$ state of TiO is around 100 ns[218] which is the same order of magnitude or slightly shorter than AlO[219]. For equivalent quenching, one can expect the radiative life-time of TiO to be the same as AlO or even shorter. However, Ti d orbitals are wide which increases its cross-section. TiO could thus be subjected to more collision than AlO molecules and further thermalization. Furthermore, the rotational state density of TiO is larger than the one of AlO as the rotator constant is lower, and it is a triplet state. The difference in energy between each state is lower and transitions are facilitated. This could explain why TiO are more thermalized than AlO molecules.

In short: *For AlO molecules, the presented results indicates that T_{rot} and T_{vib} are not equal in the plasma. Both decrease with time and on the outer-part of the plasma. T_{vib} appears to be larger than T_{rot} but the difference is reduced with time. These temperatures represent the vibrational and rotational population of the first electronic excited state. This state is mostly populated by molecules just formed and the decay time being short, the excited state is only partially relaxed because of collisions. In particular, vibrational states are less affected by collision than rotational states such that T_{vib} is more likely to represent the excited state of the molecules just after their formation while T_{rot} could be closer to the kinetic temperature of the gas. T_{vib} is high because vibration modes are excited when the molecules are formed. This excitation seems to depend on the temperature of the plasma itself. The higher the temperature of the plasma, the higher is T_{vib}. T_{rot} in contrary is closer to the kinetic temperature predicted by the model in the previous chapter. For TiO, only the rotational temperature was measured. It follows the same trend as the rotational temperature of AlO but slightly lower.*

4.5 Conclusion

This chapter presented space resolved spectroscopy of molecules in laser-generated plasma. During my PhD, I built an experimental setup able to achieve the time resolved spectroscopy on laser induced plasma with a spatial resolution up to about 150 μm and applied it on the rovibrational spectroscopy of AlO and TiO molecules. By fitting these measurements, one can obtain information on the rotational and vibrational populations of the molecules in the plasma. One can suppose these populations to be described by Boltzmann distributions and determine the emission spectrum of the molecules in the plasma depending on a temperature. However, if the molecules do not reach internal equilibrium, the vibrational and rotational populations are not described by the same temperature. In particular, the rotational temperature of the molecules is usually considered as a good probe of the kinetic temperature of the plasma.

Here, we measured the rotational and vibrational temperature of AlO molecules and the rotational temperature of TiO molecules depending on the position in the plasma and their evolution in time. These temperatures decrease with time as the plasma cools down. They also are lower on the periphery of the plasma where it is in contact with cold air. The vibrational temperature of AlO molecules is much higher than its rotational temperature meaning the internal equilibrium in the molecules is not reached as expected from chapter 2. The vibrations of the molecules are less affected by collisions with other particles than the rotations. The vibrational temperature is driven by the excitation of the molecules while the rotational temperature is closer to the kinetic temperature of the plasma. The rotational temperature of TiO is very similar to the rotational temperature of AlO but systematically about 500 K lower. This observation might be due to a better thermalization of TiO molecules. In that case it is possible that the rotational temperature of AlO molecules overestimates the kinetic temperature of the plasma.

In order to better understand the temperature of AlO molecules and the thermalization processes, one need to understand the origin of the molecules. Here the emission of AlO molecules is from the excited state $B^2\Sigma^+$. This state has a short emission life-time, explaining why the molecules are only partially thermalized. By imaging directly the plasma with an iCCD camera and filters, it is possible to determine the spatial distribution of $AlO(B^2\Sigma^+)$ molecules. The origin of the excited state remains uncertain. $AlO(B^2\Sigma^+)$ molecules appear in the periphery of the plasma and mainly when ablation occurs in the air. This state can be populated directly by the formation of the molecules from the reaction of Al and O atoms cooled down by collision with molecules of the air, or be due to the excitation of $AlO(X^2\Sigma^+)$ colliding with meta-stable molecules such as N_2^* molecules.

Further investigations in controlled atmosphere are required to precisely determine it. For instance, one could study the emission spectra in atmosphere with different concentration of N_2 molecules and $^{18}O_2$ molecules.

The temperatures deduced from molecular spectroscopy is a great tool to study laser-generated plasma. The comparison of the rotational and vibrational temperatures provides information on the internal equilibrium of the molecules. The rotational temperature is usually considered as a good probe of the kinetic temperature of heavy particles in the plasma. Studying its evolution in space and time and comparing it to the excitation temperature of the atoms would bring a new insight on the thermodynamics of the plasma and enable to further discuss LTE. However, emission life-time of the molecules is short. One needs to ensure that the rotational temperature of the excited state is indeed a good probe of the kinetic temperature of the plasma. In the next chapter, Laser-Induced Fluorescence (LIF) spectroscopy is achieved on the plasma in order to probe the ground state of AlO molecules. In particular, LIF is used to determine the rotational temperature of the ground state molecules and compare it to the one of the excited state.

Chapter 5

Laser-induced fluorescence

Tout mouvement de quelque nature qu'il soit est créateur.
Edgard Allan Poe

Abstract: *Laser-Induced Fluorescence (LIF) is achieved in AlO molecules produced in a laser-generated Plasma. The life-times of the excited* $\mathrm{AlO}(\mathrm{B}^2\Sigma^+)$ *molecules in the plasma after 10* μs *is measured equal to* 2.7 ± 0.2 *ns. This life-time is much shorter than the one measured in vacuum because of collisions and thermal quenching, even though only a few dozen collisions are estimated to occur within this time. Molecules are only partially thermalized. Such a difference with tabulated emission life-time of molecules have to be considered when calculating molecules' ratio in LIBS. Fluorescence spectra can be decomposed in two contributions: a first one which is direct fluorescence, conserving an initial population in excited state, a second one which is thermalized, populating many other quantum levels in excited state. The emission of the relaxed contribution can be approached by calculations considering population distributions following these vibrational and rotational "relaxation" processes. These populations can be modeled with Boltzmann distributions taking very different vibrational and rotational temperatures which strongly depend on the excited transitions. The direct fluorescence can be described considering a population distribution following resonant absorption of the laser. This population is directly related to the ground state population that can be modeled with a Boltzmann distribution. By fitting fluorescence spectra, one can measure the rotational temperature of the ground state molecules. After 30* μs*, this temperature is* 3153 ± 64 *K. Simultaneously, a fit of the emission of* $\mathrm{AlO}(\mathrm{B}^2\Sigma^+)$ *with no previous excitation gives* $T_{rot} = 3130 \pm 75$ *K and* $T_{vib} = 5620 \pm 240$ *K. The rotational temperature measured from emission of* $\mathrm{AlO}(\mathrm{B}^2\Sigma^+)$ *appears to be*

close to the ground state temperature after a delay of 30 μs. After 5 μs, the rotational temperature measured from emission of $AlO(B^2\Sigma^+)$ *slightly overestimates the ground state temperature of about 150 K. The thermalization of the rotational states is not complete.*

In order to better understand nucleation in plasma, Laser-Induced Fluorescence (LIF) is a great tool. A second laser is used to re-excite atoms and molecules in the plasma. Combined with LIBS, it improves detection and enables to probe the ground state of molecules and clusters that are formed late in the plasma.

My first goal was to use LIF in order to better understand the dynamics of excited AlO molecules in the plasma and in particular their de-excitation time. The study of AlO molecules fluorescence bring new insights in order to better understand the thermalization of the molecules. By fitting the intensity profiles of fluorescence spectra, it is possible to determine the temperature of the molecules $AlO(X^2\Sigma^+)$ and compare it to the temperature of the $AlO(B^2\Sigma^+)$ molecules. My second goal was to look for the evolution of species concentration in the plasma by probing the ground state of the molecules. I got interested in the Al_2O molecule which should be sufficiently stable to be observed[47] and has indeed been observed elsewhere[220,221]. Yet, this appeared more complicated than it sounds, and I was not able to observe any Al_2O molecules.

After a quick introduction of theoretical background on LIF, I present the experimental set-up I built. Then, the measurement of the AlO excited state lifetime is presented and the thermalization of the molecules is discussed. Finally, the fluorescence spectrum is fitted in order to deduce the ground state temperature of AlO molecules. Convention for spectroscopic notations are given in the annex A.

5.1 Fluorescence

In 1852, George Gabriel Stokes published in "On the change of refrangibility of light" his observations on some materials as fluorine (CaF_2)[222]. "In those bodies, [...] the colour thence arising may be seen by exposing the body to ordinary daylight, looking at it in such a direction that the regularly reflected light does not enter the eye, and excluding transmitted light by placing a piece of black cloth or velvet behind, or by some similar contrivance". The emitted light is no regular reflection because the wavelength of the emission is below the wavelength of the excitation such that one "shall accordingly speak of the phenomenon as *dispersive reflexion*". Yet he comments on this term: "I confess I do not like this term. I am

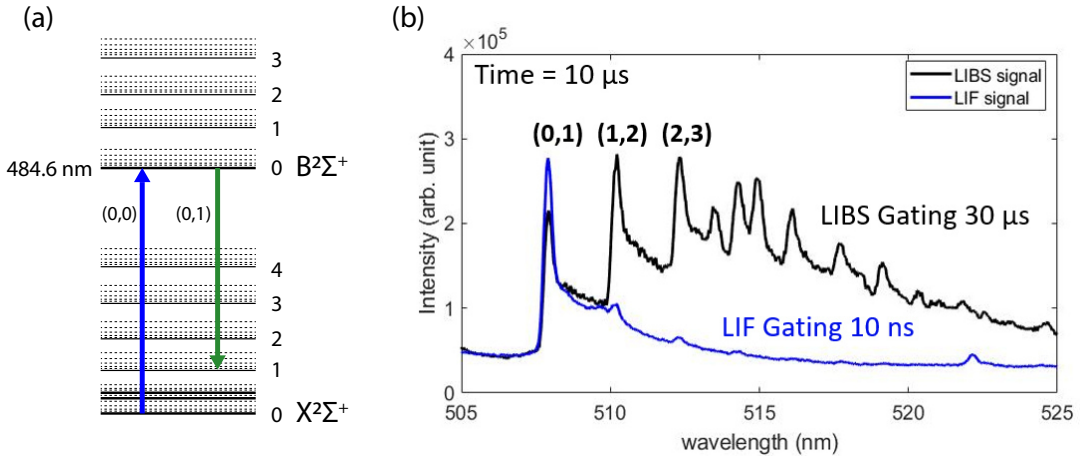

Figure 5.1: (a) Electronic structure of AlO molecule with an example of excitation transition (blue) and direct fluorescence emission (green). (b) LIBS emission spectrum of AlO molecule formed by ablation of aluminum target in air (black). The delay between the ablation and the beginning of the acquisition is 10 μs and the acquisition duration is 30 μs. LIBS-LIF signal of AlO molecule in the exact same condition after an excitation at 484.3 nm and an acquisition duration: 10 ns (blue). The intensities of both spectra are not normalized for direct comparison.

almost inclined to coin a word, and call the appearance *fluorescence*, from fluorspar, as the analogous term opalescence is derived from the name of a mineral". This is the first occurrence of this term and the difference in wavelength is soon called *Stokes shift*.

Fluorescence is a phenomenon observed in various systems such has atoms, molecules or crystals. Fluorescence occurs when the molecule absorbs a radiation and goes from the ground state to a different electronic excited state. Then, spontaneously emits light when de-exciting. In molecules, the difference in wavelength between the excitation and the fluorescence emission, that is to say the Stokes shift, can be explained by the Franck-Condon principle and Kasha's law applied to the rovibrational structure of the molecules.

When the plasma is irradiated with a given wavelength λ, the molecules can absorb a photon if there is a transition between a populated level and an empty one with a difference in energy $E = hc/\lambda$. For instance, figure 5.1 (a) represents the scheme of the rovibrational structure of AlO molecules for the two electronic states of interests $X^2\Sigma^+$ and $B^2\Sigma^+$. The $A^2\Pi_i$ state, in-between, is not investigated here. Molecules in the $X^2\Sigma^+$ electronic state with $v'' = 0$ (vibrational state) can absorb photon with a wavelength of 484.6 nm and are excited in the $B^2\Sigma^+$ state

with $v' = 0$. Such a transition will be referred to as (v', v''), in that case (0,0), corresponding to the vibrational level.

The excited molecule can then relax through different radiative channels to the ground state $X^2\Sigma^+$ state with $v'' = 0, 1, 2$ etc. Just like simple emission, the transition probability of each of this channel is proportional to the Frank-Condon factor (see section 4.1.3). If the molecule was originally excited from the $v'' = 0$ level as in the example, then the desexitation transitions have necessarily lower energies leading to *Stokes shift*. On the contrary, if the initial state is not the ground state (in a hot gas for instance), the de-excitation can have greater energy leading to an *anti-Stokes shift*.

In figure 5.1 (b) one can see the resulting emission spectrum of AlO following 484.3 nm excitation in blue compared to the emission spectrum of thermalized AlO molecule in black. The LIF spectrum shows a strong emission at 508 nm corresponding to the (0,1) de-excitation following a (0,0) excitation. This is direct LIF emission from the laser-populated excited states (v' and J'). In order to describe direct LIF emission, one also needs to consider the selection rules on the allowed rotational transition (see chapter 4, section 4.1.2). Emission to longer wavelengths corresponds to emission from higher rotational levels and from higher vibrational levels, with changes in both v' and J' quantum numbers. In that case, the excited state is not conserved between the excitation and the emission. Before de-excitation, the state of some excited molecules is changed by collision with the plasma. Collisional processes occurring in the plasma can change the quantum state of a molecule with no strict selection rule on Δv and ΔJ, (or even Δn). This is collisionally-induced LIF (CLIF).

In this example, LIF signal is integrated over 10 ns. In order to obtain equivalent intensity from LIBS, the signal has to integrate over 30 μs. LIF intensity is about 3000 times stronger than LIBS.

In short: *Laser-Induced Fluorescence (LIF) is a spectroscopic technique in which light is used to excite the molecules. Molecules in the ground state can absorb light if the energy of the photon corresponds to a difference in energy with an excited state of the molecules. This is resonant absorption. For instance,* $X^2\Sigma^+$ *AlO molecules with* $v'' = 0$ *and* $J'' \simeq 0$ *can absorb photons with* $\lambda = 484.6$ *nm to reach the* $B^2\Sigma^+$ *state with* $v' = 0$ *and* $J' \simeq 0$*. Part of the molecules de-excite from this excited state, leading to "direct fluorescence". Another part first relaxes because of collisions and de-excite from various excited states, leading to "collisionally-induced LIF" (relaxed fluorescence). These emissions can be used to study the thermalization dynamics, the life-time of the excited state or the temperatures of the molecules.*

5.2 Experimental set-up

The set-up is composed of three main parts, the ablation, the excitation and the detection interacting together as represented in figure 5.2. The ablation part is the same as the one described in the chapter 4 (see section 4.2) and will not be described here.

Excitation of the atoms and molecules in the plasma is achieved by an NT230-100 Optical Parametric Oscillator (OPO) with SH/SF extension from EKSPLA (NT230 series) using non-linear mixing of a YAG:Nd laser in order to produce broad wavelength coverage. This laser can be tuned from 220 to 1500 nm by changing the angles between the different non-linear crystals. The output power varies a lot depending on the wavelength, as plotted on figure 5.3. There are three zones, one in IR with little power (< 0.1 W at 50 Hz), one in the visible with high power ($5 - 10$ W at 50 Hz), and one in the UV range ($0.1 - 0.2$ W at 50 Hz). The pulse duration is about 5 ns with a FHWM = 3.2 ns. The repetition rate can be tuned from 10 Hz to 100 Hz. In the case of LIBS-LIF, we operate at 20 Hz in order to match the repetition rate of the ablation laser. The spectral resolution of the OPO varies from 1 to 5 cm^{-1} depending on the wavelength. Around 500 nm* the pulse FHWM=66 pm (2.6 cm^{-1}). It was measured using a DEMON spectrometer from LTB with a resolution of about 1 pm. Such a resolution is far from the resolution of pulsed dye lasers (about 0.001 cm^{-1}) and this experiment is not able to resolve completely the rotational structure in the spectra of diatomic molecules. However, OPO is much more user-friendly. The wavelength can easily be tuned automatically in order to obtain excitation/emission mapping.

This laser line is first expanded by a telescope to avoid damaging the optics (blue beam on figure 5.2). A set of two broadband mirrors (not represented on the diagram) are used to adjust the beam path in the two spatial dimensions and two angular dimensions. A bandpass can be used in order to filter harmonics and is chosen according to requirements. One percent of the laser beam is deviated in a lambda-meter WaveMaster^{TM} from Coherent in order to have precise measurement of the excitation wavelength. This measurement is recorded simultaneously with the LIF spectra. In the LIBS-LIF configuration, the OPO beam is then focused on the plasma region in order to increase signal.

Light collection optics and the spectrometer are the same as those described in the chapter 4 (see section 4.2.3). The arrangement was optimized in order to achieve the best resolution on the Shamrock spectrometer. Yet, in order to have enough signal, full vertical binning of the iCCD chip-set is used. The signal is

*region of interest for AlO molecules excitation

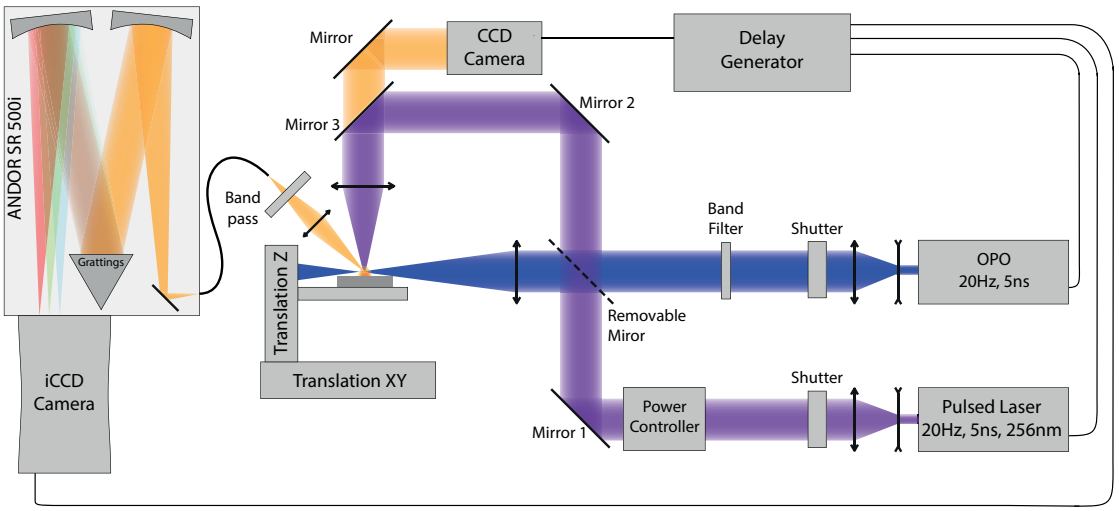

Figure 5.2: Scheme of the LIBS LIF experimental set-up.

integrated over all the fibers, sacrificing spatial resolution.

In such an experiment, the synchronization of the two lasers and the iCCD camera is crucial. It is achieved using a digital delay generator DG645 from Stanford Research System. Such a delay generator is able to create different pulses output signals with a repetition rate up to 10 MHz and a jitter bellow 25 ps.

In order to limit the jitter on the lasers, both of them are double triggered. The time between the flashlamp trigger and the Q-switch trigger is optimized for each laser[†]. The delay time between both laser pulses is adjusted by changing the Q-switch trigger time of the OPO. This delay is 0 when both laser pulses arrive at the target simultaneously. Before each measurement, the Q-switch trigger time of the OPO corresponding to a 0 delay time is measured by maximizing both laser signals on the iCCD camera with a gate width of 5 ns. The delay time is taken as the change of this Q-switch trigger time.

Acquisition delay is set by the digital delay generator while gate width is set directly in the Solis software from ANDOR. Delay usually corresponds to the OPO pulse in order to increase the LIF signal and gate width is usually 10 ns as the emission time is short. Increasing it does not increase LIF signal but adds noise. In the case of the measurement of the excitation state life-time, delay on the iCCD camera is changed in order to measure the evolution of the signal depending on

[†]It corresponds to balancing the flash exposition time which brings energy to the crystal and the de-excitation time of the crystal. Changing that time considerably reduces the power of the pulse. Usually, these triggers are generated internally.

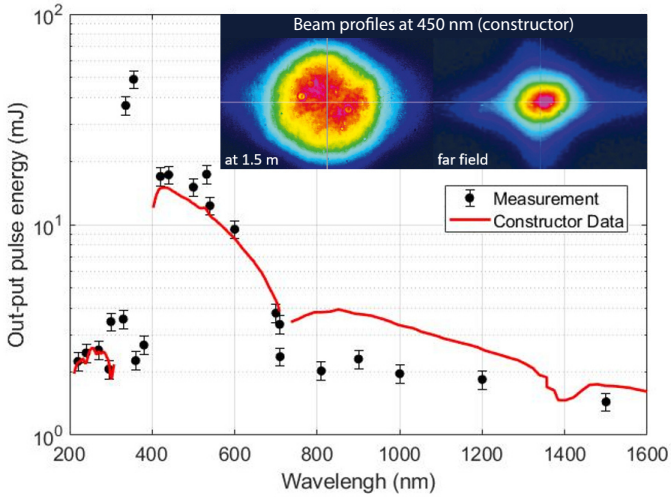

Figure 5.3: Measurement of the OPO power output at different wavelengths and data supplied by the manufacturer. Insets correspond to beam profiles measured by the manufacturer at two different distances.

time.

A second computer drives the rest of the experiment, shutters, translation, and in particular the OPO. I coded a small LabVIEW interface that enables to change the excitation wavelength of the OPO during an acquisition sequence and record the wavelength measured by the WaveMaster, so that excitation emission maps could be measured.

In short: *Here, LIF is coupled to LIBS in order to study molecules in the laser-generated plasma. The spectroscopic set-up is the same as the one described in the chapter 4 added with a tunable laser (OPO). The OPO wavelength can be tuned in order to excite precise transitions in the AlO molecules.*

5.3 Measurement on AlO

5.3.1 De-excitation time and collisions

Pulsed LIF can be used to measure the de-excitation time of AlO molecules in a laser-generated plasma. For practical purposes, it was important to know this de-excitation time in order to optimize the gate width for the acquisition. In a theoretical context, this de-excitation time also applies to LIBS emission spectrum studied in the chapter 4.

For this measurement, the ablation laser creates a plasma from a moving alumina target. The OPO wavelength is set to 487 nm in order to excite AlO (1,1) bandhead transitions. The delay between the two pulses is set to 10 μs. It corresponds to a good compromise between maximizing the LIF signal and minimizing the LIBS emission. After such a delay, the concentration of AlO remains important, but the plasma already cooled down significantly. The acquisition gating is set to its minimum (5 ns). The delay between the OPO and the acquisition is changed 30 times by 1 ns steps and starts about 5 ns before the OPO pulse. Each measurement represents an average signal from 100 pulses.

The spectra obtained are represented on figure 5.4 (a). One can observe 4 emission peaks corresponding to bandheads (0,1) at 507 nm, (1,2) at 510 nm, (2,3) at 513 nm and (3,4) at 515 nm. As expected from the de-excitation path, the (1,2) signal is more important as the vibrational level of the upper state is the one populated by the excitation. Yet, before de-excitation, other vibrational levels are populated. This is mainly due to collision with the surrounding gas[‡].

The intensity of the signal also depends on the delay time between the OPO excitation pulse and the acquisition. Before the excitation pulse, for 0 ns almost no signal is measured as the molecules are not excited. The remaining LIBS signal can be neglected. When the delay increases, the signal first increases rapidly and then decreases exponentially. By fitting this evolution, one can measure the effective radiative life-time τ of the molecules.

The intensity of the emission due to a population of molecules excited at a given time decreases exponentially. Because the excitation pulse is not short compared to the desexcitation time of the molecules, one needs to take it into account. The excitation rate of the molecules is proportional to the intensity of the laser pulse. This intensity evolves as a Gaussian function $\mathcal{G}(t)$ with a FHWM = 3.2 ns. Considering an infinite reservoir of molecules in the ground state and neglecting stimulated emission, one can write the intensity of the emission as the convolution

[‡]In larger molecules, vibrational intramolecular relaxation are usually much quicker than spontaneous fluorescence emission. Fluorescence emission corresponds to the relaxed state of the molecule as proposed by the american spectroscopist Michael Kasha in 1950[223]. In the case of small molecules such as AlO, intramolecular relaxation is not dominant.

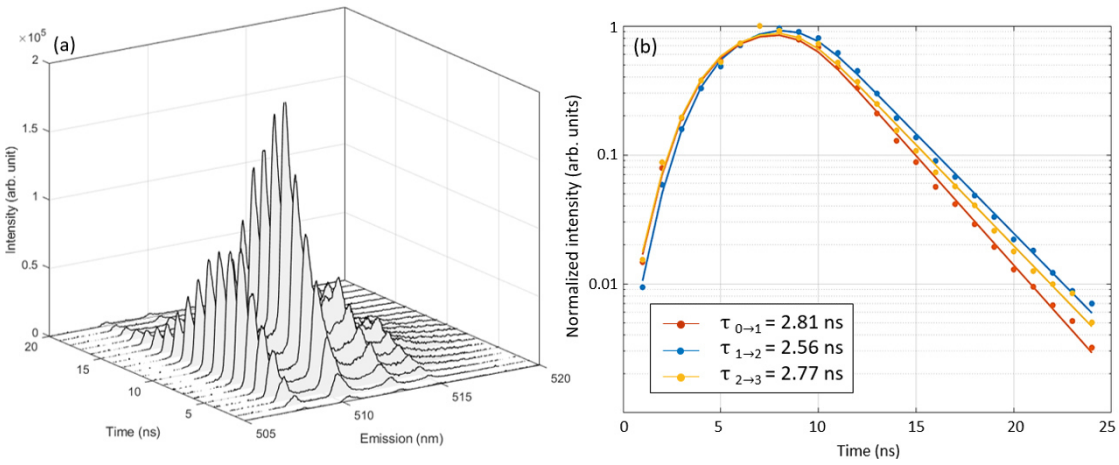

Figure 5.4: (a) LIBS-LIF spectra of AlO after 10 μs for an excitation of 487 nm corresponding to the (1,1) resonant absorption. The acquisition gate width is 5 ns and is shifted to observe the emission decay. (b) Integrated area of each peak (over 0.5 nm) normalized in terms of the time plotted in a log scale. The signal is fitted by an exponential decay with a constant τ convoluted by a Gaussian excitation pulse FHWM = 3.2 ns and a square gate of measurement of 5 ns.

product of the OPO pulse intensity and an exponential decay:

$$I(t) = \mathcal{G}(t) \circledast e^{-\frac{t}{\tau}} \tag{5.1}$$

Finally, the acquisition is not infinitely fast but integrated over a gate $\Pi(t)$ of 5 ns. The signal recorded $S(t)$ is the convolution product of the gate with the emission $I(t)$:

$$S(t) = \Pi(t) \circledast I(t). \tag{5.2}$$

Figure 5.4 (b) represents the normalized signal of the three first peaks integrated over 0.5 nm as a function of the delay time. After 10 ns, the decay is purely exponential as the excitation pulse is over. The solid lines correspond to fits of the data by the function described above considering a Gaussian function for the OPO pulse shape and a square gate for the acquisition. As we can see, it fits the measurements very well, indicating that the hypothesis of the calculation are justified. In particular, the amount of molecules in the ground state is large enough to consider it as an infinite reservoir. It also provides a measurement of the de-excitation time of these transitions: $\tau_{0,1} = 2.81$ ns, $\tau_{1,2} = 2.56$ ns, $\tau_{2,3} = 2.77$ ns. These values are very short compared to tabulated radiative life-time from NIST corresponding to $\tau \simeq 100$ ns for $v' = 0, 1, 2$[224]. Yet, such observations are consistent with Nagli et al. who reported a " decay time as rapid as OPO pulse of 4 ns [...] shorter than these

delay (μs)	n_X (cm^{-3})	T (K)	τ^{-1} (s^{-1})	number of collisions
2	2×10^{20}	6500	3.2×10^{11}	870
10	2×10^{18}	3000	2.2×10^{9}	6
30	4×10^{18}	1800	3.4×10^{9}	9

Table 5.1: Collision frequencies between atoms in the plasma and AlO molecules and average number of collisions within the life-time of AlO($B^2\Sigma^+$) state for various delays. The density of atoms and the temperatures are estimated from the model presented in the chapter 3 in the figure 3.11.

molecules radiative times". They attributed this difference to collisional quenching and thermal quenching[211]. Indeed, the typical decay time for this AlO system has been measured at low pressure (20 Pa) around 120 ns[224,219] where our measurements are made at atmospheric pressure. Such difference is important when using this radiative life-time in order to determine the ratio of species in the plasma from emission ratio[46,203]. One should take care to measure the effective radiative life-time in similar conditions.

One can estimate the typical collision frequency in the plasma between an atom X and an AlO molecule considering the kinetic temperature T of perfect gas with a density of the atoms n_X as:

$$\tau^{-1} = n_X \sigma \sqrt{\frac{8 k_B T}{\mu \pi}} \tag{5.3}$$

with μ the reduced mass of the system and σ the cross-section of collision. Just like in chapter 2, we consider here a plasma composed of 2/5 of aluminum atoms and 3/5 of oxygen atoms. The average mass of an atom is 3.39×10^{-26} kg and the mass of AlO is 7.14×10^{-26} kg such that $\mu = 2.30 \times 10^{-26}$ kg. The average radius of an atom is $r_X = 1.65$ Å such that the cross-section of the collision can be approximated by $\sigma = \pi(r_X + \sqrt{r_{Al}^2 + r_O^2})^2 = 5.12 \times 10^{-19}$ m^2[§]. The model presented in the chapter 3 gives an estimation of the atoms density and temperature in the plasma. Considering these values for different delays, one can estimate the collision frequency and the average number of collisions within the lifetime of AlO($B^2\Sigma^+$). These values are reported in table 5.3.1 for delays of 2 μs, 10 μs, and 30 μs. The uncertainties due to the model are important and one should consider these values as estimations of the order of magnitude. For a short delay, the plasma is dense

[§]Van der Waals radius is chosen because it refers to the potential which is more relevant for collision cross-sections.

and the number of collision expected is high. However, AlO molecules mostly appear after 10 μs. For such long delays, the density of the plasma drops a lot due to the blast expansion. The number of expected collisions is thus very low, less than 10, and rather stable. However, a single collision can change J by many units, explaining the collisionally-induced LIF observed in laser generated plasma despite short radiative life-time.

5.3.2 Looking for Al_2O

Usually, LIF is used in order to study the emission spectra of a system for one or several given excitation wavelengths. This was done on AlO molecules produced by laser ablation by Nagli et al. in 2016[211]. In the case of molecules such as Al_2O, with unknown structure, the task is more complicated as there is no precisely known transition to excite. As far as I am aware, only two papers claim to identify Al_2O from fluorescence spectroscopy.

The first one is a paper written by Cai et al. in 1991. They used a dye laser to excite a molecular beam in the UV region. Thanks to high resolution absorption spectroscopy, they identified Al_2O molecules from its complex rotational structure around 38249 cm^{-1} (261.44 nm). Exciting the molecules on this transition, they observed a few fluorescence signals red-shifted around 38150 cm^{-1}, 37740 cm^{-1}, 37200 cm^{-1} and 36250 cm^{-1} (262.12, 264.97, 268.82 and 275.86 nm). The fluorescence life-time of the molecules was measured to be around 100 ns. In the case of LIBS, with larger densities, one can expect this life-time to be greatly reduced. Reproducing the absorption results with our experiment is impossible because the OPO does not have enough spectral resolution. When exciting the plasma at 261.44 nm, no significant emission was observed at the fluorescence wavelength observed by Cai et al. whatever the delay time between the ablation pulse and the OPO pulse. Fluorescence measurements for such small shifts is complicated because of the OPO width and some diffusion in the plasma adding a strong background signal. To limit it, one should shift the acquisition time away from the OPO pulse, reducing the fluorescence signal in so doing.

One of the great interests of using tunable OPO is to measure excitation/emission maps of the molecules. excitation/emission mapping of molecules, or 2D fluores-

In short: *Using LIF, one can excite molecules in the plasma and determine the life-time of the excited state. For AlO molecules, the life-time of the $\Delta v = -1$ transitions is measured after 10 μs to be 2.7 ± 0.2 ns. This time is much lower than the tabulated life-time due to collisions in the plasma. Such a short life-time is important because it limits the number of collisions and the thermalization of the excited state.*

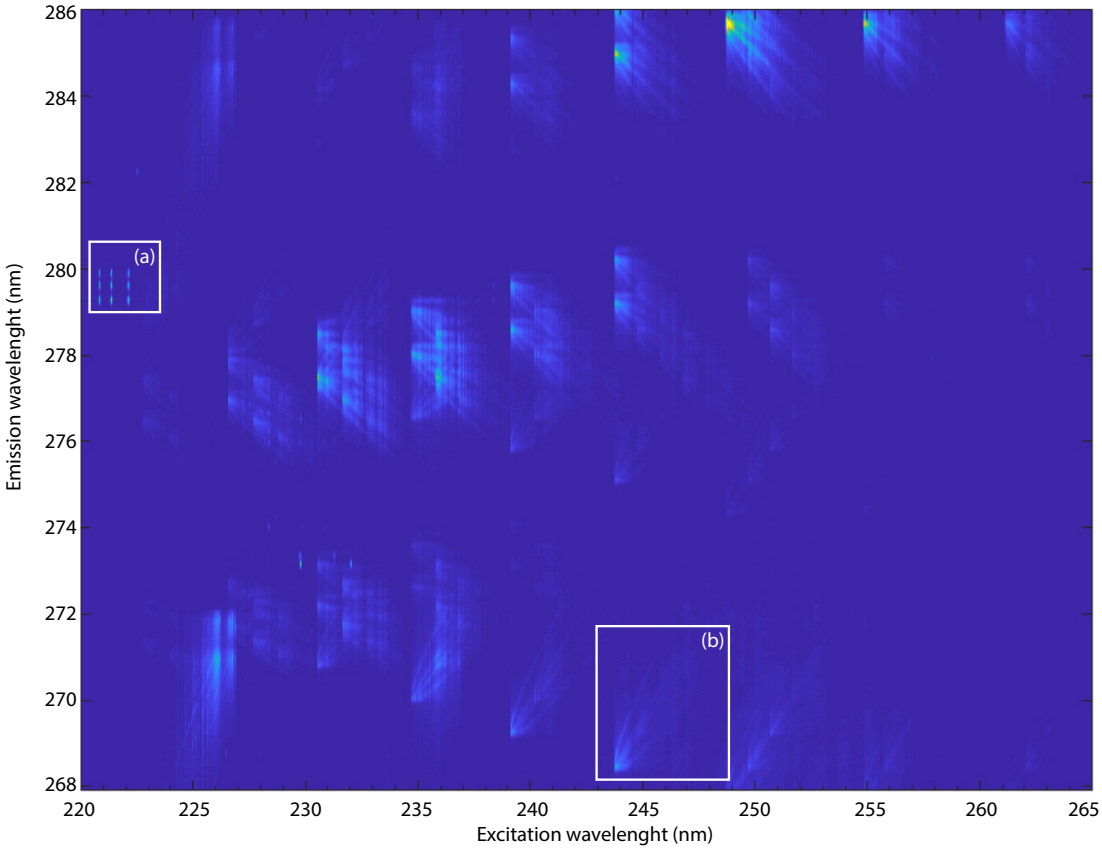

Figure 5.5: Example of the excitation/emission map measured on a plasma generated from aluminum target in air in the region of expected signal for Al_2O molecules. Delay between the ablation and OPO pulse is 30 μs and the gate width is 10 ns. Single peaks between 279 and 280 nm (a) correspond to atomic fluorescence while *fish-bone* patterns (b) correspond to diatomic molecule, in that case mostly corresponding to the $D^2\Sigma^+ - A^2\Pi_i$ system of AlO.

cence spectroscopy is developed in order to probe complex chemical environments and to elucidate rovibronic structure of polyatomic molecules[225,226,227]. On AlO, it was recently measured from a molecular beam in order to study the Stark Effect and Zeeman Effect on the transitions[228]. In the quest of finding Al_2O molecules, I measured many excitation/emission maps changing the target, the delay, the gate width, the excitation and emission region and adding argon flow. Argon is used to decrease the amount of oxygen in the plasma in order to get closer to Cai et al.'s experimental conditions. Figure 5.5 shows as an example a map measured from an aluminum target under argon flow. The excitation region was chosen to be a large UV region encompassing Cai et al. excitation range. The emission region is far

enough from the OPO wavelength for the acquisition not to saturate. The delay between the ablation pulse and the OPO is 30 μs and the gate width is 10 ns. On this map, one can observe many *fish-bone* patterns typical of diatomic molecules' fluorescence (see white square (b)). Here, most of the patterns you see are from AlO transitions in the $D^2\Sigma^+ - A^2\Pi_i$ system. Single peaks corresponds to atom's fluorescence (see white square (a)). The pattern on the bottom left, slightly different from AlO ones, appears even ablating air alone. It could correspond to NO molecules which have transitions around 226 nm. I was never able to assign such a pattern to a triatomic molecule.

A second paper claims to have found Al_2O molecules in LIBS experiment using fluorescence. It was published in 2016 by Lei Liu et al. in Optics express[221]. They used a very similar LIBS-LIF system in order to look for Al_2O molecules. They claim that series of excitations in the UV region (250.14, 255.38, 256.00 and 261.40 nm) lead to fluorescence signal of Al_2O molecules with a Stokes and anti-Stokes of about 100 meV. They base their argumentation on the fact that Cai et al. reported a transition for Al_2O at 261.44 nm, but they did not measure the same fluorescence peaks as Cai et al.. The dynamics of Al_2O Liu et al. measured from these transitions is surprisingly close to the one of AlO molecules they also measured. As we have seen on the map 5.5, this region is full of transitions corresponding to the $D^2\Sigma^+ - A^2\Pi_i$ system of AlO. It is possible that what Liu et al. measured corresponds to some AlO fluorescence of the $D^2\Sigma^+ - A^2\Pi_i$ system. In order to prove it, excitation/emission mapping of the region would be very helpful but with the actual set-up, the signal is dominated by some diffuse light from the OPO. The Stokes shifts are too small compared to the width of the OPO excitation pulse.

5.3.3 2D AlO spectrum

This section focuses on the AlO fluorescence spectroscopy of the $B^2\Sigma^+ - X^2\Sigma^+$ system and more precisely excitation corresponding to $\Delta v = 0$ transitions: (0,0), (1,1), (2,2) etc. and emission corresponding to $\Delta v = -1$ transitions: (0,1), (1,2), (2,3) etc.

In order to measure the excitation/emission spectrum of AlO molecules, a plasma is created by ablation of a pure alumina target in air. The delay between the ablation and the OPO pulse is set to 30 μs. The acquisition starts just after the OPO pulse and the gate width is 5 ns. The wavelength of the OPO is changed from 483 nm to 492 nm in steps of 0.05 nm, that is to say about the FHWM of the laser, in order to achieve the best resolution. A shortpass Filter FES0500 from Thorlabs is positioned on the OPO beam pass in order to remove any signal below 500 nm. The acquisition of the spectrum is done with the Shamrock 500i in the

range 507 nm to 516 nm. The entrance slit is 10 μm leading to a spectral resolution of the measurement of about 0.05 nm. Each spectrum is accumulated 50 times. In total this corresponds to 9000 shots or 1h 15min acquisition. A reference LIBS spectrum acquired in the same conditions but without the OPO excitation pulse is subtracted from each spectrum. Then, optical noise determined from the average intensity for $\lambda < 507.5$ nm is subtracted. The resulting 2D map is presented on figure 5.6 (c).

As expected the main emission peaks corresponds to the (0,1) fluorescence at 507.8 nm following (0,0) excitation at 484.2 nm, the (1,2) fluorescence at 510.0 nm following (1,1) excitation at 486.6 nm and the (2,3) fluorescence at 512.1 nm following the (2,2) excitation at 488.8 nm. These peaks have the largest intensities because they correspond to band-heads with a large density of nearly overlapping rovibrational transitions (See Fortrat diagram 5.6 (a)). Furthermore, the transitions for low vibration states, namely (0,0) excitation and (0,1) de-excitation, have a larger intensity. Indeed, low excited states are more populated.

On the 2D map, one can observe curved "branches". These branches correspond to direct emission from the rotational states J' populated by the laser pulse excitation. When the plasma is irradiated by the OPO at a given wavelength, some molecules will absorb photons and get excited. Absorption occurs if the difference in energy matches the energy of the photon and if the transition is allowed i.e. respects the electric dipole selection rules. For AlO $X^2\Sigma^+ - B^2\Sigma^+$ system, these include $\Delta K = \Delta J = \pm 1$ (See complete selection rules in the section 4.1.2). As discussed in the chapter 4, this corresponds to the four branches R_1, R_2 and P_1, P_2 represented in blue on figure 5.6 (a)¶. For instance, a photon of about 485.3 nm, can excite the transitions from $v'' = 0,\ K'' \simeq 16$ to $v' = 0,\ K' \simeq 16 + 1$ corresponding to $\Delta K = \Delta J = +1$ (R branch), or from $v'' = 0,\ K'' \simeq 53$ to $v' = 0,\ K' \simeq 53 - 1$ corresponding to $\Delta K = \Delta J = -1$ (P branch). Thus, two different upper states with J'_1 and J'_2 are populated from this excitation wavelength. Then, from each of these two excited states, one can consider two de-excitation paths following the selection rules applied to the observed transitions $\Delta v = -1$. These selection rules correspond to the branches R and P represented in red on the figure 5.6 (a). For this example, it corresponds to the transitions from $v' = 0,\ K' \simeq 16+1$ to $v''' = 1,\ K''' \simeq 16+1\pm1$ and from $v' = 0,\ K' \simeq 53-1$ to $v''' = 1,\ K''' \simeq 53 - 1 \pm 1$. This lead to 4 groups of transitions centered around 507.95, 508.7, 509.1 and 512.1 nm (see emission spectrum in black in the figure 5.6 (a)). This mechanism applied on all excitation wavelengths leads to the 4

¶In the case of AlO, the branch ${}^{P}Q_{12}$ and ${}^{R}Q_{21}$ corresponding to $\Delta K = \pm 1$ and $\Delta J = \pm 0$ are almost lost beneath the branches R and P. For $J > 5$, their intensities are at least 100 times lower than the ones of the branches R and P. In order to clarify the discussion, they are not plotted on the figures here but are taken into when fitting the spectra.

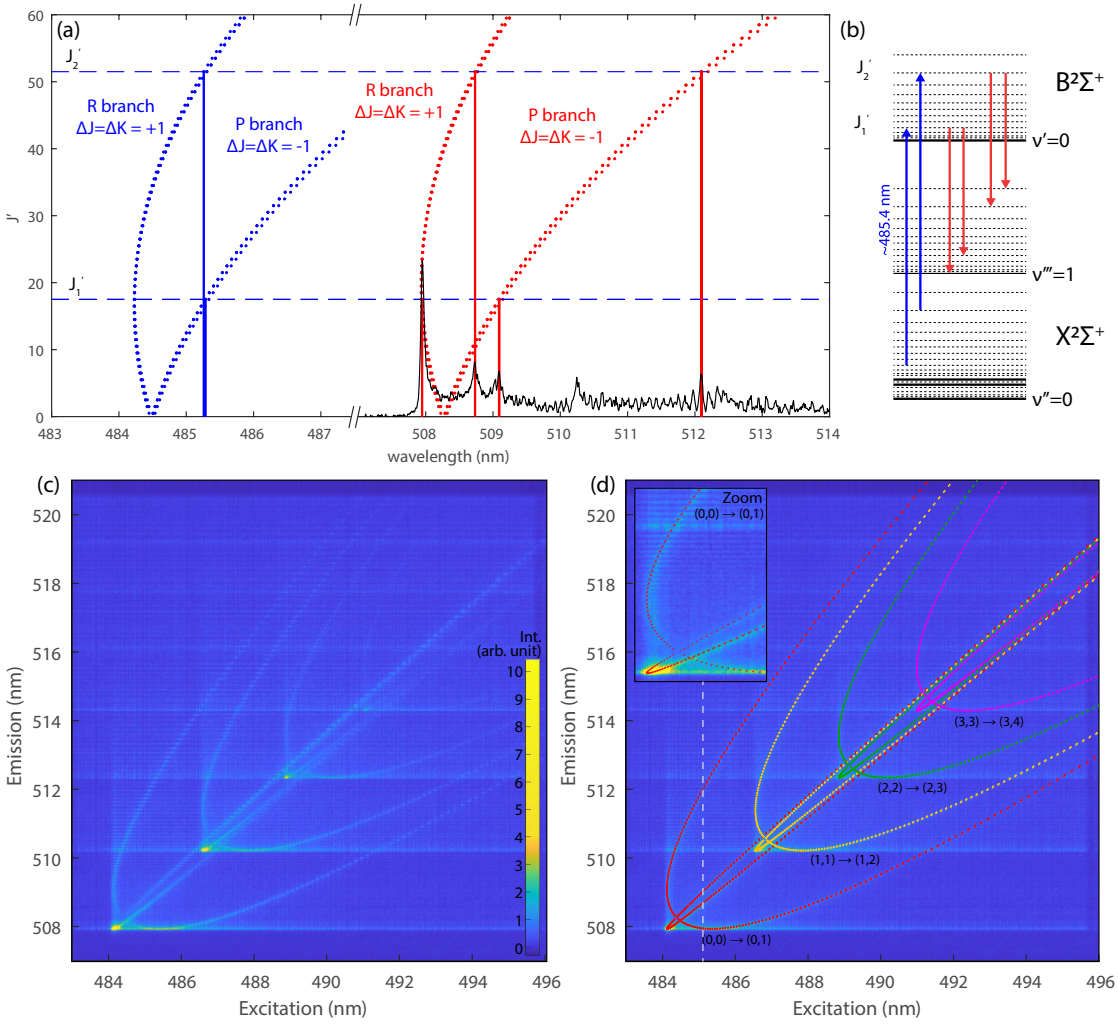

Figure 5.6: (a) Fortrat diagram for the $B^2\Sigma^+ - X^2\Sigma^+$ system of the AlO molecule calculated for the transition (0,0) in blue and (0,1) in red. For an absorption around 485.3 nm (blue line), the conservation of upper state (v', J') leads to 4 groups of emissions peaks (red lines) observed on the experimental LIF spectrum (black). (b) Same example represented on an energy level scheme (c) 2D excitation/emission of an AlO molecule for a delay of 30 μs. (d) Superposition of the 2D excitation/emission spectrum with theoretical transitions conserving v' and J' and spin number. The very weak Q branches are not shown. The spectrum presented in (a) corresponds to the white dashed line. Intersection with the four red branches correspond to the four emission peaks.

red branches in the excitation/emission map on figure 5.6 (d). The example given in the figure 5.6 (a) corresponds to the white dashed line. This reasoning also stands for the other vibrational levels and the branches are represented in yellow for $v' = 1$, green for $v' = 2$ and purple for $v' = 3$. The inset corresponds to a zoom on the (0,0) $\longrightarrow$ (0,1) bandhead transitions and shows the good agreement between the measured spectrum and the transition conserving J'. The intensity of the signal decreases for large values of J'. These states are populated by the excitation of ground state molecules with large value of J''. For a given temperature in the plasma, these states are poorly populated.

On figure 5.6 (c), one can observe horizontal lines. These horizontal lines correspond to collisionally-induced LIF. No matter the excitation wavelength, some excited molecules undergo inelastic energy transfer, changing rotation and vibration quantum numbers. Emission is observed from a multitude of excited state levels. This emission is similar to emission observed in LIBS and horizontal lines corresponds to the different peaks in the AlO emission spectrum. In particular, one can notice horizontal lines corresponding to the band-head emission at 507.8nm for the (0,0) transitions, 510.0 nm for the (1,1) transitions, 512.1 nm for the (2,2) transitions and so on.

The vertical lines observed for excitation at 484.2 nm, corresponding to (0,1) bandhead, 486.6 nm, corresponding to (1,2) bandhead etc. are due to large absorption of the OPO pulse by the ground state population of molecules due to the large density of states. This leads to an important population of excited molecules and thus a larger fluorescence signal.

In short: *The wavelength of the OPO laser pulse can be changed automatically and enables excitation/emission mapping of the plasma. Such a mapping reveals interesting features of molecules. Resonant absorption on the molecules excites states from different branches (R and P for AlO) with different angular momentum J. Part of the excited molecules keeps this angular momentum before desexcitation. This is direct LIF emission. In the case of AlO, this leads to 4 emission peaks shifting with the excitation wavelength, creating fish-bones like patterns. These patterns can be used to identify the molecules in the plasma and determine their rovibrational structure, which could be particularly interesting for unfamiliar molecules such as* Al_2O.

5.3.4 LIF spectrum calculation

In order to calculate the LIF spectrum, one has to consider both the excitation and de-excitation process from the electronic state n'' ($X^2\Sigma^+$) to the electronic state n' ($B^2\Sigma^+$). The LIF spectrum can be described as the superposition of direct fluorescence conserving J' and S' and relaxed fluorescence due to population transfer in the excited state (collisionally-induced LIF). The population redistribution can be approximated by Boltzmann distributions. By fitting the LIF spectra with a sum of both components, direct LIF and relaxed LIF, I am able to determine effective temperatures describing the redistributed states and the temperature of the ground state molecules.

Calculation of direct LIF

In order to calculate the direct LIF spectrum, I consider the following excitation/de-excitation path conserving v', and J':

$$(n'', v'', J'') \rightarrow (n', v', J') \rightarrow (n''', v''', J''') \tag{5.4}$$

The population of the ground state n'' ($X^2\Sigma^+$) is described by a rotational and vibrational temperatures T''_{rot} and T''_{vib} such that the density of molecules in the state (n'', v'', J'') is:

$$N_{n'',v'',J''} = \frac{N_{n''}}{2} \cdot (2J''+1) \cdot \frac{exp\left(-\frac{hc \cdot F_{v''}(J'')}{k_B \cdot T''_{rot}} \right)}{Qrot_{n'',v''}(T''_{rot})} \cdot \frac{exp\left(-\frac{hc \cdot G_{n''}(v'')}{k_B \cdot T''_{vib}} \right)}{Qvib_{n''}(T''_{vib})} \tag{5.5}$$

This expression is the same as the one used in chapter 4 with the difference that here it describes the ground state. Considering transitions from the same electronic state, $Qvib_{n''}(T''_{vib})$ is a constant and $Q_{rot} \simeq k_B T''_{rot}/B''_{v''}$ such that:

$$N_{n'',v'',J''} \propto (2J''+1) \cdot \frac{B_{v''}}{k_B T''_{rot}} exp\left(-\frac{hc \cdot F_{v''}(J'')}{k_B \cdot T''_{rot}} \right) \cdot exp\left(-\frac{hc \cdot G_{n''}(v'')}{k_B \cdot T''_{vib}} \right) \tag{5.6}$$

The population of the upper state (n', v', J') is considered to be zero before any excitation. This is not strictly true, but LIBS emission is much weaker than LIF signal, meaning the population of the excited state before excitation is low compared to the population after excitation. Furthermore, the LIBS contribution is subtracted from LIF spectra. When the OPO pulse passes through the plasma, some molecules absorb photons resonant with a molecular transition and are ex-

cited. The population variation of the upper state $N_{n',v',J'}$ is:

$$\frac{dN_{n',v',J'}}{dt} = \rho(\nu) \cdot B^{n',v',J'}_{n'',v'',J''} \cdot N_{n'',v'',J''} \tag{5.7}$$

with $B^{n',v',J'}_{n'',v'',J''}$ the Einstein coefficient for absorption and $\rho(\nu)$ [J.s.m^{-3}] the radiance of the OPO pulse at the resonant wavelength. The Einstein coefficient for absorption can be related to the spontaneous coefficient through the following relation:

$$\begin{aligned} B^{n',v',J'}_{n'',v'',J''} &= \frac{(2J'+1)}{(2J''+1)} \frac{c^3}{8\pi h\nu^3} A^{n',v',J'}_{n'',v'',J''} \\ B^{n',v',J'}_{n'',v'',J''} &= \frac{(2J'+1)}{(2J''+1)} \frac{c^3}{8\pi h\nu^3} A^{n',v'}_{n'',v''} \frac{S^{J'}_{J''}}{2J'+1} \\ B^{n',v',J'}_{n'',v'',J''} &= \frac{S^{J'}_{J''}}{(2J''+1)} \frac{c^3}{8\pi h\nu^3} A^{n',v'}_{n'',v''} \end{aligned} \tag{5.8}$$

The population of the upper state is given by the integration of this transition rate on the duration of the OPO pulse:

$$\begin{aligned} N_{n',v',J'} &\propto \frac{\rho(\nu)}{\nu^3} \cdot A^{n',v'}_{n'',v''} \cdot \frac{S^{J'}_{J''}}{(2J''+1)} \cdot N_{n'',v'',J''} \\ N_{n',v',J'} &\propto \frac{\rho(\nu)}{\nu^3} \cdot A^{n',v'}_{n'',v''} \cdot S^{J'}_{J''} \cdot \frac{B_{v''}}{k_B T''_{rot}} \cdot exp\left(- \frac{hc \cdot F_{v''}(J'')}{k_B \cdot T''_{rot}} \right) \cdot exp\left(- \frac{hc \cdot G_{n''}(v'')}{k_B \cdot T''_{vib}} \right) \end{aligned} \tag{5.9}$$

The emission signal is thus proportional to:

$$\begin{aligned} I^{n',v',J'}_{n''',v''',J'''} &\propto A^{n',v',J'}_{n''',v''',J'''} \cdot N_{n',v',J'} = A^{n',v'}_{n''',v'''} \cdot \frac{S^{J'}_{J'''}}{2(J'+1)} \cdot N_{n',v',J'} \\ I^{n',v',J'}_{n''',v''',J'''} &\propto \frac{\rho(\nu)}{\nu^3} \cdot A^{n',v'}_{n''',v'''} \cdot A^{n',v'}_{n'',v''} \cdot \frac{S^{J'}_{J'''} \cdot S^{J'}_{J''}}{2(J'+1)} \\ &\quad \times \frac{B_{v''}}{k_B T''_{rot}} \cdot exp\left(- \frac{hc \cdot F_{v''}(J'')}{k_B \cdot T''_{rot}} \right) \cdot exp\left(- \frac{hc \cdot G_{n''}(v'')}{k_B \cdot T''_{vib}} \right) \end{aligned} \tag{5.10}$$

Calculation of relaxed LIF

Within the effective excited state life-time, the excited state (n', v', J') population is partially redistributed over other quantum levels. The processes redistributing the population of the excited state are complex and impossible to fully determine with such a measurement. The spectral and temporal resolution are not good enough. Here we chose to describe the redistributed population using two Boltzmann distributions with effective temperatures: one for the vibrational states described by T'_{vib} and one for the rotational state described by T'_{rot}. Here, Boltzmann distributions are approximations of the real population distribution. One should consider these temperatures as parameters and not proper temperatures. The higher these parameters, the larger the population in states with high quantum levels and large energy. The intensity of each transition is proportional to:

$$I^{n',v',J'}_{n'',v''',J'''} \propto A^{n',v'}_{n',v'''} \cdot S^{J'}_{J'''} \cdot \frac{B_{v'}}{k_B T'_{rot}} \cdot exp\left(-\frac{hc \cdot F_{v'}(J')}{k_B \cdot T'_{rot}}\right) \cdot exp\left(-\frac{hc \cdot G_{n'}(v')}{k_B \cdot T'_{vib}}\right) \quad (5.11)$$

Just like in the previous chapter 4.4.1, the spectrum is calculated by summing all the transition convoluted by a Gaussian function of width σ. Both spectra are normalized by their integer. The final spectrum is the sum of both spectra pondered by a given coefficient x:

$$I = x \times \frac{I^{relaxed}_{LIF}}{\int I^{relaxed}_{LIF}} + (1-x)\frac{I^{direct}_{LIF}}{\int I^{direct}_{LIF}} \quad (5.12)$$

Here, x gives the ratio between the integrated direct LIF signal and the integrated relaxed LIF signal. The closer the value of x to one, the more important is the redistribution of the excited state.

5.3.5 Fit and Results

The fitting process is very similar to the one discussed in chapter 4, section 4.4.1. The emission spectra first have the LIBS signal subtracted. LIBS signal is obtained

In short: *The LIF spectrum can be decomposed in one direct LIF emission conserving the excited state of the molecules and a relaxed LIF emission in which the excited state (J and v) changed because of couplings and collisions. The first one can be used to probe the ground state of the molecules as emission is directly related to the excitation of these molecules. This enables to determine the temperature of the ground state molecules.*

in the exact same condition but without OPO excitation. They are then corrected for the system optical response using the black body calibration as explained in the section 4.4.1 and optical noise is removed. For each excitation wavelength λ_e, this corrected spectrum is fit to the calculated spectrum by the least squares method. Here λ_e corresponds to the max of the OPO pulse wavelength measured by the lambda-meter. For each transition, the intensity of the pulse is taken as a Lorentz function centered on λ_e and with FWHM=66 pm. The Lorentz function's width is measured on the Damon spectrometer. In contrary to the previous chapter, the emission wavelength is not a fit parameter as it is precisely determined using the OPO and the lambda-meter for calibration[‖].

Here, the fitting parameters are T''_{rot} and T''_{vib} describing the ($X^2\Sigma^+$) state, T'_{rot} and T'_{vib} describing the ($B^2\Sigma^+$) relaxed state, the Gaussian function width σ and x. T'_{rot} and T'_{vib} are determined from the relaxed LIF component of the spectrum while T''_{rot} and T''_{vib} are determined from the direct LIF component.

As seen in the chapter 4, section 4.4.1, the vibrational temperature has little effect on the shape of the emission corresponding to $\Delta v = 0$ transitions. Thus, it is very complicated to fit T''_{vib} from such an excitation path. As you can see on figure 5.7 (d), the residues of the fit considering two temperatures for the ground state has no minimum for T''_{vib} and the parameter diverges. Here, T''_{vib} has almost no influence on the determination of T''_{rot} and could be ignored. For practical reason, $T''_{rot} = T''_{vib} = T_{(X^2\Sigma^+)}$ is imposed in the fitting process by considering that the equilibrium in the ground state molecules is reached. It is very likely that both temperatures are equal for the ground state as the life-time is expected to be long enough. In order to fit both temperatures of the ground state, one should consider exciting other transitions such as $\Delta v = \pm 1$. For excitation wavelengths lower than 486.5 nm, $v = 0$ is the only excited state and the fit does not depend on T''_{vib}. This range is particularly useful to fit T''_{rot} even if $T''_{rot} \neq T''_{vib}$.

Figure 5.7 (c) corresponds to the residues map of (b) depending on T'_{rot} and T'_{vib} describing the excited state redistribution for the other parameters kept constant. The red point corresponds to the fitted parameters. The convergence here is very similar to the one described in the chapter 4, section 4.4.1 and enables to determine both the rotational and the vibrational temperatures describing the excited state population after redistribution.

Figure 5.7 (a) and (b) represent the calculated LIF spectrum (in red) fitted on the LIF spectrum measured (in black) for an excitation of 484.80 nm and 488.30 nm respectively. On the bottom of the panel are represented the direct LIF contribution in magenta and the relaxed LIF contribution in blue. The calculated

[‖]30 OPO pulses are recorded for different wavelengths within the detection range and the emission wavelength is measured simultaneously by the lambda-meter. The positions of the peaks are determined using Lorentz fit and the calibration is done using a third order polynomial function.

LIF spectrum manage to accurately reproduce the shape and intensities of the LIF spectrum. On this spectral range, direct LIF represents only 6 to 16% of the integrated intensity signal. However, it is easy to identify as this signal is very well localized. Most of the intensity (around 90%) corresponds to relaxed state emission. This emphasizes the fact that, even if direct LIF is observed, collisions are sufficient to redistribute the excited states of numerous molecules.

Results of the fitted temperatures for each excitation wavelength are presented on figure 5.8. (a) corresponds to the Fortrat diagram of AlO molecules in the excitation range $\Delta v = 0$ for $v' = v'' = 1$ to $v' = v'' = 4$. Vertical dashed lines corresponds to the position of the bandhead. (b) corresponds to the fitted T'_{rot} and T'_{vib} describing the excited relaxed state. One can first notice that the rotational temperature is higher than the vibrational temperature. This might seem surprising regarding the chapter 4, but remember that these temperatures represent the population of the AlO molecules after resonant absorption. There is no direct comparison with the results of the previous chapter.

For excitation below 484 nm, the LIF signal is weak and no direct LIF is observed. The OPO is not resonant with any $\Delta v = 0$ transitions. It corresponds to relaxed LIF signal providing from other resonant absorption for instance $\Delta v = +1$ with large values of J'' and v'' (see Fortrat diagram in figure 4.7). In that case, $T_{X^2\Sigma^+}$ is not measured and $T'_{rot} \simeq 6000\ K$ and $T'_{vib} \simeq 5000\ K$. These values are large because they are the consequence of excitation for large values of J' and v'.

Between 484.5 nm and 486.5 nm, the transitions for $v = 0$ are excited. This leads to an important LIF signal. Here, $T'_{vib} \simeq 2000\ K$ is really low. One can understand that as the fact that excitation corresponds to the lower vibrational level. Even after redistribution of the excited states**, most of the molecules remain in a low vibrational state. Hence, the low vibrational temperature. Around 484.5 nm, the rotational temperature T'_{rot} drops to $\simeq 4000\ K$. This range corresponds to the $v = 0$ bandhead with a large density of rovibrational transition with low values of J. Even after redistribution, most of the molecules remain in a low rotational state. Hence, the drop of the rotational temperature. In contrary to the vibrational temperature, T'_{rot} increases between 484.5 nm and 486.5 nm as the transition excited have larger and larger values of J.

Between 487 nm and 488.8 nm, the transitions for $v = 0$ and $v = 1$ are excited. One can observe a jump in the vibrational temperature. In this range, the excited states correspond to the first two vibrational states. After mixing, the molecules remain with higher vibrational states. At the position of the (1,1) bandhead, the vibrational temperature peaks. In this region, the density of the transition corresponding to $v = 1$ is larger and most of the excited molecules end in this

**Generally, changes of the excited state reducing the energy of the system are favored.

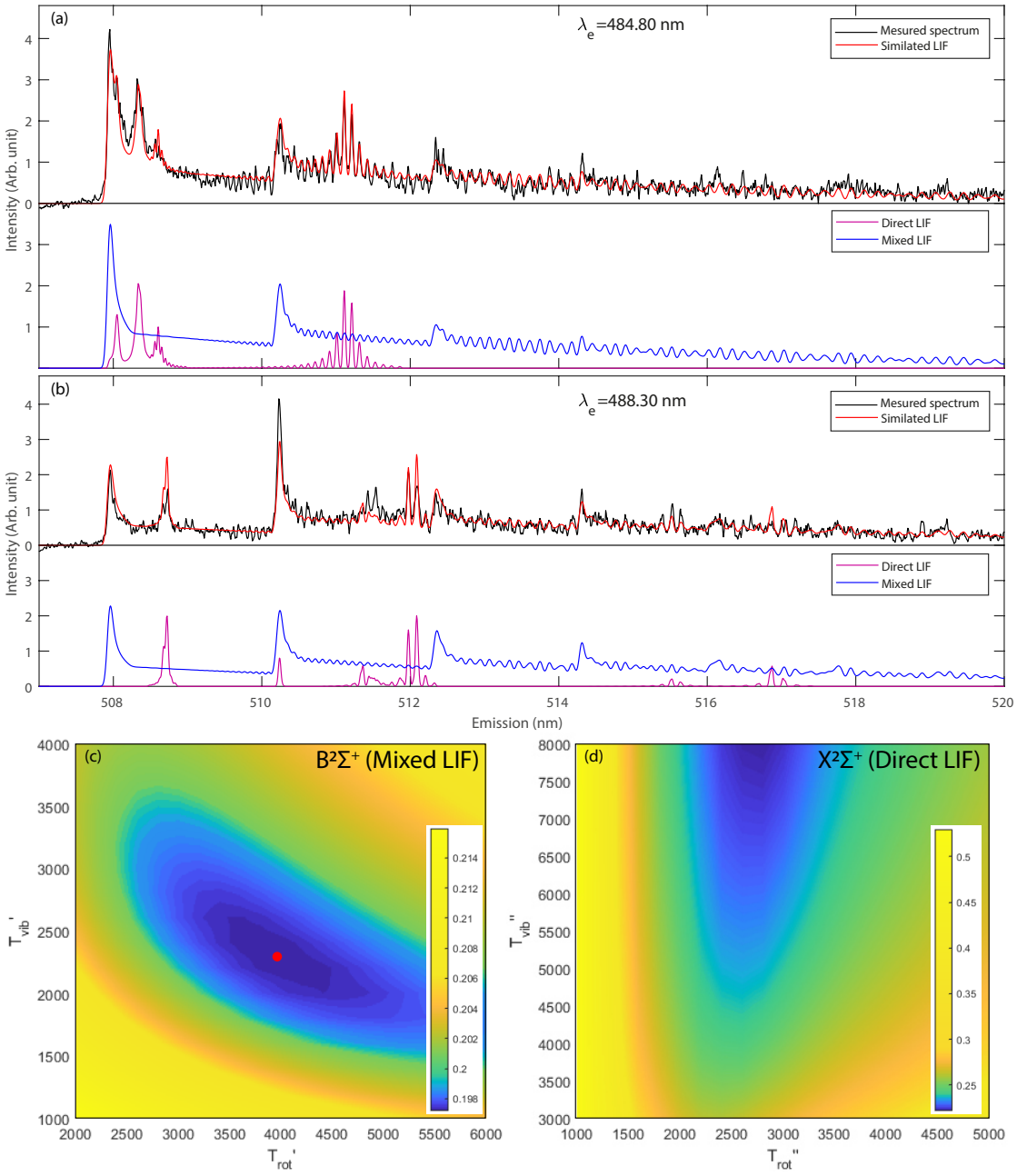

Figure 5.7: Example of fitted LIF spectrum (red) on measured spectrum for a delay of 30 μs (black) for the excitation wavelength 484.80 nm (a) and 488.30 nm (b) considering a single temperature $T_{X^2\Sigma^+}$ for the ground state. Lower panels represent the relaxed LIF contribution (blue) and the direct LIF contribution (magenta). (c) corresponds to the residues map of (b) depending on T'_{rot} and T'_{vib} describing the excited relaxed state for the other parameters kept constant. The red point corresponds to the fitted parameters. (d) corresponds to the residues map of (b) depending on T''_{rot} and T''_{vib} describing the ground state for the other parameters kept constant. In the following fit, $T''_{rot} = T''_{vib} = T_{X^2\Sigma^+}$ in order to avoid the T''_{vib} diverging.

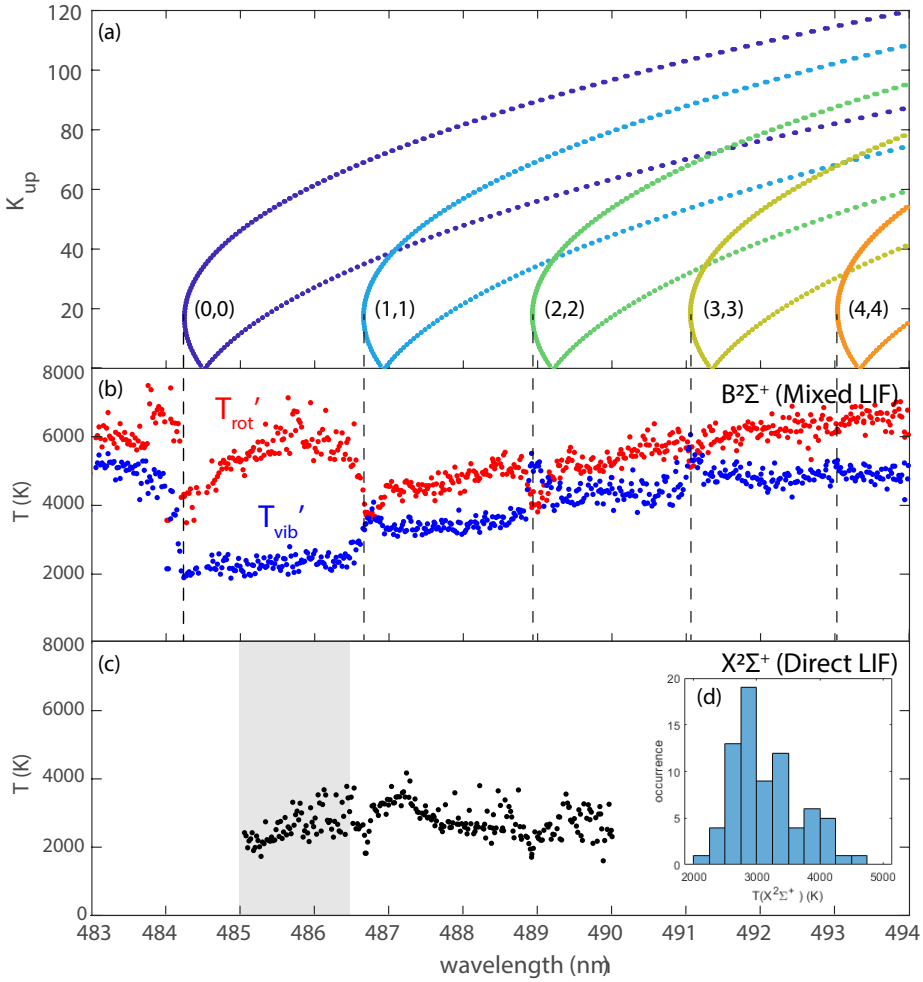

Figure 5.8: (a) Fortrat diagram for the $\Delta v = 0$ excited transitions. (b) Rotational (red) and vibrational (blue) temperatures describing the relaxed LIF emission depending on the excitation wavelength. (c) Temperature of the ground state ($X^2\Sigma^+$) depending on the excitation wavelength measured from the direct LIF emission. (d) Histogram of the ground state ($X^2\Sigma^+$) temperatures corresponding to the selected excitation range in gray. The average value is 3153 K, the standard deviation is 552 K and the standard error is 64 K.

state, hence the increase of the vibrational temperature. For larger wavelength, the difference in state density between $v = 1$ and $v = 0$ is less important and T'_{vib} drops a little. On the contrary, the rotational temperature first drops before increasing for the exact same reason as presented for $v = 0$. The amplitude of the variation is less important as the superposition of both bands smooth the effect.

This pattern keeps going for each of the excited bands with the same observations.

On figure 5.8 (c) is represented the fitted temperature of the ground state $T_{X^2\Sigma^+}$ depending on the excitation wavelength. This temperature is fitted from the direct LIF contribution. Before, 484 nm it is not defined as there is no direct LIF signal. For excitation in the band head $v = 0$, only one group of rotational transition with similar K are excited, and the rotational ground temperature is poorly defined. For excitation wavelength above 484.6 nm, both R and P branches are excited with different K value and the fit on $T_{X^2\Sigma^+}$ converges. After 490 nm, the intensity of the direct LIF signal is too low and the fit on $T_{X^2\Sigma^+}$ does not converge anymore. $T_{X^2\Sigma^+}$ appears to be rather constant on the whole excitation range as expected. It should only depend on the ground state of the molecules. One can notice a slight peak after the $v = 1$ headband. In this region, large resonant intensity and auto-absorption might impact the fit. In order to determine the $T_{X^2\Sigma^+}$ with the best accuracy, I chose to average its values for excitation wavelength between 485 and 486.5 nm (gray range). In that range, $T_{X^2\Sigma^+} = T''_{rot}$. It does not depend on T''_{vib} as only one vibrational state is excited. The histogram $T_{X^2\Sigma^+}$ in this range is potted in (d). The average value is 3153 K, the standard deviation is 552 K and the standard error is 64 K.

This temperature should be compared to the temperatures of the AlO excited state measured from emission spectroscopy. Usually, the rotational temperature of the excited state is assumed equal to the temperature of the ground state. Emission of AlO molecules has been measured before and after the 2D scanning without OPO excitation and fitted by the same process as presented in the chapter 4.4.1. From this fit, one can deduce the vibrational and rotational temperature of the $B^2\Sigma^+$ without any OPO excitation. Values obtained for the vibrational temperatures are: $T_{vib}^{B^2\Sigma^+} = 5385$ and 5858 K which lead to an average of about 5620 ± 240 K. Values obtained for the rotational temperatures are: $T_{rot}^{B^2\Sigma^+} = 3205$ and 3058 K which lead to an average of about 3130 ± 75 K. These values and variations are consistent with the measured values in the previous chapter for a delay of 30 μs (see section 4.4.2). Here, one can see that the rotational temperature of the excited state $T_{rot}^{B^2\Sigma^+}$ seems in good agreement with the rotational temperature of the excited state for a delay of 30 μs. For such a delay, it appears that the rotational temperature of the excited state matches the rotational

temperature of the ground state.

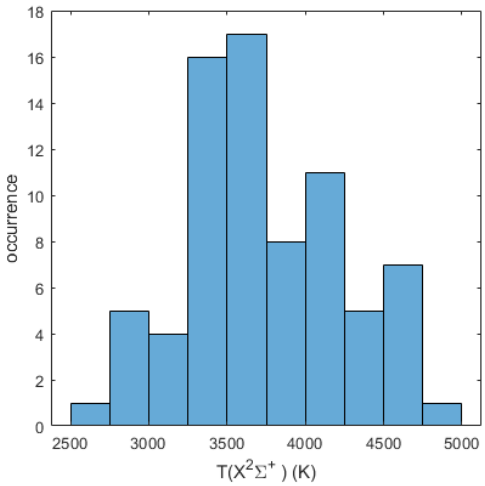

Figure 5.9: Histogram of the ground state ($X^2\Sigma^+$) temperatures corresponding to the excitation range 485-486.5 nm for a delay of 5 μs. The average value is 3728 K, the standard deviation is 547 K and the standard error is 63 K.

The same experiment was run with a delay between the pulse ablation and the OPO excitation of 5 μs. In this case, the fit on the direct emission provides a vibrational temperature $T_{vib}^{B^2\Sigma^+} = 6857 \pm 250$ K and a rotational temperature of $T_{rot}^{B^2\Sigma^+} = 3845 \pm 75$ K. These values are consistent with the measured values in the previous chapter for a delay of 5 μs (see section 4.4.2). The distribution of the ground state temperatures $T_{X^2\Sigma^+}$ for the excitation range 485-486.5 nm is reported in the figure 5.9. The average value is 3702 K, the standard deviation is 531 K and the standard error is 61 K. Here, one can see that the rotational temperature of the excited state $T_{rot}^{B^2\Sigma^+}$ slightly overestimates the rotational temperature of the excited state for a delay of 5 μs. In that case, the equilibrium between both rotational distribution is not completely reached.

5.4 Conclusion

During my PhD, I built the 2D LIBS-LIF experiments in order to excite atoms and molecules in a laser-generated plasma using a tunable pulsed laser. LIF increases atomic emission by a few orders of magnitude and enables micro LIBS measurements. 2D LIF or emission-excitation maps of the plasma enable to investigate the complex composition of the plasma. It allows easy identification of molecules from characteristic patterns and might be used to identify larger molecules in the research on nucleation. In the framework of my PhD, I used LIF in order to study the thermalization of AlO molecules in the plasma.

In the previous chapter, the spatio-temporal emission of AlO($B^2\Sigma^+$) molecules in the laser-generated plasma was discussed. The difference in the rotational and vibrational temperatures of the molecules proves that the AlO($B^2\Sigma^+$) molecules are not at the equilibrium. Usually, the rotational temperature of the excited state is assumed to be equal to the temperature of the ground state. This is true if the collisions with the gas are numerous enough to thermalize this excited state. One can wonder if this assumption is true considering that thermal equilibrium is not reached within the excited molecules. In order to answer this question, Laser-Induced Fluorescence (LIF) is used to probe the ground state of the molecules.

First, LIF was used to measure the de-excitation time $\tau = 2.7 \pm 0.2$ ns of the $B^2\Sigma^+$ state of AlO molecules. This time is much shorter than tabulated values in vacuum because of collisional quenching in the plasma. Such a difference between tabulated values and effective life-time has to be considered for the calculation of the molecules' concentration in LIBS.

Within this life-time, and considering the expected density and temperature of the plasma from the chapter 3, the estimated number of collisions is only a few tens. This number of collision is enough to reduce drastically the life-time of the excited molecules but not enough to fully thermalize it, hence the difference between the vibrational and rotational temperatures.

LIF emission can be decomposed in two contribution, direct fluorescence conserving the excited rovibrational state (about 10% of the signal) and relaxed flu-

In short: *The temperatures of the ground state molecules in the plasma is determined from the fit of the emission spectrum. After* 30 μs *this temperature appears to be similar to the rotational temperature of the first excited state determined from LIBS spectroscopy. For such a delay, the rotational temperature of the first excited state matches the one of the ground state and equilibrium between both rotational population is achieved. In contrary, after* 5 μs*, the rotational temperature of the first excited state overestimates the ground state temperature of about 150 K. The equilibrium between both population is not achieved.*

orescence in which the excited state is not conserved (about 90% of the signal). Most of the molecules are thus partially thermalized through collisions. By fitting the LIF spectra of AlO molecules 30 μs after ablation, I was able to determine rotational and vibrational temperatures describing the resultant populations over many rotational and vibrational levels of the relaxed state and the temperature of the ground electronic state of AlO($X^2\Sigma^+$). Excited state population distribution are quite well described using Boltzmann population for the excited state. The emission of the molecules keeps the memory of the excitation path. Yet, the rotational and vibrational temperatures are not the same, meaning the molecules did not reach full internal equilibrium. Furthermore, both temperatures depend strongly on the excited wavelength. Within the excited state life-time, collisions are not sufficient to reach equilibrium from an initial state strongly out of equilibrium.

The ground state temperature of the molecules is measured to be 3153 ± 64 K. Simultaneously, the rotational temperature of the first excited state is measured to be 3130 ± 75 K. Both of these temperatures are very close. For a delay of 30 μs, the AlO($B^2\Sigma^+$) rotational temperature appears to be good probe of the ground state temperature. In contrary, for a delay of 5 μs, the AlO($B^2\Sigma^+$) rotational temperature is measured at 3845 ± 75 K while the ground state temperature is 3702 ± 61 K. The rotational temperature of the excited state is not equal to the ground state temperature, equilibrium between both rotational population is not fully achieved. From previous consideration on the relaxed LIF state, one can expect the thermalization of the excited state to be only partial. This could explain the fact that AlO($B^2\Sigma^+$) rotational temperature is above the ground state temperature. These LIF measurements can be easily coupled with the space resolved spectroscopy I used earlier. It would be very interesting to reproduce them for different delay time and with spatial resolution.

Chapter 6

General Conclusion

Laser generated plasma is a complex and interesting system. The deposition of the pulse laser energy leads to a brutal phase transition and the formation of a plasma. This plasma is composed of molecules, atoms, ions, and electrons reacting together and with the environment. Understanding the kinetics and thermodynamics of the plasma is essential in order to better understand the composition of the plasma, its temperature and the nucleation process of clusters and nanoparticles. In this thesis, we explored these different aspects of laser generated plasmas and several experimental techniques used to investigate them.

Chapter 2 was dedicated to a new microcanonical model able to describe nucleation in laser generated plasma. In complement to other theoretical approaches based on a detailed description of the reaction kinetics, this model is able to provide the evolution of clusters size distribution from diatomic molecules to clusters of several hundreds of atoms. This model is universal and relies on (i) global properties of the plasma such as densities and temperature and (ii) average properties of the clusters such as the reaction energy of a monomer or the distribution of the energy in the cluster. Because of its universality, the model developed here is versatile and can be modified to describe many nucleation processes. It is based on activated complex theory and Weisskopf model in order to determine a system of kinetic equations describing nucleation. In contrary to previous models, this one does not consider equipartition of the energy in the clusters. The description of the clusters is done using the microcanonical ensemble and partial spreading of the energy on the vibration modes of the clusters. This innovative approach succeed to describe nucleation of anisotropic and out-of-equilibrium clusters where previous models, based on canonical ensemble, failed.

In particular, we show that the model reproduces the size distribution of aluminum oxide clusters. The reaction energy of the clusters corresponds to the aver-

age of desorption energies measured on 21 identified reactions. This average value is one order of magnitude below theoretical reaction energy determined by DFT calculation on clusters in the most stable configuration. It indicates that the clusters formed in laser generated plasma do not reach thermodynamics equilibrium and are not necessarily produced in the most stable configuration. Furthermore, the energy distribution in aluminum oxide clusters is localized and equipartition is not true. Energy is localized in some vibration modes and the geometry of the clusters might not be the most stable one.

Chapter 3 presented measurements of the pressure in the plasma considering the dynamics of the generated shock-wave. Pressure is an important thermodynamic parameter influencing the formation of the clusters. In laser generated plasma, one can expect the pressure to vary drastically as observed in explosions. Taylor's blast model is a very general model describing the evolution of an explosion considering only the pulse energy and the gas density. It would be very convenient to use this model for laser ablation, but previous studies show some discrepancies between the dynamics of the shock-front and the prediction of the model. In this work we show that this model perfectly describes laser ablation for various pulse energies and materials provided that the anisotropy of the blast is taken into account. Indeed, the shock-front is not fully hemispherical. Most of the blast energy is directed perpendicularly to the target surface where the shock-front velocity is larger. We show that the pressure given by Taylor's model is consistent with the pressure measured behind the shock-front for delays larger than 20 ns. Before that, the real pressure saturates to a few tens of MPa and is given by $P[\text{MPa}] = (37.4 \pm 20) \times (\text{E [mJ]})^{2/5}$.

According to Taylor's model, the pressure behind the shock-front should be rather homogeneous. We propose to use this theoretical evolution of the pressure as input for modelling the evolution of the plasma. One can model the evolution of laser generated plasma considering Local Thermodynamics Equilibrium (LTE). In the framework of LTE, one can assume Saha-Erggert's law relating the densities of electrons, ions, and neutrals and the temperature of the plasma. Usually the electron density and the temperature are measured by spectroscopy and the pressure can be deduced from the densities of the species, the temperature, and an equation of state. In that case, the temperature corresponds to the excitation temperatures of the ions and the atoms. Applying this model on experimental measurements might lead to pressure value in strong disagreement with this work. Here, we show that Saha-Erggert's law strongly depends on the measurement of the temperature. A small variation of the temperature leads to strong variations of the composition of the plasma and pressure. Errors in the measurement of the temperature in plasma might be due to (i) strong temperature gradients or (ii) non

uniqueness of the temperature. In the first case, the temperature in the plasma is not uniform. Atomic emission is dominated by hot areas with a large electronic density favoring re-excitation. The temperature measured through the emission of these atoms overestimates the average temperature of the plasma. This can be overcome by local measurement of the temperature. In the second case, the kinetic temperature of heavy particles, driving the pressure in low ionized plasma, is slightly below the kinetic temperature of the electrons, driving the excitation of the atoms. Here, the overestimation of the average temperature arises from the difference between both temperatures. Considering different temperatures in the plasma might appear in contradiction with LTE. However, a lower kinetic temperature for heavy particles does not necessarily repeal the validity of Saha-Erggert's law considering an equilibrium between the electronic state of the atoms and the kinetic temperature of the electrons. One should endeavor to measure the kinetic temperature of heavy particles in the plasma in order to better understand it.

Chapter 4 studied the spatial evolution of the emission and temperatures of AlO and TiO molecules in laser generated plasma. The rotational temperature of the molecules is often considered as a good probe of the kinetic temperature of heavy particles as it is strongly influenced by collisions. From local spectroscopy measurements of $AlO(B^2\Sigma^+)$ and $TiO(A^3\Phi_r)$ emission, we determined the rotational and vibrational temperatures of AlO excited state and the rotational temperature of TiO excited state. This is done by fitting theoretical emission spectra considering the rotational and the vibrational populations to be described by Boltzmann distributions. Here the temperatures measured are related to the excited state of the molecules. $AlO(B^2\Sigma^+)$ molecules are likely to be formed by the reaction of an aluminum atom with an oxygen atom being cooled down by the quenching gas just as presented in the chapter 2. It can also be formed by collision of a ground state molecule with a metastable molecule (N_2^*, Ar^* etc.). Both formation paths are consistent with $AlO(B^2\Sigma^+)$ emission observed in the periphery of the plasma.

In $AlO(B^2\Sigma^+)$ molecules, both temperatures are not equal. The vibrational temperature is systematically larger than the rotational temperature. This measurement proves that the equilibrium is not fully reached within the molecules. The vibrational modes of the molecules are more excited than the rotational modes. The energy is not evenly spread in the molecules as intuited with the microcanonical model. A simple explanation is that the molecules are formed excited, but the rotational population is thermalized faster because of collisions with heavy particles. The rotational temperature is thus closer to the kinetic temperature of the plasma than the vibrational temperature. This difference in temperatures decreases with time, indicating that excited molecules are closer to equilibrium for later time in the plasma. The temperatures of the molecules appears directly

related to the temperature of the plasma. It decreases with the laser pulse energy and with time, while molecules on the periphery are also colder. The evolution of the rotational temperature of TiO molecules is very similar to the one of AlO molecules but systematically lower. This can be explained by a larger cross-section of TiO molecules leading to a larger number of collisions favoring their thermalization. The rotational temperature of TiO molecules seems to better probe the kinetic temperature of heavy particles in the plasma. The range and the evolution of the rotational temperature measured in this chapter are consistent with the average kinetic temperature of the plasma estimated in the chapter 3 for similar ablation conditions.

Chapter 5 presented Laser-Induced Fluorescence measurements on the plasma. An Optical Parametric Oscillator (OPO) is coupled to the LIBS set-up in order to excite the plasma with a light pulse of a chosen wavelength. Resonant absorption followed by fluorescence of the species in the plasma increases the signal by four order of magnitude. By changing automatically the wavelength of the OPO pulse and its delay with the ablation pulse, it is possible to measure excitation/emission maps of the plasma for different delay times. The pattern due to direct fluorescence of molecules is interesting to identify molecules and determine the complex composition of the plasma along its evolution. This can be an interesting tool in the research of molecules forming in the plasma during nucleation.

The fluorescence emission of the molecules can also be studied in order to better understand the excited state and the ground state of the molecule. By following the evolution of the fluorescence signal of AlO molecules following a resonant excitation, we measured the effective life-time of the excited state. This effective life-time is much shorter compared to the tabulated value in vacuum because of collision with the environment. When considering emission life-time of molecules in laser generated plasma, for instance in order to determine ratio of densities from ratio of emission signals, one should not rely on tabulated values. Finally, one can fit LIF spectra in order to determine the temperature of the ground state. LIF emission of the AlO($B^2\Sigma^+$) molecules can be described by the sum of a direct LIF emission (about 10% of the intensity) which conserves the excited state after resonant absorption, and relaxed LIF emission (about 90% of the intensity) which corresponds to a population redistributed over the quantum levels because of collisions. On the one hand, the redistributed population can be approximated by Boltzmann distributions with given vibrational and rotational temperatures. These parameters strongly dependent on the excitation wavelength as the population of the excited state keeps the memory of the excitation paths despite redistribution. Within the effective life-time of the excited state, molecules do not reach equilibrium. On the other hand, the direct LIF emission is related to the population of the ground state

that is excited. By fitting this emission, we determined the temperature of the ground state of AlO molecules for a short delay of 5 μs and a long delay of 30 μs. The temperature of the ground state molecules has better chance to correspond to the kinetic temperature of heavy particles in the plasma as their life-time before reacting is expected to be larger than the emission life-time of the excited state. After 30 μs, the ground state temperature is equal to the rotational temperature of AlO($B^2\Sigma^+$) molecules. However, after only 5 μs the ground state temperature is slightly below the rotational temperature of AlO($B^2\Sigma^+$) molecules. In that case, thermalization of the rotational state of AlO($B^2\Sigma^+$) molecules is not complete and its rotational temperature slightly over-estimate the temperature of the plasma.

Thermodynamics and nucleation in laser-generated plasma are complex and rich topics at the interface between plasma physics, chemistry, optics, and spectroscopy. With this work, I endeavor to investigate several aspects of this issue, from a general nucleation model able to describe the growth of particles in the plasma, to the determination of average thermodynamic quantities such as the pressure, and the local measurement of molecular emission used to investigate their temperatures. In laser-generated plasma, the aluminum oxygen molecules and clusters are not formed at the equilibrium. One should not describe them using a single temperature or the canonical ensemble. However, the rotational temperature of diatomic molecules remains a good probe of the kinetic temperature of heavy particles in the plasma. In particular the rotational temperature of the ground state that can be measured using laser-induced fluorescence. Such local measurement of the rotational temperatures of molecules can be used in order to further discuss LTE in laser generated plasma. Compared to local measurements of the excitation temperature of atoms one could discuss their equality and the uniqueness of the temperature in the plasma depending on time and position. Finally, one could modify the microcanonical model in order to take into account the electron density, the densities of the ions, the kinetic temperature(s) and the pressure in the plasma in order to have a refined description of the clusters and molecules in laser generated plasma.

Annexes

Annex A

Spectroscopy notations

This annex is a sum-up of the convention for spectroscopic notations used in the manuscript. For more details, please refer to the chapter 3.

Notation for the molecules level

In this manuscript:

- n refers to the electronic level
- v refers to the vibrational level
- J refers to the "rotational" level (angular momentum)

In the case of AlO molecules, the rotational level might be referred by K instead as it is more relevant to describes the transitions*.

The excited state is designed by a *prime* symbol (n', v', J' or K') while the ground state is designed by a *double prime* symbol (n'', v'', J'' or K'').

In the chapter 5, the same convention is used, and *triple prime* symbol is used for the ground state after de-excitation (n''', v''', J''' or K''').

*$\mathbf{K} = \mathbf{\Lambda} + \mathbf{N}$ with $\mathbf{N}$ the kinetic momentum of the nuclei rotation and $\mathbf{\Lambda}$ the projection of the total orbital kinetic momentum of the electrons on the molecule axis.

The electronic state name corresponds to the following convention:

$$\mathrm{L}^{2\mathrm{S}+1}[\Lambda]_{\Omega}$$

with:

Electronic state n	0	1	2	3	4
Notation L	X	A/a	B/b	C/c	D/d
$\lvert\Lambda\rvert$	0	1	2	3	4
Notation [Λ]	Σ	Π	Δ	Φ	Γ

The letter L corresponds to the electronic state n. S is the spin number, Λ is the projection on the molecule axis of the total orbital kinetic momentum of the electron, and $\Omega = \Lambda + \Sigma$ with Σ the projection on the molecule axis of the spin.

Notation for the transitions

For each molecule described in the manuscript, the band systems observed correspond to transitions between defined electronic level ($\mathrm{X}^2\Sigma^2 - \mathrm{B}^2\Sigma^+$ for AlO and $\mathrm{X}^3\Delta_\mathrm{r} - \mathrm{A}^3\Phi_\mathrm{r}$ for TiO) The electronic levels are thus not systematically specified. The transition between the two upper state (v', J') and the down state (v'', J'') is noted (v', v'') with $\Delta v = v' - v''$, $\Delta J = J' - J''$, and $\Delta K = J' - J''$.

Branch notation

The convention for the branches name is:

$$^{\Delta K}\Delta J_{ij}$$

with:

$\Delta J = J' - J''$		-1	0	1	
$\Delta K = K' - K''$	-2	-1	0	1	2
Letter	O	P	Q	R	S

i and j indicate the spin projection (1 if $+1/2$ and 2 if -1/2) of the upper state ($'$) and the down state ($''$) respectively. If $\Delta K = \Delta J$, only ΔJ is written and if $i = j$ only one number is written.

Annex B

Constants of diatomic molecules

B.1 AlO Molecules (blue-green system)

B.1.1 Energy levels

Rotational levels

According to Kovacs[195], one can write the energy for the level $J = K + \frac{1}{2}$:

$$F_{1v}(K) = B_v \cdot K(K+1) - D_v \cdot \Big(K(K+1)\Big)^2 + \frac{1}{2}\gamma_v \cdot K, \tag{B.1}$$

while for the level $J = K - \frac{1}{2}$:

$$F_{2v}(K) = B_v \cdot K(K+1) - D_v \cdot \Big(K(K+1)\Big)^2 - \frac{1}{2}\gamma_v \cdot (K+1), \tag{B.2}$$

The index 1 or 2 stands for the spin projection value $+1/2$ and $-1/2$ respectively. For each vibrational level v, we are using tabulated value for B_v, D_v and γ_v from Saskena et al.[230] reported in table B.1.

Electronic and vibrational levels

The energy levels for vibrations are described by a Taylor's expansion:

$$G_e(v) = w_e\left(v + \frac{1}{2}\right) - w_e x_e\left(v + \frac{1}{2}\right)^2 + w_e y_e\left(v + \frac{1}{2}\right)^3 \tag{B.3}$$

Table B.1: Molecular constants for rotational levels (see eqs. B.1 and B.2).

$X^2\Sigma^+$				$B^2\Sigma^+$			
v	B_v	$10^6 \times D_v$	γ_v	v	B_v	$10^6 \times D_v$	γ_v
	cm^{-1}	cm^{-1}	cm^{-1}		cm^{-1}	cm^{-1}	cm^{-1}
0	0.638492	1.101	0.00172	0	0.601855	1.158	-0.01091
1	0.632691	1.110	0.00315	1	0.597342	1.153	-0.01099
2	0.626875	1.128	0.00532	2	0.592855	1.144	-0.01093
3	0.621021	1.114	0.00824	3	0.588417	1.139	-0.01097
4	0.615114	1.115	0.01228	4	0.584008	1.135	-0.01091
5	0.609176	1.184	0.01946	5	0.579597	1.124	-0.01093
6	0.603114	1.273	0.02429	6	0.575234	1.123	-0.01107
7	0.596860	1.669	0.03473	7	0.570890	1.115	-0.01091
				8	0.566544	1.106	-0.01119

Table B.2: Molecular constants for vibrational and electronic levels (see eqs. B.3) in cm^{-1}.

$X^2\Sigma^+$		$B^2\Sigma^+$	
T_e	0.0	T_e	20689.041
w_e	979.524	w_e	870.369
$w_e x_e$	7.036	$w_e x_e$	3.651
$w_e y_e$	-0.00106	$w_e y_e$	0.00096

Table B.3: Einstein coefficient A_{ev} [1/s] from Hebert et al.[229] for AlO blue-green band system ($B^2\Sigma^+$-$X^2\Sigma^+$).

v'/v''	0	1	2	3	4	5	6	7	8	9	10
0	6.34E6	1.91E6	4.29E5	6.89E4	0	0	0	0	0	0	0
1	3.00E6	2.26E6	2.34E6	9.27E5	2.08E5	0	0	0	0	0	0
2	1.02E6	2.99E6	7.01E5	2.21E6	1.37E6	4.00E5	0	0	0	0	0
3	2.78E5	1.7E6	2.24E6	1.62E5	1.91E6	1.74E6	6.22E5	0	0	0	0
4	0	6.51E5	1.89E6	1.48E6	1.98E4	1.60E6	2.02E6	8.59E5	0	0	0
5	0	1.89E5	9.55E5	1.76E6	9.04E5	1.69E4	1.33E6	2.23E6	1.10E6	0	0
6	0	0	3.46E5	1.12E6	1.48E6	5.21E5	4.46E4	1.10E6	2.38E6	1.32E6	0
7	0	0	1.05E5	5.23E5	1.24E6	1.24E6	3.01E5	7.75E4	9.96E5	2.64E6	1.63E6
8	0	0	0	2.25E5	8.21E5	1.51E6	1.20E6	2.00E5	1.23E5	1.12E6	3.52E6
9	0	0	0	0	5.86E5	1.67E6	2.49E6	1.61E6	1.77E5	2.38E5	1.87E6
10	0	0	0	0	0	1.03E6	2.40E6	3.01E6	1.61E6	1.11E5	3.19E5

with w_e the wavenumber of the oscillator, $w_e x_e$ and $w_e y_e$ anharmonicity parameters. We are using the transition reported in Saskena et al.[230] except that there is a typo in the original article on the electronic level value T_e of the level $B^2\Sigma^+$ that we have corrected (20685.041 $\rightarrow$ 20689.041) by crosschecking with other authors. The values of the parameters are reported in table B.2.

Fortrat Diagram

The total energy of a level, expressed as a wavenumber here, is given by:

$$\nu(e, v, K, i) \texttt{ [1/cm]} = T_e + G_n(v) + F_{iv}(K). \tag{B.4}$$

We have compare the compute Fortrat diagram from our code to the transition indexed in Launila et al.[231] (see figure 4.7). Our spectra are also compared to spectra obtained using the program PGOPHER.

Note: Energies are computed for transition in vacuum, and then we are accounting the shift due to the refractive index of the air when comparing computed wavelengths to measured wavelengths with our experimental setup ($\lambda_{vacuum} = n \times \lambda_{air}$).

B.1.2 Transition probability

Höln-London parameter are computed for each transition using formula from Kovacs[195].

For each vibrational state v' of the excited electronic state, because of the high rotational temperature, the partition function of the rotational states are assumed to reach the value :

$$Q_{rot_{n',v'}}(T_{rot}) = \frac{k_B T_{rot}}{B_{v'}}. \tag{B.5}$$

The partition functions of the vibrational and electronic state are not computed since they are identical for each transition observed.

Finally, we are using the Einstein coefficient A_{ev} [1/s] from Hebert et al.[229] reported in table B.3.

Note: The program also accepts Absolute Band Strength S_{vv} [u.a.], then the Einstein coefficients A_{ev} are deduced using the formula:

$$A_{ev} \texttt{ [1/s]} = 1.013 \times 10^{-6} \; S_{vv} \texttt{ [u.a.]} \; \nu_{ev}^3 \texttt{ [1/cm]} \tag{B.6}$$

with ν_{ev} the wavenumber corresponding to the elec-vib transition.

B.2 TiO Molecules (γ system)

B.2.1 Electronic and Rotational-vibrational levels

We are using the formalism described by Hermann et al.[201]. For each vibrational and electronic level, the energy is approached by:

$$T(J) = T_v + B_v J(J+1) - D_v \left[J(J+1)\right]^2 + H_v \left[J(J+1)\right]^3 + L_v \left[J(J+1)\right]^4 . \quad \text{(B.7)}$$

The value of the parameters T_v, B_v, D_v, H_v, and L_v for each state, namely $A^3\Phi_2$, $A^3\Phi_3$, $A^3\Phi_4$, $X^3\Delta_1$, $X^3\Delta_2$, and $X^3\Delta_3$, are taken from Table 2 in Hermann et al.[201].

B.2.2 Transition probability

Höln-London parameter are computed for each transition using formula from J. B. Tatum[232]. The energies used to compute the population of the vibrational and rotational states are defined from equation B.7:

- For a given electronic states, the vibrational energy $G_e(v)$ corresponds to $T_v - T_{v=0}$, where T_v and $T_{v=0}$ refer to the tabulated data of the electronic state.
- For a given electronic state and a given vibrational state, the rotational energy $F(J)$ corresponds to $T(J) - T_v$.

For each vibrational state v' of the excited electronic state, because of the high rotational temperature, the partition function of the rotational states are assumed to reach the value :

$$Q_{rot_{n',v'}}(T_{rot}) = \frac{k_B T_{rot}}{B_{v'}}. \quad \text{(B.8)}$$

The partition functions of the vibrational and electronic state are not computed.

Finally, we are using the Franck-Condon factors $q_{v'v''}$ from Ram et al.[233] reported in Hermann et al.[201] (with an additional value for q_{54}). Franck-Condon factors $q_{v'v''}$ are displayed in Table B.4.

Table B.4: Franck-Condon factors $q_{v'v''}$ from Hermann et al.[201].

v'/v''	0	1	2	3	4
0	0.7191	0.2365	0.0398	0.0042	0.0003
1	0.2362	0.3188	0.3317	0.0971	0.0148
2	0.0400	0.3294	0.1038	0.3350	0.0155
3	0.0044	0.0976	0.3291	0.0143	0.2860
4	0.0003	0.0159	0.0155	0.2758	0.0020
5	0	0	0	0	0.210

Annex C

Theoretical chemistry calculations

In this annex is presented some theoretical background in order to understand the theoretical calculations ran on alumina clusters in the chapter 2. It enables to explain the origin of notations, and the meaning of the different calculations.

First, the Streitz potential used to described interaction between atoms in oxides is introduced with the embedded-atom method. This method is the first step used to calculate cluster geometry from random distribution of atoms. Then *ab initio* calculation is explained with the basic formalism used for quantum calculation and the associated approximations. It is interesting to compare this approach with the calculation for diatomic molecules reported in the chapter 4. Finally, the Density Functional Theory (DFT) is introduced with its formalism and notation. In particular, the Hybrid-GGA (B3LYP) procedure used for the cluster optimization is explained.

C.1 Streitz potential

While metals are already well described by simple potential that can be used in large simulations[42], oxides are more challenging. The ionic and dielectric nature of the material leads to more complicated electronic structure. In 1994 F.H. Streitz and J.W. Mintmire developed a computational method for molecular-dynamic simulations of alumina[127]. This method explicitly includes variable charge transfer between anions and cations and describes accurately the elastic properties and surface energies of the clusters.

C.1.1 Coulomb repulsion

The dominant interaction in metal oxides is the Coulomb electrostatic interaction. The electrostatic energy is composed of one term depending on the partial charge of the atoms q_i, the local atomic energy, and another term corresponding to the interaction between atoms V_{ij}:

$$E_{es} = \sum_i E_i(q_i) + \frac{1}{2}\sum_{i \neq j} V_{ij}(r_{ij}, q_i, q_j) \tag{C.1}$$

with r_{ij} the distance between the atoms. One can then consider a second order Taylor expansion of the local atomic energy:

$$E_i(q_i) = E_i(0) + \chi_i^0 q_i + \frac{1}{2} J_i^0 q_i^2 \tag{C.2}$$

where χ_i^0 corresponds to the electro-negativity and where J_i^0 corresponds to a self-Coulomb repulsion. The Coulomb pair interaction $V_{ij}(r_{ij}, q_i, q_j)$ is given by:

$$V_{ij}(r_{ij}, q_i, q_j) = \int\int d^3r_1 d^3r_2 \frac{\rho_i(r_1, q_i)\rho_j(r_2, q_j)}{r_{12}} \tag{C.3}$$

and one can take as atomic charge density:

$$\rho_i(r, q_i) = \mathcal{Z}_i \delta(r - r_i) + (q_i - \mathcal{Z}_i) f_i(r - r_i) \tag{C.4}$$

with $\mathcal{Z}_i$ is an effective core charge lower the total nuclear charge of the atom because taking into account the core electrons screening. f_i describes the radial distribution of the valence charges in space. In this model, f_i is chosen as a simple decreasing exponential just like a $1s$ Slater's orbital:

$$f_i(|r - r_i|) = \frac{\zeta_i^3}{\pi} e^{-2\zeta_i |r - r_i|} \tag{C.5}$$

More sophisticated functions could be used, but it would complexify the calculation. Analytical expressions of the different integrals can be found in order to improve the calculation time[234].

C.1.2 Embedded-Atom Method

The Coulomb repulsion cannot be the only one considered for describing atoms interactions. One need to consider a short distance repulsive potential. A usual empirical potential is the Embedded-Atom Method (EAM):

$$E_{EAM} = \sum_i F_i[\rho_i] + \sum_{i<j} \phi_{ij}(r_{ij}) \tag{C.6}$$

with $F_i[\rho_i]$ the energy required to embed atom i in a local electron density ρ_i and $\phi_{ij}(r_{ij})$ the residual pair-pair interaction. $F_i[\rho_i]$ is chosen as the Finnis-Sinclair form for calculation convenience:

$$F_i[\rho_i] = -A_i\sqrt{\frac{\rho_i}{\xi_i}} \tag{C.7}$$

with ρ_i the local atomic density which is the sum of all the electronic densities of the different atoms, and A a paramter.

$\phi_{ij}(r_{ij})$ is the pair-potential, defined for each pair of atoms that is to say O-O, Al-Al, Al-O:

$$\phi_{ij}(r) = 2B_{ij}e^{-\frac{\beta_{ij}}{2}(r-r^*_{ij})} - C_{ij}[1+\alpha_{ij}(r-r^*_{ij})]e^{-\alpha_{ij}(r-r^*_{ij})} \tag{C.8}$$

with B, C, β and α parameters and r^* the equilibrium distance. After all, the total energy can be calculated has $E_{tot} = E_{es} + E_{EAM}$ and the force exerted on each atom is $-\nabla E_{tot}$. Thus, for any initial configuration and set of parameters one can calculate the energy, derive the force, move the atoms accordingly and repeat it. By iteration one can find configuration corresponding to local minima.

C.1.3 Fitted parameters

In order to find the parameters, Streitz and Mintmire calculated the cohesive energy, cationic charge, pressures, forces on the nuclei, elastic constants, and unrelaxed surface energies for the (0001) and (1012) surfaces of α-alumina and compared them to experimental values or first-principles theoretical results. All the fitted parameters are summarized in figure C.1.

TABLE I. Optimized ES+ potential parameters for aluminum and oxygen.

	Atomic parameters					
	χ (eV)	J (eV)	ζ (Å^{-1})	Z	A (eV)	ξ
Al	0.000 000	10.328 655	0.968 438	0.746 759	0.763 905	0.147 699
O	5.484 763	14.035 715	2.143 957	0.000 000	2.116 850	1.000 000
	Pair parameters					
	r^* (Å)	α (Å^{-1})	β (Å^{-1})	B (eV)	C (eV)	
Al-Al	3.365 875	1.767 488	2.017 519	0.075 016	0.159 472	
O-O	2.005 092	8.389 842	6.871 329	1.693 145	1.865 072	
Al-O	2.358 570	4.233 670	4.507 976	0.154 548	0.094 594	

Figure C.1: Fitted parameters of the Streitz model on α-alumina[127].

C.2 *Ab initio* calculations

If one needs to know precisely the relative energies of different clusters or molecules, semi-empirical potentials are not enough. One needs to use quantum mechanics in order to describe the system. From only fundamental constants and theoretical equations, one could be able to know the state of any system without any hypothesis. This is the so-called *ab initio* method: "from the beginning". However, to be able to run such calculations, simplifications have to be made, this is the Hartree-Fock calculation method. Different improvements can be implemented in order to get always closer to the true solution (Post Hartree-Fock methods).

Many of the concepts and approximations presented here are the same as the one introduced in the chapter 4 in the case of diatomic molecules. In particular, the concept of molecular Hamiltonian and the Born-Oppenheimer approximation is further developed.

C.2.1 Introduction

Quantum mechanic describes molecules as a wave-function $\Psi(\vec{r}, t)$. It contains all the information of the system. The function wave is driven in space and in time by the Schrödinger equation introduced by Erwin Schrödinger in 1926:

$$\hat{H}_{mol}\Psi(\vec{r}, t) = i\hbar\frac{\partial\Psi}{\partial t} \tag{C.9}$$

where $\hat{H}_{mol}$ is the Hamiltonian describing the system. In the stationary case, the energy of the system is directly related to the Hamiltonian:

$$\hat{H}_{mol}\Psi(\vec{r}) = E(\vec{r})\Psi(\vec{r}) \tag{C.10}$$

such that the total energy of the system can be calculated knowing only the Hamiltonian and the wave function:

$$E = \frac{\langle \Psi | \hat{H}_{mol} | \Psi \rangle}{\langle \Psi | \Psi \rangle} \tag{C.11}$$

For a molecule composed of A nuclei (of mass M_n, atomic number Z_n and positioned in R_n for $n \in [1, A]$) and B electrons (of mass m_e and positioned in r_i for $i \in [1, N]$) (See figure C.2), the Hamiltonian can be written as a kinetic part for nuclei T_n, a repulsion interaction between nuclei V_{nn}, a kinetic part for electrons T_e, a repulsion interaction between electrons V_{ee} and finally an attractive interaction between electrons and nuclei V_{en}:

$$\hat{H}_{mol} = \hat{T}_n + \hat{V}_{nn} + \hat{T}_e + \hat{V}_{ee} + \hat{V}_{en} \tag{C.12}$$

$$\hat{H}_{mol} = -\sum_{n=1}^{A} \frac{\nabla^2_{R_n}}{2M_n} + \sum_{n,m=1}^{A} \frac{Z_n Z_m e^2}{8\pi\epsilon_0 |R_n - R_m|} - \sum_{i=1}^{B} \frac{\nabla^2_{r_i}}{2m_e} + \sum_{i,j=1}^{B} \frac{e^2}{8\pi\epsilon_0 |r_i - r_j|} - \sum_{n=1}^{A} \sum_{i=1}^{B} \frac{Z_n e}{4\pi\epsilon_0 |R_n - r_i|} \tag{C.13}$$

where $\nabla^2_{R_n} = \frac{\partial}{\partial R_n}$ and $\nabla^2_{r_i} = \frac{\partial}{\partial r_i}$ the partial derivatives over space coordinates of the nuclei and the electrons respectively. This system can only be analytically solved for very simple systems (the hydrogen atom and the molecule H_2^+) and has an enormous calculation cost for molecules of more than a few atoms. Thus, approximations need to be made.

Born-Oppenheimer approximation[235] uses the fact that the mass of nuclei is much larger than the mass of electrons such that the nuclei can be considered still for the electrons. The electrons instantaneously react to any movement of the nuclei. Thus, the problem can be decomposed in two parts:

- The electrons Hamiltonian $\hat{H}_{elec} = T_e + V_{ee} + V_{en}$ considering fixed nuclei. This one can be solved for any set of nuclei positions $\{R\}$ and gives $E_e(\{R\}, r)$ the local potential of the electronic cloud.

- The nuclei Hamiltonian $\hat{H}_{nucl} = T_n + V_{nn} + E_e$ which does not consider each electron, but a potential created by a given electronic configuration.

At this point, the electronic Hamiltonian can be written for a given set of nuclei positions. The total electronic wave function can be computed and leads to

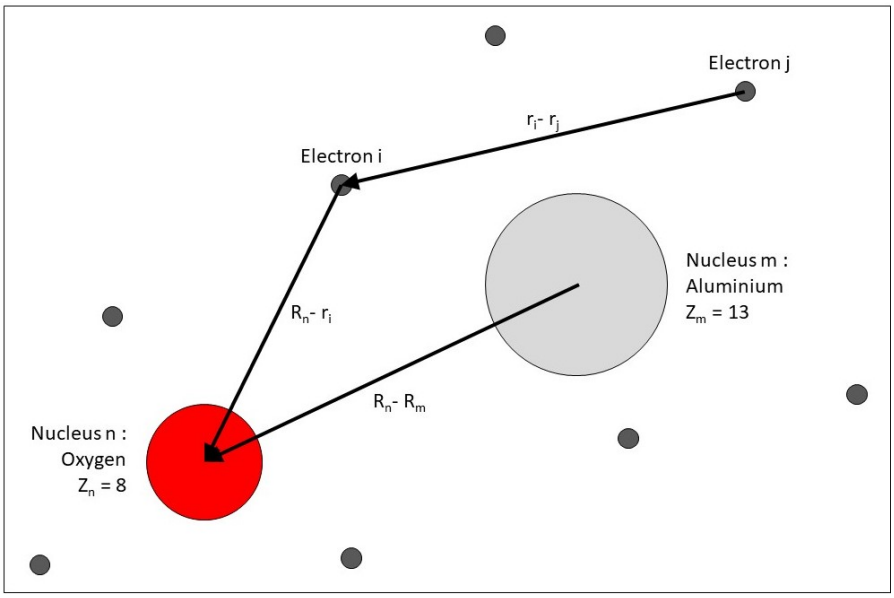

Figure C.2: Classical representation of AlO molecular system. Nuclei positions are referred to as R_n for $n \in [1, A]$ while electrons positions are referred to as r_i for $i \in [1, N]$. Z_n is the atomic number of the nuclei n and M_n is its mass. m_e is the mass of the electron.

the electronic energy. This is used in order to write down the nuclei Hamiltonian which will then be solved.

C.2.2 Hartree-Fock

The Hartree-Fock method (HF) is based on the orbital approximation. In this approximation, there is no interaction between the electrons. The electrons' Hamiltonian can be decomposed in the Hamiltonian of single electron and the total wave-function expressed as a combination of the single electron's wave-functions. This is the Hartree method. In the HF method, the interaction term is not neglected but averaged.

A condensed way to write down the electronic wave-function for B electrons is:

$$\begin{aligned}
\Psi_e &= \frac{1}{\sqrt{B!}} \sum_{i=0}^{B-1} (-1)^i \mathcal{P}_i [\phi_1(\vec{r}_1)\phi_2(\vec{r}_2)...\phi_B(\vec{r}_B)] \\
\Psi_e &= \frac{1}{\sqrt{B!}} [\mathbb{1} - \sum_{ij} P_{ij} + \sum_{ijk} P_{ijk}...][\phi_1(\vec{r}_1)\phi_2(\vec{r}_2)...\phi_B(\vec{r}_B)] \\
\Psi_e &= \mathcal{A}[\phi_1(\vec{r}_1)\phi_2(\vec{r}_2)...\phi_B(\vec{r}_B)]
\end{aligned} \tag{C.14}$$

where $\mathcal{P}_i$ is a permutation operator at $i+1$ indices and ϕ_i is the spin-orbital wave function written as the product of a spatial part φ_i and a spin part $\sigma_i(s_i)$. This can also be written with $P_{ij...}$ operators permuting the corresponding indices. One can notice that these notations are equivalent to the Slater's determinant:

$$\Psi_{e_1,e_2...e_B}(r_1, r_2...r_B) = \frac{1}{\sqrt{B!}} \begin{vmatrix} \phi_1(r_1) & \phi_1(r_2) & ... & \phi_1(r_B) \\ \phi_2(r_1) & \phi_2(r_2) & ... & \phi_2(r_B) \\ \vdots & \vdots & \vdots & \vdots \\ \phi_B(r_1) & \phi_B(r_2) & ... & \phi_B(r_B) \end{vmatrix} \tag{C.15}$$

Overall, this is simply an antisymmetric operator $\mathcal{A}$ applied on the product $\phi_1(\vec{r}_1)\phi_2(\vec{r}_2)...\phi_B(\vec{r}_B)$. One can show that $\mathcal{A}$ commutes with H_e and that $\mathcal{A}^\dagger\mathcal{A} = \sqrt{B!}\mathcal{A}$ such that the electronic HF energy becomes:

$$\begin{aligned}
E_e &= \langle \Psi_e | \hat{H}_e | \Psi_e \rangle \\
E_e &= \langle \phi_1(\vec{r}_1)\phi_2(\vec{r}_2)...\phi_B(\vec{r}_B) | \mathcal{A}^\dagger \hat{H}_e \mathcal{A} | \phi_1(\vec{r}_1)\phi_2(\vec{r}_2)...\phi_B(\vec{r}_B) \rangle \\
E_e &= \langle \phi_1(\vec{r}_1)\phi_2(\vec{r}_2)...\phi_B(\vec{r}_B) | \hat{H}_e [\mathbb{1} - \sum_{ij} P_{ij} + \sum_{ijk} P_{ijk}...] | \phi_1(\vec{r}_1)\phi_2(\vec{r}_2)...\phi_B(\vec{r}_B) \rangle
\end{aligned} \tag{C.16}$$

Where electronic Hamiltonian can be written:

$$\begin{aligned}\hat{H}_e &= \sum_{i=1}^{B} hi + \frac{1}{2}\sum_{i,j}^{B} g_{ij} \\ h_i &= -\frac{\nabla^2_{r_i}}{2m_e} - \sum_{n=1}^{A}\frac{Z_n e}{4\pi\epsilon_0|R_n - r_i|} \quad \text{(monoelectronic)} \\ g_{ij} &= \frac{e^2}{4\pi\epsilon_0|r_i - r_j|} \qquad\qquad\qquad\quad \text{(interaction)}\end{aligned} \tag{C.17}$$

So that:

$$\begin{aligned}E_e = \langle\phi_1(\vec{r}_1)\phi_2(\vec{r}_2)...\phi_B(\vec{r}_B)[\sum_{i=1}^{B} h_i + \frac{1}{2}\sum_{i,j}^{B} g_{ij}] \\ [\mathbb{1} - \sum_{lm} P_{lm} + \sum_{lmn} P_{lmn}...]\,|\phi_1(\vec{r}_1)\phi_2(\vec{r}_2)...\phi_B(\vec{r}_B)\rangle\end{aligned} \tag{C.18}$$

The h_i operator acts only on $\vec{r}_i$ components such that any $\langle\phi_1(\vec{r}_1)\phi_2(\vec{r}_2)...\phi_B(\vec{r}_B)|h_i P_{lmn...}|\phi_1(\vec{r}_1)\phi_2(\vec{r}_2)...\phi_B(\vec{r}_B)\rangle$ can be decomposed as a first part, on which h_i acts (the wave-functions depending on $\vec{r}_i$), and a remnant part. Because the permutation inverts at least two indices, the remnant part can be written as $\langle...\phi_l(\vec{r}_j)...|...\phi_m(\vec{r}_j)...\rangle$ $(l \neq m)$ which is zero because of the wave-function orthogonality. Only the product with the identity is not zero. The same reasoning leads to a similar conclusion for g_{ij} but this time the first permutation P_{ij} leads also to a non-zero term. Thus, we obtain:

$$\begin{aligned}\langle\phi_1(\vec{r}_1)...\phi_B(\vec{r}_B)|g_{ij}\mathbb{1}|\phi_1(\vec{r}_1)...\phi_B(\vec{r}_B)\rangle &= \langle\phi_i(\vec{r}_i)\phi_j(\vec{r}_j)|g_{ij}|\phi_i(\vec{r}_i)\phi_j(\vec{r}_j)\rangle = J_{ij} \\ \langle\phi_1(\vec{r}_1)...\phi_B(\vec{r}_B)|g_{ij}P_{ij}|\phi_1(\vec{r}_1)...\phi_B(\vec{r}_B)\rangle &= \langle\phi_i(\vec{r}_i)\phi_j(\vec{r}_j)|\, g_{ij}\,|\phi_j(\vec{r}_i)\phi_i(\vec{r}_j)\rangle = K_{ij}\end{aligned} \tag{C.19}$$

J_{ij} is the so-called Coulomb integral representing the Coulomb repulsion between the electronic densities $|\phi_i(\vec{r}_i)|^2$ and $|\phi_j(\vec{r}_j)|^2$. K_{ij} is the exchange integral with no classical equivalent. Thus, the electronic energy can be written as:

$$E_e = \sum_{i=1}^{B}\langle\phi_i(\vec{r}_i)|h_i|\phi_i(\vec{r}_i)\rangle + \frac{1}{2}\sum_{i,j}^{B}(J_{ij} - K_{ij}) \tag{C.20}$$

Here the problem is already much simpler, and we expressed the electronic energy

as the sum of $B^2/2 + B$ integrals The wave-function expression is not known *a priori*. However, any wave-function created from the orbital ϕ_i have an energy higher or equal to the wave-function of the ground-state. Thus, using the Lagrange multiplier method with ϕ_i, one can minimize the energy E_e and find the ground-state wave-function. The derivation of this calculus will not be presented here but can be found in the PhD manuscript of L. Barnes[236]. The minimization leads to a condition over $|\phi_i\rangle$:

$$F_i \left|\phi_i(\vec{r}_i)\right\rangle = \sum_j^B \lambda_{ij} \left|\phi_i(\vec{r}_i)\right\rangle \tag{C.21}$$

with λ_{ij} real, $F_i = h_i + \sum_j^B (J_j - K_j)$ the Fock operator where J_j is the Coulomb operator (the averaged Coulomb interaction created by the electrons $i \neq j$) and K_j the exchange operator:

$$\begin{aligned} J_i \left|\phi_j(\vec{r}_j)\right\rangle &= \left\langle\phi_i(\vec{r}_i)\right|g_{ij}\left|\phi_i(\vec{r}_i)\right\rangle \left|\phi_j(\vec{r}_j)\right\rangle \\ K_i \left|\phi_j(\vec{r}_j)\right\rangle &= \left\langle\phi_i(\vec{r}_i)\right| g_{ij} \left|\phi_j(\vec{r}_i)\right\rangle \left|\phi_i(\vec{r}_j)\right\rangle \end{aligned} \tag{C.22}$$

One can diagonalize this problem and find the energies associated to each orbitals ϵ_i in the canonic base:

$$F_i \left|\phi'_i(\vec{r}_i)\right\rangle = \lambda_{ii} \left|\phi'_i(\vec{r}_i)\right\rangle = \epsilon_i \left|\phi'_i(\vec{r}_i)\right\rangle \tag{C.23}$$

However, the Fock operator depends on $|\phi'_i(\vec{r}_i)\rangle$ through the Coulomb and exchange operators. Thus, this system is solved thanks to iterative method. This method is called self-consistent field (SCF).

Linear combination of atomic orbitals

For large systems, the SCF method fails to converge quickly enough and the molecular orbital are computed from atomic orbitals. The spatial part of the spin-orbit wave-function is written as a linear combination of atomic orbitals (LCAO), such that:

$$\varphi_i = \sum_\mu c_{\mu i} \chi_\mu \tag{C.24}$$

where $c_{\mu i}$ are weight coefficients associated to each atomic base function χ_μ for the electronic orbital φ_i. The χ_μ functions are centred around the corresponding nucleus and can have different expression depending on the model chosen: Slater exponents, Gaussian functions, plane waves, etc. This enables to construct *a priori* the expression of the electron orbitals which is then optimized.

Atomic Basis

The first atomic basis was introduiced by Slater in 1930.[237]:

$$\chi_\mu^{Slater} = N x^m y^n z^o e^{-\zeta r} \tag{C.25}$$

with N a normalization constant, ζ is the diffusivity constant giving information on the orbital broadness, x, y, z the Cartesian coordinates and m, m, o integers such that $m + n + o = l$ where l is the quantum atomic number. Slater-type orbitals (STOs) possess exponential decay at long range and Cartesian coordinate dependence that gives a good approximation of hydrogen-like orbitals for small orbitals (See fig. C.3). However, unlike the hydrogen-like Schrödinger orbitals, STOs have no radial nodes.

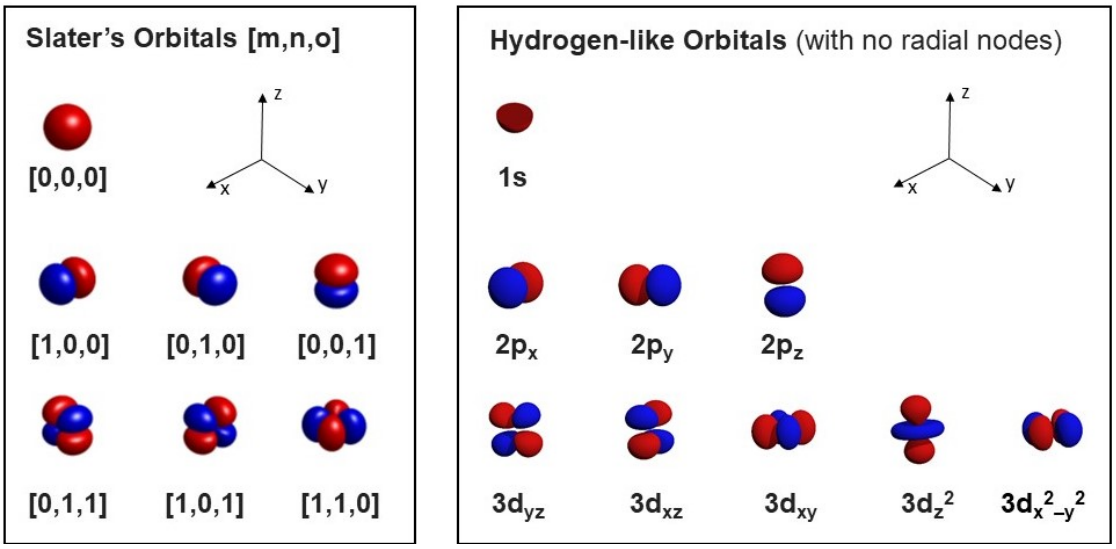

Figure C.3: Isosurface plot of some Slater's orbitals and hydrogen-like orbitals modulus for $n \leq 3$[238]. Blue is for negative values of the wave-function and red for positive ones. One can observe the similitude of most of them expect the orbitals $3d_z^2$ and $3d_{x^2-y^2}$ which can't be well reproduced. Note that here, orbitals with radial nodes ($2s$, $3p_x$, $3p_y$ and $3p_z$) are not represented because Slater's orbitals have non.

Of course one can think of using several Slater's orbitals in order to address this issue. For instance, the spherical orbital 1s is very well-adjusted by $[m, n, o] = [0, 0, 0]$ Slater's orbital (see fig.C.3) and both have a single decaying exponent as radial part. On the other hand, the orbital 2s has a radial node in $r = a_0$ but

can still be reproduced by a linear combination of two $[m, n, o] = [0, 0, 0]$ Slater's orbital (see fig.C.4).

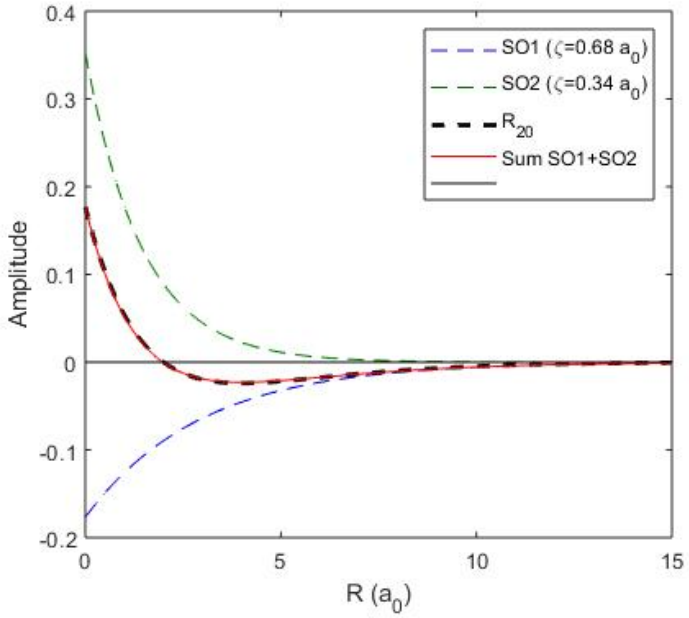

Figure C.4: Plot of the radial part of the orbit 2s (black dashed line): $R_{20}(r) = \left(\frac{1}{a_0}\right)^{\frac{3}{2}} \frac{1}{4\sqrt{2}} \left(1 - \frac{r}{2a_0}\right) e^{-\frac{r}{2a_0}}$. One can see that this nodal function can be approximated by the sum (red line) of two Slater's orbital $[m, n, o] = [0, 0, 0]$ SO1 (dashed green line) and SO2 (dashed blue line).

However, STO are not interesting when it comes to calculation. Indeed, the product of two STO is not an STO what makes the integral calculation much longer:

$$e^{-\alpha|\vec{r}-\vec{R_A}|}.e^{-\beta|\vec{r}-\vec{R_B}|} \neq Ke^{-\gamma|\vec{r}-\vec{R_C}|} \tag{C.26}$$

This is why other basis are used as the Gaussian Type Orbital (GTO):

$$\chi_\mu^{Gaussian} = Nx^m y^n z^o e^{-\zeta r^2} \tag{C.27}$$

Such an orbit is very interesting because the product of two Gaussian functions is a Gaussian function. However, it is not as close as STO to atom orbitals. The limit behaviours are not the same. For instance, the derivative of a Gaussian function in zero is zero while the derivative of an exponential is not. Thus, in order to approximate correctly atomic wave-functions, one needs at least three GTO or even six for a core electron as shown on figure C.5. If the GTO are used straight

forward, this increase a lot the number of coefficient that need to be optimized during the calculation. In order to limit the number of coefficients, so called *contracted* orbitals are usually used. They are pre-determined linear combination of *primitives* GTO:

$$\chi_\mu^{contracted} = \sum_{w=1}^{b} d_{w\mu} \chi_\mu^{primitives} \tag{C.28}$$

and the coefficients $d_{w\mu}$ are fixed. Then only a limited number of these contracted orbitals is optimized.

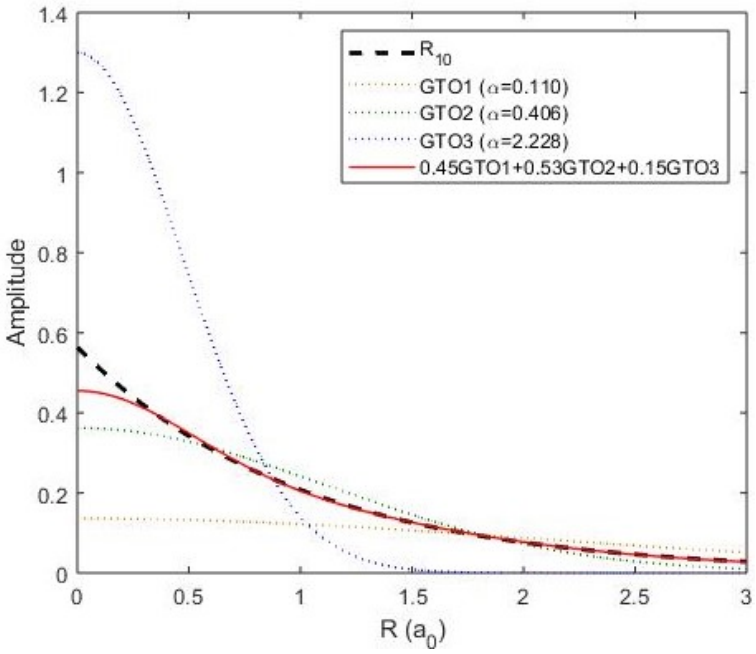

Figure C.5: Plot of the radial part of the orbit 1s (black dashed line): $R_{10}(r) = \left(\frac{1}{a_0}\right)^{\frac{1}{2}} e^{-\frac{r}{a_0}}$. One can see that this function (red line) can be approximated by the linear combination of 3 Gaussian functions $GTO(r) = \left(\frac{2\alpha_i}{\pi}\right)^{\frac{3}{4}} e^{-\alpha_i r^2}$ (dashed lines).

Concerning the valence bonds in molecules, they are very much delocalized around different atoms. In order to correctly describe them, the valence orbitals are *demultiplied*: each orbital is substituted by several orbitals with different spatial extensions. *Polarisation* orbitals are also used. These are asymmetrical orbitals that can fit the electronic distribution of a polar bond. Let's consider a hydrogen atom ($1s^1$) in an electric field. If only s orbitals are used, it is impossible to take into account the deformation of the electronic cloud due to the electric field. So

p-orbital are added on that purpose.

Pople basis

Pople basis of functions are the main basis used in the calculations presented here. In this work, we used the basis 6-311++G(3df,3pd)[239,240,241]. The first numer (6) corresponds to the number of primitive Gaussian functions used for the core wavefunctions. The following numbers (3,1 and 1) reffer to the valence functions used to describe the valence electrons and their value corresponds to the number of primitive Gaussian functions used in each of the valence functions. For instance, here, there is three numbers so three valence functions described by 3, 1 and 1 primitive Gaussian functions respectivelly. + and ++ correspond to the use of diffuse orbitals respectively for non-hydrogen en hydrogen atoms. Finally, the code (3df,3pd) specify the set of polarization functions used. For instance here it corresponds to three sets of d-orbital functions and one set of f-orbital functions for non-hydrogen atoms and three sets of p-orbitals functions and one set of d-orbital functions for hydrogen.

Spin and multiplicity

Until now the spin was not much discussed. In order to consider it in the HF calculation, one need to consider different cases if the electrons are paired or not.

Considering the Pauli exclusion principle, a single orbit can be populated by two electrons with opposite spins. In that case, one can show that the spatial part of both electrons (spin-orbit integrated over the spins) obeys the same equations as developed previously with a spatial restricted Fock operator $F_i^x = h_i^x + \sum_j^{B/2}(2J_j^x - K_j^x)$[236]. This is the *Restricted Hartree-Fock* construction (RHF).

If the number of electrons is odd, or in peculiar cases like oxygen and dioxygen (See fig. C.6), the multiplicity $(2S+1)$ is not 0 because the number of electrons of each spin are not equal and some electrons are unpaired. *A priori* all the paired electrons should have the same spatial part. But usually different spatial part for each electron are considered because it is much easier to code. This is the so called *Unrestricted open-shell Hartree-Fock* construction (UHF). The drawback of this method is that a single Slater determinant of several orbitals for different spins is not a satisfactory eigenfunction of the total spin operator $\mathbf{S}^2$. The ground state is contaminated by excited states.

The solution would be to force the paired electrons to have the same spatial part. This is called the *Restricted Open-shell Hartree-Fock* construction (ROHF).

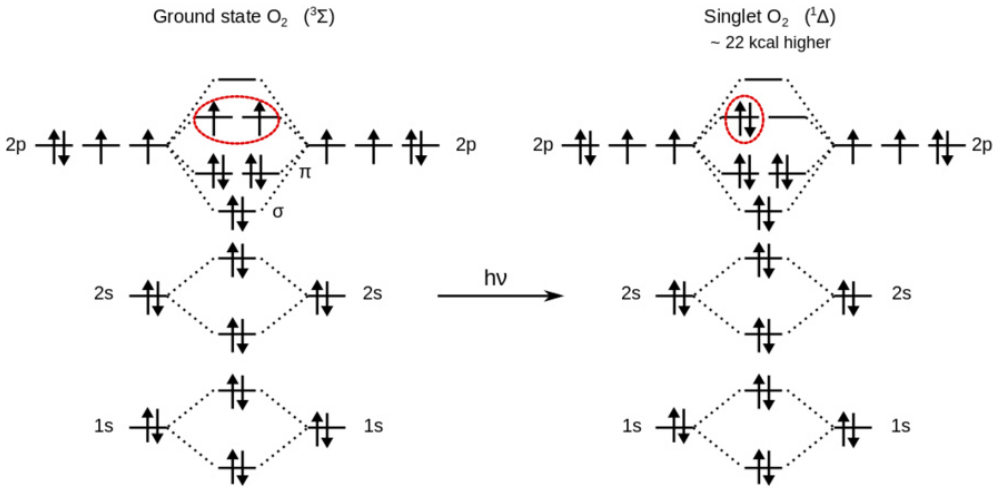

Figure C.6: Construction of the ground state (left) and triplet state (right) of the dioxygen molecule from the oxygen ground state. One can notice that the singlet is not always the less energetic state.

C.2.3 Electronic correlation

The orbital approximation implies that the presence probability of two electrons are independent and the electrons are not correlated. In the HF method, the interaction between the electrons appears only through a mean potential which does not take into account instantaneous effect. When two electrons have different spins, they can occupy the same orbital according to the Pauli exclusion principle but that doesn't mean they don't interact. On the contrary, evolving in the same area, the Coulombian repulsion has to be considered. This is the dynamic correlation but this interaction does not appear in the mean potential.

Configuration interaction (CI)

The first trick to introduce correlation between paired electrons is to consider the different excited states of the molecules. Electrons are placed in unoccupied or virtual orbitals. One would need to consider all the possible excited state: all the mono-excited states where only one electron is excited, all the double-excited states where two electrons are excited, etc. Each of these situations corresponds to a Slater determinant that is solved as discussed previously. The final wavefunction is written as a linear combination of these determinant and the different coefficients are optimized through variational method.

Of course the number of determinants explodes with the number of electrons and usually one have to stop the development at some point. SCI would consider

only the single excitation, SDCI the single and double excitations, etc.

Let's notice that with $full$-CI, considering all the excited states and with an infinite atomic basis, one obtains the exact theoretical wave-function.

Møller and Plesset perturbation theory (MP)

Another way to consider interactions is through perturbation theory. As seen previously, the exact Hamiltonian describing the electrons is $\hat{H}_e = \sum_{i=1}^{B} hi + \frac{1}{2}\sum_{i,j}^{B} g_{ij}$. In the HF method, the interaction potential between two electrons g_{ij} is averaged, and lead to an approximated Hamiltonian $\hat{H}_{HF} = \sum_i^B F_i = \sum_i^B [h_i + \sum_j^B (J_j - K_j)]$ with J_j and K_j the averaged interactions. One can write the exact Hamiltonian as $\hat{H}_0 = \hat{H}_{HF}$ added with a perturbation W so that:

$$\begin{aligned} \hat{H}_e &= \hat{H}_0 + \lambda W \\ W &= \frac{1}{2}\sum_{i,j}^{B} g_{ij} - \sum_{i,j}^{B} (J_j - K_j) \end{aligned} \tag{C.29}$$

One can then search the wave-function and the energy as Taylor expansions when $\lambda \to 0$. For each order of λ an equation is obtained and the order zero correspond the HF solution. One can then derive the several correction terms: MP2 until the second order, MP3 until the third order, etc.

Complete Active Space Multi-configuration (CASSCF)

Sometimes considering only the occupied orbitals is not enough to describe correctly the system. Then one can consider a bigger *active space* that is to say the orbitals of the external electrons. Usually, for a singlet, the two external electrons can be described by one orbital. But in the case treated here for instance, some clusters were symmetrical with two charges delocalized on both side of the cluster. Their orbitals have the same energy yet are different. One can add another virtual orbital in order to describe them: two electrons described by two orbitals. This is written CASSCF(2,2). CASSCF is a powerful tool in that case. With only MP2 (or even CCSD, more precise), the energy calculated can be several eV different from the real one. Yet it has many subtleties and is a struggling point for the convergence of the calculations.

Here, CASSCF + MP2 is used. The energy is calculated adding the perturbations (MP2) of all the di-excitations of the CASSCF determinant. This gives a very good value of the energy of the clusters even charged.

C.3 Density Functional Theory optimization (DFT)

The HF method and its variations are based on the wave-function of the whole molecule. For a molecule composed of B electrons, it consists in a 4B variables function with 3 spatial variables and 1 spin variable for each electron. If N_f basis function were used to construct the molecule wave-function, the calculation time goes like N_f^4 for HF methods, N_f^5 for MP2 and N_f^6 for CISD. Hence, in order to keep good precision, the calculations become quickly enormous. The Density functional theory was introduced in order to take into account correlation and limit the calculations while keeping a good precision. The electronic wave function is taken as one Slater's determinant but the energy is a functional of the electronic density depending on space and spin. Instead of considering a 4B variable function, one considers a 4 variable (3 space and 1 spin) functional of the electronic density. This leads to much simpler calculations: the calculation time goes like N_f^3 or N_f^4 for hybrid functional (see section C.3.4). However, it is not a systematic method and no analytic solution exists.

One can write the energy of the system as:

$$E = \int -\frac{1}{2}\nabla^2\rho_1(\vec{r}_1)d\vec{r}_1 - \sum_A \int \frac{Z_A}{|\vec{r}_1 - \vec{R}_A|}\rho_1(\vec{r}_1)d\vec{r}_1 + \int\int \frac{\rho_2(\vec{r}_1,\vec{r}_2)}{|\vec{r}_1 - \vec{r}_2|}d\vec{r}_1 d\vec{r}_2 \quad \text{(C.30)}$$

The first term corresponds to the kinetic energy of the electrons and the second term corresponds to the attraction of the electrons by the nuclei. They are both expressed in terms of the electron density $\rho_1(\vec{r}_1)$. The last term corresponds to the electron energy and is written in terms of the two-electron density $\rho_2(\vec{r}_1,\vec{r}_2)$ defined as:

$$\rho_2(\vec{r}_1,\vec{r}_2) = C_2^B \int ... \int |\Psi(\vec{r}_1,\vec{r}_2...\vec{r}_B)|^2 d\vec{r}_3...d\vec{r}_B \quad \text{(C.31)}$$

with $\Psi(\vec{r}_1,\vec{r}_2...\vec{r}_B)$ the molecule wave-function. Here is contained all the electronic correlation of the system. However, it is impossible to construct this density without knowing *a priori* the complete wave-function. Hopefully the two Hohenberg-Kohn theorems show that the energy can actually be written only in terms of $\rho_1(\vec{r}_1)$[242].

C.3.1 Hohenberg-Kohn theorems

First Theorem: The external interaction potential of a system of particles is only determined, within an additive constant, by the single particle density in the ground state. Indeed, one can show that two different potentials cannot lead to

the same single particle density in the ground state[236]. Therefor, the external potential is a unique functional of the single particle density.

Second Theorem: For any external interacting potential, it exists a universal functional $E[\rho]$ representing the energy of the system such that the ground state energy of the system is the minimum of this functional obtained for the ground state density ρ_0.

Thus, the total energy of the system expressed in the equation C.30 can be written as:

$$E[\rho] = F_{HK}[\rho] + \int V_{ext}(\vec{r})\rho(\vec{r})d\vec{r} \tag{C.32}$$

where $V_{ext}(\vec{r}) = \sum_A \frac{Z_A}{|\vec{r}_1 - \vec{R}_A|}$ is the external interaction potential created by the nuclei and $F_{HK}[\rho]$ is the Hohenberg-Kohn functional depending only on the electron density and representing the kinetic and electron-electron interaction terms. If one know this functional, one can minimize $E[\rho]$ and solve the problem. However, $F_{HK}[\rho]$ is not known *a priori*.

C.3.2 Kohn-Sham theory

In their theory, Kohn and Sham consider interacting electrons as non-interacting electrons in a well-chosen external potential V_s.[243]. Energy balance gives:

$$\begin{aligned} E[\rho] &= T_s[\rho] + \int \rho(\vec{r})V_s[\rho]d\vec{r} \\ V_s[\rho] &= V_{ext} + V_{xc}(\vec{r}) + \int \frac{\rho(\vec{r'})}{|\vec{r} - \vec{r'}|}d\vec{r} \end{aligned} \tag{C.33}$$

where $T_s[\rho]$ is the kinetic part and $V_{xc}(\vec{r})$ is the exchange-correlation potential. However, just like $F_{HK}[\rho]$, the exchange-correlation is not known *a priori* and one need to implement some *ad hoc* expression.

Then, knowing $V_s[\rho]$, one can minimize $E[\rho]$ and find the associated density of electron ρ. This density lead to a new potential V_s. Just like in the HF method, an iterative process is used in order to find the converging solution.

C.3.3 Density functional approximations

Many expressions of exchange-correlation potential can be used. Here are developed the different potentials used in our calculations (B3LYP).

Local spin density approximation (LSDA) The local spin density approximation is to consider that locally the density of electrons is the one of a uniform gas for each spin[244]. That is to say spatial variations of the density are smooth enough.

One can show that in the limit of low and high density, the exchange interaction potential of spin α and spin β electron populations can be written as $\epsilon_x[\rho_\alpha, \rho_\beta] = -2^{1/3}C_x(\rho_\alpha^{1/3} + \rho_\beta^{1/3})$ such that:

$$E_x^{LSDA} = -\int \epsilon_x \rho d\vec{r} = -2^{1/3}C_x \int (\rho_\alpha^{4/3} + \rho_\beta^{4/3}) d\vec{r} \tag{C.34}$$

For intermediate density, one should provide some correction due to correlation. Vosko, Wilk and Nusair produced analytic fit of this correction (E_c^{VWN})[245].

Generalized gradient approximation (GGA) The generalized gradient approximation is a correction to the local spin density approximation. This time the spatial variation of the density in considered in the expression of the exchange correlation potential.

One of the first exchange correction was developed by A.D. Becke in 1988[246]:

$$\Delta E_x^{B88} = -\beta \rho^{\frac{1}{3}} \frac{x^2}{1 + 6\beta x sinh^{-1} x} \quad \text{with} \quad x = \frac{|\nabla \rho|}{\rho^{\frac{4}{3}}} \tag{C.35}$$

where β is a parameter adjusted on noble gas experimental data.

The same way, Lee, Yang and Parr adjusted a correlation correction depending on four parameters on atomic helium experimental data: E_c^{LYP}[247].

C.3.4 Hybrid-GGA (B3LYP)

One can mix these different expressions of potential with the HF one in order to create a so called hybrid exchange-correlation potential. The most famous one and the one that was used here is the B3LYP exchange-correlation potential[248]:

$$E_{xc}^{B3LYP} = 0.2E_x^{HF} + 0.8E_x^{LSDA} + 0.72\Delta E_x^{B88} + 0.81E_c^{LYP} + 0.19E_c^{VWN} \tag{C.36}$$

where the numerical factors were adjusted on experimental data.

Annex D

Shock-wave dynamics in water

Abstract: *Simple and universal relations between the laser pulse energy and the pressure at the ablation point are investigated using the propagation of the generated shock-waves in water. The pressure measured from the dynamics of the shock-wave can be determined by the fluency of the laser pulse only. The shock-wave position in water is measured using shadowgraph imaging and an iCCD camera with a 5 ns gating. In water, the shock-wave velocity appears to be hyper-sonic during the first 50 ns. Its speed can be related to the pressure using the Gilmore model including Tait's equation. The ablation pressure is found out to go up to several GPa and increases as the square root of the laser fluency. We checked that the pressure can be determined from the pulse fluency and the acoustic impedances considering Berth-Fabbro's approach.*

D.1 Introduction

In order to better understand nucleation, it is essential to determine the pressure condition during ablation as developed in the chapter 3. In complement of the measurements in the air, I also studied the ablation pressure in water. Laser ablation in liquids (LAL) is used to produce a colloidal solution of nanoparticles. The development of a simple approach to determine the pressure during laser ablation is of great interest to investigate laser ablation processes and their impact on the target[249]. Large pressure at the ablation point could explain the formation of meta-stable phases, such as the production of nanodiamonds from carbon target[40,175].

Determining the pressure at the ablation point is no easy task because of the transient nature of the plasma (from ns-μs) and small spatial extension (submilimetric). One way to measure the pressure at the ablation spot is based on the

shock wave dynamics. In water, the pressure of the shock-wave have been widely investigated by Vogel et al. considering water breakdown[48] and can be described using Gilmore's model including the isotropic Tait's equation.

The shock-waves are generated by a 5 ns UV light pulsed laser focused on a gold target and an alumina target in water. The energy of the pulse is tune on a large range from 0.1 to 50 mJ. Image of the shock-waves are obtained by shadowgraph imaging using an intensified camera. In liquid, the results of Vogel et al. for water breakdown can apply for laser ablation of a target. Furthermore, the pressure measured at the ablation spot are is consistent with the simple Berth-Fabbro's approach considering energy balance considering the fluency of the pulse, the consumption of energy due to phase transition and momentum.

D.2 Measurement Set-up

The third harmonic of a YAG-Nd pulsed laser (355 nm, 5 ns, 9 Hz, 60 mJ per pulse) is focused either on a mono-crystal of alumina or on a pure target of gold (99.99% from Neyco) in order to study metals and dielectric. Sapphire crystal was grown by Czochralski (Cz) technique with radio frequency induction heating in iridium crucible[173,174]. The ablation is performed either at ambient condition in air, or for targets immersed in 1 cm of deionized water. The laser-induced plasma triggers a hemispheric shock wave observed by shadowgraph imaging. The shadowgraph setup presented on figure D.1 is composed of a 30 mW cw diode laser (445 nm) illuminating an iCCD camera from Andor (reference, 1024×1024 pixels). An objective Zoom 6000 from Navitar is mounted on the iCCD camera. In the case of water, in order to increase further the zoom, a lens with a focal distance of 100 mm is added. In that configuration, the resolution of a pixel is 2 μm. The iCCD records the image of the ablation point with a gating of 5 ns. The delay between the ablation pulse and the camera is controlled by a digital delay/pulse generator DG645 from Stanford Research Systems. Each image is acquired with a given delay after a pulse. The energy of the pulse is measured with a Nova II power meter mounted with a high energy pyroelectric sensor.

Figure D.2 (a) shows laser generated shock waves in water for an alumina target and a pulse energy of 41 ± 2 mJ (70 ± 30 GW/cm^2). In that case, we used a 2x2 binning of the camera pixels in order to obtain a better signal over noise ratio (resolution of 4 μm). The ablation of particles in water on the laser path leads to spherical shock-waves above the main one, making the measurement uneasy. In order to limit these phenomena, the water was changed between each measurement. The oblique shock-waves are due to coupling to the liquid of shock-waves propagating in the solid and the liquid (see Annex E).

Note that the characteristics of the laser have little importance on the obser-

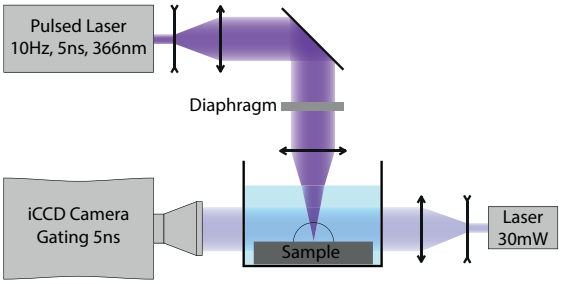

Figure D.1: Simplified scheme of the measurement apparatus of the shock waves in water.

vation of the phenomena. Shock waves have been observed in many configurations[250,251,252,253,40,254,255,256,257,258].

D.3 Propagation in water

In the case of propagation in water, the shock wave dynamics can be related to the pressure as reported by Vogel et. al[48] for a laser focused in water by using the Gilmore model including the isotropic Tait's equation which fits experimental data for pressures up to 2 500 MPa[259]. It enables to determine the pressure of the shock-wave p_s from its velocity u_s:

$$p_s = (p_\infty + B)\left(\frac{2nu_s^2}{(n+1)c_0^2} - \frac{n-1}{n+1}\right) - B \tag{D.1}$$

with $c_0 = 1483$ m/s the sound velocity in water, $p_\infty = 10^5$ Pa the room pressure, and B and n, Tait's parameters. In the case of water, $B = 314\times10^6$ Pa and n=7[260].

Figure D.2 (b) represents for 3 different pulse energy (0.8, 2.8 and 27.8 mJ) the position of the shock wave averaged on 4 different measurements. It corresponds to the distance perpendicular to the target between the bottom of the plasma and the position of the shock-wave. The ablation depends a lot on the water cleanliness. For instance, dusts or bubbles on the laser path might prevent ablation of the target. Every frame recorded while no ablation sound was eared were discarded. Despite these precautions, the position of the shock-wave in water fluctuates much more than in the air and discards the possibility to compute a satisfying derivative. In order to obtain the initial pressure, we fitted the position of the shock-wave for $t < 100$ ns by a second order polynomial curve (solid lines in figure D.2 (b)). It enables to estimate the derivative for $t = 0$ that is to say the initial speed of the

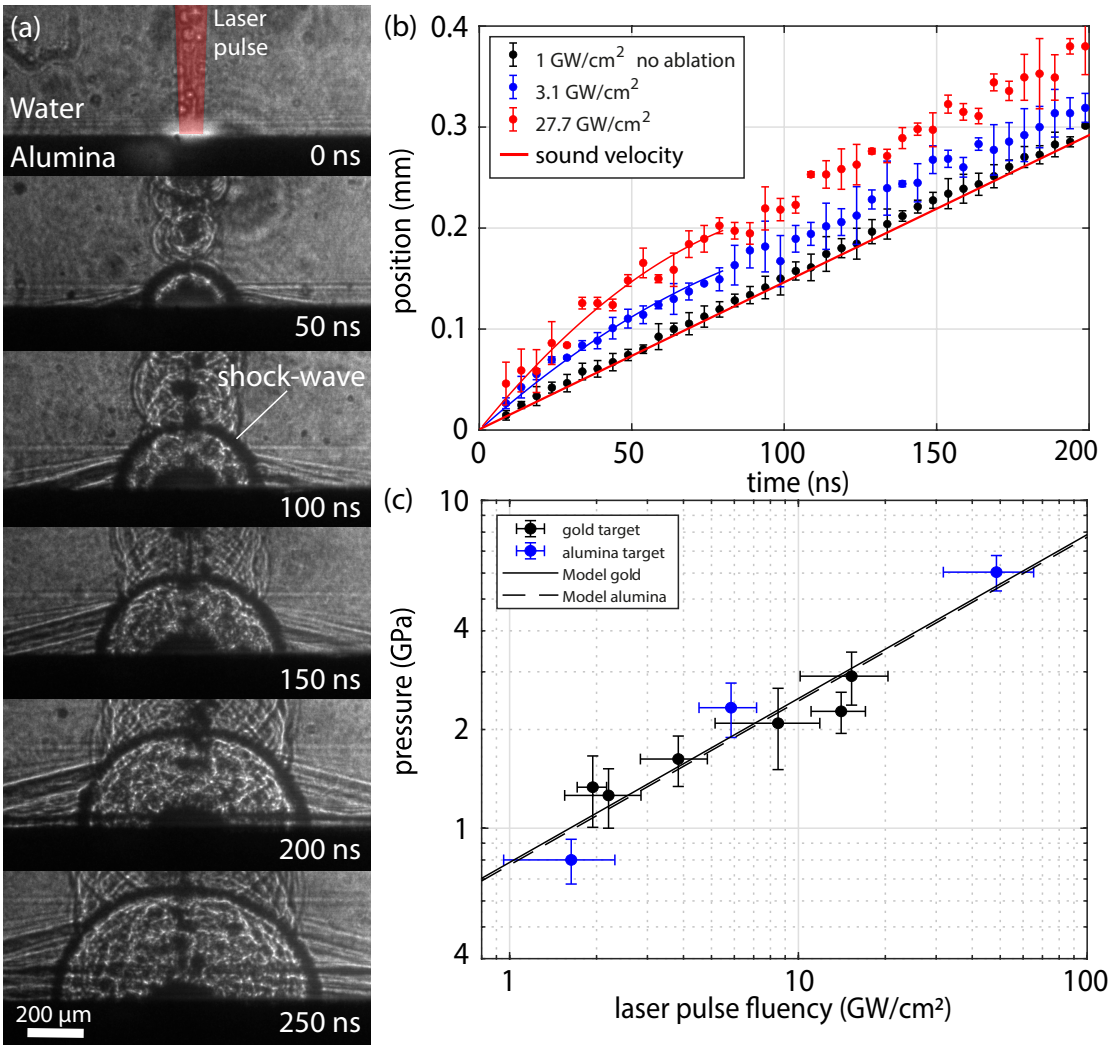

Figure D.2: (a) Shadowgraph images of the ablation of an alumina target in water for the different delays. (b) Time evolution of the shock wave position averaged on 4 measurement on gold target at different fluency. The red line correspond to the propagation of a wave at the sound velocity in water (1483 m/s). The black solid curves represents the second order polynomial fit on the data form time below 60 ns. These fit are used to determine the initial velocity of the shock-wave. (c) Measured pressure on gold target and alumina target using the initial velocity of the shock-wave for different fluency of the laser. The black solid line corresponds to the Berth-Fabbro Model.

shock-wave and the error and thus the pressure at the ablation point. When there is no ablation (black dots), the shock-wave goes at the speed of the sound velocity (red solid line). The initial pressure values measured are reported in figure D.2 (c) depending on the laser fluency. The black dots correspond to measurements on a gold target while the blue dots corresponds to a measurement on an alumina target.

The fluency is calculated by dividing the energy of the laser pulse by its duration and the laser spot diameter measured on the first image. Because of non-linearities, some energy is lost in water before reaching the target. We estimated the loss to be independent on the fluency of the laser as shown in figure D.3. In order to estimate the losses, the laser was shined through a transparent tank without water and with 2 cm of water (double of the experimental conditions). Without focalization, no difference in energy was measured as the water is transparent at 355 nm. Yet when focalized in the middle of the tank (without water breakdown), the energy of the pulse drops by $49 \pm 5\%$. In the case of ablation, the laser path correspond to the upper half of this experiment. One can thus estimate the loss to be 30%* and independent on the pulse energy (see figure D.3). The fluency is corrected accordingly.

In the case of confined environment, Berth and Fabbro proposed a simple model to determine the pressure at the ablation point depending on the fluency of the laser[261]:

$$P(MPa) = 10\sqrt{\frac{a}{2a+3}ZI} \tag{D.2}$$

a represents the fraction of the energy involved in the phase transition while the fraction $(1-a)$ is used for the ionization of the gas. Z the interface acoustic impedance [g.cm^{-2}s^{-1}] such that $2/Z = 1/Z_{water} + 1/Z_{target}$ with $Z_{water} = 1.65 \times 10^5$g.cm^{-2}s^{-1}, $Z_{gold} = 62.6 \times 10^5$g.cm^{-2}s^{-1} and $Z_{alumina} = 25.5 \times 10^5$g.cm^{-2}s^{-1}. I is the fluency of the laser in GW/cm^2.

The pressure depending on the fluency of the laser is represented in figure D.2 (c). The solid black line and dashed black line corresponds to the model for $a = 0.06$ in the case of a gold target and in the case of an alumina target respectively. Z is almost the same for both target as it depends mostly on Z_{water} and both line are almost superimposed. Usually, a is slightly larger (0.1-0.2) as reported by Fabbro et al.[261] but might vary depending on the ablation conditions, laser wavelength, pulse duration, etc. However, it seems that the target material (metal *vs* oxide) has little influence on the measured pressure which depends mostly on the laser fluency. This observation is similar to the one in air with a pressure

*Considering the absorption proportional to the intensity.

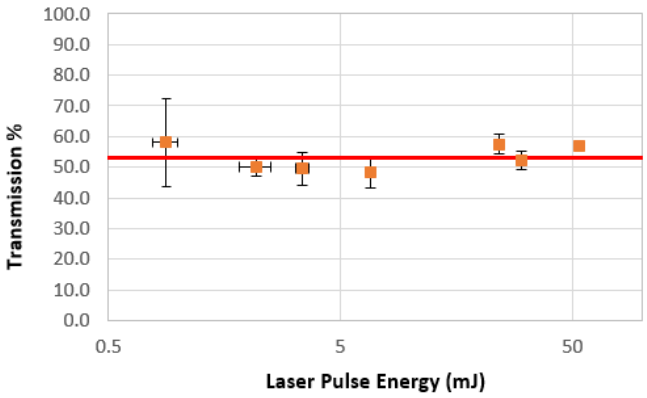

Figure D.3: Measured transmission of the laser pulse focused in water depending on the pulse energy. These measurements correspond to ablation in 1 cm of water.

depending only on the pulse energy (see chapter 3). The main difference remains that the liquid strongly confines the expansion leading to much higher pressure up to a few GPa. Some anisotropy can be expected as in the air. Unfortunately, the precision in the measurements is not good enough to measure significant variation in the shock-wave velocity Here, the pressure discussed is the one deduced from the velocity of the shock-wave in a direction perpendicular to the target's surface.

D.4 Conclusion

The study of the dynamics of laser-generated in water enables to determine the pressure at the ablation point. Its speed decreases very fast to reach the sound velocity within 70 ns. By estimating the initial velocity of the shock-wave, one can use Vogel's work to determine the pressure of the initial point. Because of the confined environment, this pressure appears much higher than in the air and can reach up to 4 GPa for laser pulse fluency of about 70 GW/cm^2. Such an extreme pressure are likely to explain the phase transition observed in PLAL and the damaged of the target. It is also an interesting parameter to take into account while considering nucleation process of the nanoparticles. In particular, the first cluster might be formed in extreme conditions and in metastable crystal structure.

These measured pressures can be described by with Berth and Fabbro's model with $a = 0.06$ for a broad range of laser pulse fluency and on both gold target and alumina target. One can thus use this simple model considering only the acoustic impedance of the target and liquid, and the laser pulse fluency in order to determine the pressure at the ablation point.

Annex E

Measurement of elastic moduli

Abstract: *This annex develops an original technique to accurately measure the Poisson's ratio ν and the ratio E/ρ between the Young's modulus and the density of materials. It is easy to implement, and it requires no calibration. A laser pulse is focused on the sample immersed in a liquid, creating a mechanical excitation of the material at its interface with the liquid. A leaky-Rayleigh surface wave and a longitudinal wave are generated in the sample. Couplings with the liquids create head waves observed in the liquid with time resolved shadowgraph technique using an iCCD camera. Measuring the angle of the head waves with the target enables to determine the velocities of the waves and the elastic moduli of the target material.*

E.1 Introduction

E.1.1 Measurements of mechanical properties

When measuring the dynamics of shock-waves in water, one can observe, surprising Head shock-waves (see figure E.2). These shock-waves are the results of mechanical waves in the target coupling with the liquid. We developed a way to deduce from these observations the elastic moduli for homogeneous isotropic materials. The theoretical investigation of these waves was achieved with the help of the intern Théo Vidril who carried out these calculations also in the case of anisotropic materials (not reported here). For this study, I want to acknowledge the great work of the interns Théo Vidril and Mehdi Fawaz with whom I worked on this project.

Elastic properties remain hard to estimate on materials or samples for which standard methods are unsuitable. Usual techniques based on mechanical deformation of a sample under some constrains provides poor results on hard samples such are crystals or ceramics. It also requires specific sample geometry. For such

materials, elastic moduli can be determined through acoustics. A sound waves are sent thought the sample and the velocities of the waves in the sample is deduced from the times of flight. The precision of the measurement depends a lot on the sample geometry. It usually demands specific sample preparation[262]. Other techniques, more specific, required high technicality. To date sound velocities can be measured using Brilloin spectroscopy leading to the Young's modulus for known optical index and densities. Complex measurement techniques as Computed X-Ray Tomography[263], shear-wave ultrasound elastography and MyotonPRO[264] have been developed to measure the Poisson's ratio. Laser generation of surface waves has been used to measure single crystal elastic constants[265]. We developed here a method based on the measurement of the velocities of laser-generated waves, namely the leaky-Rayleigh surface wave and the longitudinal wave.

E.1.2 Surface waves

When considering the interface of a solid with vacuum, one can determine the existence of the surface wave called Rayleigh's wave. In the case of an interface with a liquid, Rayleigh's wave becomes evanescent, the leaky-Rayleigh's wave, and another surface wave appears, the Scholte wave.

The observation and characterization of leaky-surface waves have a great interests in mechanics and seismology. For instance, meta-barriers are engineered to shield seismic surface waves[266,267,268,269]. Furthermore, coupling between the surface waves and its environment is already observed under the sea and in ionosphere following large earthquakes[270]. It is already used to measure surface wave and have been investigated theoretically[271,272]. Leaky-surface waves can also play a role in the propagation of seismic waves in guided environment like on floating ice on the top of shallow water[273,274]. In mechanics, surface waves are used for monitoring surface cracks[275,276], lubrication film[277], but also to investigate the damage induced by tensile stress on materials and thin films[278,279].

Surface waves such as leaky-Rayleigh waves can be difficult to observe. Propagation velocity is large (a few hundreds of meters per seconds) and it corresponds to small displacement of the surface. Until now, in order to measure surface waves, laboratories uses either interferometry on reflexive surface[278,280,281] or times of flight measurements with mechanical or optical detection techniques[282,283]. In the first case, one need to have a reflexive surface and a complex interferometer apparatus[272]. In the second case, one can only observe the time delay between emission in detection. And in both case, the coupling with the environment is not observed.

Laser-induced mechanical waves are also unintentionally released in laser ablation–based synthesis methods of clusters and nanoparticles (Pulsed Laser Ablation in Liquids[284], Pulsed Laser Deposition etc.) or laser ablation-based chemical analy-

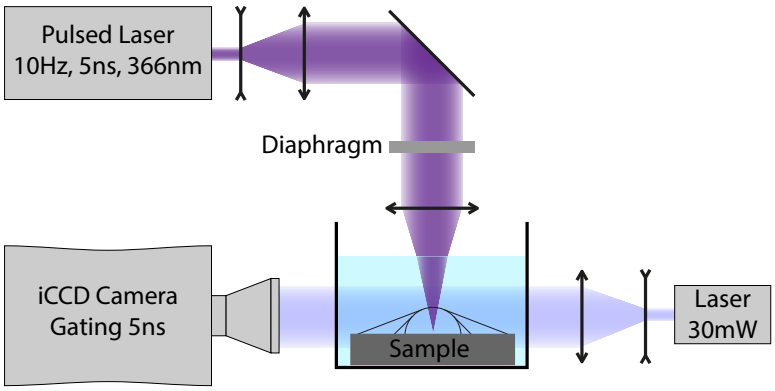

Figure E.1: Outline of the measurement apparatus.

sis techniques (Laser-Induced Breakdown Spectroscopy, Laser-Ablation Molecular Isotopic Spectrometry etc.). Laser-generated shock waves have been extensively reported in Laser Ablation in Liquids[250,251,252,253,40,254,255] and Schmidt head waves, sometimes also named Mach cones, have been observed in the liquids[256,257,258], as well as in the target[285,286]. Laser-generated shock waves are an issue because they can damage the target (see supplementary material in Chemin et al.[50]), but also lead to local changes of the crystal structure of the target[40,287,288,289,175].

E.2 Measurements

E.2.1 Experimental Set-up

A pulsed laser is used in order to trigger surface shock-front and observe the shock-wave[290,291] in liquids using shadowgraphy[48]. The third harmonic of a YAG-Nd pulsed laser (355 nm, 5 ns, 10 Hz, 0.5-100 mW) is focused on various samples immersed in water. The shadowgraph setup is composed of a 30 mW cw diode laser (445 nm) and an iCCD camera from Andor (reference, 1024×1024 pixels) as shown on figure E.1 (b). An objective Zoom 6000 from Navitar is mounted on the iCCD camera with a spatial resolution of 44 μm. The iCCD records the image of the ablation point at a time delay with the laser pulse of ~ 1 μs and a gating of 5 ns. It is better to work slightly out of focus to increase the contrast. The delay between the ablation pulse and the camera is controlled by a digital delay/pulse generator DG645 from Stanford Research Systems.

The characteristics of the ablation laser have little importance on the observation of the phenomena and shock waves in laser ablation in liquids (LAL) have

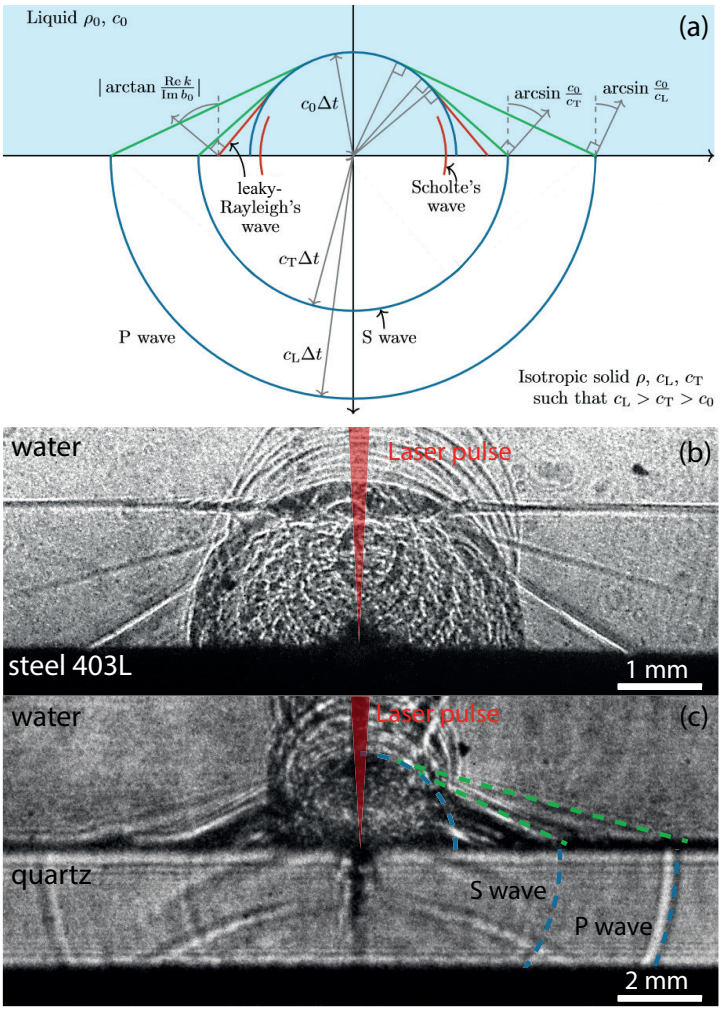

Figure E.2: (a) Representation of the different observed waves. (b) image obtained by shadowgraphy technique with a gating of 5 ns, 1 μs after laser shot. The horizontal shock wave correspond to homogeneous heating of the target by diffused laser light in the water. The oblique shock waves in the water are generated by (i) the leaky-Rayleigh surface wave and (ii) the bulk P-wave. The spherical wave corresponds to the laser-generated compression wave in the liquids. (c) image obtained by shadowgraphy of the ablation on quartz plate. The transparency of the material enables to observe the bulk waves and reflections on the bottom of the plate.

been observed in many configurations[250,251,252,253,40,254,255,256,257,258].

This measurement method was tested on 7 different material in order to demonstrate its efficiency. Materials are selected to be isotropic in order to simplify the calculations. They are referenced in the table E.5 with their tabulated mechanical properties. Despite being roughly flat, no particular attention have been given to the surface state of the material.

The power of the laser needs to be high enough to trigger the shock wave but can be reduced to minimize the damage to the sample. A complete study of the laser power influence of the signal and target surface is given in the section E.3.6. In the case of a silicon buffer, 9 mW was enough to measure both angles. After 20 shots, the crater created was only a few μm deep and 200 μm wide. This technique remains gentle on the sample. Of course, the impact of the laser pulse on the target depends also on the target itself, a brittle target being more likely to be damaged as the pressure can reach a few GPa (see annex D)

E.2.2 Observations

Typical images obtained are shown in figure E.2 for a steel target (b) and a transparent quartz plate (c). At steel target is used for illustration because shock-waves are particularly clear with this material. The quartz target is used because it is transparent and enables to observe the shock-front in the bulk material. Figure E.2 (a) corresponds to a scheme of the different waves observed. First one can observe in the liquid a hemispherical shock-wave propagation from the ablation spot. This shock-wave is the one discussed in the annex D. On figure E.2 (b) one can observe on the top of this hemispherical shock-wave, a horizontal line. It corresponds to a shock-front generated by the fast expansion of the target's surface absorbing diffused light from the laser pulse. This shock-front appears even if the laser is not focused and if there is no ablation. On figure E.2 (c), the horizontal wave is not observed because the quartz sample is transparent and diffused light is not absorbed. In the quartz plate, one can observe two hemispherical shock-front corresponding to the transverse propagation mode (S-wave) and the longitudinal propagation mode (P-wave). P-waves are faster than S-waves and come first. One can also notice the reflection of the P-wave front on the quartz plate's bottom. Oblique lines corresponds to shock-front generated by the coupling waves propagating in the sample and the liquid. On figure E.2 (c), one can notice that the first one forms a small angle with the target in a position corresponding to the P-wave location. This shock-front arises from the coupling of the bulk P-wave with the liquid. The second one forms a larger angle with the target in a position close to the P-wave location. It corresponds to the coupling of the surface leaky-Rayleigh wave with the liquid. The position of the leaky-Rayleigh wave is really close to the position of

the P-wave as represented on figure E.2 (a). One can wonder is the resulting wave observed in the liquid is due to the S-wave or the leaky-Rayleigh wave. Measured velocities are in better agreement of the leaky-Rayleigh wave, which is more likely to have strong couplings with the liquid (see figure E.4 (b)). The surface Scholte wave cannot be observed as it is localized just inside the hemispherical shock-wave, in a very disturbed area.

For materials with bulk waves velocities lower than the sound velocity in the liquid (c_0), one cannot actually observe these waves. For instance, one cannot observe the leaky-Rayleigh wave in the case of gold target in water because the S-wave velocity is too low. These observations are very similar to observations from Zhang et al. with a similar measurement set-up and shock waves created by nano pulse lithotripsy[292].

E.3 Wave velocities and elastic moduli

It is possible to measure the elastic moduli from the shock-front observation. The shock-front angle due to the P-wave and the leaky Rayleigh waves provides the velocity of the bulk S-wave and P-wave respectively. Using both of these velocities, one can deduce the ratio E/ρ and ν, with E the Young modulus, ρ the density of the material and ν the Poisson ratio. In a first part, an approximated solution considering the Rayleigh wave (defined in vacuum) instead of the pseudo-Rayleigh wave is exposed. This approximation lead to a systematic error of a few percent in the end result which is usually less than the error on the measurement due to the accuracy of the angle determination (see section E.3.5). In a second part, the exact solution considering pseudo-Rayleigh waves is treated which implies heavier calculation.

E.3.1 Approximated solution

Here the pseudo-Rayleigh wave is assimilated to the Rayleigh wave defined for the interface between a solid and vacuum. In that case, an approach solution of the Rayleigh wave velocity c_R is given by[293]:

$$c_R = c_T \sqrt{\frac{28\nu + 22}{21\nu + 29}} \tag{E.1}$$

with c_T the velocity of the transverse wave (S-wave) and ν the Poisson's ratio. The relation between the angles and the velocities are:

$$\begin{aligned} \sin(\theta_R) &= \frac{c_0}{c_R} \\ \sin(\theta_L) &= \frac{c_0}{c_L} \end{aligned} \tag{E.2}$$

with c_0 the sound velocity in the liquid, c_L the velocity of the longitudinal wave (P-wave) and θ_R and θ_L the angles of both waves with the direction perpendicular to the surface. For an isotropic material, the mechanical parameters E and ν are related to c_L and c_T through:

$$\begin{aligned} c_T &= \sqrt{\frac{1}{2(1+\nu)}\frac{E}{\rho}} \\ c_L &= \sqrt{\frac{1-\nu}{(1+\nu)(1-2\nu)}\frac{E}{\rho}} \end{aligned} \tag{E.3}$$

Combining both equations, one can deduce that:

$$\left(\frac{c_T}{c_L}\right)^2 = \frac{1-2\nu}{2(1-\nu)} \tag{E.4}$$

and using equation E.1 we introduce γ which depends only on ν as:

$$\gamma = \left(\frac{c_R}{c_L}\right)^2 = \frac{1-2\nu}{2(1-\nu)} \times \frac{28\nu+22}{21\nu+29} \tag{E.5}$$

Inversion of this equation gives a solution of ν depending only on γ:

$$\nu = \frac{4-4\gamma-\sqrt{625\gamma^2-1075\gamma+324}}{7(3\gamma-4)} \tag{E.6}$$

with

$$\gamma = \left(\frac{c_R}{c_L}\right)^2 = \left(\frac{\sin(\theta_L)}{\sin(\theta_R)}\right)^2 \tag{E.7}$$

Here one can notice that the measurement of the Poisson's ratio from the measurement of both angle does not depend on the sound velocity in the liquid (c_0) nor the density of the material (ρ). It does not depend on any calibration.

One can then calculate the ratio E/ρ as:

$$\frac{E}{\rho} = 2(1+\nu)\frac{21\nu+29}{28\nu+22}\left(\frac{c_0}{\sin(\theta_R)}\right)^2 \tag{E.8}$$

or:

$$\frac{E}{\rho} = \frac{(1+\nu)(1-2\nu)}{1-\nu}\left(\frac{c_0}{\sin(\theta_L)}\right)^2 \tag{E.9}$$

depending on the angles measured with the better precision, or an average of both.

In the case of the approximated solution, the propagation of the error can be fully calculated and is presented in the section E.3.5.

E.3.2 Exact solution

The second calculation method consider the leaky-Rayleigh wave. In that case, there is no approximation, and we just consider that $c_0 < c_T < c_L$. The velocity of the pseudo-Rayleigh wave is given by the complex root of the following polynomial[294]:

$$P(c) = \left[\left(2-\frac{c^2}{c_T^2}\right)^4\left(1-\frac{c^2}{c_0^2}\right) - 16\left(1-\frac{c^2}{c_T^2}\right)\left(1-\frac{c^2}{c_L^2}\right)\left(1-\frac{c^2}{c_0^2}\right) - \frac{\rho_0^2c^8}{\rho^2c_T^8}\left(1-\frac{c^2}{c_L^2}\right)\right]^2 - 64\frac{\rho_0^2c^8}{\rho^2c_T^8}\left(1-\frac{c^2}{c_T^2}\right)\left(1-\frac{c^2}{c_L^2}\right)^2\left(1-\frac{c^2}{c_0^2}\right) \tag{E.10}$$

with ρ_0 the density of the liquid. The complex root corresponding to the leaky-Rayleigh velocity $\bar{c}_{RF}$ has to verify three condition (C1, C2 and C3):

(C1) $\bar{c}_{RF}$ has to be solution of:

$$\left(2\frac{c_T^2}{\bar{c}_{RF}^2}-1\right)^2 - 4\frac{c_T^2}{\bar{c}_{RF}^2}\sqrt{\frac{c_T^2}{\bar{c}_{RF}^2}-\frac{c_T^2}{c_L^2}}\sqrt{\frac{c_T^2}{\bar{c}_{RF}^2}-1} \pm\frac{\rho_0}{\rho}\frac{\sqrt{\frac{c_T^2}{\bar{c}_{RF}^2}-\frac{c_T^2}{c_L^2}}}{\sqrt{\frac{c_T^2}{\bar{c}_{RF}^2}-\frac{c_T^2}{c_0^2}}} = 0. \tag{E.11}$$

here, the real part of $\sqrt{}$ are by convention positive.

(C2)

$$\mathrm{Re}(\bar{c}_{RF})\mathrm{Im}(\bar{c}_{RF}) > 0 \tag{E.12}$$

(C3) The absolute value of $\bar{c}_{RF}$ real part is lower than the transverse wave velocity:

$$|\mathrm{Re}(\bar{c}_{RF})| < c_T \tag{E.13}$$

The roots of $P(c)$ corresponding to these criteria are down to two with opposite signs. They correspond to the same evanescent wave reversing time. The relation between the measured angle θ_R and $\bar{c}_{RF}$ is:

$$\tan(\theta_R) = \left| \frac{\mathrm{Re}\left(\frac{1}{\bar{c}_{RF}}\right)}{\mathrm{Im}\left(\sqrt{\frac{1}{\bar{c}_{RF}^2} - \frac{1}{c_0^2}}\right)} \right| \tag{E.14}$$

c_L can be easily determined from the measurement of the angle associated with the L-wave using equation E.2. From known values of c_L, c_0, ρ_0 and ρ, and a given value of c_T one can deduce the roots of E.10 and select the one corresponding to leaky-Rayleigh wave thanks to the conditions E.11-E.13 giving $\bar{c}_{RF}(c_T)$. The equation E.14 provides the angle $\theta_R^{calc}(c_T)$ one should observe for this value of c_T. The difference with the measured angles $\Delta\theta_R(c_T) = \theta_R^{calc}(c_T) - \theta_R^{meas}$ is minimized in order to obtain the measured value of c_T. One can then use measured values of c_T and c_L and the equation E.3 to determine the elastic moduli of the target material.

E.3.3 Measurement condition

In order to be able to measure elastic moduli, one need to be able to observe both waves in the liquid. The conditions for that are $c_R > c_0$ and $c_L > c_0$. It depends both on the target material properties and sound velocity in the liquid. In figure E.3 (right), one can observe the condition on E/ρ and ν for the observation of both waves. It was calculated considering the Rayleigh wave approximation and various liquids. Rectangles correspond to the range of elastic moduli of common materials. One can observe that water is suited to measure most of them. Yet, for soft metals like gold or plastics like PVC, other liquids with lower sound velocities are required such as Perfluoro-n-hexane. Materials such as rubber or skin cannot be characterized by this technique. Figure E.3 (right) represents the same conditions to observe the shock-front due to L-wave only. This can be useful to measure its velocity.

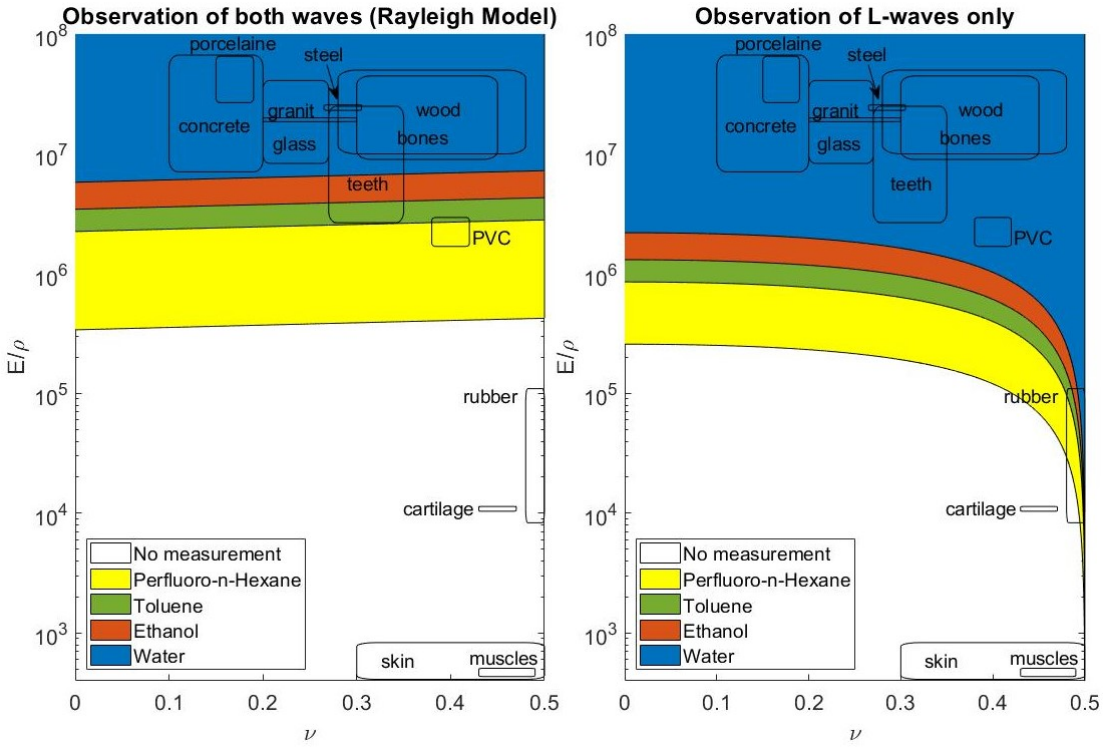

Figure E.3: Condition on E/ρ and ν of the material for observation of both longitudinal L wave (P-wave) and Rayleigh wave or only L wave depending on the liquid used.

E.3.4 Results

In order to test the measurement technique, we selected 7 materials known as isentropic: YAG, YIG, GGG, Al, Al_2O_3, $LiNBO_3$ and Ti (see the column samples in the table E.5). Crystals and ceramics are grown in the laboratory by Czochralski (Cz) technique with radio frequency induction heating in an iridium crucible in the team of Kheirreddine Lebbou. Metals are pure targets. The interest of using isotropic materials is to test the measurement technique without considering the dependence of the sound velocities over the propagation direction. A quantification of the anisotropy of each material is given by the coefficient reported in the column A^U of the table E.5. It corresponds to the universal anisotropy index[295]. For a perfect isotropic material $A^U = 0$ and the higher it is, the less isotropic is the material.

On each of these sample the angles were measured from images corresponding to ablation in water. Measurement was done by hand on ImageJ. The average is given in the column "direct measurement" of the table E.5. Depending on the

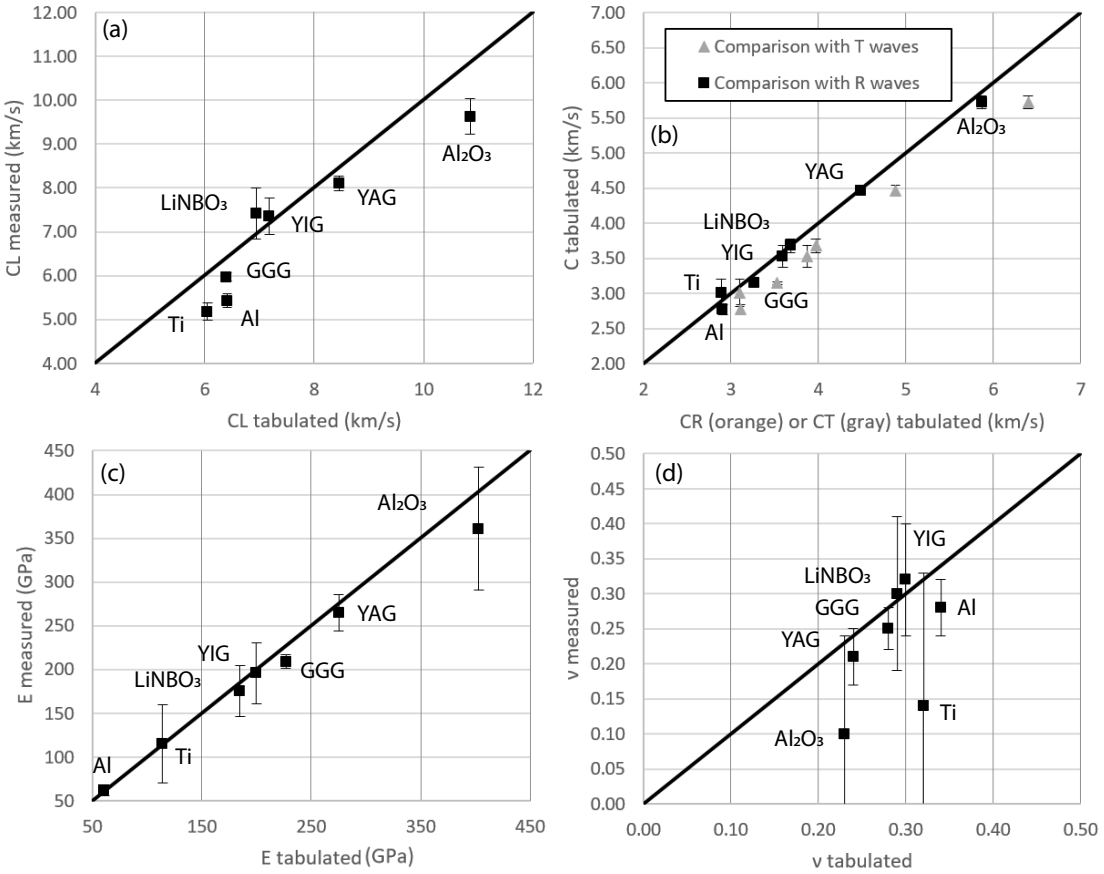

Figure E.4: (a) Comparison between the longitudinal wave (P-wave) velocities c_L measured and tabulated on the materials presented in the table E.5. (b) Comparison between the transverse wave (S-wave) velocity c_T and leaky-Rayleigh wave velocity c_R tabulated and the measured wave velocity. Comparison between the measured and tabulated Young's coefficient E (c) and Poisson ratio ν (d).

samples and the quality of the images, an average is calculated from 6 to more than 20 images. The error corresponds to the standard error multiplied by the student coefficient for a confidence level of 95%.

Figure E.4 (a) corresponds to the comparison between the longitudinal velocities measured from the θ_L measurement considering the relation $sin(\theta_L) = c_0/c_L$ and the tabulated values[297,296,131]. Error bars corresponds to the propagation of the error on the angle considering the sound velocity in the liquid to be known ($c_0 = 1483\ m/s$). Discrepancies can arise from differences between the tabulated value and the real values for the measured sample.

Samples	Direct measurement		Calculated from Rayleigh		Calculated from Leaky-Rayleigh		Tabulated values				
	θ_L (°)	θ_R (°)	ν (independent of ρ)	E (Gpa)	ν	E (Gpa)	A^U	ρ (kg/m3)	ν	E (Gpa)	Ref
YAG	10.54 ± 0.21	19.34 ± 0.33	0.21 ± 0.03	265 ± 15	0.21 ± 0.04	265 ± 21	0.0002	4560	0.25	272	[Huang2012]
YIG	11.62 ± 0.67	24.82 ± 1.28	0.32 ± 0.04	196 ± 34	0.32 ± 0.08	196 ± 35	0.0009	5170	0.30	201	[CRC]
GGG	14.37 ± 0.25	28.01 ± 0.24	0.26 ± 0.02	208 ± 10	0.25 ± 0.03	209 ± 8	0.0038	7096	0.28	226	[Kushibiki2002]
Al	15.82 ± 0.44	32.30 ± 0.90	0.28 ± 0.03	62 ± 5	0.28 ± 0.04	62 ± 6	0.0488	2699	0.34	70	[CRC]
Al_2O_3	8.85 ± 0.37	14.98 ± 0.24	0.10 ± 0.09	362 ± 34	0.10 ± 0.14	361 ± 70	0.1682	3990	0.23	403	[CRC]
$LiNBO_3$	11.53 ± 0.91	23.74 ± 0.72	0.30 ± 0.05	176 ± 37	0.30 ± 0.11	175 ± 29	0.1683	4300	0.29	185	[CRC]
Ti	16.60 ± 0.63	29.44 ± 2.19	0.15 ± 0.13	115 ± 14	0.14 ± 0.19	115 ± 45	0.1717	4506	0.32	114	[CRC]

Figure E.5: Table of the different target materials used, the measured angles, deduced velocities and elastic moduli. A^u corresponds to the Universal elastic anisotropy index[295]. Tabulated value are extracted from Huang et al.[296], Kushibiki et al.[297] and CRC handbook[131].

Figure E.4 (b) corresponds to a comparison of the measured velocity from the θ_R measurement considering the relation $sin(\theta_R) = c_0/c_R$ and the tabulated values of c_R (in black) and c_T (in gray)[297,296,131]. The measured velocities are in better agreement with the c_R from tabulated values, which indicates that the observed wave-front is indeed due to the Rayleigh wave and not to the transverse wave (S-wave). Here, the relation corresponds to the Rayleigh wave approximation. The values of c_R considering the leaky Rayleigh wave are not shown here because they are so close to the approximated solution one cannot make the difference on the plot.

Results on the calculation of E and ρ are given in the table E.5 in the case of the Rayleigh approximation and considering the leaky-Rayleigh solution. Both calculation techniques lead to extremely similar results and differences can only be seen on the last digit, within the error range. These values are compared of the tabulated values (see table E.5) in figure E.4 (c) for the Young modulus and figure E.4 (d) for the Poisson's ratio. Errors are given by the propagation of the error on the angle measurements considering the tabulated densities. The Young modulus is in very good agreement with the tabulated values and with good uncertainties. Poisson's ratio is harder to determine because of the large uncertainties.

E.3.5 Precision of the measurement

The technique presented here might become an interesting tool to measure elastic moduli. In that perspective, a precise discussion on the error is important. Here

is presented the error propagation on the calculation method using the Rayleigh approximation. In particular, it is interesting to see how the error on the angles' measurement impacts the error on the results.

The error on the angle measurement arises from three different origins: (i) the process repeatability (ii) the imaging and (iii) the image processing.

In the first case, it is a statistical fluctuation difficult to control. In the second case, one need to ensure the fact that there is no deformation of the image for the angle measurement. This error can be easily measured by imaging geometrical patterns in the same configuration of the experiment. In our case, we checked that the deformation of the angle was below 0.1^o for a right angle, that is to say about 1% of the measurement. In the third case, the error depends strongly on the angle measurement technique. Here manual pointing on ImageJ was used. The error comes mainly from the blurriness of the image. With our images, one is able to measure an angle with an error of about 0.1^o for clear images and 0.5^o for the worst images used. In both cases, the error (ii) and (iii) appears to be negligible with respect to (i). It is thus possible to adopt a statistical treatment for the error. By increasing the number of measurements, one can reduce the error on the average. For a given confidence level on the result, one can thus adapt the number of measurements considering no other origin for the error.

Definition of the error

The repeatability of the measurement come from the statistical distribution of the measurements θ_i (i=L, R) on the same sample. One can estimate the true value of the angle with the average $\bar{\theta}_i$ of n_i measurements θ_i and an interval for a two-sides $100 \times (1-x)$ % confidence given by:

$$\left[\bar{\theta}_i - t_{x/2}^{n_i-1}\frac{s}{\sqrt{n_i}}, \bar{\theta}_i + t_{x/2}^{n_i-1}\frac{s}{\sqrt{n_i}}\right] \tag{E.15}$$

where $t_{x/2}^{n_i-1}$ is the Student's coefficient and s_i the unbiased estimate of the variance given by:

$$s_i^2 = \frac{1}{n_i - 1}\sum_{j=1}^{n}(\theta_j - \bar{\theta}_i)^2 \tag{E.16}$$

The larger is the number of measurements, the more precise is the estimation of the average. In our case, this error appears to be larger than the error on the angle measurement. In figure E.6 (a) we can show the distribution deviation from the average of all the 379 measurements done on all the samples. As expected, this follow a binomial distribution with a global standard deviation of $s_{\theta_i} = 1.0^o$. One can expect that this standard deviation is a good estimation of the true value

considering the large number of measurements. This distribution actually consider both the error due to the variability between two measurements but also the variability when we measured the angle. We believe these variations come mostly from the target surface state as it changes from one measurement to another. By using a clean, polished surface, one can expect this distribution to spread less. Indeed, 46 measurements are done on Si buffer whose surface is very much clean and the distribution has a deviation of about $\sigma = 0.65^o$ (see figure E.6 (b)).

In order to calculate the error on ν and E, we considered the error propagation as following. Let us consider a quantity $f(a_j)$ with a_j some random variable with a standard deviation s_j. In our case f is ν or E and a_j correspond to the two angles θ_L and θ_T. Thus, we have that f is also a random variable and its deviation can be calculated as:

$$s_f^2 = \sum_j \left(\frac{\partial f}{\partial a_j}\right)^2 s_j^2 \tag{E.17}$$

Then one can define a confidence interval exactly the same way we did for angles.

Calculation of the error on E and ν

In the case of E, its expression also depends on C_{liq} and ρ which are not random variables but which have some uncertainties. Here, these errors are not considered for the clarity of the calculation and discussion.

In order to simplify the calculation, we introduce $X_i = sin(\theta_i)^2$ and $\gamma = X_L/X_R$.

$$s_{X_i}^2 = \left(\frac{\partial X_i}{\partial \theta_i}\right)^2 s_{\theta_i}^2 \qquad \text{and} \qquad \left(\frac{s_{X_i}}{X_i}\right)^2 = \left(2\frac{s_{\theta_i}}{tan(\theta_i)}\right)^2 \tag{E.18}$$

$$s_\gamma^2 = \left(\frac{\partial \gamma}{\partial X_L}\right)^2 s_{X_L}^2 + \left(\frac{\partial \gamma}{\partial X_R}\right)^2 s_{X_R}^2 \qquad \text{and} \qquad \left(\frac{s_\gamma}{\gamma}\right)^2 = \left(\frac{s_{X_L}}{X_L}\right)^2 + \left(\frac{s_{X_R}}{X_R}\right)^2 \tag{E.19}$$

Because ν depends only on γ one can directly write the standard deviation as:

$$s_\nu^2 = \left(\frac{\partial \nu}{\partial \gamma}\right)^2 s_\gamma^2 \qquad \text{and} \qquad \left(\frac{s_\nu}{\nu}\right)^2 = \mathcal{F}(\gamma)^2 \left(\frac{s_\gamma}{\gamma}\right)^2 \tag{E.20}$$

with

$$\mathcal{F}(\gamma) = \frac{\gamma}{4 - 4\gamma - \sqrt{625\gamma^2 - 1075\gamma + 324}} \frac{8\sqrt{625\gamma^2 - 1075\gamma + 324} + 1775\gamma - 2356}{2(3\gamma - 4)\sqrt{625\gamma^2 - 1075\gamma + 324}} \tag{E.21}$$

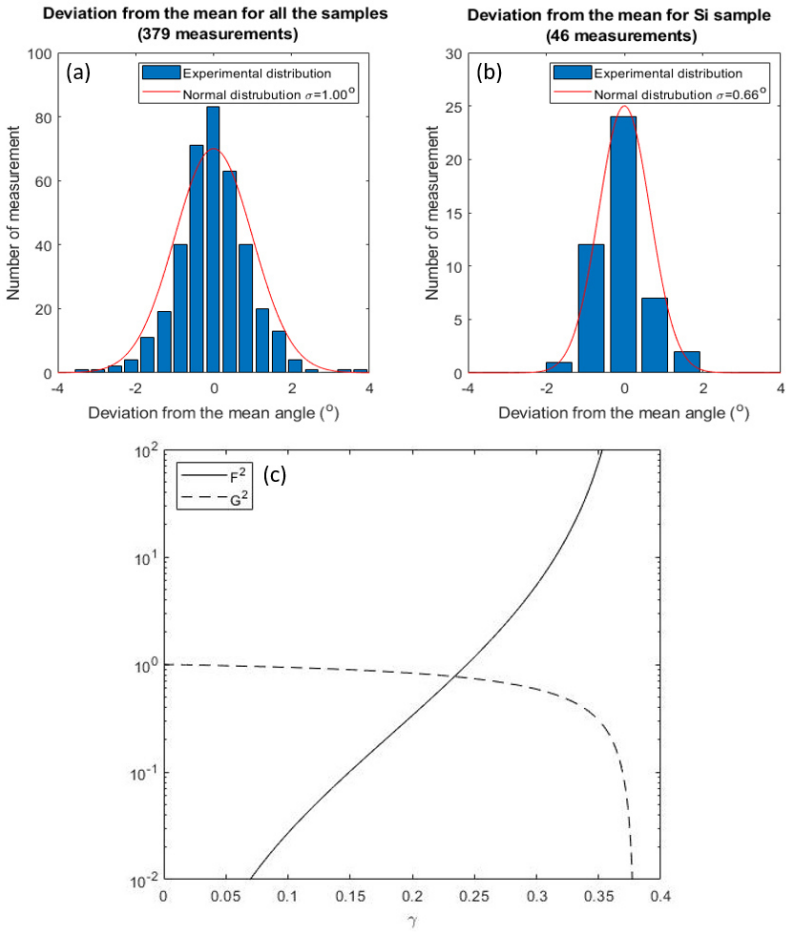

Figure E.6: Distribution of the variations from the average computed for all our 379 measurements (a) and the 46 measurements on Si buffer (b). Red curves corresponds to normal distributions with σ corresponding to the experimental standard deviation of the distributions. Evolution of the Error functions $\mathcal{F}$ (c) and $\mathcal{G}$ (d) in terms of γ. Plot of the relative error s_ν/ν (e) and s_E/E (f) in terms of the two angles measured, considering the average s_θ measured from (a).

The value of $\mathcal{F}(\gamma)^2$ depending on γ is represented on figure E.6 (c) with a solid line. This function increases extremely fast with the value of γ and explains why the error on ν is so important for materials with large γ values.

E depends on X_L or X_R such that:

$$s_E^2 = \left(\frac{\partial E}{\partial X_L}\right)^2 s_{X_L}^2 + \left(\frac{\partial E}{\partial X_R}\right)^2 s_{X_R}^2 \tag{E.22}$$

and

$$\left(\frac{s_E}{E}\right)^2 = (1+\mathcal{G}(\gamma)^2)\left(\frac{s_{X_L}}{X_L}\right)^2 + \mathcal{G}(\gamma)^2\left(\frac{s_{X_R}}{X_R}\right)^2 \tag{E.23}$$

with:

$$\mathcal{G}(\gamma) = \frac{2\nu^2(2-\nu)}{(1-\nu)(1+\nu)(1-2\nu)}\mathcal{F}(\gamma) \tag{E.24}$$

with ν a function of γ:

$$\nu = \frac{4-4\gamma-\sqrt{625\gamma^2-1075\gamma+324}}{7(3\gamma-4)}. \tag{E.25}$$

The value of $\mathcal{G}(\gamma)^2$ depending on γ is represented on figure E.6 (c) with a dashed line. $\mathcal{G}(\gamma)^2$ decreases with γ. For low values of γ, $\mathcal{G}(\gamma)^2 \simeq 1$ and the error on the measurement of θ_L is two times more important than the one on θ_R. This trend increases with γ and for $\gamma > 0.35$ the error on θ_R becomes negligible. There is no value of γ for which the error diverges. This explains why the precision on E is better.

E.3.6 Threshold in power density

The laser power was set using a diaphragm cutting part of the laser beam and measured using a Nova II power meter mounted with a high energy pyroelectric sensor. For each power, the target was shot in the exact same condition 20 times. Shadowgraph images were recorded at the same time. The target chosen is a buffer of silicon. The very clean surface of the buffer enable clear observation of the ablation spot. In order to characterize how much our measurement is destructive, the craters are imaged with a VHX7020 microscope from Keyence which enable topography measurement (see figure E.7 (a-d)). 9 different pulse powers were used from 0.5 to 90 mW indexed from 1 to 9. Measurements enable to measure the topography on the crater and measure its diameter (e), depth (f), and volume (g). The higher the energy of the pulse, the larger the crater and the more invasive the measurement. In parallel, shock wave imaging for laser power of 0.5, 9 and 90 mW is reported in figure E.7 (h). When the power is too low (0.5 mW), ablation is not strong enough to observe oblique shock-wave easily and measure the elastic moduli. In order to better quantify the possibility of measurement from an image, one can define some *signal intensity*. If the signal intensity is large enough, one should be able to measure an angle. The signal intensity (see figure E.7 (i)) is defined as the sum of the pixel difference between one image and a background image taken just before the shutter opens, without ablation. This sum is down on the area of the

image on the right of the hemispherical shock wave. In this experiment, it was found that the measurement was possible with a power of 9 mW (signal intensity $> 1 \times 10^{10}$) which corresponds to a crater of about 200 μm diameter. The depth of the crater is very low and never exceed 3 μm. Thus, the volume ablated material for a use-full measurement is about 3×10^4 μm^3 that is to say in the case of silicon 70 ng for 20 pulses. These measurements are done with 20 shots on the same spot in order to enable depth measurement. In order to measure the 20 angles, one could rather change the ablation spot. This would increase the damage surface but reduce the depths.

E.4 Conclusion

Observation of the laser-generated shock-waves in a liquid enables to observe shock-fronts due to the propagation of P-waves in the bulk material and leaky-Rayleigh surface waves. The angle formed by these shock-fronts and the target surface can be directly related to the wave velocities. The measurement of these velocities can then be related to the mechanical properties of the material. In particular, one can use Rayleigh-wave approximation to easily measure the local Poisson's ratio and Young modulus of isotropic material. This technique has been tested on 7 different isotropic materials and give results in good agreement with tabulated values. The error due to Rayleigh-wave approximation is negligible compared to the exact solution given by the leaky-Rayleigh wave. In the case of an anisotropic material, one should consider the direction of propagation of the wave. In that case, changing the orientation of the sample would enable to determine the elastic tensor coefficients. The precision of the measurement is limited by the repeatability of the ablation process. By increasing the number of measurements, one can reduce the standard error on the average.

This technique is patented. It offers many advantages. It is an easy way to measure Poisson's ration and the ratio E/ρ with E the young modulus and ρ the material density. This process requires no preparation of the sample (smoothing, shaping, size calibration). It is low invasive, it removes only a few nanograms of material. It could be used also for archaeological purpose. The measurement is fast and provides values with a few percent errors. This could be used for new material development or for quality control even directly on the finished product. The process is not sensitive to surface aspect such are roughness or thin coating.

This technique requires little conditions. The sample has to be regular enough on the observed range (a few mm) for the angle to be well-defined. One should take care that the sample is not soluble in the liquid used. One need the Rayleigh velocity and P-wave velocity to be both larger than the sound wave velocity in the liquid.

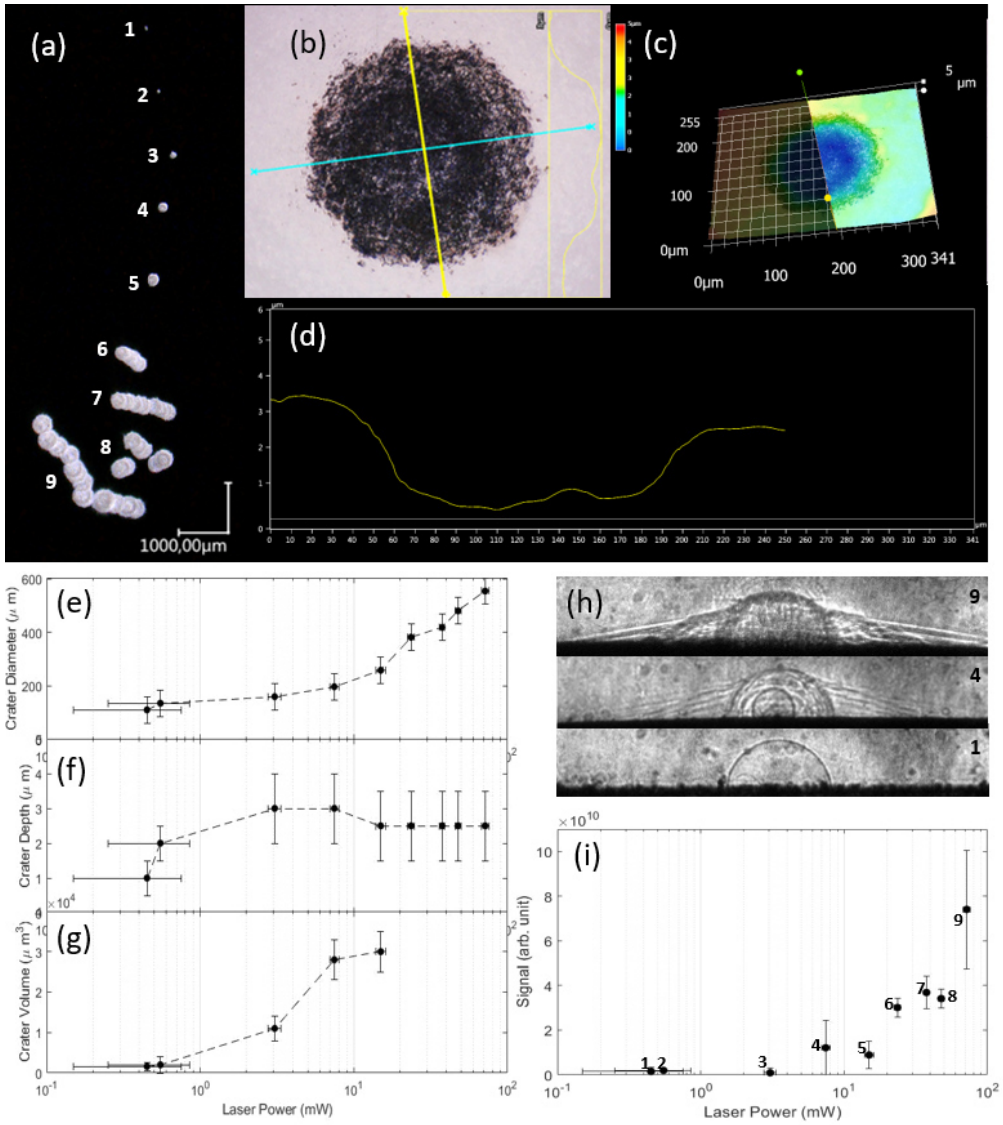

Figure E.7: Influence of the laser power on the observation of the phenomena and the surface state of a Si buffer sample. (a) Image of the craters obtained after 20 shots for different laser power. (b) Imaging of the crater 3 for a 3 mW laser power. (d) Profile of this crater for a 3 mW measured with a VHX7020 microscope from a 3D reconstitution of the crater (c). Evolution of the crater diameter (e), crater depth (f), and crater volume (g). (h) Shadowgraph images obtained for $0.5, 9$ and 90 mW laser power. (i) Evolution of the oblique shock waves signal with the laser power.

Annex F

Doping nanoparticles

F.1 Introduction

During my PhD, I also worked on the formation of nanoparticles generated by Pulsed Laser Ablation in Liquids (PLAL). This topic is developed by David Amans at the ILM for the generation of colloidal solution of nanoparticles. The formation of the nanoparticles in PLAL raises similar questions to nucleation in gas phase. Major differences are the conditions in the plasma with higher densities, larger cooling rate and larger pressure.

One of the question raised by nucleation in liquids is the influence of the liquid composition in the nucleation process. Influence of the liquid is important on the formation of the nanoparticles. For instance, oxide particles are generated from pure metallic targets in water and carbon shell appears for ablation in organic liquids. One can wonder when and to what extent atoms from the liquid enter the nucleation process. In particular, is it possible to dope the nanoparticles with atoms from the liquid?

Here, the impact of the liquid composition on the nucleation is studied by ablating pure Gd_2O_3 target in water containing Eu salts. The study of the produced nanoparticles shows that the Eu atoms are part of the nucleation process and form Gd_2O_3 : Eu monoclinique nanoparticles.

F.2 Article

Nanoscale Advances

PAPER

View Article Online
View Journal | View Issue

Check for updates

Cite this: *Nanoscale Adv.*, 2019, **1**, 3963

Doping nanoparticles using pulsed laser ablation in a liquid containing the doping agent†

Arsène Chemin,[a] Julien Lam,[b] Gaétan Laurens,[a] Florian Trichard,[a] Vincent Motto-Ros,[a] Gilles Ledoux,[a] Vítězslav Jarý,[c] Valentyn Laguta,[c] Martin Nikl,[c] Christophe Dujardin[a] and David Amans*[a]

Received 8th April 2019
Accepted 22nd August 2019

DOI: 10.1039/c9na00223e

rsc.li/nanoscale-advances

While doping of semiconductors or oxides is crucial for numerous technological applications, its control remains difficult especially when the material is reduced down to the nanometric scale. In this paper, we show that pulsed laser ablation of an undoped solid target in an aqueous solution containing activator ions offers a new way to synthesise doped-nanoparticles. The doping efficiency is evaluated for laser ablation of an undoped Gd_2O_3 target in aqueous solutions of $EuCl_3$ with molar concentration from 10^{-5} mol L^{-1} to 10^{-3} mol L^{-1}. Thanks to luminescence experiments, we show that the europium ions penetrate the core of the synthesised monoclinic Gd_2O_3 nanoparticles. We also show that the concentration of the activators in the nanoparticles is proportional to the initial concentration in europium ions in the aqueous solution, and a doping of about 1% ([Eu]/[Gd] atomic ratio) is reached. On the one hand, this work could open new ways for the synthesis of doped nanomaterials. On the other hand, it also raises the question of undesired penetration of impurities in laser-generated nanoparticles in liquids.

Open Access Article. Published on 30 August 2019. Downloaded on 5/6/2021 2:48:50 PM.
This article is licensed under a Creative Commons Attribution 3.0 Unported Licence.

1 Introduction

Doping of semi-conductors and oxides has been pivotal in the development of modern technologies as it enables one to finely tune electronic and optical properties of the materials.[1–6] At the nanometric scale, a crucial glass ceiling remains in the ability to control the doping mechanisms.[7,8] Indeed, being able to dope on demand nanoparticles with the desired impurities is still challenging because of self-purification mechanisms[9] or affinity issues between the impurities and the particles' surface during their growth.[10] In this context, the impurity positioning is a key aspect at the nanometric scale,[9,11] and chemical synthesis methods do not always succeed at inserting the doping elements inside the nanoparticles core.[12,13]

Alternative bottom-up techniques, where the system undergoes highly non-equilibrium transitions, could be a possible route towards the control of doping in nanoparticles. Since the nineties,[14] PLAL has proven its reliability and its versatility to synthesise nanomaterials,[15–23] including doped nanoparticles.[24–30] PLAL provides clean and ligand-free surfaces,[31] and can be operated continuously with production rates of several grams per hour.[32,33] Standard route to obtain doped nanoparticles with this technique is to prepare a doped bulk material as a pellet using solid state reaction before ablation. Preparing a doped pellet is nevertheless not always straightforward since it requires to follow thermodynamic equilibrium pathways. Alternatively, using the solvent as support for the doping agent exhibits high interests because activators can be incorporated within the nanoparticle's matrix in a one step process.

The fundamental mechanisms of PLAL have been studied in a large number of contributions. For each laser pulse, the ablation of the target leads to a hot and dense plasma.[34–37] In the case of nanosecond pulses, it has been shown that the nascent plasma and the liquid partially merge in the first few hundred nanoseconds.[38] A fast energy transfer from the laser pulse to the liquid is then supported by the nascent plasma. Solvent molecules are vaporised to form a vapour bubble, mainly composed of the solvent molecules with respect to the ablated matter.[19,39] Accordingly, atoms from the solvent can significantly contribute to the final stoichiometry of the nanoparticles. Indeed, numerous oxides were obtained starting from pure metal targets ablated in water.[40–47] Furthermore, carbon nitride nanoparticles were obtained following the ablation of a carbon target in ammonia.[48,49] Similarly, the ablation of iron targets in various organic solvents led to iron-based nanoparticles including iron carbide (Fe_3C), iron oxides, amorphous and crystalline iron.[50,51] The fast cooling (a few microseconds) of the plasma mixed with solvent vaporised molecules leads to the

[a]Univ Lyon, Univ Claude Bernard Lyon 1, CNRS, Institut Lumière Matière, F-69622, Villeurbanne, France. E-mail: david.amans@univ-lyon1.fr
[b]Center for Nonlinear Phenomena and Complex Systems, Université Libre de Bruxelles, Code Postal 231, Boulevard du Triomphe, 1050 Brussels, Belgium
[c]Inst Phys AS CR, Cukrovarnicka 10, Prague 16200, Czech Republic

† Electronic supplementary information (ESI) available. See DOI: 10.1039/c9na00223e

Open Access Article. Published on 30 August 2019. Downloaded on 5/6/2021 2:48:50 PM.
This article is licensed under a Creative Commons Attribution 3.0 Unported Licence.

nucleation and growth of nanoparticles with size ranging from few nanometers to a few tens of nanometers. Their composition can combine species from the ablated target and the solvent. Although the role of the solvent molecules was already evidenced, the role of solvated ions or impurities is still poorly documented. Using plasma spectroscopy, Matsumoto *et al.*[52] showed the transfer of Li^+ and Na^+ ions dissolved in the liquid into the plasma. Using SAXS, Letzel *et al.* showed that in the case of a gold target ablation, adding Cl^- ions in the aqueous solution allows for a size quenching of the gold nanoparticles. The size quenching is observed early within the cavitation bubble.[53] Such results demonstrate that the Cl^- ions already play an important role during the condensation of the plasma by interacting with the nanoparticle surface during their growth. However, these ions that were added within the solvent could also penetrate the nanoparticles core. While such mechanism has not been investigated so far, it would offer a new route to dope the nanoparticles by ablating undoped materials in a salt solution. In addition, it also raises the question of the penetration of unwanted impurities from the solvent which can hinder the expected properties of the particles.

In order to evaluate the contribution of the solvent as a doping media in PLAL, we performed the ablation of undoped monoclinic phase Gd_2O_3 targets immersed in aqueous solutions of $EuCl_3$, for various salt concentrations. Gd_2O_3:Eu^{3+} is a well-known red luminescent sesquioxyde[26,54,55] containing gadolinium which is also known as contrast agent for nuclear magnetic resonance imaging,[56,57] but also as radiosensitizer.[58] In addition, Eu^{3+} luminescence is sensitive to the crystal structure, since it highly depends on the crystal field symmetry of the crystallographic sites. Eu^{3+} luminescence is thus known as a very efficient structural probe. X-ray diffraction (XRD), selected area electron diffraction (SAED) and high resolution transmission electron microscope (HRTEM) measurements reveal that the generated nanoparticles are in the monoclinic phase. Luminescence properties (emission and excitation) allow to clearly discriminate between emission from Eu^{3+} ions in the core of the monoclinic Gd_2O_3 nanoparticles, and emission from the remaining salts or Eu^{3+} adsorbed on the Gd_2O_3 surface. Furthermore, the [Eu]/[Gd] ratio has been quantified inside the plasma. Indeed, the amount of vaporised solvent, and then the number of europium atoms inside the plasma are obtained from fast imaging of the laser-induced cavitation bubble, while the number of gadolinium atoms is deduced from product weighing. The deduced [Eu]/[Gd] ratio inside the plasma will be confronted to laser-induced breakdown spectroscopy (LIBS) performed on the dried powder for the highest doped sample.

2 Experimental section

Synthesis (PLAL)

A graphical summary of the synthesis parameters is displayed in Fig. 1. The ablation set-up uses a laser source based on a Master Oscillator Power Amplifier (MOPA) architecture from Fibercryst company. The beam from a passively Q-switched kilohertz Nd:YAG laser (1 kHz), operated at 1064 nm, is amplified using

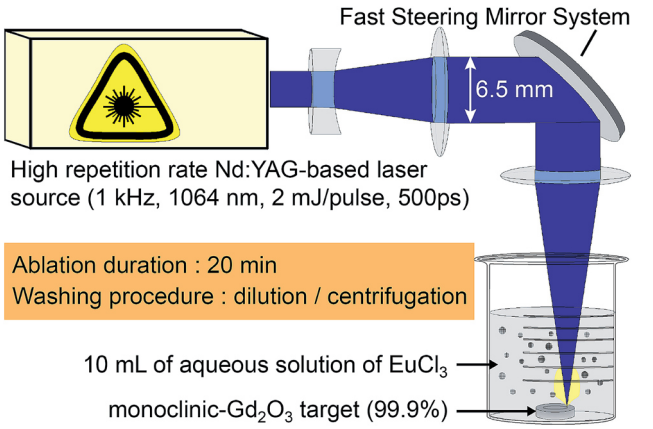

Fig. 1 Graphical summary of the synthesis parameters.

a laser gain module (*Taranis* module), which consists in a diode-pumped Nd:YAG single crystal fiber.[59] Each pulse is 500 ps long and has an energy of 1.5 mJ. The Gaussian TEM00 beam (beam quality $M^2 < 1.3$) is expended to reach a $1/e^2$ diameter $2w$ of 6.5 mm, and is then focused at the surface of the target using a F-Theta scan lens with 160 mm focal length. The expected beam waist $2w_0$ on the target is then 44 μm. It leads to a surface power density of 2×10^{11} W cm^{-2}.

The targets of pure Gd_2O_3 are made from a powder of gadolinium(III) oxide with a purity of 99.9% (Sigma-Aldrich, CAS number 12064-62-9). The powder is pressed and then annealed in an oven at 1400 °C during 6 h. X-ray diffraction shows that the targets are in the monoclinic phase (see Fig. S5 in ESI†).

Synthesis parameters are reported in Table 1. For each synthesis, a target is positioned in a 50 mL beaker filled with 10 mL of a solution of deionized water and Eu(III) ions. Europium(III) chloride hexahydrate from Strem Chemicals (CAS number 13759-92-7) with a purity of 99.9% is dissolved in order to reach five different concentrations from 10^{-5} mol L^{-1} to 10^{-3} mol L^{-1}. The maximum concentration is defined by a technical limitation of our current protocol. From 5×10^{-3} mol L^{-1} the solution remains milky and the ablation efficiency drastically decreases because of the scattering of the laser light. By keeping the salt concentration below 10^{-3} mol L^{-1}, we ensure the reproducibility of the ablated mass. Steering mirrors are used to move the ablation spot on the target over a squared area of 11 mm side. The ablation spot is moved of 10 μm every 5 shots forming lines, and each line is 30 μm spaced. The whole solution is gently stirred using a magnetic stirrer to evacuate the produced nanoparticles from the ablation spot. Each synthesis lasts for 20 min (1.2 million shots), then only the supernatant is collected in order to avoid microparticles resulting from a possible target crumbling because of the laser-induced shockwaves.[60] Nanoparticles are collected by centrifuging the supernatant at 21 036 RCF during 10 min and washed with 10 mL of deionized water to remove europium salt. After centrifugation, the resulting material composed of clean powder is dissolved in 300 μL of deionized water and put into a vessel made from UV plastic (1 cm^2). For each sample the water is then evaporated in order to obtain

 This journal is © The Royal Society of Chemistry 2019

Open Access Article. Published on 30 August 2019. Downloaded on 5/6/2021 2:48:50 PM.
This article is licensed under a Creative Commons Attribution 3.0 Unported Licence.

Table 1 Samples preparation for the different characterisation techniques (see text for details). The cut-off diameter of the sub-micronic particles selection is about 800 nm (see Fig. S3 in ESI). The measurement of the ablated mass per pulse is described in ESI. 2.0 ng of nanoparticles are produced for each laser pulse

Characterisation techniques	Ablation duration [min]	Solution volume [mL]	Salt concentration [mol L^{-1}]	Purification process
Luminescence, HRTEM, SAED	20	10	10^{-5} to 10^{-3}	Sedimentation and 1 washing
Luminescence (sample C)	20	10	None then 10^{-3}	Sedimentation and 1 washing
LIBS	20	10	10^{-3}	Sedimentation and 10 washings
XRD	400	200	10^{-3}	1 washing and sub-micronic particles selection (<800 nm)
Ablated mass per pulse	315 & 380	200	10^{-3}	1 washing and sub-micronic particles selection (<800 nm)

uniform films with the same thickness enabling intensity comparison on the measured luminescence spectra.

A negative control sample (named C) is synthesized in pure deionized water during 20 min. Then $EuCl_3$ salt is added to reach a concentration of 10^{-3} mol L^{-1}. The colloidal solution is stirred and then washed following the above procedure. The luminescence from the sample C will correspond to adsorbed Eu^{3+} ions on the surface of the nanoparticles.

Characterisation

X-ray diffraction (XRD). X-ray powder diffraction patterns are recorded at room temperature on a Bruker D8 Advance diffractometer equipped with a sealed Cu X-ray tube and a linear LYNXEYE XE detector. The $K_{\alpha 2}$ contribution is removed in the X-ray diffraction pattern shown in Fig. 3a. The XRD are performed on nanoparticles produced with the same protocol (target, laser parameters), but scaled up in order to produce above 50 mg: 400 min long ablation in a 200 mL $EuCl_3$ solution at 10^{-3} mol L^{-1}. Contrary to the luminescence analysis, XRD is very sensitive to possible residual micronic powder due to laser-induced undoped target crumbling. A purification step is thus added for this analysis. The colloidal solution is poured in 9 cm high tubes (filling height 7 cm) and gently centrifuged at 50 RCF during 10 min. The supernatant is then collected. All the particles larger than 817 nm settle down and are thus removed, and only a few percent of the nanoparticles smaller than 100 nm are removed (see Fig. S3 in ESI†).

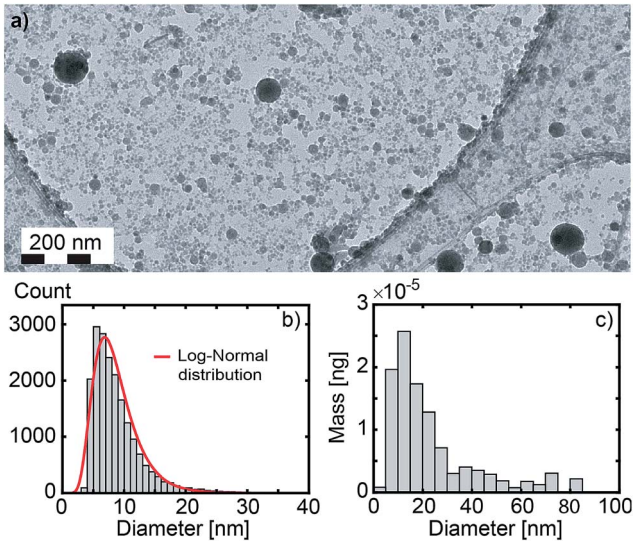

Fig. 2 (a) Large field image (×20k) of Gd_2O_3 nanoparticles. (b) Size distribution of 19 310 nanoparticles deduced from 3 large field images (see Fig. S4 in ESI†) including image (a). The red curve corresponds to a log-normal distribution fit (median size = 8.0 nm, standard deviation = 3.6 nm). (c) Corresponding mass distribution of the nanoparticles (median size = 19.7 nm).

Transmission electron microscopy (TEM). For each synthesis, a droplet of the as-produced colloidal solution is poured onto a 400-mesh copper grid covered with ultra-thin carbon on holey carbon support film (reference 01 824 from Ted Pella, Inc.). Transmission Electron Microscopy (TEM) experiments are carried out on a JEOL 2100 HT microscope operating at 200 kV. High resolution images are acquired using a Gatan Orius 200 camera and electronic diffraction patterns are analysed with the Digital Micrograph software from Gatan (see Fig. 3e and f). Selected area electron diffraction (SAED) patterns are averaged radially in order to obtain the diffraction pattern shown in Fig. 3b. Amorphous contribution of the carbon layer was approximated by an exponential and removed. Because a few thousands of particles are probed simultaneously, such a pattern can be interpreted as the powder pattern of the smallest nanoparticles (a few nanometers), even if contribution from larger particles are observed (see bright spots in the SAED from particles of a few tens of nanometers). As a consequence, such a pattern should be more considered as a fingerprint than a quantitative powder pattern. The size distribution in Fig. 2b is obtained from three different large field TEM images, including Fig. 2a. Nanoparticles were automatically detected with the plug-in *Particles Sizer* in *ImageJ*[61] and diameters were deduced from their areas.

Luminescence. To measure the luminescence spectra displayed in Fig. 4b, samples were excited by a UV LED source from Thorlabs (LED290W) emitting at 293 nm (FWHM = 13 nm). The luminescence was collected by an optical fiber and fed into a monochromator (Triax 320 from Jobin Yvon) with a Peltier-cooled charge coupled device (CCD) array detector. Calibration of the wavelengths was performed with a spectral calibration lamp. Each spectrum displayed corresponds to the

Open Access Article. Published on 30 August 2019. Downloaded on 5/6/2021 2:48:50 PM.
This article is licensed under a Creative Commons Attribution 3.0 Unported Licence.

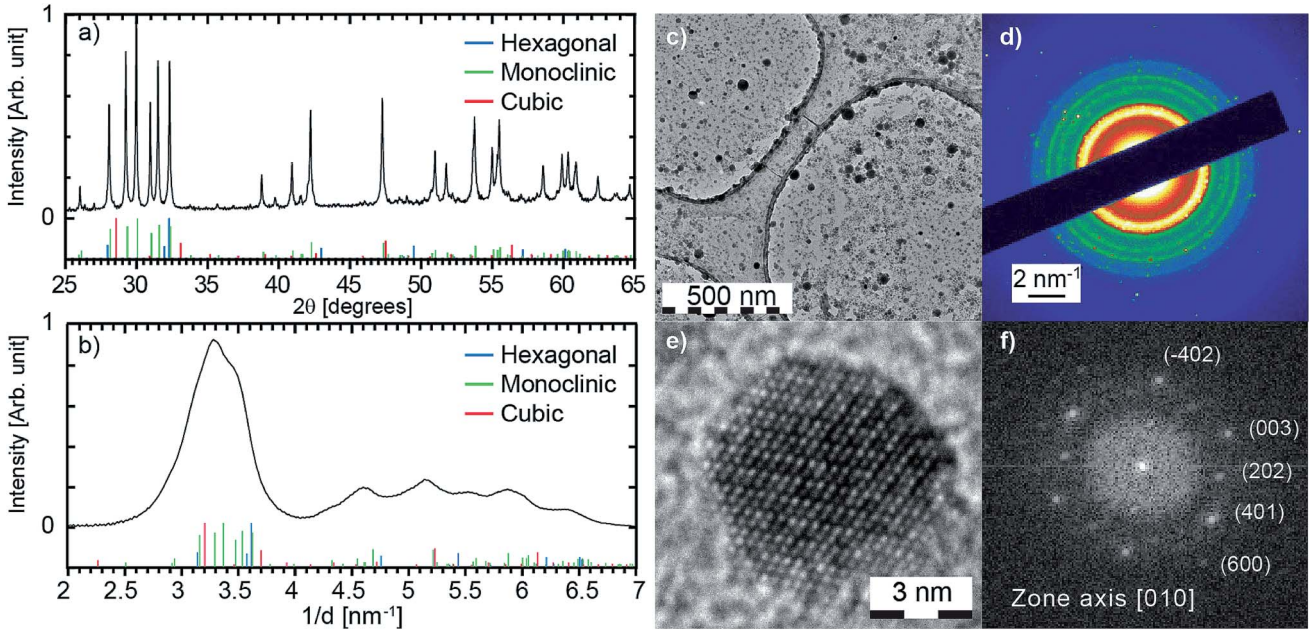

Fig. 3 (a) X-ray diffraction pattern of the long synthesis sample (see text for details). The theoretical peak positions for cubic (Powder Diffraction File 00-012-0797 from ICDD), hexagonal (04-016-2410) and monoclinic (00-042-1465) crystal structures are displayed. (b) Diffraction pattern obtained by radial averaging of the selected area electron diffraction (SAED) shown in (d). The selected area corresponds to image (c). (e) HRTEM image of a particle in the monoclinic phase and (f) the associated fast Fourier transform.

accumulation of 15 measurements with an accumulation time of 5 s each. The position of the sample and settings were systematically kept identical in order to achieve the same light collection efficiency and to provide accurate comparison of the intensities.

Fig. 5 shows photoluminescence excitation (PLE) spectrum. PLE was measured by a custom made spectrofluorometer 5000M Horiba Jobin Yvon, using a steady state deuterium lamp as excitation source. Single grating monochromators and photon counting photomultiplier based detectors were used for the emission light collection. The spectrum was corrected from the wavelength dependence of the light source intensity.

[Eu]/[Gd] atomic ratio

Because of the strong interaction between the laser generated plasma and the liquid, a significant amount of liquid and salt is vaporised for each pulse.[39] The combination of the matter from the vaporised liquid and from the ablated target is the starting material forming the doped nanoparticles. It is thus crucial to evaluate the [Eu]/[Gd] atomic ratio in the plasma, which is deduced from two distinct measurements. On the one hand, the average number of gadolinium atoms in the plasma is obtained from the amount of gadolinium oxide vaporised: 2.0 ng per pulse estimated from product weighing (standard deviation 0.18 ng, see ESI†), leading to 6.6×10^{12} Gd atoms per pulse (standard deviation 0.6×10^{12}). On the other hand, for the average number of europium atoms in the plasma, we first computed the amount of vaporised solvent and then assumed that the europium concentration is the same in the liquid solution and in the vaporised solvent because of the extremely fast vaporisation. Such assumption is justified by recent works from Tamura *et al.* which showed that in the first hundred nanoseconds the nascent plasma and the liquid partially merge.[64] As a result, the solvent vaporisation is fast enough that the ions dissolved in the liquid can directly transfer into the plasma.[52] To obtain the amount of vaporised liquid, the dynamics of the bubbles is recorded using shadowgraph.[19,39]

Shadowgraph imaging

The shadowgraph images are collected by an ultrafast camera (Phantom v711 from Vision Research) coupled with a zoom lens system (Zoom 6000 from Navitar). The light source is a continuum HeNe laser (632.8 nm, $P = 13$ mW) coupled to a diffuser. The camera frame rate is 215 800 frames per second. Each image is 128×128 px^2 representing 1.44×1.44 mm^2. The resolution is 22 μm. A complete schematic description of the experimental setup is given in ref. 39. Data from 35 bubbles have been used to provide statistical analysis. The average lifetime of the first oscillation is 106 μs (standard deviation 17 μs). The average maximum bubble radius is 0.46 mm (standard deviation 0.1 mm). The bubble lifetime until the first collapse follows a linear trend with respect to the maximum bubble radius. Such a behaviour is consistent with the theoretical Rayleigh collapse time[65] (dashed red curve in Fig. 6a), even if the measured lifetimes appeared somewhat longer than the theoretical ones. After the first collapse, rebounds of smaller bubbles can also be observed. The pressure in the vapour bubble is deduced from the Rayleigh–Plesset (RP) equation. The processing of data using RP equation is fully described in our previous work.[39] The bubbles follow an isentropic process until

 This journal is © The Royal Society of Chemistry 2019

Open Access Article. Published on 30 August 2019. Downloaded on 5/6/2021 2:48:50 PM.
This article is licensed under a Creative Commons Attribution 3.0 Unported Licence.

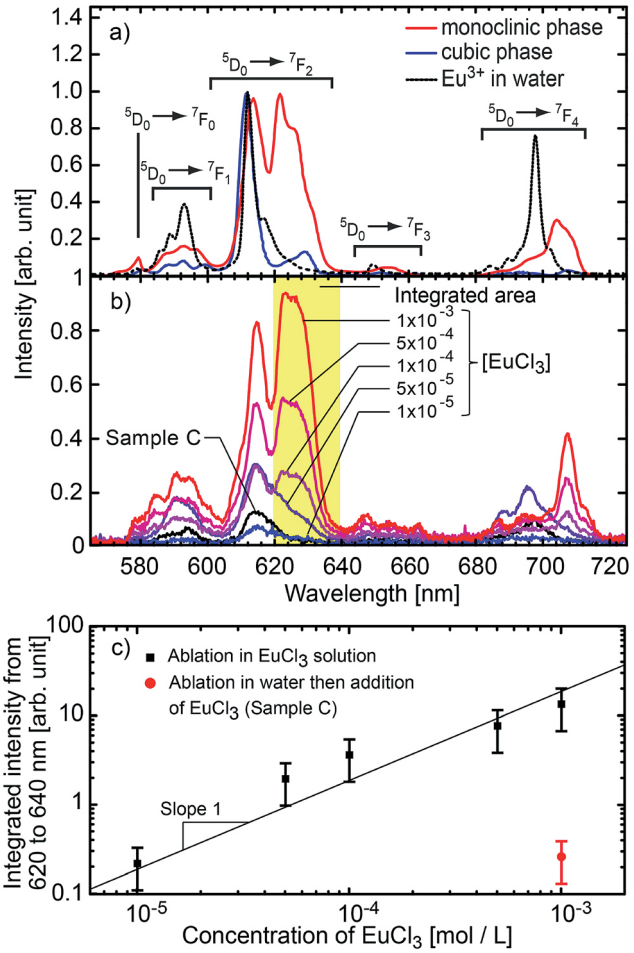

Fig. 4 (a) Luminescence spectra of reference Gd_2O_3:Eu monoclinic nanospheres,[62] cubic nanoplatelets,[63] and europium(III) chloride hexahydrate salt. (b) Luminescence spectra of the nanoparticles obtained by ablation of pure gadolinia in Eu^{3+} solution at different concentrations. The black line corresponds to the reference sample C, *i.e.* undoped nanoparticles matured in a 10^{-3} mol L^{-1} solution of $EuCl_3$ and then washed. The spectral resolution is 2 nm (FWHM). (c) Integrated signal between 620 nm and 640 nm for each concentration (monoclinic signature). The red dot corresponds to the signal from the reference sample C. The error bars correspond to the standard deviation of the amount of ablated material over 5 ablations. Solid line is a reading guide representing a linear power law.

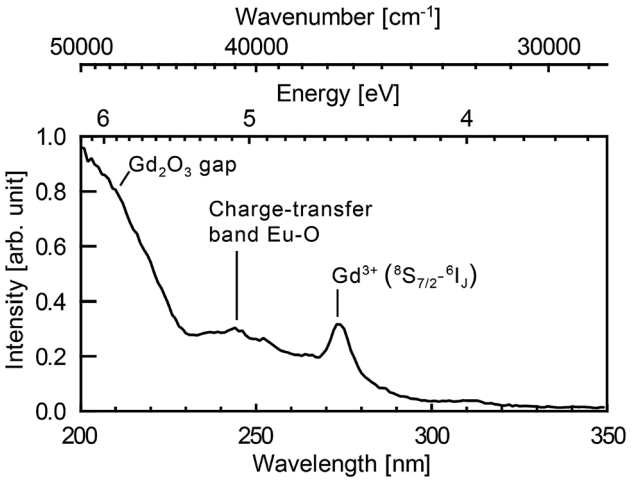

Fig. 5 Excitation spectrum of the nanoparticles synthesised in a solution of 10^{-3} mol L^{-1} of europium salt. Emission at 625 nm integrated over 32 nm (FWHM of the spectral resolution). The spectral resolution of the excitation spectrum is 4 nm.

the first collapse. Assuming the ideal gas law holds, a lower limit of the number of vapour molecules inside the bubble is obtained assuming that the vapour temperature remains lower than the water critical temperature (T_c = 647 K). The average number $\langle N \rangle$ of vapour molecules is 2×10^{15} (standard deviation 1.3×10^{15}). The latent heat of vaporisation of 2×10^{15} water molecules corresponds to 0.14 mJ (9% of the laser pulse energy). The vapour bubbles are therefore mostly composed of water molecules with respect to the number of ablated atoms (see Fig. 6b). For a 10^{-3} mol L^{-1} $EuCl_3$ solution, the deduced amount of europium ions in each bubble is estimated to be 3.6×10^{10} (standard deviation 2.4×10^{10}). It leads to an atomic ratio [Eu]/[Gd] in the plasma of 0.55% (standard deviation 0.37%).

Laser-induced breakdown spectroscopy (LIBS)

The resulting [Eu]/[Gd] atomic ratio in the produced nanoparticles is deduced from LIBS. LIBS method is today considered as a robust analytical method and numerous articles in the literature report on its quantification ability.[66–71] Moreover, Fig. S1 in ESI† shows that LIBS is reliable to quantified the [Eu]/[Gd] atomic ratio in the case of europium-doped Gd_2O_3 for [Eu]/[Gd] extending from 0.1% to 3%. LIBS only consumes a few μg of nanoparticles powder per analysis, which is a significant advantage in regards to other analytical techniques, such as ICP methods which require at least 100 mg of materials. Few hundreds of μg of nanoparticles powder are deposited on a microscope slide with the help of a double-sided adhesive tape. The micro-LIBS instrumentation used Nd:YAG laser pulses of 1064 nm, with an energy of 2 mJ, a pulse duration of 8 ns, and a repetition rate of 20 Hz. Details about the experimental setup can be found in ref. 72 and 73. In order to spatially confine the plasma, the measurements were performed at room temperature with argon gas flowing through the plasma region (1.5 L min^{-1}). A beam shutter was used to control the delivery of the laser pulse to the sample. A unique plasma was produced for each sampling position. In total, 30 single shots spectra were recorded for each sample. The light emitted by the plasma plume was collected and focused onto the entrance of an optical fibre bundle. This fibre bundle was composed of 19 fibres with a 200 μm core diameter. It was connected to a Czerny–Turner spectrometer equipped with a 2400 L mm^{-1} grating blazed at 300 nm and an intensified charge-coupled device (ICCD) camera (Shamrock 500 and iStar, Andor Technology). The ICCD camera was synchronised to the Q-switch of the laser and the spectrum acquisition was performed with delay and gate of 2 μs and 2 μs, respectively. For such delayed gate, the plasma cooling leads to a lowest electronic temperature which inhibits the emission from the highest excitation levels, and then the emission of gadolinium (major element). It leads to a better

Open Access Article. Published on 30 August 2019. Downloaded on 5/6/2021 2:48:50 PM.
This article is licensed under a Creative Commons Attribution 3.0 Unported Licence.

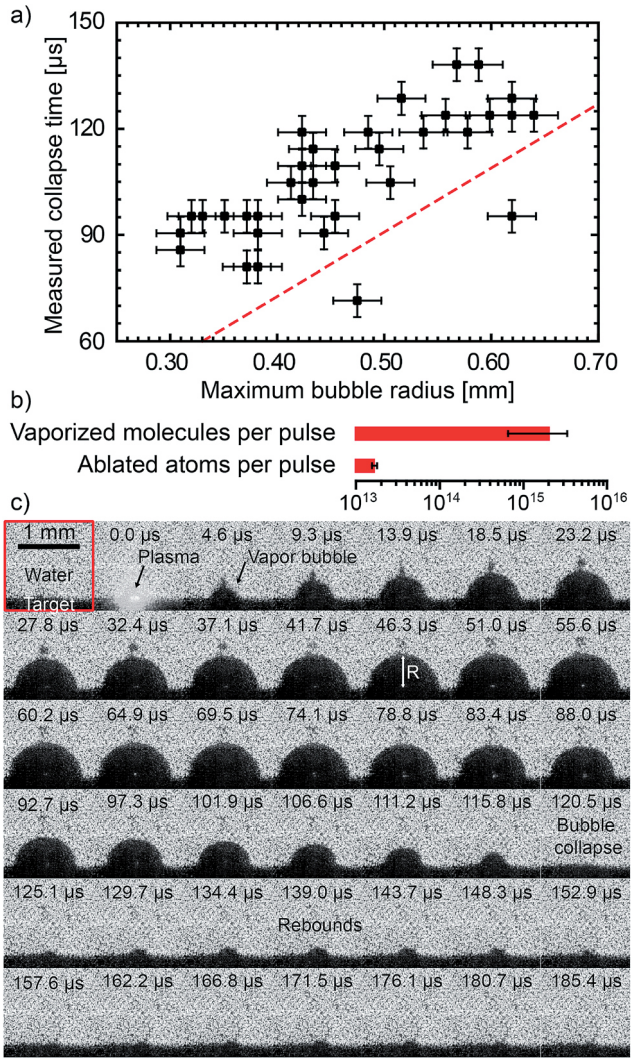

Fig. 6 (a) Bubble lifetime (first collapse) as a function of the maximum bubble radius R_M. Dots correspond to 35 individual bubbles. The red dashed line corresponds to the theoretical Rayleigh collapse time[65] for an oscillation $T_{RCL} = 1.83R_M\sqrt{\frac{\rho}{P_0}}$ ($\rho = 997$ kg m^{-3} water density and $P_0 = 101$ kPa external pressure). (b) The averaged amount of vaporised molecules per pulse is deduced from the dynamics of 35 bubbles. The error bar corresponds to 68% confidence interval (±standard deviation computed from 35 bubbles). The amount of ablated atoms per pulse is deduced from the product weighing (see ESI†). (c) Shadowgraph snapshots of a laser-generated bubble. The numbers stand for the delay after the nanosecond laser pulse.

visibility of the selected EuI line. The width of the entrance slit of the spectrometer was set to 15 µm. With this configuration, a typical spectral resolution of 0.05 nm is achieved. All the data treatment was realised by using the lines EuI at 466.18 nm and GdI at 460.29 nm (see Fig. 7). These lines were chosen because they are rather isolated and did not show any apparent saturation effects. The net intensities of both emission lines were extracted using a baseline subtraction. The relative calibration of the [Eu]/[Gd] atomic ratio was performed using a reference sample, containing an [Eu]/[Gd] atomic ratio of 1%.

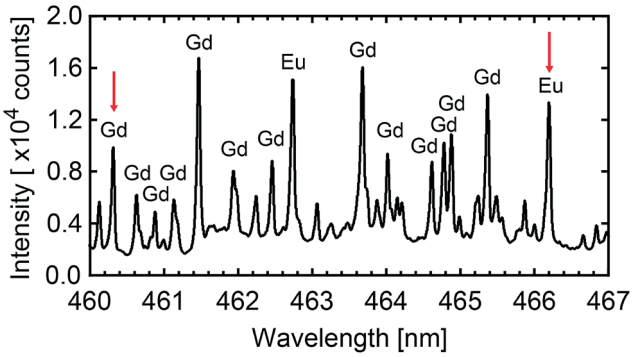

Fig. 7 LIBS spectroscopy. Typical atomic emission observed on a sample of Gd_2O_3:Eu nanoparticles. The red arrows show both lines used to quantify the atomic ratio [Eu]/[Gd].

3 Results and discussion

Nanoparticles characterisation

Size distribution. The typical size distribution (particle count) and mass distribution (mass weighted size distribution) are shown in Fig. 2b and c, respectively. The size distribution (particle count) follows a log-normal distribution. Red curve corresponds to the fitted log-normal distribution with a median size of 8.0 nm. Yet, a second population of larger nanoparticles up to 100 nm is observed. Being rare, their number is negligible in comparison to the first population but their mass is not. As shown in Fig. 2c, half of the produced mass corresponds to nanoparticles with a diameter larger than 19.7 nm. Indeed, bimodal size distributions are generally observed,[74–77] with a first fraction of particles with sizes below 20 nm and a second fraction of particles of a few tens of nanometers. The origin of bimodal size distributions in femto- and picosecond laser ablation in liquids has been addressed by Shih *et al.* using a large-scale atomistic simulation.[78–80] Looking at the ablation of silver, they suggested a critical role of the dynamic interactions between the ablation plume and the liquid environment. Nucleation and growth of small nanoparticles occur in an expanding metal–liquid mixing region, while the larger particles originate from the fragmentation of the molten layer on the target through Rayleigh–Taylor instabilities.[80] The bimodal size distribution is expected to appear very early during the plasma cooling. Small angle X-ray scattering (SAXS) supports the early appearance of the bimodal size distribution.[53,81–84] It also shows that the nanoparticles remain confined in the vapour bubble during a few hundred microseconds, until the bubble collapses. Following this scenario, only the fraction of the smallest particles originated from the plasma condensation is expected to be doped in the core.

Crystallographic phase. First, XRD measurement performed on the obtained nanoparticles at a large scale is shown in Fig. 3a. The pattern clearly corresponds to a monoclinic phase, and no obvious impurity phases are detected. The Scherrer equation is applied to peak widths (FWHM) of the six main peaks observed in the powder diffraction pattern between 28.15° and 32.4° ((111), (401), (−402), (003), (−310) and (−112)).

This journal is © The Royal Society of Chemistry 2019

Open Access Article. Published on 30 August 2019. Downloaded on 5/6/2021 2:48:50 PM.
This article is licensed under a Creative Commons Attribution 3.0 Unported Licence.

It leads to an average domain size of 54 nm. It appears that the diffraction pattern is mostly governed by the largest particles, which is consistent with a median size of 19.7 nm for the mass weighted size distribution (see Fig. 2c). Therefore, SAED and HRTEM are also employed to investigate the crystal structure of the smallest nanoparticles (<10 nm). Typical low resolution TEM and high resolution TEM captured on the sample synthesised with 10^{-4} mol L^{-1} of $EuCl_3$ salt are displayed in Fig. 3c and e respectively. The diffraction pattern is deduced from a radial averaging of the SAED acquired on a large area [see Fig. 3b–d]. Such a pattern being acquired over few thousand nanoparticles is similar to their powder diffraction pattern. Again, the monoclinic Gd_2O_3 diffraction pattern explains very well the experimental observation. Then FFT has been performed on about 25 high resolution images of particles as shown in Fig. 3e and f. Crystallographic planes always match monoclinic phase. Altogether, XRD, SAED and HRTEM show that a monoclinic phase is obtained for both the largest and the smallest gadolinium oxide nanoparticles. This is consistent with previous reports on PLAL-generated doped and undoped-Gd_2O_3 nanoparticles of above 10 nm. Indeed, monoclinic Gd_2O_3 nanoparticles have been produced from laser ablation of a pure Gd target in water.[41] Monoclinic nanoparticles of co-doped Gd_2O_3 phosphors have been produced from laser ablation of co-doped Gd_2O_3 target, namely Gd_2O_3:Er,Yb[27] and Gd_2O_3:Yb,Tm.[30]

At room pressure and temperature, the cubic phase is the most stable form for Gd_2O_3 bulk crystal. Monoclinic phase is observed for temperature higher than 1130 °C.[85] However, a crossover in polymorph stability is often reported at the nanoscale. For several oxides such as Al_2O_3, TiO_2, and ZrO_2, the differences in surface energy stabilise polymorphs that are metastable in the bulk when a critical surface area is exceeded.[86] Same behaviour has been reported for nanoparticles synthesised by laser ablation of a Gd_2O_3:Eu pellet in a Low Energy Cluster Beam Deposition setup. The particles with a size lower than 2.8 nm are mainly in the monoclinic phase while the larger ones are mainly in the cubic phase.[54] PLAL seems to enable the stabilisation of larger particles in the monoclinic phase. Large energy deposition, leading to a plasma of a few thousands of kelvin,[19,37] combined with very fast cooling rate above 10 K ns^{-1} (ref. 19) can contribute to the stabilisation of metastable phases.

Evidence of core doping: luminescence properties

The Eu^{3+} emission strongly depends on the crystal field and thus on the symmetry of the crystallographic sites. The radiative transition intensities can be deduced from Judd–Ofelt theory,[87,88] and extensive simulations have been performed to look at the influence of the crystal-field on the trivalent lanthanide emission and absorption.[89–93] As an example, in cubic-Gd_2O_3, Eu^{3+} are in crystal sites with C_2 symmetry and S_6 symmetry.[47,94] It leads to an emission spectrum which can be easily distinguished from the emission spectrum of Eu^{3+} in monoclinic-Gd_2O_3 characterized by three non-equivalent C_s crystallographic sites[47] (see Fig. 4a). The luminescence lines are thus a signature of the occupied crystallographic sites. Moreover, the crystal field on surface sites is different from the crystal field in the core of the matrix.

Fig. 4b shows the emission spectra of the samples when excited at 293 nm (FWHM 13 nm). This excitation wavelength covers both the charge-transfer band Eu–O and the $^8S_{7/2} \rightarrow {}^6I_J$ intra-configurational transition of Gd^{3+} (see Fig. 5). It then favours the excitation of the europium ions in the vicinity of gadolinium or oxygen atoms. Eu_2O_3 is not expected since a strong luminescence quenching appears in pure Eu_2O_3. In Fig. 4b, we can observe the europium emission corresponding to the intra-configurational transitions $^5D_0 \rightarrow {}^7F_J$ for J in [0, 4] (see Fig. 4a). For samples ablated in $EuCl_3$ solutions (coloured curves), luminescence spectra have features consistent with Eu^{3+} emission for europium in the C_s crystallographic sites of monoclinic Gd_2O_3 (620–640 nm band and 705–720 nm band). The observed emission broadening comes from an inhomogeneous broadening commonly reported for nanoparticles of lanthanide-doped sesquioxydes when they are not annealed.[24,26,55,95,96] Moreover, Gd^{3+} and Eu^{3+} have identical outer electronic orbitals and Gd_2O_3 is an ionic structure, it is then highly unlikely to find Eu^{3+} in an interstitial position. At last, a more direct assessment of the core doping comes from the negative control sample (sample C). It corresponds to pure Gd_2O_3 nanoparticles matured in a solution of $EuCl_3$ (10^{-3} mol L^{-1}). Sample C only exhibits moderate emission in the 580–600 nm, 610–620 nm and 680–705 nm wavelength ranges which corresponds to the emission from surface-adsorbed Eu^{3+} or remaining europium salt, but not from Eu-doped monoclinic Gd_2O_3 (see Fig. 4a). Emission and excitation spectra, as well as the negative control sample, show that the europium ions penetrate the core of the nanoparticles during the growth.

Doping efficiency

In the following, we will quantify the amount of europium doping atoms inside Gd_2O_3 matrix. A first insight is given by the luminescence intensity comparison. Fig. 4c shows the integrated signal between 620 and 640 nm which corresponds to a characteristic feature of Eu^{3+} emission in monoclinic Gd_2O_3. Even if complex growth mechanisms involving highly non-equilibrium processes are at stake, our results demonstrate that the luminescence intensity is proportional to the $EuCl_3$ concentration over two orders of magnitude. The linear trend also shows that the luminescence concentration quenching mechanism does not appear, which is confirmed by the emission lifetime remaining milliseconds (see ESI†). The absence of quenching shows that the atomic ratio [Eu]/[Gd] remains below a few percents in the nanoparticles.[97,98] In addition, the ratio is measured using LIBS on powder synthesised in a solution of 10^{-3} mol L^{-1}, then washed ten times to avoid any remaining salt (see Fig. S2 in ESI†). LIBS measurement leads to an atomic ratio [Eu]/[Gd] equal to 0.83% (standard deviation 0.015%). This value is reliable with respect to the LIBS sensitivity (see Fig. S1 in ESI†). Moreover, this value is consistent with the ratio in the plasma equal to 0.55% (standard deviation 0.37%).

Open Access Article. Published on 30 August 2019. Downloaded on 5/6/2021 2:48:50 PM.
This article is licensed under a Creative Commons Attribution 3.0 Unported Licence.

Mechanism of nanoparticles generation

The nanoparticles with a size bellow a few tens of nanometers are assumed to nucleate and grow during the fast plasma cooling.[78–80] In such a scenario, the ratio [Eu]/[Gd] in the nanoparticles core would linearly depend on the ratio [Eu]/[Gd] in the plasma. Indeed, Gd and Eu atoms are very similar in size and electronic properties and almost no differences are to be expected in the condensation process. Our findings are consistent with such a scenario, including a fast vaporisation of the solvent during the plasma lifetime,[52] and nucleation/growth mechanisms taking places during the fast plasma cooling. Moreover, the fast cooling rate above 10 K ns^{-1} (ref. 19) can contribute to the stabilisation of the monoclinic crystal structure which is supposed to be metastable for the particle size reported in our work.

4 Conclusions

Laser ablation of a gadolinium oxide in an europium chloride solution leads to europium doped gadolinium oxide nanoparticles in the monoclinic structure. We then demonstrated experimentally that impurities from the solvent can effectively penetrate the core of the nanoparticles as they grow. With our technique, the doped nanomaterials are indeed obtained in a highly versatile single step process. We reached a doping of about 1% ([Eu]/[Gd] atomic ratio), and we showed that the doping concentration is proportional to the initial concentration of europium ions in the solvent over two orders of magnitude. This finding is an additional confirmation to the current understanding of the generation process of the nanoparticles of a few nanometers in PLAL: (i) the interaction between the laser generated plasma and the liquid leads to solvent vaporisation, and (ii) following a fast cooling of the plasma, nucleation and growth of the nanoparticles occurs in an environment composed of ablated target and vaporised solvent. This work could open new ways for the synthesis of doped nanomaterials, but it also raises the question of undesired penetration of impurities in laser-generated nanoparticles in liquids.

Conflicts of interest

There are no conflicts to declare.

Acknowledgements

We wish to thank Fibercryst company for the custom-development of the MOPA based laser source, as well as for their technical support. We wish to thank Isabelle Trenque for Rietveld analysis. The ablation setup was funded by the French innovation agency OSEO (*ALL-Mat* project). The collaboration between the Lyon University and the Institute of Physics of the Czech Academy of Sciences is funded through the European project ASCIMAT, in the framework of the European program H2020-TWINN-2015. LIBS measurement has been done on the Optalyse Plateform funded by the "région Auvergne Rhône Alpes".

References

1 D. Chen and Y. Wang, *Nanoscale*, 2013, **5**, 4621–4637.
2 J. Y. Kim, O. Voznyy, D. Zhitomirsky and E. H. Sargent, *Adv. Mater.*, 2013, **25**, 4986–5010.
3 P. Wu and X.-P. Yan, *Chem. Soc. Rev.*, 2013, **42**, 5489–5521.
4 E. Hemmer, N. Venkatachalam, H. Hyodo, A. Hattori, Y. Ebina, H. Kishimoto and K. Soga, *Nanoscale*, 2013, **5**, 11339–11361.
5 N. Pradhan, S. Das Adhikari, A. Nag and D. D. Sarma, *Angew. Chem., Int. Ed.*, 2017, **56**, 7038–7054.
6 L. Labrador-Paez, E. C. Ximendes, P. Rodriguez-Sevilla, D. H. Ortgies, U. Rocha, C. Jacinto, E. Martin Rodriguez, P. Haro-Gonzalez and D. Jaque, *Nanoscale*, 2018, **10**, 12935–12956.
7 D. J. Norris, A. L. Efros and S. C. Erwin, *Science*, 2008, **319**, 1776–1779.
8 D. Mocatta, G. Cohen, J. Schattner, O. Millo, E. Rabani and U. Banin, *Science*, 2011, **332**, 77–81.
9 G. M. Dalpian and J. R. Chelikowsky, *Phys. Rev. Lett.*, 2006, **96**, 226802.
10 S. C. Erwin, L. J. Zu, M. I. Haftel, A. L. Efros, T. A. Kennedy and D. J. Norris, *Nature*, 2005, **436**, 91–94.
11 T. L. Chan, M. L. Tiago, E. Kaxiras and J. R. Chelikowsky, *Nano Lett.*, 2008, **8**, 596–600.
12 D. E. Perea, E. R. Hemesath, E. J. Schwalbach, J. L. Lensch-Falk, P. W. Voorhees and L. J. Lauhon, *Nat. Nanotechnol.*, 2009, **4**, 315–319.
13 F. V. Mikulec, M. Kuno, M. Bennati, D. A. Hall, R. G. Griffin and M. G. Bawendi, *J. Am. Chem. Soc.*, 2000, **122**, 2532–2540.
14 D. Amans, W. Cai and S. Barcikowski, *Appl. Surf. Sci.*, 2019, **488**, 445–454.
15 H. Zeng, X.-W. Du, S. C. Singh, S. A. Kulinich, S. Yang, J. He and W. Cai, *Adv. Funct. Mater.*, 2012, **22**, 1333–1353.
16 Z. Yan and D. B. Chrisey, *J. Photochem. Photobiol., C*, 2012, **13**, 204–223.
17 S. Barcikowski and G. Compagnini, *Phys. Chem. Chem. Phys.*, 2013, **15**, 3022–3026.
18 V. Amendola and M. Meneghetti, *Phys. Chem. Chem. Phys.*, 2013, **15**, 3027–3046.
19 D. Amans, M. Diouf, G. Ledoux and C. Dujardin, *J. Colloid Interface Sci.*, 2017, **489**, 114–125.
20 D. Zhang, B. Gökce and S. Barcikowski, *Chem. Rev.*, 2017, **117**, 3990–4103.
21 J. Xiao, P. Liu, C. X. Wang and G. W. Yang, *Prog. Mater. Sci.*, 2017, **87**, 140–220.
22 D. Zhang, J. Liu, P. Li, Z. Tian and C. Liang, *ChemNanoMat*, 2017, **3**, 512–533.
23 J. Zhang, M. Chaker and D. Ma, *J. Colloid Interface Sci.*, 2017, **489**, 138–149.
24 G. Ledoux, D. Amans, C. Dujardin and K. Masenelli-Varlot, *Nanotechnology*, 2009, **20**, 445605.
25 N. V. Tarasenko and A. V. Butsen, *Quantum Electron.*, 2010, **40**, 986–1003.

 This journal is © The Royal Society of Chemistry 2019

Open Access Article. Published on 30 August 2019. Downloaded on 5/6/2021 2:48:50 PM. This article is licensed under a Creative Commons Attribution 3.0 Unported Licence.

26 D. Amans, C. Malaterre, M. Diouf, C. Mancini, F. Chaput, G. Ledoux, G. Breton, Y. Guillin, C. Dujardin, K. Masenelli-Varlot and P. Perriat, *J. Phys. Chem. C*, 2011, **115**, 5131–5139.
27 S. K. Singh, K. Kumar and S. B. Rai, *Mater. Sci. Eng., B*, 2010, **166**, 180–184.
28 T. Nunokawa, O. Odawara and H. Wada, *Mater. Res. Express*, 2014, **1**, 035043.
29 J. Zheng, Z. Zheng, W. Gong, X. Hu, W. Gao, X. Ren and H. Zhao, *Chem. Phys. Lett.*, 2008, **465**, 275–278.
30 J. Liu, X. Tian, H. Chen, Y. Shao, G. Yang and D. Chen, *Appl. Surf. Sci.*, 2015, **348**, 60–65.
31 STREM Chemicals sells nanoparticles produced by pulsed laser ablation in liquids (see http://particular.eu/start.html), as IMRA America, Inc. (see http://nano.imra.com/). Nara Machinery Co. LTD sells Laser Ablation system dedicated to PLAL synthesis (see http://www.nara-m.co.jp/english/product/particle/las.html).
32 C. L. Sajti, R. Sattari, B. N. Chichkov and S. Barcikowski, *J. Phys. Chem. C*, 2010, **114**, 2421–2427.
33 R. Streubel, S. Barcikowski and B. Gökce, *Opt. Lett.*, 2016, **41**, 1486–1489.
34 T. Sakka, K. Saito and Y. H. Ogata, *J. Appl. Phys.*, 2005, **97**, 014902.
35 A. De Giacomo, M. Dell'Aglio, O. De Pascale and M. Capitelli, *Spectrochim. Acta, Part B*, 2007, **62**, 721–738.
36 A. De Giacomo, M. Dell'Aglio, A. Santagata, R. Gaudiuso, O. De Pascale, P. Wagener, G. C. Messina, G. Compagnini and S. Barcikowski, *Phys. Chem. Chem. Phys.*, 2013, **15**, 3083–3092.
37 J. Lam, D. Amans, F. Chaput, M. Diouf, G. Ledoux, N. Mary, K. Masenelli-Varlot, V. Motto-Ros and C. Dujardin, *Phys. Chem. Chem. Phys.*, 2014, **16**, 963–973.
38 A. Tamura, A. Matsumoto, K. Fukami, N. Nishi and T. Sakka, *J. Appl. Phys.*, 2015, **117**, 173304.
39 J. Lam, J. Lombard, C. Dujardin, G. Ledoux, S. Merabia and D. Amans, *Appl. Phys. Lett.*, 2016, **108**, 074104.
40 J. S. Golightly and A. W. Castleman, *J. Phys. Chem. B*, 2006, **110**, 19979–19984.
41 N. V. Tarasenko, A. V. Butsen and A. A. Nevar, *Appl. Phys. A: Mater. Sci. Process.*, 2008, **93**, 837–841.
42 Q. A. Drmosh, M. A. Gondal, Z. H. Yamani and T. A. Saleh, *Appl. Surf. Sci.*, 2010, **256**, 4661–4666.
43 A. Nath and A. Khare, *J. Appl. Phys.*, 2011, **110**, 043111.
44 V. Amendola, P. Riello, S. Polizzi, S. Fiameni, C. Innocenti, C. Sangregorio and M. Meneghetti, *J. Mater. Chem.*, 2011, **21**, 18665–18673.
45 E. Fazio, A. M. Mezzasalma, G. Mondio, F. Neri and R. Saija, *Appl. Surf. Sci.*, 2013, **272**, 30–35.
46 B. K. Pandey, A. K. Shahi and R. Gopal, *Appl. Surf. Sci.*, 2013, **283**, 430–437.
47 X. Y. Liu, Y. Q. Gao and G. W. Yang, *Nanoscale*, 2016, **8**, 4227–4235.
48 L. Yang, P. W. May, L. Yin, R. Brown and T. B. Scott, *Chem. Mater.*, 2006, **18**, 5058–5064.
49 L. Yang, P. W. May, L. Yin, J. A. Smith and K. N. Rosser, *J. Nanopart. Res.*, 2007, **9**, 1181–1185.
50 V. Amendola, P. Riello and M. Meneghetti, *J. Phys. Chem. C*, 2011, **115**, 5140–5146.
51 A. Kanitz, J. S. Hoppius, M. del Mar Sanz, M. Maicas, A. Ostendorf and E. L. Gurevich, *ChemPhysChem*, 2017, **18**, 1155–1164.
52 A. Matsumoto, A. Tamura, T. Honda, T. Hirota, K. Kobayashi, S. Katakura, N. Nishi, K. ichi Amano, K. Fukami and T. Sakka, *J. Phys. Chem. C*, 2015, **119**, 26506–26511.
53 A. Letzel, B. Gökce, P. Wagener, S. Ibrahimkutty, A. Menzel, A. Plech and S. Barcikowski, *J. Phys. Chem. C*, 2017, **121**, 5356–5365.
54 D. Nicolas, B. Masenelli, P. Melinon, E. Bernstein, C. Dujardin, G. Ledoux and C. Esnouf, *J. Chem. Phys.*, 2006, **125**, 171104.
55 B. Mercier, G. Ledoux, C. Dujardin, D. Nicolas, B. Masenelli, P. Melinon and G. Bergeret, *J. Chem. Phys.*, 2007, **126**, 044507.
56 L. Zhou, Z. Gu, X. Liu, W. Yin, G. Tian, L. Yan, S. Jin, W. Ren, G. Xing, W. Li, X. Chang, Z. Hu and Y. Zhao, *J. Mater. Chem.*, 2012, **22**, 966–974.
57 N. Luo, C. Yang, X. Tian, J. Xiao, J. Liu, F. Chen, D. Zhang, D. Xu, Y. Zhang, G. Yang, D. Chen and L. Li, *J. Mater. Chem. B*, 2014, **2**, 5891–5897.
58 S. Dufort, G. Le Duc, M. Salomé, V. Bentivegna, L. Sancey, E. Bräuer-Krisch, H. Requardt, F. Lux, J.-L. Coll, P. Perriat, S. Roux and O. Tillement, *Sci. Rep.*, 2016, **6**, 29678.
59 I. Martial, F. Balembois, J. Didierjean and P. Georges, *Opt. Express*, 2011, **19**, 11667.
60 L. Berthe, R. Fabbro, P. Peyre, L. Tollier and E. Bartnicki, *J. Appl. Phys.*, 1997, **82**, 2826.
61 T. Wagner and J. Eglinger, *Thorstenwagner/ij-particlesizer: v1.0.9 Snapshot release*, 2017.
62 D. Wawrzynczyk, M. Nyk, A. Bednarkiewicz, W. Strek and M. Samoc, *J. Nanopart. Res.*, 2014, **16**, 2690.
63 N. M. Maalej, A. Qurashi, A. A. Assadi, R. Maalej, M. N. Shaikh, M. Ilyas and M. A. Gondal, *Nanoscale Res. Lett.*, 2015, **10**, 215.
64 A. Tamura, A. Matsumoto, K. Fukami, N. Nishi and T. Sakka, *J. Appl. Phys.*, 2015, **117**, 173304.
65 L. Rayleigh, *Philos. Mag.*, 1917, **34**, 94–98.
66 E. Negre, V. Motto-Ros, F. Pelascini, S. Lauper, D. Denis and J. Yu, *J. Anal. At. Spectrom.*, 2015, **30**, 417–425.
67 J. Menneveux, F. Wang, S. Lu, X. Bai, V. Motto-Ros, N. Gilon, Y. Chen and J. Yu, *Spectrochim. Acta, Part B*, 2015, **109**, 9–15.
68 S. J. Pandey, M. Martinez, F. Pelascini, V. Motto-Ros, M. Baudelet and R. M. Gaume, *Opt. Mater. Express*, 2017, **7**, 627–632.
69 S. C. Jantzi, V. Motto-Ros, F. Trichard, Y. Markushin, N. Melikechi and A. De Giacomo, *Spectrochim. Acta, Part B*, 2016, **115**, 52–63.
70 C. Gerhard, J. Hermann, L. Mercadier, L. Loewenthal, E. Axente, C. R. Luculescu, T. Sarnet, M. Serltis and W. Vioel, *Spectrochim. Acta, Part B*, 2014, **101**, 32–45.
71 D. A. Hartzler, C. R. Bhatt, J. C. Jain and D. L. McIntyre, *J. Energy Resour. Technol.*, 2019, **141**, 070704.

Open Access Article. Published on 30 August 2019. Downloaded on 5/6/2021 2:48:50 PM.
This article is licensed under a Creative Commons Attribution 3.0 Unported Licence.

72 V. Motto-Ros, E. Negre, F. Pelascini, G. Panczer and J. Yu, *Spectrochim. Acta, Part B*, 2014, **92**, 60–69.
73 L. Sancey, V. Motto-Ros, B. Busser, S. Kotb, J. M. Benoit, A. Piednoir, F. Lux, O. Tillement, G. Panczer and J. Yu, *Sci. Rep.*, 2014, **4**, 6065.
74 J.-P. Sylvestre, A. V. Kabashin, E. Sacher and M. Meunier, *Appl. Phys. A: Mater. Sci. Process.*, 2005, **80**, 753–758.
75 G. Cristoforetti, E. Pitzalis, R. Spiniello, R. Ishak and M. Muniz-Miranda, *J. Phys. Chem. C*, 2011, **115**, 5073–5083.
76 G. Cristoforetti, E. Pitzalis, R. Spiniello, R. Ishak, F. Giammanco, M. Muniz-Miranda and S. Caporali, *Appl. Surf. Sci.*, 2012, **258**, 3289–3297.
77 G. Marzun, J. Nakamura, X. Zhang, S. Barcikowski and P. Wagener, *Appl. Surf. Sci.*, 2015, **348**, 75–84.
78 C.-Y. Shih, C. Wu, M. V. Shugaev and L. V. Zhigilei, *J. Colloid Interface Sci.*, 2017, **489**, 3–17.
79 C.-Y. Shih, M. V. Shugaev, C. Wu and L. V. Zhigilei, *J. Phys. Chem. C*, 2017, **121**, 16549–16567.
80 C.-Y. Shih, R. Streubel, J. Heberle, A. Letzel, M. V. Shugaev, C. Wu, M. Schmidt, B. Gökce, S. Barcikowski and L. V. Zhigilei, *Nanoscale*, 2018, **10**, 6900–6910.
81 S. Ibrahimkutty, P. Wagener, A. Menzel, A. Plech and S. Barcikowski, *Appl. Phys. Lett.*, 2012, **101**, 103104.
82 P. Wagener, S. Ibrahimkutty, A. Menzel, A. Plech and S. Barcikowski, *Phys. Chem. Chem. Phys.*, 2013, **15**, 3068–3074.
83 S. Ibrahimkutty, P. Wagener, T. d. S. Rolo, D. Karpov, A. Menzel, T. Baumbach, S. Barcikowski and A. Plech, *Sci. Rep.*, 2015, **5**, 16313.
84 S. Reich, P. Schönfeld, P. Wagener, A. Letzel, S. Ibrahimkutty, B. Gökce, S. Barcikowski, A. Menzel, T. dos Santos Rolo and A. Plech, *J. Colloid Interface Sci.*, 2017, **489**, 106–113.
85 M. Foex and J.-P. Traverse, *Comptes Rendus des Séances de l'Academie des Sciences Série C: Sciences Chimiques Ser. C*, 1966, **262**, 636–639.
86 A. Navrotsky, *Geochem. Trans.*, 2003, **4**, 34–37.
87 B. R. Judd, *Phys. Rev.*, 1962, **127**, 750–761.
88 G. S. Ofelt, *J. Chem. Phys.*, 1962, **37**, 511–520.
89 S. Chaussedent, A. Monteil, M. Ferrari and L. Del Longo, *Philos. Mag. B*, 1998, **77**, 681–688.
90 G. Cormier, J. A. Capobianco, C. A. Morrison and A. Monteil, *Phys. Rev. B: Condens. Matter Mater. Phys.*, 1993, **48**, 16290–16303.
91 C. A. Morrison and R. P. Leavitt, *J. Chem. Phys.*, 1979, **71**, 2366–2374.
92 R. P. Leavitt and C. A. Morrison, *J. Chem. Phys.*, 1980, **73**, 749–757.
93 B. Masenelli, G. Ledoux, D. Amans, C. Dujardin and P. Melinon, *Nanotechnology*, 2012, **23**, 305706.
94 M. Buijs, A. Meyerink and G. Blasse, *J. Lumin.*, 1987, **37**, 9–20.
95 B. M. Tissue, *Chem. Mater.*, 1998, **10**, 2837–2845.
96 G. Ledoux, Y. Leconte, D. Amans, C. Dujardin, L. Combemale, N. Herlin-Boime and C. Reynaud, *Solid State Phenom.*, 2007, **128**, 157–163.
97 O. Meza, E. G. Villabona-Leal, L. A. Diaz-Torres, H. Desirena, J. Rodríguez-López and E. Pérez, *J. Phys. Chem. A*, 2014, **118**, 1390–1396.
98 M. A. Flores-Gonzalez, C. Louis, R. Bazzi, G. Ledoux, K. Lebbou, S. Roux, P. Perriat and O. Tillement, *Appl. Phys. A: Mater. Sci. Process.*, 2005, **81**, 1385–1391.

 This journal is © The Royal Society of Chemistry 2019

Electronic Supplementary Material (ESI) for Nanoscale Advances.
This journal is © The Royal Society of Chemistry 2019

Doping nanoparticles using pulsed laser ablation in a liquid containing the doping agent - Supplementary material

Arsène Chemin, * Julien Lam, † Gaetan Laurens, * Florian Trichard, *
Vincent Motto-Ros, * Gilles Ledoux, * Vítězslav Jarý, ‡ Valentyn Laguta, †
Martin Nikl, † Christophe Dujardin, * David Amans, §*

Quantitative sensitivity of LIBS

Figure 1 shows an assay performed on the quantitative sensitivity of LIBS in the case of europium-doped Gd_2O_3. The experimental conditions detailed below are identical to those reported in the manuscript with the exception of the Gd I emission at 462.44 nm was used, which is similar to the Gd I at 460.29 nm (both are rather isolated and did not show any apparent saturation effects). For europium the lines Eu I at 466.18 nm is used (see Figure 1a). The micro-LIBS instrumentation used Nd:YAG laser pulses of 1064 nm, with an energy of 2 mJ, a pulse duration of 8 ns, and a repetition rate of 20 Hz. Details about the experimental setup can be found in references [1, 2]. In order to spatially confine the plasma, the measurements were performed at room temperature with argon gas flowing through the plasma region (1.5 $L.min^{-1}$). A beam shutter was used to control the delivery of the laser pulse to the sample. A unique plasma was produced for each sampling position. In total, 30 single shots spectra were recorded for each sample. The light emitted by the plasma plume was collected and focused onto the entrance of an optical fibre bundle. This fibre bundle was composed of 19 fibres with a 200 μm core diameter. It was connected to a Czerny−Turner spectrometer equipped with a 2400 l/mm grating blazed at 300 nm and an intensified charge−coupled device (ICCD) camera (Shamrock 500 and iStar, Andor Technology). The ICCD camera was synchronised to the Q-switch of the laser and the spectrum acquisition was performed with delay and gate of 2 μs and 2 μs, respectively. For such delayed gate, the plasma cooling leads to a lowest electronic temperature which inhibits the emission from the highest excitation levels, and then the emission of gadolinium (major element). It leads to a better visibility of the selected Eu I line. The width of the entrance slit of the spectrometer was set to 15 μm. With this configuration, a typical spectral resolution of 0.05 nm is achieved. The net intensities of both emission lines were extracted using a baseline subtraction.

Four reference samples with an [Eu]/[Gd] atomic ratio extending from 0.1 % to 3 % are measured (Particles synthesized by polyol-mediated synthesis [3]). Figure 1b shows measured [Eu]/[Gd] atomic ratio performed on the four reference samples. The linear regression conducted to a good linearity (R^2=0.996) and confidence hyperboles [4] were plotted (95% confidence level). It shows that the concentration measured for the 10^{-3} mol/L sample lies in the concentration range for which LIBS measurements are relevant.

*Univ Lyon, Univ Claude Bernard Lyon 1, CNRS, Institut Lumière Matière, F-69622, Villeurbanne, France.
†Center for Nonlinear Phenomena and Complex Systems, Code Postal 231, Université Libre de Bruxelles, Boulevard du Triomphe, 1050 Brussels, Belgium
‡Inst Phys AS CR, Cukrovarnicka 10, Prague 16200, Czech Republic
§corresponding author

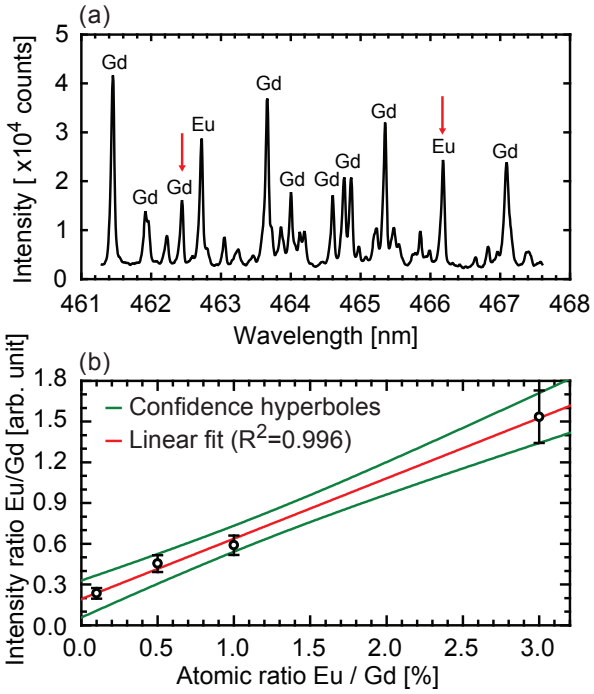

Figure 1: Measurement on samples washed only one times. (a) LIBS spectroscopy. Typical atomic emission observed on a sample of Gd_2O_3:Eu^{3+} nanoparticles. The red arrows show both lines used to quantify the atomic ratio [Eu]/[Gd] in (b). (b) Four reference samples (dots) from polyol-mediated synthesis [3], with a [Eu]/[Gd] atomic ratio range extending from 0.1% to 3%. The error bars correspond to the standard deviation computed from 30 successive measurements. The linear regression conducted to a rather good linearity (R^2=0.996). Confidence hyperboles are plotted in green (95% confidence level).

Purification procedure efficiency evaluated by LIBS

Because each characterisation requires different quality of purification and amount of matter, three synthesis were achieved in the same conditions than described in the main manuscript for an $EuCl_3$ salt concentration of 10^{-3} mol.L^{-1}. The first one (1P, for Luminescence) was washed according to the previous protocol. The second one (2P, for DRX) was washed twice and the third one (10P, for LIBS) was washed ten times. Figure 2a shows the normalised luminescence spectra of the samples recorded on a FS5 Spectrofluorometer (excitation from 265 nm to 275 nm, spectral resolution 1 nm, integration time 0.3 s, each spectrum is averaged over five acquisitions). Figure 2b shows the amount of Europium in each sample evaluated by LIBS. We can assume than after ten washing, there is no remaining solvated salt. It also appears that the purification has no significant influence on the luminescence spectra. This is consistent with the excitation wavelengths used, which cover both the charge-transfer band Eu-O and the $^8S_{7/2} \rightarrow {}^6I_J$ intra-configurational transition of Gd^{3+}. It then favours the excitation of the europium ions in the core of the Gd_2O_3 matrix, or surface-adsorbed europium.

Ablated mass per pulse

The amount of ablated mass is determined by weighting size selected particles resulting from two different ablations. They are respectively performed during 380 min and 315 min in 200 mL of $EuCl_3$ solution at 10^{-3} mol.L^{-1}. The ablation duration enables to produce a significant amount of material. After ablation, the colloidal solution is poured in 9 cm high tubes (filling height 7 cm) and gently centrifuged at 50 RCF (rotor diameter 10.4 cm) during 10 min. The supernatant is then collected. All the particles larger than 817 nm settle down and are thus removed, and only a few percents of the nanoparticles smaller than 100 nm are removed (see Figure 3). The supernatant is centrifuged at 13130 RCF during 14 h in order to precipitate the nanoparticles. The targets, the particles larger than 817 nm and the nanoparticles (<817 nm) are dried out in an oven at 90 ^{o}C during 10 h and weighted on a micro-balance separately. 2.0 ng (Standard deviation 0.18 ng) of nanoparticles is produced for each laser pulse, which corresponds to only 13 % of the ablated material. According to the mass weighted size distribution, it corresponds to nanoparticles smaller than 100 nm.

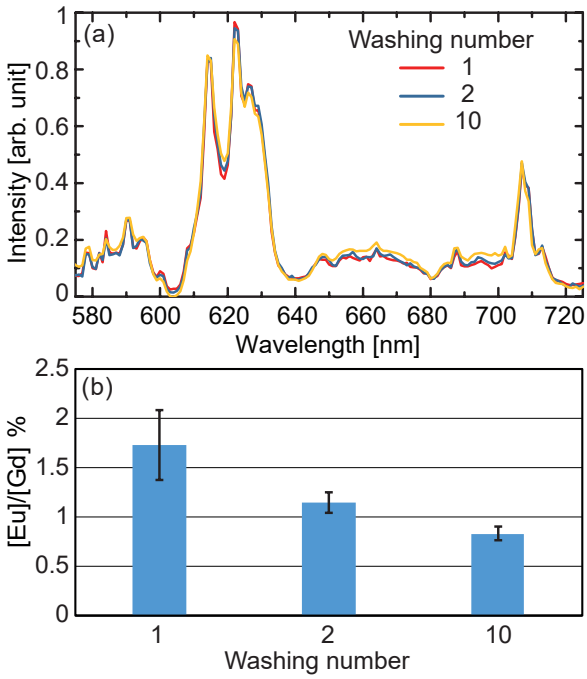

Figure 2: a) Luminescence spectra of the nanoparticles obtained by ablation of pure gadolinia in Eu^{3+} solution at 10^{-3} mol.L^{-1} washed 1, 2 and 10 times. b) [Eu]/[Gd] percentage in the corresponding samples measured by LIBS. Error bars correspond to the confidence interval of 99.7% (three times the standard deviation).

Size distribution

The typical size and mass distribution are calculated from three different large field TEM images shown in figures 4a,b,c. Nanoparticles were automatically detected using *ImageJ* software and its plug-in *Particles Sizer* [5]. Figure 4d shows the detected particles in red from the image c. The diameters were defined as the area equivalent diameter.

X-ray diffraction

The X-ray diffraction patterns displayed in figure 5 clearly show that both nanoparticles and targets are monoclinic Gd_2O_3. No obvious impurity phases are detected. The intensities in the nanoparticle's pattern fit very well the theoretical powder diffraction intensities. The peaks are broadened compared to the target's pattern. According to Scherrer equation applied to peak widths, the diffraction pattern is governed by the larger particles. The intensities in the target's pattern deviate from the theoretical powder diffraction intensities. It shows that the elaboration procedure of the pellets (annealed pressed powder) leads to a partial grain orientation.

Excitation spectrum and luminescence decay

Figure 6 shows photoluminescence excitation (PLE) spectrum and photoluminescence decay curve. They were measured by a custom made spectrofluorometer 5000M Horiba Jobin Yvon, using a steady state deuterium lamp (PLE spectrum) and a microsecond xenon pulsed flash lamp (PL decay) as excitation sources. Single grating monochromators and photon counting photomultiplier based detectors were used for the emission light collection. Spectra were corrected for the instrumental response and a convolution procedure was applied to the decay curves to determine true decay times (SpectraSolve software package, Ames Photonics).

The luminescence lifetime in the millisecond range (see figure 6b) is consistent with the emission from

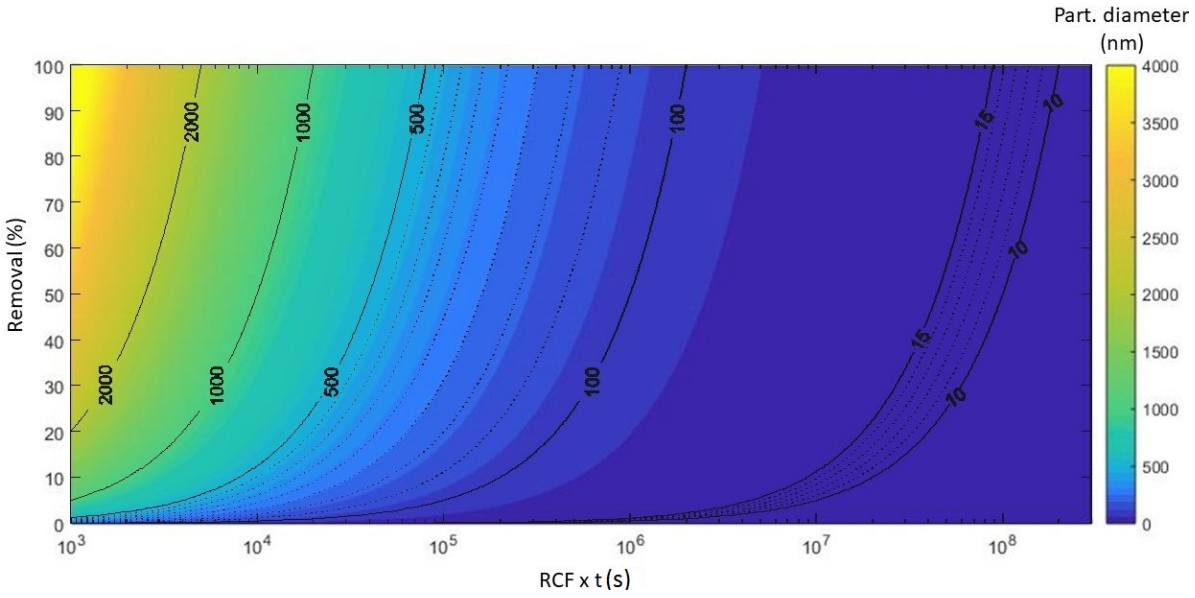

Figure 3: Percentage of removal for different size of Gd_2O_3 particles (density 7.41 g.cm^{-3}) in water as a function of the Relative Centrifugal Force times the centrifugation duration. The tube filling height is 7 cm. The velocity of sedimentation is based on the Stoke's law. The sub-micronic particles selection performed corresponds to $RCF \times t = 50 * 600 = 3 \times 10^4$.

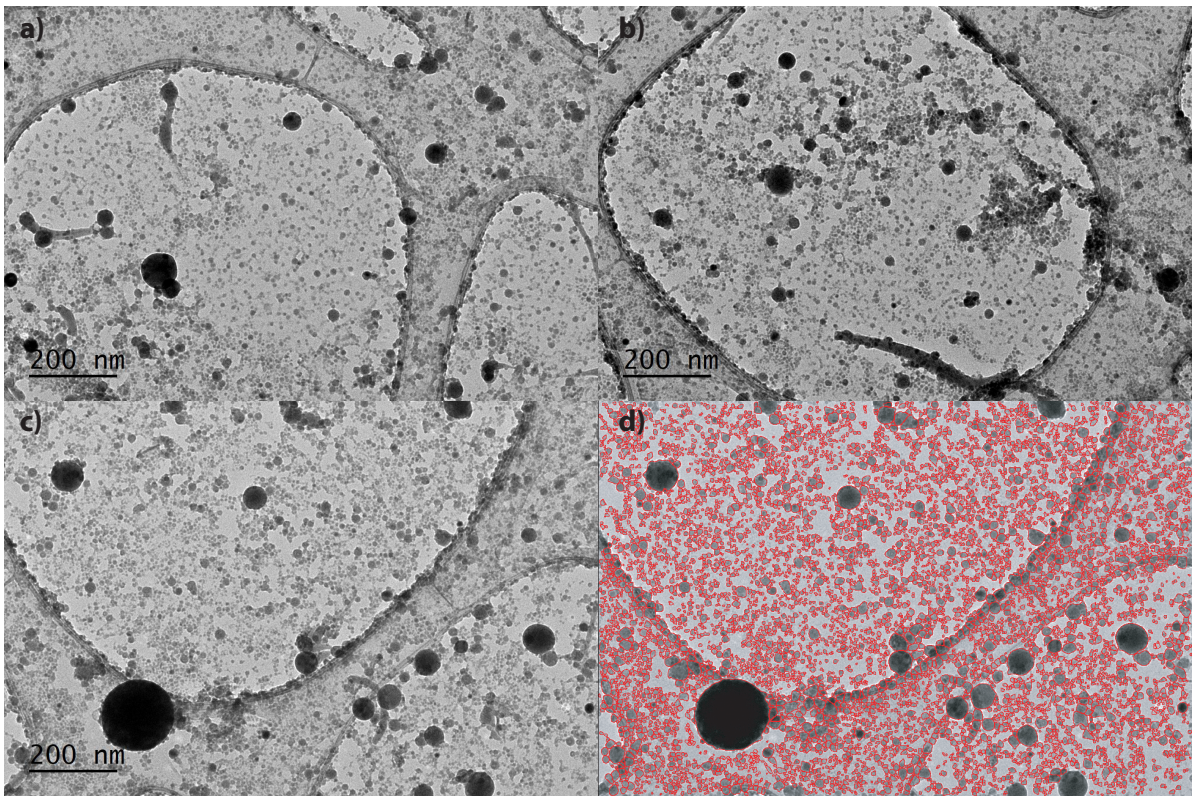

Figure 4: a,b,c) Large field images used to compute the size distribution. d) corresponds to the image processing performs on image c) using the plug-in *Particles Sizer* [5] of *ImageJ* software.

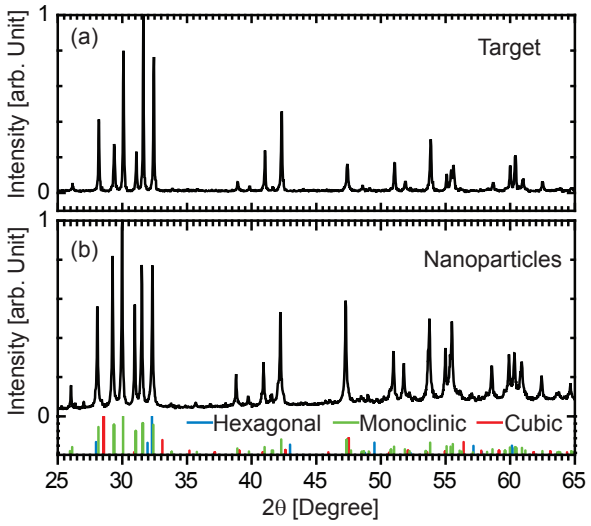

Figure 5: X-ray diffraction pattern measured on a bulk target (a), and on the dry nanoparticles (b). The theoretical peak positions for cubic (Powder Diffraction File 00-012-0797 from ICDD), hexagonal (04-016-2410) and monoclinic (00-042-1465) crystal structures are displayed.

forbidden f-f transition. The biexponential fitting is consistent with the reported in-homogeneous broadening of the luminescent spectra.

Reference

[1] V. Motto-Ros, E. Negre, F. Pelascini, G. Panczer, and J. Yu. Precise alignment of the collection fiber assisted by real-time plasma imaging in laser-induced breakdown spectroscopy. Spectroc. Acta Pt. B, 92:60–69, FEB 1 2014.

[2] L. Sancey, V. Motto-Ros, B. Busser, S. Kotb, J. M. Benoit, A. Piednoir, F. Lux, O. Tillement, G. Panczer, and J. Yu. Laser spectrometry for multi-elemental imaging of biological tissues. Sci. Rep., 4:6065, AUG 14 2014.

[3] M. A. Flores-Gonzalez, C. Louis, R. Bazzi, G. Ledoux, K. Lebbou, S. Roux, P. Perriat, and O. Tillement. Elaboration of nanostructured Eu^{3+}-doped Gd_2O_3 phosphor fine spherical powders using polyol-mediated synthesis. Appl. Phys. A, 81(7):1385–1391, NOV 2005.

[4] Jean-Michel Mermet. Calibration in atomic spectrometry: A tutorial review dealing with quality criteria, weighting procedures and possible curvatures. Spectroc. Acta Pt. B, 65(7):509–523, JUL 2010.

[5] Thorsten Wagner and Jan Eglinger. thorstenwagner/ij-particlesizer: v1.0.9 Snapshot release, jun 2017.

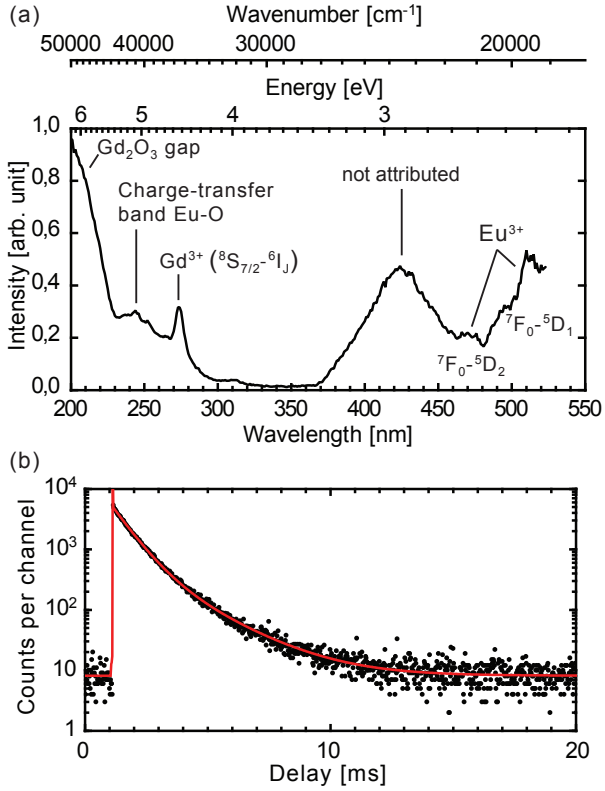

Figure 6: (a) Excitation spectrum of the nanoparticles synthesized in a solution of 10^{-3} mol.L^{-1} of europium salts. Emission at 625 nm integrated over 32 nm (FWHM of the spectral resolution). The spectral resolution of the excitation spectrum is 4 nm. (b) The black curve corresponds to the luminescence decay for excitation at 274 nm (^6I_J level of Gd^{3+}) and emission at 630 nm. The spectral resolution is 6 nm on both emission and excitation. The red curve corresponds to a biexponential fitting : 4382 exp(-t/725.3 μs) + 667 exp(-t/1977 μs)+8.

Bibliography

[1] Albert Einstein. Zum quantentheorie der strahlung (on the quantum theory of radiation). Mitteilungen der Physikalischen Gesellsch Zürich, 18:47–62, 1916.

[2] Jim P Gordon, Herb J Zeiger, and Charles H Townes. Molecular microwave oscillator and new hyperfine structure in the microwave spectrum of n h 3. Physical Review, 95(1):282, 1954.

[3] Jeff Hecht. A short history of laser development. Applied optics, 49(25):F99–F122, 2010.

[4] Gérard Mourou Christine Labaune. 50 ans du laser dans la ville lumière, volume 129. Unknown, 2010.

[5] Theodore H Maiman. Stimulated optical radiation in ruby. nature, 187(4736):493–494, 1960.

[6] AD White and JD Rigden. Continuous gas maser operation in visible. Proceedings of the Institute of Radio Engineers, 50(7):1697, 1962.

[7] JE Geusic, HM Marcos, and LeGrand Van Uitert. Laser oscillations in nd-doped yttrium aluminum, yttrium gallium and gadolinium garnets. Applied Physics Letters, 4(10):182–184, 1964.

[8] F Brench. Optical microemission stimulated by a ruby master. Appl. Spectros, 16:59, 1962.

[9] Howard M. Smith and A. F. Turner. Vacuum deposited thin films using a ruby laser. Appl. Opt., 4(1):147–148, Jan 1965.

[10] MA Hernandez-Perez, C Garapon, C Champeaux, and JC Orlianges. Structural and optical properties of phenylalanine and tyrosine thin films prepared by pulsed laser deposition. In Journal of Physics: Conference Series, volume 59, page 154. IOP Publishing, 2007.

[11] MA Hernandez-Perez, C Garapon, C Champeaux, P Shahgaldian, A Coleman, and J Mugnier. Pulsed laser deposition of bovine serum albumin protein thin films. Applied Surface Science, 208:658–662, 2003.

[12] Sebastien Rabaste, Nahid Amstutz, Andreas Hauser, and Anne Pillonnet. Optical properties of thin films of [ru (bpy) 3][na cr (ox) 3] polymeric networks. Applied Physics Letters, 87(25):251904, 2005.

[13] Stephan Guy, Laure Guy, Amina Bensalah-Ledoux, Antonio Pereira, Vincent Grenard, Olivier Cosso, and Teophile Vautey. Pure chiral organic thin films with high isotropic optical activity synthesized by uv pulsed laser deposition. Journal of Materials Chemistry, 19(38):7093–7097, 2009.

[14] S Guy, A Bensalah-Ledoux, A Lambert, Y Guillin, L Guy, and JC Mulatier. Chiral organic thin films: How far pulsed laser deposition can conserve chirality. Thin Solid Films, 520(20):6440–6445, 2012.

[15] Kenneth A Lincoln. Improved instrumentation for time-resolved mass spectrometry with application to laser-vaporization of solid materials. International Journal of Mass Spectrometry and Ion Physics, 2(1):75–83, 1969.

[16] JF Friichtenicht. Laser-generated pulsed atomic beams. Review of Scientific Instruments, 45(1):51–56, 1974.

[17] Michael A Duncan. Invited review article: laser vaporization cluster sources. Review of Scientific Instruments, 83(4):041101, 2012.

[18] Yasuo Iida, Akira Tsuge, Yoshinori Uwamino, Hisashi Morikawa, and Toshio Ishizuka. Laser ablation in a liquid medium as a technique for solid sampling. Journal of analytical atomic spectrometry, 6(7):541–544, 1991.

[19] Dongshi Zhang, Bilal Gökce, and Stephan Barcikowski. Laser synthesis and processing of colloids: fundamentals and applications. Chemical reviews, 117(5):3990–4103, 2017.

[20] Dongshi Zhang, Jun Liu, Pengfei Li, Zhenfei Tian, and Changhao Liang. Recent advances in surfactant-free, surface-charged, and defect-rich catalysts developed by laser ablation and processing in liquids. ChemNanoMat, 3(8):512–533, 2017.

[21] Vincenzo Amendola and Moreno Meneghetti. Laser ablation synthesis in solution and size manipulation of noble metal nanoparticles. Physical chemistry chemical physics, 11(20):3805–3821, 2009.

[22] Heberton Wender, Marcos L Andreazza, Ricardo RB Correia, Sérgio R Teixeira, and Jairton Dupont. Synthesis of gold nanoparticles by laser ablation of an au foil inside and outside ionic liquids. Nanoscale, 3(3):1240–1245, 2011.

[23] Giuseppe Compagnini, Alessandro A Scalisi, and Orazio Puglisi. Ablation of noble metals in liquids: a method to obtain nanoparticles in a thin polymeric film. Physical Chemistry Chemical Physics, 4(12):2787–2791, 2002.

[24] Jurij Jakobi, Svea Petersen, Ana Meneéndez-Manjón, Philipp Wagener, and Stephan Barcikowski. Magnetic alloy nanoparticles from laser ablation in cyclopentanone and their embedding into a photoresist. Langmuir, 26(10):6892–6897, 2010.

[25] N Takada, T Sasaki, and K Sasaki. Synthesis of crystalline tin and si particles by laser ablation in liquid nitrogen. Applied Physics A, 93(4):833–836, 2008.

[26] Nushin Tabatabaie and Davoud Dorranian. Effect of fluence on carbon nanostructures produced by laser ablation in liquid nitrogen. Applied Physics A, 122(5):558, 2016.

[27] Toru Kato, Sven Stauss, Satoshi Kato, Keiichiro Urabe, Motoyoshi Baba, Tohru Suemoto, and Kazuo Terashima. Pulsed laser ablation plasmas generated in co2 under high-pressure conditions up to supercritical fluid. Applied Physics Letters, 101(22):224103, 2012.

[28] Carmen Streich, Laura Akkari, Christina Decker, Jenny Bormann, Christoph Rehbock, Andreas Müller-Schiffmann, Felix Carlsson Niemeyer, Luitgard Nagel-Steger, Dieter Willbold, Barbara Sacca, et al. Characterizing the effect of multivalent conjugates composed of aβ-specific ligands and metal nanoparticles on neurotoxic fibrillar aggregation. ACS nano, 10(8):7582–7597, 2016.

[29] Tomohiro Ikehata, Yuji Onodera, Takashi Nunokawa, Tomohisa Hirano, Shun-ichiro Ogura, Toshiaki Kamachi, Osamu Odawara, and Hiroyuki Wada. Photodynamic therapy using upconversion nanoparticles prepared by laser ablation in liquid. Applied Surface Science, 348:54–59, 2015.

[30] Jianming Zhang, Mohamed Chaker, and Dongling Ma. Pulsed laser ablation based synthesis of colloidal metal nanoparticles for catalytic applications. Journal of colloid and interface science, 489:138–149, 2017.

[31] Churong Ma, Jiahao Yan, Yingcong Huang, and Guowei Yang. Directional scattering in a germanium nanosphere in the visible light region. Advanced Optical Materials, 5(24):1700761, 2017.

[32] Vincenzo Amendola, Stefano Scaramuzza, Stefano Agnoli, Gaetano Granozzi, Moreno Meneghetti, Giulio Campo, Valentina Bonanni, Francesco Pineider, Claudio Sangregorio, Paolo Ghigna, et al. Laser generation of iron-doped silver nanotruffles with magnetic and plasmonic properties. Nano research, 8(12):4007–4023, 2015.

[33] Carlos Doñate-Buendía, Felix Frömel, Markus B Wilms, René Streubel, Jochen Tenkamp, Tim Hupfeld, Milen Nachev, Emine Gökce, Andreas Weisheit, Stephan Barcikowski, et al. Oxide dispersion-strengthened alloys generated by laser metal deposition of laser-generated nanoparticle-metal powder composites. Materials & Design, 154:360–369, 2018.

[34] Linas Jonušauskas, Marcus Lau, Peter Gruber, Bilal Gökce, Stephan Barcikowski, Mangirdas Malinauskas, and Aleksandr Ovsianikov. Plasmon assisted 3d microstructuring of gold nanoparticle-doped polymers. Nanotechnology, 27(15):154001, 2016.

[35] Dongshi Zhang and Bilal Gökce. Perspective of laser-prototyping nanoparticle-polymer composites. Applied Surface Science, 392:991–1003, 2017.

[36] Elisabeth Maurer, Stephan Barcikowski, and Bilal Gökce. Process chain for the fabrication of nanoparticle polymer composites by laser ablation synthesis. Chemical Engineering & Technology, 40(9):1535–1543, 2017.

[37] Marie Godet, Véronique Vergès-Belmin, Christine Andraud, Mandana Saheb, Judith Monnier, Eric Leroy, Julie Bourgon, and Laurent Binet. Laser yellowing effect: study of the nanophases created by laser irradiation of synthetic black crusts using transmission electron microscopy (tem) and electron paramagnetic resonance (epr) spectroscopy. In Proceeding of the LACONA 11 congress, Krakow, 2017.

[38] Claude Phipps. Laser ablation and its applications, volume 129. Springer, 2007.

[39] Zijie Yan and Douglas B Chrisey. Pulsed laser ablation in liquid for micro-/nanostructure generation. Journal of Photochemistry and Photobiology C: Photochemistry Reviews, 13(3):204–223, 2012.

[40] David Amans, Mouhamed Diouf, Julien Lam, Gilles Ledoux, and Christophe Dujardin. Origin of the nano-carbon allotropes in pulsed laser ablation in liquids synthesis. J. Colloid Interface Sci., 489:114–125, MAR 1 2017.

[41] Vincenzo Amendola and Moreno Meneghetti. What controls the composition and the structure of nanomaterials generated by laser ablation in liquid solution? Physical Chemistry Chemical Physics, 15(9):3027–3046, 2013.

[42] Cheng-Yu Shih, René Streubel, Johannes Heberle, Alexander Letzel, Maxim V Shugaev, Chengping Wu, Michael Schmidt, Bilal Gökce, Stephan Barcikowski, and Leonid V Zhigilei. Two mechanisms of nanoparticle generation in picosecond laser ablation in liquids: the origin of the bimodal size distribution. Nanoscale, 10(15):6900–6910, 2018.

[43] Mark-Robert Kalus, Stephan Barcikowski, and Bilal Gökce. How the physicochemical properties of the bulk material affect the ablation crater profile, mass balance, and bubble dynamics during single-pulse, nanosecond laser ablation in water. Chemistry A European Journal, 27(19):5978, 2021.

[44] Sarah Dittrich, René Streubel, Cormac McDonnell, Heinz P Huber, Stephan Barcikowski, and Bilal Gökce. Comparison of the productivity and ablation efficiency of different laser classes for laser ablation of gold in water and air. Applied Physics A, 125(6):1–10, 2019.

[45] Sébastien Besner, Andrei V Kabashin, Francoise M Winnik, and Michel Meunier. Ultrafast laser based "green" synthesis of non-toxic nanoparticles in aqueous solutions. Applied Physics A, 93(4):955–959, 2008.

[46] Julien Lam, David Amans, Christophe Dujardin, Gilles Ledoux, and Abdul-Rahman Allouche. Atomistic mechanisms for the nucleation of aluminum oxide nanoparticles. The Journal of Physical Chemistry A, 119(33):8944–8949, 2015.

[47] Julien Lam, Vincent Motto-Ros, Dimitri Misiak, Christophe Dujardin, Gilles Ledoux, and David Amans. Investigation of local thermodynamic equilibrium in laser-induced plasmas: Measurements of rotational and excitation temperatures at long time scales. Spectrochim. Acta B, 101:86–92, 2014.

[48] Alfred Vogel, S Busch, and U Parlitz. Shock wave emission and cavitation bubble generation by picosecond and nanosecond optical breakdown in water. The Journal of the Acoustical Society of America, 100(1):148–165, 1996.

[49] Julien Lam, Julien Lombard, Christophe Dujardin, Gilles Ledoux, Samy Merabia, and David Amans. Dynamical study of bubble expansion following laser ablation in liquids. Appl. Phys. Lett., 108(7):074104, FEB 15 2016.

[50] Arsène Chemin, Julien Lam, Gaétan Laurens, Florian Trichard, Vincent Motto-Ros, Gilles Ledoux, Vítězslav Jarỳ, Valentyn Laguta, Martin Nikl,

Christophe Dujardin, et al. Doping nanoparticles using pulsed laser ablation in a liquid containing the doping agent. Nanoscale Advances, 1(10):3963–3972, 2019.

[51] Ayumu Matsumoto, Ayaka Tamura, Takaya Honda, Tsuyoshi Hirota, Kazuya Kobayashi, Seiji Katakura, Naoya Nishi, Ken-ichi Amano, Kazuhiro Fukami, and Tetsuo Sakka. Transfer of the species dissolved in a liquid into laser ablation plasma: an approach using emission spectroscopy. The Journal of Physical Chemistry C, 119(47):26506–26511, 2015.

[52] Jun Liu, Changhao Liang, Zhenfei Tian, Shuyuan Zhang, and Guosheng Shao. Spontaneous growth and chemical reduction ability of ge nanoparticles. Scientific reports, 3:1741, 2013.

[53] P Liu, YL Cao, XY Chen, and GW Yang. Trapping high-pressure nanophase of ge upon laser ablation in liquid. Crystal Growth and Design, 9(3):1390–1393, 2008.

[54] Bianca Haberl, Malcolm Guthrie, Brad D Malone, Jesse S Smith, Stanislav V Sinogeikin, Marvin L Cohen, James S Williams, Guoyin Shen, and Jodie E Bradby. Controlled formation of metastable germanium polymorphs. Physical Review B, 89(14):144111, 2014.

[55] J M McHale, A Auroux, A J Perrotta, and A Navrotsky. Surface energies and thermodynamic phase stability in nanocrystalline aluminas. Science, 277:788, 1997.

[56] J M McHale, A Navrotsky, and A J Perrotta. Effects of increased surface area and chemisorbed H2O on the relative stability of nanocrystalline gamma-Al2O3 and alpha-Al2O3. J. Phys. Chem. B, 101(4):603–613, JAN 23 1997.

[57] A. H. Tavakoli, P. S. Maram, S. J. Widgeon, J. Rufner, K. van Benthem, S. Ushakov, S. Sen, and A. Navrotsky. Amorphous alumina nanoparticles: Structure, surface energy, and thermodynamic phase stability. J. Phys. Chem. C, 117:17123 – 17130, 2013.

[58] Th Posch, F Kerschbaum, H Mutschke, D Fabian, J Dorschner, and J Hron. On the origin of the 13 mu m feature. a study of iso-sws spectra of oxygen-rich agb stars. Astronomy and Astrophysics, 352:609–618, 1999.

[59] E Dendy Sloan. Fundamental principles and applications of natural gas hydrates. Nature, 426(6964):353–359, 2003.

[60] M Volmer and H Flood. Droplet formation in steaming. Z Phys. Chem A-Chem. Thermodyn. Kinet. Elektrochem. Eigensch.lehre, 170(3/4):273–285, 1934.

[61] Richard Becker and Werner Döring. Kinetische behandlung der keimbildung in übersättigten dämpfen. Annalen der Physik, 416(8):719–752, 1935.

[62] J Feder, K C Russell, J Lothe, and G M Pound. Homogeneous nucleation and growth of droplets in vapours. Adv. Phys., 15:111, 1966.

[63] Jels Boulangier, David Gobrecht, Leen Decin, Alex de Koter, and Jeremy Yates. Developing a self-consistent agb wind model–ii. non-classical, non-equilibrium polymer nucleation in a chemical mixture. Monthly Notices of the Royal Astronomical Society, 489(4):4890–4911, 2019.

[64] F. F. Abraham. Homogeneous nucleation theory. New York: Academic Press, 1974.

[65] Joonas Merikanto, Evgeni Zapadinsky, Antti Lauri, and Hanna Vehkamäki. Origin of the failure of classical nucleation theory: Incorrect description of the smallest clusters. Phys. Rev. Lett., 98(14):145702, 2007.

[66] J Lothe and G M Pound. Reconsiderations of nucleation theory. J. Chem. Phys., 36(8):2080, 1962.

[67] Y Viisanen, R Strey, and H Reiss. Homogeneous Nucleation Rates of Water. J. Chem. Phys., 99(6):4680–4692, SEP 15 1993.

[68] Y Viisanen and R Strey. Homogeneous Nucleation Rates of n-Butanol. J. Chem. Phys., 101(9):7835–7843, NOV 1 1994.

[69] James F. Lutsko and Miguel A. Duran-Olivencia. Classical Nucleation Theory from a Dynamical Approach to Nucleation. J. Chem. Phys., 138(24):244908, 2013.

[70] James F. Lutsko and Miguel A. Durán-Olivencia. A Two-Parameter Extension of Classical Nucleation Theory. J. Phys.: Condens. Matter, 27:235101, 2015.

[71] J Hruby, Y Viisanen, and R Strey. Homogeneous Nucleation Rates for n-Pentanol in Argon: Determination of the Critical Cluster Size. J. Chem. Phys., 104(13):5181–5187, APR 1 1996.

[72] S Sen and T Mukerji. A Generalized Classical Nucleation Theory for Rough Interfaces: Application in the Analysis of Homogeneous Nucleation in Silicate Liquids. J. Non-Cryst. Solids, 246(3):229–239, 1999.

[73] Wilhelm Ostwald. Studien über die bildung und umwandlung fester körper. Zeitschrift für physikalische Chemie, 22(1):289–330, 1897.

[74] T Threlfall. Structural and Thermodynamic Explanations of Ostwald's Rule. Org. Process Res. Dev., 7(6):1017–1027, 2003.

[75] Tian Hui Zhang and Xiang Yang Liu. Nucleation: What Happens at the Initial Stage? Angew. Chem.-Int. Edit., 48(7):1308–1312, 2009.

[76] F Baletto, C Mottet, and R Ferrando. Reentrant Morphology Transition in the Growth of Free Silver Nanoclusters. Phys. Rev. Lett., 84(24):5544, 2000.

[77] F Baletto, C Mottet, and R Ferrando. Microscopic Mechanisms of the Growth of Metastable Silver Icosahedra. Phys. Rev. B, 63(15):155408, 2001.

[78] Shinnosuke Ishizuka, Yuki Kimura, Tomoya Yamazaki, Tetsuya Hama, Naoki Watanabe, and Akira Kouchi. Two-Step Process in Homogeneous Nucleation of Alumina in Supersaturated Vapor. Chem. Mat., 28(23):8732–8741, DEC 13 2016.

[79] Shinnosuke Ishizuka, Yuki Kimura, Jun Kawano, Rafael Escribano, Tomoya Yamazaki, Tetsuya Hama, and Rikako Sato. Immiscibility of Nucleating Aluminum Oxide Nanoparticles in Vapor. J. Phys. Chem. C, 122(43):25092–25101, NOV 1 2018.

[80] David Gobrecht, Stefan T. Bromley, John M. C. Plane, Leen Decin, and Sergio Cristallo. On the onset of dust formation in agb stars. Proceedings of the International Astronomical Union, 14(S343):119–128, 2018.

[81] Danny Perez, Laurent J Lewis, Patrick Lorazo, and Michel Meunier. Ablation of molecular solids under nanosecond laser pulses: The role of inertial confinement. Applied physics letters, 89(14):141907, 2006.

[82] NM Bulgakova and AV Bulgakov. Pulsed laser ablation of solids: transition from normal vaporization to phase explosion. Applied Physics A, 73(2):199–208, 2001.

[83] Patrick Lorazo, Laurent J Lewis, and Michel Meunier. Short-pulse laser ablation of solids: from phase explosion to fragmentation. Physical review letters, 91(22):225502, 2003.

[84] Patrick Lorazo, Laurent J Lewis, and Michel Meunier. Thermodynamic pathways to melting, ablation, and solidification in absorbing solids under pulsed laser irradiation. Physical Review B, 73(13):134108, 2006.

[85] Cheng-Yu Shih, Chengping Wu, Maxim V Shugaev, and Leonid V Zhigilei. Atomistic modeling of nanoparticle generation in short pulse laser ablation of thin metal films in water. J. Colloid Interface Sci., 489:3–17, 2017.

[86] Xia Wu, Shanshan Chen, Yan Sun, and Youcun Chen. Geometrical structures of gold clusters on gupta and sutton-chen potentials. Computational and Theoretical Chemistry, 1002:43–48, 2012.

[87] Gaétan Laurens, David Amans, Julien Lam, and Abdul-Rahman Allouche. Comparison of aluminum oxide empirical potentials from cluster to nanoparticle. Physical Review B, 101(4):045427, 2020.

[88] Xavier Baumann, Ph Teulet, Y Cressault, and Arnaud Bultel. Study on reaction rates for 2t sf6 plasma: application to chemical kinetics of a decaying arc in high voltage circuit breakers. In Journal of Physics: Conference Series, volume 1243, page 012007. IOP Publishing, 2019.

[89] Amal Allouch, Jonathan Mougenot, Armelle Michau, Swaminathan Prasanna, Khaled Hassouni, Mahamadou Seydou, François Maurel, and Pascal Brault. On the stable forms of carbon clusters produced in low pressure sputtering discharge. In 24th International Symposium on Plasma Chemistry, 2019.

[90] Masatoshi Saba, Takafumi Kato, and Tatsuo Oguchi. Reaction modeling study on the combustion of aluminum in gas phase: The al+ o2 and related reactions. Combustion and Flame, 225:535–550.

[91] Alexander M Savel'ev and Alexander M Starik. The formation of (al2o3) n clusters as a probable mechanism of aluminum oxide nucleation during the combustion of aluminized fuels: Numerical analysis. Combustion and Flame, 196:223–236, 2018.

[92] MJ McGrath, T Olenius, IK Ortega, V Loukonen, P Paasonen, T Kurtén, M Kulmala, and H Vehkamäki. Atmospheric cluster dynamics code: a flexible method for solution of the birth-death equations. Atmospheric Chemistry and Physics, 12(5):2345–2355, 2012.

[93] Seyyed Ali Davari and Dibyendu Mukherjee. Kinetic monte carlo simulation for homogeneous nucleation of metal nanoparticles during vapor phase synthesis. AIChE Journal, 64(1):18–28, 2018.

[94] Christoph Köhn, Martin Bødker Enghoff, and Henrik Svensmark. A 3d particle monte carlo approach to studying nucleation. Journal of Computational Physics, 363:30–38, 2018.

[95] Henry Eyring. The activated complex and the absolute rate of chemical reactions. Chem. Rev., 17(1):65–77, 1935.

[96] Henry Eyring. The activated complex in chemical reactions. J. Chem. Phys., 3(2):107–115, 1935.

[97] P. Davidovits and M Faist. On the condensation sticking coefficient - a quantitative discussion. J. Chem. Phys., 74(1):637–643, 1981.

[98] Louis Stevenson Kassel. Studies in homogeneous gas reactions. i. J. Phys. Chem., 32(2):225–242, 1928.

[99] L S Kassel. Studies in homogeneous gas reactions. ii. introduction of quantum theory. J. Phys. Chem., 32(7):1065–1079, 1928.

[100] Oscar Knefler Rice and Herman C Ramsperger. Theories of unimolecular gas reactions at low pressures. J. Am. Chem. Soc., 49(7):1617–1629, 1927.

[101] Rudolph A Marcus. Unimolecular dissociations and free radical recombination reactions. J. Chem. Phys., 20(3):359–364, 1952.

[102] A. W. Castleman and K. H. a. Bowen. Clusters: Structure, energetics, and dynamics of intermediate states of matter. J. Phys. Chem., 100(31):12911–12944, 1996.

[103] J J Breen, K Kilgore, K Stephan, R Hofmann-Sievert, B D Kay, R G Keesee, T D Märk, and A W Castleman Jr. The use of similarity profiles in studying cluster formation in molecular beams: Evidence for the role of pre-existing dimers. Chem. Phys., 91(2):305–313, 1984.

[104] O Hagena and W Henkes. Determination of the effective ionization cross sections in condensed molecular beams. Z. Naturforsch., 20, 1965.

[105] J Bauchert and O. F. Hagena. Massenbestimmung ionisierter agglomerate in kondensierten molekularstrahlen nach einer elektrischen gegenfeldmethode. Z. Naturforsch. A, 20(9):1135+, 1965.

[106] T A Milne and F T Greene. Mass spectrometry in inorganic chemistry. Advan. Chem. Ser., 72:68, 1968.

[107] James B Anderson. Molecular beams from nozzle sources. Gas Dynamics, pages 1–91, 1974.

[108] Ronald P Andres. Homogeneous nucleation from the vapor phase. Ind. Eng. Chem., 57(10):24–31, 1965.

[109] J. B. Anderson, R. P. Andres, and J. B. Fenn. Supersonic Nozzle Beams, pages 275–317. John Wiley & Sons, Ltd, 2007.

[110] Paul C Engelking. Determination of cluster binding energy from evaporative lifetime and average kinetic energy release: Application to (co2)+ n and ar+ n clusters. J. Chem. Phys., 87(2):936–940, 1987.

[111] P C Engelking. Photoinduced evaporation of charged clusters. J. Chem. Phys., 85(5):3103–3110, 1986.

[112] E Cottancin, M Pellarin, J Lermé, B Baguenard, B Palpant, J-L Vialle, and M Broyer. Unimolecular dissociation of trivalent metal cluster ions: The size evolution of metallic bonding. J. Chem. Phys., 107(3):757–771, 1997.

[113] E Cottancin, M Pellarin, J Lerme, B Palpant, B Baguenard, J-L Vialle, and M Broyer. Unimolecular dissociation of trivalent metal cluster ions (al n+, ga n+, in n+): evidence for a transition from covalent to metallic bonding. Z. Phys. D, 40(1):288–293, 1997.

[114] P. A. Hervieux and D. H. E. Gross. Evaporation of hot mesoscopic atomic metal clusters. Z. Phys. D, 33:295–299, 1995.

[115] Jean-Marc L'Hermite and Sébastien Zamith. Macroscopic extension of rrk and weisskopf models of unimolecular evaporation. EPL, 100(2):23001, 2012.

[116] G F Bertsch, N Oberhofer, and S Stringari. Evaporation of atoms from metal clusters. Z. Phys. D, 20(1):123–125, 1991.

[117] Klavs Hansen. Statistical emission processes of clusters. Philos. Mag. B, 79(9):1413–1425, 1999.

[118] C Bréchignac, H Busch, Ph Cahuzac, and J Leygnier. Dissociation pathways and binding energies of lithium clusters from evaporation experiments. J. Chem. Phys., 101(8):6992–7002, 1994.

[119] V. Weisskopf. Statistics and nuclear reactions. Phys. Rev., 52:295–303, Aug 1937.

[120] Patrice Mélinon and Michel Broyer. Les agrégats: Introduction au nano-monde. EDP Sciences, 2021.

[121] Philo of Byzantium. De septem mundi miraculis, volume 2. III century.

[122] Ellen L Spotz, William A Seitz, and J. L. Franklin. Translational energy of fragments of ion decomposition and totality of states functions. J. Chem. Phys., 51(11):5142–5148, 1969.

[123] Max A Haney and J L Franklin. Correlation of excess energies of electron-impact dissociations with the translational energies of the products. J. Chem. Phys., 48(9):4093–4097, 1968.

[124] Gerhard Herzberg and Klaus Peter Huber. Molecular Spectra and Molecular Structure. Van Nostrand Reinhold, 1979.

[125] Henry Eyring. The activated complex in chemical reactions. J. Chem. Phys., 3(2):107–115, 1935.

[126] Michael J Frisch, Gary W Trucks, H Bernhard Schlegel, Gustavo E Scuseria, Michael A Robb, James R Cheeseman, Giovanni Scalmani, Vincenzo Barone, Benedetta Mennucci, GA ea Petersson, et al. Gaussian 09 revision d. 01. 2014.

[127] FH Streitz and JW Mintmire. Electrostatic potentials for metal-oxide surfaces and interfaces. Physical Review B, 50(16):11996, 1994.

[128] Toshiaki Nagata, Ken Miyajima, and Fumitaka Mafuné. Stable stoichiometry of gas-phase cerium oxide cluster ions and their reactions with co. J. Phys. Chem. A, 119(10):1813–1819, 2015.

[129] D Mukherjee, CG Sonwane, and MR Zachariah. Kinetic monte carlo simulation of the effect of coalescence energy release on the size and shape evolution of nanoparticles grown as an aerosol. The Journal of chemical physics, 119(6):3391–3404, 2003.

[130] S Charton, V Blet, and JP Corriou. A simplified model for real gas expansion between two reservoirs connected by a thin tube. Chem. Eng. Sci., 51(2):295–308, 1996.

[131] John A. Dean. Lange's Handbook of Chemistry. McGraw-Hill New York, 10th Edition, 1969.

[132] W. A. Deheer. The physics of simple metal-clusters - experimental aspects and simple-models. Rev. Mod. Phys., 65(3, 1):611–676, JUL 1993.

[133] M Brack. The physics of simple metal-clusters - self-consistent jellium model and semiclassical approaches. Rev. Mod. Phys., 65(3, 1):677–732, JUL 1993.

[134] T P Martin. Shells of atoms. Phys. Rep.-Rev. Sec. Phys. Lett., 273(4):199–241, AUG 1996.

[135] Sayyadul Arafin, Ram N Singh, and Abraham K George. Extension of lindemann's formula to study the pressure dependence of melting temperature. Int. J. Thermophys., 33(6):1013–1022, 2012.

[136] Charles Kittel and Ching-yao Fong. Quantum theory of solids, volume 3. Wiley New York, 1963.

[137] GA Slack. Solid State Physics, volume 34. F Seitz and D Turnbull, New York: Academic, 1979.

[138] J H Gieske and G R Barsch. Pressure dependence of the elastic constants of single crystalline aluminum oxide. Phys. Status Solidi, 29(1):121–131, 1968.

[139] Yu-Ran Luo. Comprehensive handbook of chemical bond energies. CRC press, 2007.

[140] TE Itina and A Voloshko. Nanoparticle formation by laser ablation in air and by spark discharges at atmospheric pressure. Applied Physics B, 113(3):473–478, 2013.

[141] Qianli Ma, Vincent Motto-Ros, Xueshi Bai, and Jin Yu. Experimental investigation of the structure and the dynamics of nanosecond laser-induced plasma in 1-atm argon ambient gas. Applied Physics Letters, 103(20):204101, 2013.

[142] Bartlomej Pokrzywka, Agata Mendys, K. Dzierżęga, Michal Grabiec, and Stéphane Pellerin. Laser light scattering in a laser-induced argon plasma: Investigations of the shock wave. Spectrochimica Acta Part B: Atomic Spectroscopy, 74:24–30, 2012.

[143] David M Surmick, Daryl J Dagel, and Christian G Parigger. Spatial molecular alo temperature distributions in laser-induced plasma. Atoms, 7(3):86, 2019.

[144] KR Manes, ML Spaeth, JJ Adams, MW Bowers, JD Bude, CW Carr, AD Conder, DA Cross, SG Demos, JMG Di Nicola, et al. Damage mechanisms avoided or managed for nif large optics. Fusion Science and Technology, 69(1):146–249, 2016.

[145] Xiaocheng Zhang, Yong Jiang, Rong Qiu, Jiuling Meng, Jingrui Cao, Changjiang Zhang, Yupeng Zhao, and Tao Lü. Concentric ring damage on the front surface of fused silica induced by a nanosecond laser. Optical Materials Express, 9(12):4811–4817, 2019.

[146] Alfred Vogel and Vasan Venugopalan. Mechanisms of pulsed laser ablation of biological tissues. Chemical reviews, 103(2):577–644, 2003.

[147] Hervé K Nguendon, Neige Faivre, Bastian Meylan, Sergey Shevchik, Georg Rauter, Raphael Guzman, Philippe C Cattin, Kilian Wasmer, and Azhar Zam. Characterization of ablated porcine bone and muscle using laser-induced acoustic wave method for tissue differentiation. In European Conference on Biomedical Optics, page 104170N. Optical Society of America, 2017.

[148] Zhaoyang Chen, Annemie Bogaerts, and Akos Vertes. Phase explosion in atmospheric pressure infrared laser ablation from water-rich targets. Applied Physics Letters, 89(4):041503, 2006.

[149] Sebastian Kraft, Joerg Schille, Stefan Mauersberger, Lutz Schneider, and Udo Loeschner. Pump-probe imaging for process control and optimization in high-speed laser micro machining. In Laser-based Micro-and Nanoprocessing XIV, volume 11268, page 112681H. International Society for Optics and Photonics, 2020.

[150] Jitka Metelkova, Daniel Ordnung, Yannis Kinds, and Brecht Van Hooreweder. Novel strategy for quality improvement of up-facing inclined surfaces of lpbf parts by combining laser-induced shock waves and in situ laser remelting. Journal of Materials Processing Technology, 290:116981, 2021.

[151] Baptiste Chide, Sylvestre Maurice, Agnès Cousin, Bruno Bousquet, David Mimoun, Olivier Beyssac, Pierre-Yves Meslin, and Roger C Wiens. Recording laser-induced sparks on mars with the supercam microphone. Spectrochimica Acta Part B: Atomic Spectroscopy, 174:106000, 2020.

[152] Geoffrey Ingram Taylor. The formation of a blast wave by a very intense explosion.-ii. the atomic explosion of 1945. Proceedings of the Royal Society of London. Series A. Mathematical and Physical Sciences, 201(1065):175–186, 1950.

[153] Patrick Mora. Theoretical model of absorption of laser light by a plasma. The Physics of Fluids, 25(6):1051–1056, 1982.

[154] Claire E Max, CF McKee, and WC Mead. A model for laser driven ablative implosions. The Physics of Fluids, 23(8):1620–1645, 1980.

[155] WM Manheimer, DG Colombant, and JH Gardner. Steady-state planar ablative flow. The Physics of Fluids, 25(9):1644–1652, 1982.

[156] Rémy Fabbro, Claire Max, and Edouard Fabre. Planar laser-driven ablation: Effect of inhibited electron thermal conduction. The Physics of fluids, 28(5):1463–1481, 1985.

[157] B Meyer and G Thiell. Experimental scaling laws for ablation parameters in plane target–laser interaction with 1.06 μm and 0.35 μm laser wavelengths. The Physics of fluids, 27(1):302–311, 1984.

[158] Claire Ellen Max, Christopher F McKee, and WC Mead. Scaling of ablative laser-fusion implosions. Physical Review Letters, 45(1):28, 1980.

[159] John Lindl. Development of the indirect-drive approach to inertial confinement fusion and the target physics basis for ignition and gain. Physics of plasmas, 2(11):3933–4024, 1995.

[160] A Ng, D Pasini, P Celliers, D Parfeniuk, L Da Silva, and J Kwan. Ablation scaling in steady-state ablation dominated by inverse-bremsstrahlung absorption. Applied physics letters, 45(10):1046–1048, 1984.

[161] DE Fratanduono, TR Boehly, PM Celliers, MA Barrios, JH Eggert, RF Smith, DG Hicks, GW Collins, and DD Meyerhofer. The direct measurement of ablation pressure driven by 351-nm laser radiation. Journal of Applied Physics, 110(7):073110, 2011.

[162] Geoffrey Ingram Taylor. The formation of a blast wave by a very intense explosion i. theoretical discussion. Proceedings of the Royal Society of London. Series A. Mathematical and Physical Sciences, 201(1065):159–174, 1950.

[163] Cristian Porneala and David A Willis. Time-resolved dynamics of nanosecond laser-induced phase explosion. Journal of Physics D: Applied Physics, 42(15):155503, 2009.

[164] Santiago Palanco, Salvatore Marino, Mercedes Gabás, Shanti Bijani, Luis Ayala, and José R Ramos-Barrado. Particle formation and plasma radiative losses during laser ablation suitability of the sedov-taylor scaling. Optics express, 22(13):16552–16557, 2014.

[165] SH Jeong, R Greif, and RE Russo. Shock wave and material vapour plume propagation during excimer laser ablation of aluminium samples. Journal of Physics D: Applied Physics, 32(19):2578, 1999.

[166] Thomas A Schmitz, Joachim Koch, Detlef Guenther, and Renato Zenobi. Early plume and shock wave dynamics in atmospheric-pressure ultraviolet-laser ablation of different matrix-assisted laser ablation matrices. Journal of Applied Physics, 109(12):123106, 2011.

[167] SH Jeong, R Greif, and RE Russo. Propagation of the shock wave generated from excimer laser heating of aluminum targets in comparison with ideal blast wave theory. Applied surface science, 127:1029–1034, 1998.

[168] X Chen, BM Bian, ZH Shen, J Lu, and XW Ni. Equations of laser-induced plasma shock wave motion in air. Microwave and Optical Technology Letters, 38(1):75–79, 2003.

[169] Zhaoyang Chen and Akos Vertes. Early plume expansion in atmospheric pressure midinfrared laser ablation of water-rich targets. Physical Review E, 77(3):036316, 2008.

[170] Janez Diaci and Janez Možina. A study of blast waveforms detected simultaneously by a microphone and a laser probe during laser ablation. Applied Physics A, 55(4):352–358, 1992.

[171] Jack J Yoh, Hyunhee Lee, Jihee Choi, Kyung-cheol Lee, and Ki-hong Kim. Ablation-induced explosion of metal using a high-power nd: Yag laser. Journal of Applied Physics, 103(4):043511, 2008.

[172] Charles Phelps, Carl J Druffner, Glen P Perram, and Rand R Biggers. Shock front dynamics in the pulsed laser deposition of yba2cu3o7- x. Journal of Physics D: Applied Physics, 40(15):4447, 2007.

[173] H. Li, E. A. Ghezal, A. Nehari, G. Alombert-Goget, A. Brenier, and K. Lebbou. Bubbles defects distribution in sapphire bulk crystals grown by Czochralski technique. Opt. Mater., 35(5):1071, 2013.

[174] H. Li, E. A. Ghezal, G. Alombert-Goget, G. Breton, J. M. Ingargiola, A. Brenier, and K. Lebbou. Qualitative and quantitative bubbles defects analysis in undoped and Ti-doped sapphire crystals grown by Czochralski technique. Opt. Mater., 37:132, 2014.

[175] Dominik Kraus, A Ravasio, M Gauthier, DO Gericke, J Vorberger, S Frydrych, J Helfrich, LB Fletcher, G Schaumann, B Nagler, et al. Nanosecond formation of diamond and lonsdaleite by shock compression of graphite. Nature communications, 7(1):1–6, 2016.

[176] J Hermann and C Dutouquet. Local thermal equilibrium plasma modeling for analyses of gas-phase reactions during reactive-laser ablation. J. Appl. Phys., 91(12):10188–10193, 2002.

[177] Jörg Hermann, Antonella Lorusso, Alessio Perrone, Francesco Strafella, Christophe Dutouquet, and Béatrice Torralba. Simulation of emission spectra from nonuniform reactive laser-induced plasmas. Physical Review E, 92(5):053103, 2015.

[178] Jörg Hermann, Emanuel Axente, Valentin Craciun, Aya Taleb, and Frédéric Pelascini. Evaluation of pressure in a plasma produced by laser ablation of steel. Spectrochimica Acta Part B: Atomic Spectroscopy, 143:63–70, 2018.

[179] Olivier Barthélemy, Joëlle Margot, Stéphane Laville, François Vidal, Mohamed Chaker, Boris Le Drogoff, Tudor W Johnston, and Mohamad Sabsabi. Investigation of the state of local thermodynamic equilibrium of a laser-produced aluminum plasma. Applied spectroscopy, 59(4):529–536, 2005.

[180] Iole Armenise, Mario Capitelli, Claudine Gorse, Mario Cacciatore, and Maria Rutigliano. Nonequilibrium vibrational kinetics of an o/o mixture hitting a catalytic surface. Journal of Spacecraft and Rockets, 37(3):318–323, 2000.

[181] Gabriele Cristoforetti, Alessandro De Giacomo, M Dell'Aglio, Stefano Legnaioli, Elisabetta Tognoni, Vincenzo Palleschi, and Nicolo Omenetto. Local thermodynamic equilibrium in laser-induced breakdown spectroscopy: beyond the mcwhirter criterion. Spectrochimica Acta Part B: Atomic Spectroscopy, 65(1):86–95, 2010.

[182] M Cvejić, Krzysztof Dzierżęga, and Tomasz Pięta. Investigation of thermodynamic equilibrium in laser-induced aluminum plasma using the h alpha line profiles and thomson scattering spectra. Applied Physics Letters, 107(2):024102, 2015.

[183] John D Hey. Criteria for local thermal equilibrium in non-hydrogenic plasmas. Journal of Quantitative Spectroscopy and Radiative Transfer, 16(1):69–75, 1976.

[184] Mario Capitelli, Francesco Capitelli, and Alexander Eletskii. Non-equilibrium and equilibrium problems in laser-induced plasmas. Spectrochimica Acta Part B: Atomic Spectroscopy, 55(6):559–574, 2000.

[185] Anne Hahn, Timo Stoever, Gerrit Paasche, Marian Loebler, Katrin Sternberg, Henning Rohm, and Stephan Barcikowski. Therapeutic Window for Bioactive Nanocomposites Fabricated by Laser Ablation in Polymer-Doped Organic Liquids. Adv. Eng. Mater., 12(5, SI):B156–B162, 2010.

[186] Yong Zhang, Zhenyang Zhao, Tao Xu, GuangHui Niu, Ying Liu, and Yixiang Duan. Characterization of local thermodynamic equilibrium in a laser-induced aluminum alloy plasma. Applied optics, 55(10):2741–2747, 2016.

[187] G Cristoforetti, E Tognoni, and LA Gizzi. Thermodynamic equilibrium states in laser-induced plasmas: from the general case to laser-induced breakdown spectroscopy plasmas. Spectrochimica Acta Part B: Atomic Spectroscopy, 90:1–22, 2013.

[188] Jörg Hermann, David Grojo, Emanuel Axente, and Valentin Craciun. Local thermodynamic equilibrium in a laser-induced plasma evidenced by blackbody radiation. Spectrochimica Acta Part B: Atomic Spectroscopy, 144:82–86, 2018.

[189] C Colon, G Hatem, E Verdugo, P Ruiz, and J Campos. Measurement of the stark broadening and shift parameters for several ultraviolet lines of singly ionized aluminum. Journal of applied physics, 73(10):4752–4758, 1993.

[190] Michel Moisan, Danielle Kéroack, and Luc Stafford. Physique atomique et spectroscopie optique. EDP sciences, 2017.

[191] QL Ma, Vincent Motto-Ros, WQ Lei, Myriam Boueri, XS Bai, LJ Zheng, HP Zeng, and Jin Yu. Temporal and spatial dynamics of laser-induced aluminum plasma in argon background at atmospheric pressure: Interplay with the ambient gas. Spectrochimica Acta Part B: Atomic Spectroscopy, 65(11):896–907, 2010.

[192] Kévin Touchet, Frédéric Chartier, Jörg Hermann, and Jean-Baptiste Sirven. Laser-induced breakdown self-reversal isotopic spectrometry for isotopic analysis of lithium. Spectrochimica Acta Part B: Atomic Spectroscopy, 168:105868, 2020.

[193] Xueshi Bai, Vincent Motto-Ros, Wenqi Lei, Lijuan Zheng, and Jin Yu. Experimental determination of the temperature range of alo molecular emission in laser-induced aluminum plasma in air. Spectrochimica Acta Part B: Atomic Spectroscopy, 99:193–200, 2014.

[194] Pengxu Ran, Huaming Hou, and Sheng-Nian Luo. Molecule formation induced by non-uniform plume–air interactions in laser induced plasma. Journal of Analytical Atomic Spectrometry, 32(11):2254–2262, 2017.

[195] Istvan Kovacs. Rotational Structure in the Spectra of the Diatomic Molecules. Institute of Physics Publishing, London, November 1969.

[196] Maxime Ribière. Spectroscopies d'émission et d'absorption appliquées à l'analyse de plasmas produits par impulsion laser. Thèse de doctorat, Faculté des sciences de Rouen, November 2008.

[197] Xavier Mercier. Spectroscopie électronique : Notions de base et fondamentales. Diaporama présenté lors des Journées du réseau Plasmas Froids du CNRS tenues du 9 au 12 octobre 2012. INSIS, CNRS. PC2A, Université LILLE I, UFR Chimie.

[198] C Zenouda, P Blottiau, G Chambaud, and P Rosmus. Theoretical study of the electronic states of alo and alo-. Journal of Molecular Structure: THEOCHEM, 458(1-2):61–72, 1998.

[199] Géraldine Bontemps Faure. Spectroscopie moléculaire : calcul de spectres, mesures des températures de rotation et de vibration dans les plasmas thermiques. Thèse de doctorat, Université Blaise Pascal, Clermont-Ferrand 2, January 1997.

[200] Olli Launila and Lars-Erik Berg. Spectroscopy of AlO: Combined analysis of the $A^2\Pi_i \rightarrow X^2\Sigma^+$ and $B^2\Sigma^+ \rightarrow X^2\Sigma^+$ transitions. Journal of Molecular Spectroscopy, 265:10–14, January 2011.

[201] J. Hermann, A. Perrone, and C. Dutouquet. Analyses of the TiO-γ system for temperature measurements in a laser-induced plasma. J. Phys. B, 34:153–164, 2001.

[202] John G. Phillips. Molecular Constants of the TiO Molecule. Astrophysical Journal Supplement, 26:313, December 1973.

[203] Julien Lam, David Amans, Frederic Chaput, Mouhamed Diouf, Gilles Ledoux, Nicolas Mary, Karine Masenelli-Varlot, Vincent Motto-Ros, and Christophe Dujardin. γ-Al_2O_3 nanoparticles synthesised by pulsed laser ablation in liquids: a plasma analysis. Physical Chemistry Chemical Physics, 16(3):963–973, December 2013. Publisher: The Royal Society of Chemistry.

[204] Ying Huang, Grant A Risha, Vigor Yang, and Richard A Yetter. Effect of particle size on combustion of aluminum particle dust in air. Combustion and Flame, 156(1):5–13, 2009.

[205] Olivier Varenne, Paul-Guy Fournier, Janine Fournier, Boujemâa Bellaoui, Abdel-Ilah Faké, Joëlle Rostas, and Guy Taieb. Internal population distribution of the b state of alo formed by fast ion beam bombardment or laser ablation of an al2o3 (al) surface. Nuclear Instruments and Methods in Physics Research Section B: Beam Interactions with Materials and Atoms, 171(3):259–276, 2000.

[206] Kazuo Kasatani, Hiroshi Higashide, Hisanori Shinohara, and Hiroyasu Sato. Chemiluminescent reactions studied by laser ablation. detection of alo (b $2\sigma+$) in the al+ o2 system. Chemical physics letters, 174(1):71–74, 1990.

[207] K M Praveen, C V Pious, S Thomas, and Y Grohens. Non-thermal plasma technology for polymeric materials. Applications in Composites, Nanostructured Mateiasl and Biomedical Fields, pages 1–21, 2019.

[208] Xueshi Bai, Fan Cao, Vincent Motto-Ros, Qianli Ma, Yanping Chen, and Jin Yu. Morphology and characteristics of laser-induced aluminum plasma in argon and in air: a comparative study. Spectrochimica Acta Part B: Atomic Spectroscopy, 113:158–166, 2015.

[209] Alessandro De Giacomo and Jörg Hermann. Laser-induced plasma emission: from atomic to molecular spectra. Journal of Physics D: Applied Physics, 50(18):183002, 2017.

[210] A De Giacomo, M Dell'Aglio, O De Pascale, R Gaudiuso, V Palleschi, C Parigger, and A Woods. Plasma processes and emission spectra in laser induced plasmas: a point of view. Spectrochimica Acta Part B: Atomic Spectroscopy, 100:180–188, 2014.

[211] Lev Nagli and Michael Gaft. Combining laser-induced breakdown spectroscopy with molecular laser-induced fluorescence. Applied spectroscopy, 70(4):585–592, 2016.

[212] Sven Hofmann, AFH Van Gessel, Tiny Verreycken, and P Bruggeman. Power dissipation, gas temperatures and electron densities of cold atmospheric pressure helium and argon rf plasma jets. Plasma Sources Science and Technology, 20(6):065010, 2011.

[213] Colin M Western, Luke Carter-Blatchford, Patrick Crozet, Amanda J Ross, Jérôme Morville, and Dennis W Tokaryk. The spectrum of n2 from 4,500 to 15,700 cm- 1 revisited with pgopher. Journal of Quantitative Spectroscopy and Radiative Transfer, 219:127–141, 2018.

[214] QY Zhang, DQ Shi, W Xu, CY Miao, CY Ma, CS Ren, C Zhang, and Z Yi. Determination of vibrational and rotational temperatures in highly constricted nitrogen plasmas by fitting the second positive system of n2 molecules. AIP Advances, 5(5):057158, 2015.

[215] J Raud, M Laan, and I Jõgi. Rotational temperatures of n2 (c, 0) and oh (a, 0) as gas temperature estimates in the middle pressure ar/o2 discharge. Journal of Physics D: Applied Physics, 44(34):345201, 2011.

[216] Tiny Verreycken, DC Schram, Christophe Leys, and P Bruggeman. Spectroscopic study of an atmospheric pressure dc glow discharge with a water electrode in atomic and molecular gases. Plasma Sources Science and Technology, 19(4):045004, 2010.

[217] Malcolm W Chase. Nist-janaf thermochemical tables for oxygen fluorides. Journal of physical and chemical reference data, 25(2):551–603, 1996.

[218] IM Hedgecock, C Naulin, and M Costes. Measurements of the radiative lifetimes of tio (aˆ 3phi, bˆ 3pi, cˆ 3delta, cˆ 1phi, fˆ 1delta, eˆ 3pi) states. Astronomy and Astrophysics, 304:667, 1995.

[219] SE Johnson, G Capelle, and HP Broida. Laser excited fluorescence and radiative lifetimes of alo (b $2\sigma+$- x $2\sigma+$). The Journal of Chemical Physics, 56(1):663–665, 1972.

[220] Mingfang Cai, Christopher C Carter, Terry A Miller, and VE Bondybey. Fluorescence excitation and resolved emission spectra of supersonically cooled al2o. The Journal of chemical physics, 95(1):73–79, 1991.

[221] Lei Liu, Leimin Deng, Lisha Fan, Xi Huang, Yao Lu, Xiaokang Shen, Lan Jiang, Jean-François Silvain, and Yongfeng Lu. Time-resolved resonance fluorescence spectroscopy for study of chemical reactions in laser-induced plasmas. Optics express, 25(22):27000–27007, 2017.

[222] George Gabriel Stokes. Xxx. on the change of refrangibility of light. Philosophical transactions of the Royal Society of London, 142:463–562, 1852.

[223] Michael Kasha. Characterization of electronic transitions in complex molecules. Discussions of the Faraday society, 9:14–19, 1950.

[224] PJ Dagdigian, H W_ Cruse, and R_N Zare. Laser fluorescence study of alo formed in the reaction al+ o2: Product state distribution, dissociation energy, and radiative lifetime. The Journal of Chemical Physics, 62(5):1824–1833, 1975.

[225] Neil J Reilly, Timothy W Schmidt, and Scott H Kable. Two-dimensional fluorescence (excitation/emission) spectroscopy as a probe of complex chemical environments. The Journal of Physical Chemistry A, 110(45):12355–12359, 2006.

[226] Jason R Gascooke, Ula N Alexander, and Warren D Lawrance. Two dimensional laser induced fluorescence spectroscopy: A powerful technique for elucidating rovibronic structure in electronic transitions of polyatomic molecules. The Journal of chemical physics, 134(18):184301, 2011.

[227] Jason R Gascooke and Warren D Lawrance. Two dimensional laser induced fluorescence in the gas phase: a spectroscopic tool for studying molecular spectroscopy and dynamics. The European Physical Journal D, 71(11):1–15, 2017.

[228] Xilin Bai and Timothy C Steimle. The stark effect, zeeman effect, and transition dipole moments for the b $2\sigma+$- x $2\sigma+$ band of aluminum monoxide, alo. The Astrophysical Journal, 889(2):147, 2020.

[229] G R Hebert, R W Nicholls, and C Linton. Absolute band strengths for the alo blue-green($B^2\Sigma - X^2\Sigma$) band system. J. Quant. Spectrosc. Radiat. Transf., 23:229, 1980.

[230] M. D. Saksena, M. N. Deo, K. Sunanda, S. H. Behere, and C. T. Londhe. Fourier transform spectral study of $B^2\Sigma^+ - X^2\Sigma^+$ system of AlO. J. Mol. Spectrosc., 247:47, 2008.

[231] O. Launila and L-E Berg. Spectroscopy of AlO: Combined analysis of the $A^2\Pi_i \rightarrow X^2\Sigma^+$ and $B^2\Sigma^+ \rightarrow X^2\Sigma^+$ transitions. J. Mol. Spectrosc., 265:10, 2011.

[232] J. B. Tatum. Höln-London Factors for $^3\Phi - {}^3\Delta$ Systems. Mon. Not. Roy. Astron. Soc., 141:459–467, 1968.

[233] R. S. Ram, P. F. Bernath, M. Dulick, and L. Wallace. The $A^3\Phi - X^3\Delta$ System (γ bands) of TiO: Laboratory and sunspot measurements. Astrophys. J., 122:331–353, 1999.

[234] Co Co J Roothaan. A study of two-center integrals useful in calculations on molecular structure. i. The Journal of Chemical Physics, 19(12):1445–1458, 1951.

[235] M. Born and R. Oppenheimer. Zur quantentheorie der molekeln. Annalen der Physik, 389(20):457–484.

[236] Loic Barnes. Theoretical study of saccharides : structures and infrared spectra. Theses, Université de Lyon, September 2017.

[237] J. C. Slater. Atomic shielding constants. Phys. Rev., 36:57–64, Jul 1930.

[238] Dhatfield. Atomic orbital, 2012.

[239] Michael J Frisch, John A Pople, and J Stephen Binkley. Self-consistent molecular orbital methods 25. supplementary functions for gaussian basis sets. The Journal of chemical physics, 80(7):3265–3269, 1984.

[240] RBJS Krishnan, J Stephen Binkley, Rolf Seeger, and John A Pople. Self-consistent molecular orbital methods. xx. a basis set for correlated wave functions. The Journal of Chemical Physics, 72(1):650–654, 1980.

[241] Warren J Hehre, Robert Ditchfield, and John A Pople. Self—consistent molecular orbital methods. xii. further extensions of gaussian—type basis sets for use in molecular orbital studies of organic molecules. The Journal of Chemical Physics, 56(5):2257–2261, 1972.

[242] Pierre Hohenberg and Walter Kohn. Inhomogeneous electron gas. Physical review, 136(3B):B864, 1964.

[243] Walter Kohn and Lu Jeu Sham. Self-consistent equations including exchange and correlation effects. Physical review, 140(4A):A1133, 1965.

[244] GL Oliver and JP Perdew. Spin-density gradient expansion for the kinetic energy. Physical Review A, 20(2):397, 1979.

[245] Seymour H Vosko, Leslie Wilk, and Marwan Nusair. Accurate spin-dependent electron liquid correlation energies for local spin density calculations: a critical analysis. Canadian Journal of physics, 58(8):1200–1211, 1980.

[246] Axel D Becke. Density-functional exchange-energy approximation with correct asymptotic behavior. Physical review A, 38(6):3098, 1988.

[247] Chengteh Lee, Weitao Yang, and Robert G Parr. Development of the colle-salvetti correlation-energy formula into a functional of the electron density. Physical review B, 37(2):785, 1988.

[248] Axel D Becke. Density-functional thermochemistry. iii. the role of exact exchange. The Journal of chemical physics, 98(7):5648–5652, 1993.

[249] S K Sundaram and Eric Mazur. Inducing and probing non-thermal transitions in semiconductors using femtosecond laser pulses. Nature materials, 1(4):217–224, 2002.

[250] Koichi Sasaki, Tetsutaro Nakano, Wafaa Soliman, and Noriharu Takada. Effect of pressurization on the dynamics of a cavitation bubble induced by liquid-phase laser ablation. Appl. Phys. Express, 2:046501, 2009.

[251] M. Tiberi, A. Simonelli, G. Cristoforetti, P. Marsili, F. Giammanco, and E. Giorgetti. Effect of picosecond laser induced cavitation bubbles generated on Au targets in a nanoparticle production set-up. Appl. Phys. A-Mater. Sci. Process., 110(4):857–861, 2013.

[252] J. Tomko, J. J. Naddeo, R. Jimenez, Y. Tan, M. Steiner, J. M. Fitz-Gerald, D. M. Bubb, and S. M. O'Malley. Size and polydispersity trends found in gold nanoparticles synthesized by laser ablation in liquids. Phys. Chem. Chem. Phys., 17(25):16327–16333, 2015.

[253] Rie Tanabe, Thao T. P. Nguyen, Takahiro Sugiura, and Yoshiro Ito. Bubble dynamics in metal nanoparticle formation by laser ablation in liquid studied through high-speed laser stroboscopic videography. Appl. Surf. Sci., 351:327–331, 2015.

[254] Thao Thi Phuong Nguyen, Rie Tanabe-Yamagishi, and Yoshiro Ito. Effects of liquid depth on the expansion and collapse of a hemispherical cavitation bubble induced in nanosecond pulsed laser ablation of a solid in liquid. Opt. Lasers Eng., 126:UNSP 105937, MAR 2020.

[255] Jiangyou Long, Matthew Eliceiri, Zacharias Vangelatos, Yoonsoo Rho, Letian Wang, Zhengliang Su, Xiaozhu Xie, Yongkang Zhang, and Costas P. Grigoropoulos. Early dynamics of cavitation bubbles generated during ns laser ablation of submerged targets. Opt. Express, 28(10):14300–14309, May 2020.

[256] L. Marti-Lopez, R. Ocana, J. A. Porro, M. Morales, and J. L. Ocana. Optical observation of shock waves and cavitation bubbles in high intensity laser-induced shock processes. Appl. Optics, 48(19):3671–3680, JUL 1 2009.

[257] Haofeng Hu, Tiegen Liu, and Hongchen Zhai. Comparison of femtosecond laser ablation of aluminum in water and in air by time-resolved optical diagnosis. Opt. Express, 23(2):628–635, 2015.

[258] Zhi Zhang, Aosong Wang, Jian Wu, YanZhang Liu, Dapeng Huang, Yan Qiu, and Jilong Li. Spatial confinement effects of bubbles produced by laser ablation in liquids. AIP Adv., 9(12):125048, 2019.

[259] JM Richardson, AB Arons, and RR Halverson. Hydrodynamic properties of sea water at the front of a shock wave. The Journal of Chemical Physics, 15(11):785–794, 1947.

[260] Sadi Ridah. Shock waves in water. Journal of applied physics, 64(1):152–158, 1988.

[261] R Fabbro, J Fournier, P Ballard, D Devaux, and J Virmont. Physical study of laser-produced plasma in confined geometry. J. Appl. Phys., 68:775, 1990.

[262] Shih-Jeh Wu, Pei-Chieh Chin, and Hawking Liu. Measurement of elastic properties of brittle materials by ultrasonic and indentation methods. Applied Sciences, 9(10):2067, 2019.

[263] Hansang Kim, Lawrence Yoo, Andrew Shin, and Joseph L Demer. Determination of poisson ratio of bovine extraocular muscle by computed x-ray tomography. BioMed research international, 2013:197479, 2013.

[264] YN Feng, YP Li, CL Liu, and ZJ Zhang. Assessing the elastic properties of skeletal muscle and tendon using shearwave ultrasound elastography and myotonpro. Scientific reports, 8(1):1–9, 2018.

[265] D. Gasteau, N. Chigarev, L. Ducousso-Ganjehi, V. E. Gusev, F. Jenson, P. Calmon, and V. Tournat. Single crystal elastic constants evaluated with surface acoustic waves generated and detected by lasers within polycrystalline steel samples. J. Appl. Phys., 119(4):043103, 2016.

[266] Antonio Palermo, Sebastian Krödel, Alessandro Marzani, and Chiara Daraio. Engineered metabarrier as shield from seismic surface waves. Scientific reports, 6(1):1–10, 2016.

[267] Andrea Colombi, Daniel Colquitt, Philippe Roux, Sebastien Guenneau, and Richard V Craster. A seismic metamaterial: The resonant metawedge. Scientific reports, 6(1):1–6, 2016.

[268] Andrea Colombi, Victoria Ageeva, Richard J Smith, Adam Clare, Rikesh Patel, Matt Clark, Daniel Colquitt, Philippe Roux, Sebastien Guenneau, and Richard V Craster. Enhanced sensing and conversion of ultrasonic rayleigh waves by elastic metasurfaces. Scientific reports, 7(1):1–9, 2017.

[269] Dongbo Zhang, Jinfeng Zhao, Bernard Bonello, Fenglin Zhang, Weitao Yuan, Yongdong Pan, and Zheng Zhong. Investigation of surface acoustic wave propagation in composite pillar based phononic crystals within both local resonance and bragg scattering mechanism regimes. Journal of Physics D: Applied Physics, 50(43):435602, 2017.

[270] Giovanni Occhipinti, Florent Aden-Antoniow, Aurélien Bablet, Jean-Philippe Molinie, and Thomas Farges. Surface waves magnitude estimation from ionospheric signature of rayleigh waves measured by doppler sounder and oth radar. Scientific reports, 8(1):1–7, 2018.

[271] Jinying Zhu, John S Popovics, and Frank Schubert. Leaky rayleigh and scholte waves at the fluid–solid interface subjected to transient point loading. The Journal of the Acoustical Society of America, 116(4):2101–2110, 2004.

[272] Zhao Yan. Influence of acoustic leakage at fluid–solid interface on interferometric detection of surface acoustic wave. Optik, 125(10):2458–2462, 2014.

[273] Tor Arne Johansen, Bent Ole Ruud, and Gaute Hope. Seismic on floating ice on shallow water: Observations and modeling of guided wave modes. Geophysics, 84(2):P1–P13, 2019.

[274] Marcus Landschulze. Seismic wave propagation in floating ice sheets–a comparison of numerical approaches and forward modelling. Near Surface Geophysics, 16(5):493–505, 2018.

[275] X Jian, Y Fan, RS Edwards, and S Dixon. Surface-breaking crack gauging with the use of laser-generated rayleigh waves. Journal of applied physics, 100(6):064907, 2006.

[276] Suyun Ham and John S Popovics. Application of contactless ultrasound toward automated inspection of concrete structures. Automation in Construction, 58:155–164, 2015.

[277] Jakub Chmelar, Karel Petr, Pavel Mossoczy, and Vojtech Dynybyl. Experimental study of lubrication film monitoring in a roller bearing by utilization of surface acoustic waves. Tribology International, 141:105908, 2020.

[278] David Veysset, AA Maznev, István A Veres, Thomas Pezeril, Steven E Kooi, Alexey M Lomonosov, and Keith A Nelson. Acoustical breakdown of materials by focusing of laser-generated rayleigh surface waves. Applied Physics Letters, 111(3):031901, 2017.

[279] David Veysset, Steven E Kooi, Ryadh Haferssas, Mostafa Hassani-Gangaraj, Mohammad Islam, AA Maznev, Yevheniia Chernukha, Xiaoguang Zhao, Keiichi Nakagawa, Dmitro Martynowych, et al. Glass fracture by focusing of laser-generated nanosecond surface acoustic waves. Scripta Materialia, 158:42–45, 2019.

[280] RE Vines, Shin-ichiro Tamura, and JP Wolfe. Surface acoustic wave focusing and induced rayleigh waves. Physical review letters, 74(14):2729, 1995.

[281] Younghoon Sohn and Sridhar Krishnaswamy. Interaction of a scanning laser-generated ultrasonic line source with a surface-breaking flaw. The Journal of the Acoustical Society of America, 115(1):172–181, 2004.

[282] Al A Kolomenskii, AM Lomonosov, R Kuschnereit, P Hess, and VE Gusev. Laser generation and detection of strongly nonlinear elastic surface pulses. Physical review letters, 79(7):1325, 1997.

[283] A Lomonosov, VG Mikhalevich, P Hess, E Yu Knight, Mark F Hamilton, and EA Zabolotskaya. Laser-generated nonlinear rayleigh waves with shocks. The Journal of the Acoustical Society of America, 105(4):2093–2096, 1999.

[284] David Amans, Weiping Cai, and Stephan Barcikowski. Status and demand of research to bring laser generation of nanoparticles in liquids to maturity. Appl. Surf. Sci., 488:445–454, 2019.

[285] T. T. P. Nguyen, R. Tanabe, and Y. Ito. Laser-induced shock process in under-liquid regime studied by time-resolved photoelasticity imaging technique. Appl. Phys. Lett., 102(12):124103, 2013.

[286] Thao Thi Phuong Nguyen, Rie Tanabe-Yamagishi, and Yoshiro Ito. Impact of liquid layer thickness on the dynamics of nano- to sub-microsecond phenomena of nanosecond pulsed laser ablation in liquid. Appl. Surf. Sci., 470:250–258, 2019.

[287] G W Yang, J B Wang, and Q X Liu. Preparation of nano-crystalline diamonds using pulsed laser induced reactive quenching. J. Phys.-Condes. Matter, 10(35):7923–7927, SEP 7 1998.

[288] X. D. Ren, S. X. Tang, L. M. Zheng, S. Q. Yuan, N. F. Ren, H. M. Yang, Y. Wang, W. F. Zhou, and S. D. Xu. Direct transfer-adsorption: The new molecular dynamics transition mechanism of nano-diamond preparation by laser shock processing. J. Cryst. Growth, 421:1–7, JUL 1 2015.

[289] P Liu, Y. L. Cao, X. Y. Chen, and G. W. Yang. Trapping high-pressure nanophase of ge upon laser ablation in liquid. Crystal Growth & Design, 9(3):1390–1393, 2009.

[290] R Fabbro, J Fournier, P Ballard, D Devaux, and J Virmont. Physical study of laser-produced plasma in confined geometry. Journal of applied physics, 68(2):775–784, 1990.

[291] L Berthe, R Fabbro, P Peyre, L Tollier, and E Bartnicki. Shock waves from a water-confined laser-generated plasma. Journal of Applied Physics, 82(6):2826–2832, 1997.

[292] Ying Zhang, Chen Yang, Hao Qiang, and Pei Zhong. Nanosecond shock wave-induced surface acoustic waves and dynamic fracture at fluid-solid boundaries. Physical Review Research, 1(3):033068, 2019.

[293] Daniel Royer and Dominique Clorennec. An improved approximation for the rayleigh wave equation. Ultrasonics, 46(1):23–24, 2007.

[294] Christ Glorieux, Kris Van de Rostyne, Keith Nelson, Weimin Gao, Walter Lauriks, and Jan Thoen. On the character of acoustic waves at the interface between hard and soft solids and liquids. The Journal of the Acoustical Society of America, 110(3):1299–1306, 2001.

[295] Shivakumar I. Ranganathan and Martin Ostoja-Starzewski. Universal elastic anisotropy index. Phys. Rev. Lett., 101(5), 2008.

[296] Zuocai Huang, Jing Feng, and Wei Pan. Elastic properties of YAG: First-principles calculation and experimental investigation. Solid State Sci., 14(9):1327–1332, 2012.

[297] J Kushibiki, M Arakawa, and R Okabe. High-accuracy standard specimens for the line-focus-beam ultrasonic material characterization system. IEEE Trans. Ultrason. Ferroelectr. Freq. Control, 49(6):827–835, 2002.